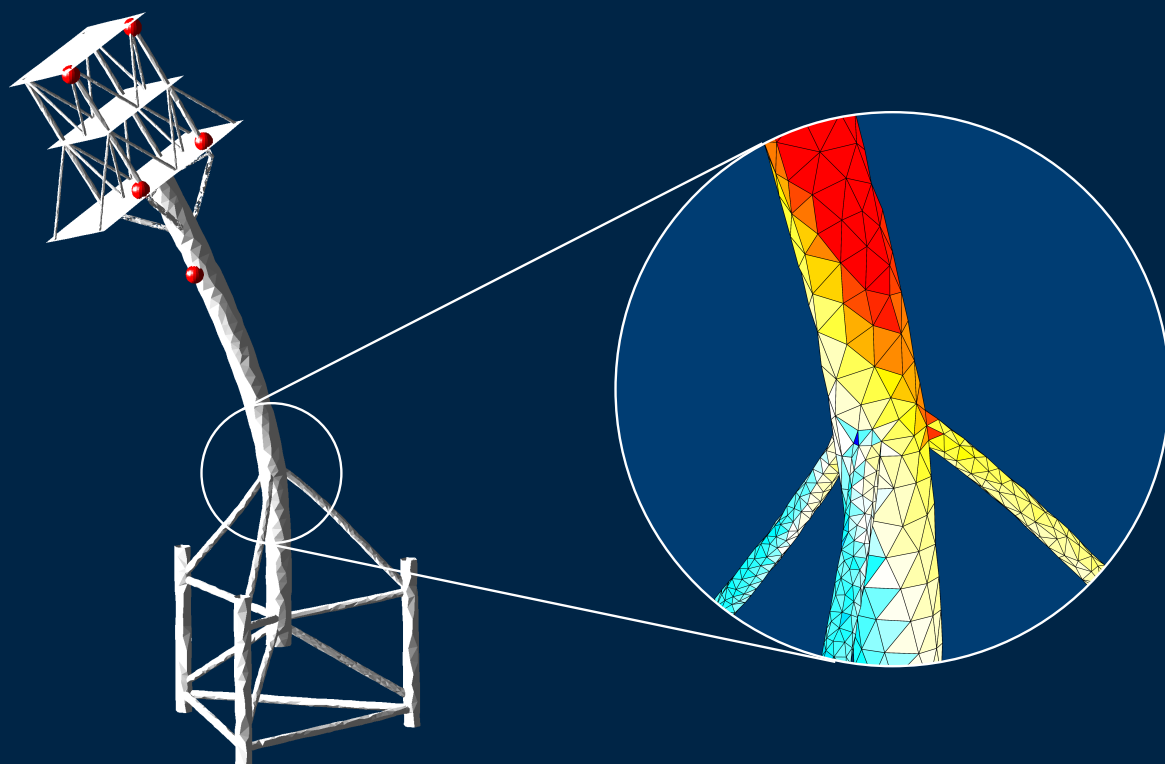


STRESS ESTIMATION OF OFFSHORE STRUCTURES



Marius Tarpø
Department of Engineering
Aarhus University

A dissertation submitted for the degree of
Doctor of Philosophy

July, 2020



AARHUS
UNIVERSITY

DEPARTMENT OF ENGINEERING

AARHUS UNIVERSITY

DOCTORAL THESIS

Stress Estimation of Offshore Structures

Author:
Marius Tarpø

Supervisors:
Christos Georgakis, Aarhus University
Rune Brincker, Technical University of Denmark

*A thesis submitted in fulfilment of the requirements
for the degree of Doctor of Philosophy*

in the

Structural Dynamics and Monitoring Group
Department of Engineering, Aarhus University

July 28th 2020



AARHUS
UNIVERSITY

DEPARTMENT OF ENGINEERING

Thesis Submitted: July 28th, 2020

Ph.D. Supervisors: Professor Christos Georgakis
Department of Engineering, Aarhus University, Denmark
Professor Rune Brincker
Department of Civil Engineering, Technical University of Denmark, Denmark

Ph.D. Committee: Associate Professor Jochen Teizer (chair)
Department of Engineering, Aarhus University, Denmark
Professor Christof Devriend
Department of Mechanical Engineering, Vrije Universiteit Brussel, Belgium
Senior Researcher Dmitri Tcherniak
Bruel and Kjaer Sound and Vibration Measurements A/S, Denmark

Defence date: October 13th, 2020, online and at Navitas, Aarhus, Denmark

Revision date: November 2020

Revision comments: *In this revision, there are minor corrections for language, corrections of layout, updated status of papers, and the addition of a single reference in section 2.3*

Declaration of authorship

I, Marius Tarpø, declare that this thesis entitled, “Stress Estimation of Offshore Structures” and the work presented in it are my own. I confirm that:

- This work was conducted wholly or mainly while in candidature for a research degree at Aarhus University.
- Where any part of this thesis has previously been submitted for a degree or any other qualification at this University or any other institution, this has been clearly stated.
- Where I have consulted the published work of others, this is always clearly attributed.
- Where I have quoted from the work of others, the source is always given. Except for such quotations, this thesis is entirely my work.
- I have acknowledged all main sources of help.
- Where the thesis is based on work performed by myself jointly with others, I have made clear exactly what was done by others and what I have contributed myself.

Abstract

Offshore structures are subjected to a harsh environment where the fluctuating waves continuously strain the structures and these forces cause the initiation and propagation of cracks in the structures. In other words, the structures accumulate fatigue damage, which eventually leads to structural failure. To avoid fatigue failure, the operational lifetime of a structure is limited to a design lifetime in which the structure is safe for operation. This design process is based on precautionous stochastic assessments, norms, and industry standards that simplify the actual structure and environment in such a manner that it involves little risk of structural failure.

As many structures in the North Sea approach the end of their design lifetime, the owners are faced with a dilemma: either abandon the field or replace the structures. Another option is the lifetime extension of the existing structures. This requires a reduction of the uncertainties in the design process - such as the stress history in fatigue-critical location. Unfortunately, these locations are often inaccessible or directly harmful to the sensors due to the hostile environment of the ocean. This thesis focuses on virtual sensing to estimate the stress/strain response of offshore structures by indirect measurements. The thesis addresses the state of the art and maps some essential issues within stress/strain estimation. In this thesis, stress/strain estimation is applied to different test specimens to address certain scientific issues. Parts of the thesis relate to the calibration of the system model for virtual sensing by operational modal analysis.

Resumé

Offshore-konstruktioner udsættes for et hårdt miljø, hvor de vekslende bølger kontinuerligt belaster konstruktionerne, og disse kræfter medfører initiering og udbredelse af revner i strukturerne. Med andre ord akkumulerer konstruktionerne skader i form af udmattelse af materialet, hvilket til sidst fører til strukturel svigt. For at undgå udmattelsesbrud er driftslevetiden for en konstruktion begrænset til en design-levetid, hvor konstruktionen er sikker under drift. Denne designproces er baseret på forsigtige stokastiske vurderinger, normer og industristandarder, der forenkler den faktiske struktur og miljø på en sådan måde, at det indebærer en lille risiko for konstruktionssvigt.

Da mange strukturer i Nordsøen nærmer sig afslutningen på designlevetiden, står ejerne over for et dilemma: enten skal de forlade feltet eller erstatte strukturer. En helt anden mulighed er udvidelse af levetiden af de eksisterende konstruktioner. Dette kræver en reduktion af usikkerheden fra designprocessen - ligesom spændingshistorikken i kritiske lokationer for udmattelse. Desværre er disse placeringer ofte utilgængelige eller direkte skadelige for sensorerne grundet det fjendtlige miljø, som opstår på grund af havet. Denne afhandling fokuserer på virtuel sensing for at estimere spændinger/tøjninger af offshore konstruktioner ved indirekte målinger. Afhandlingen adresserer den aktuelle og nyeste teori og anvendelsesmuligheder, og den kortlægger nogle væsentlige problemer indenfor spænding/tøjning estimering. I denne afhandling anvendes spænding/tøjning estimering på forskellige testeksempler for at adressere visse videnskabelige problemer. Dele af afhandlingen vedrører kalibrering af systemmodellen til virtuel sensing ved anvendelse af operationel modal analyse.

Acknowledgements

It takes a lot of hard work to accumulate and write a Ph.D. thesis. During this Ph.D. project, my eyesight has worsened and my hairline has receded further back than I like to acknowledge. Fortunately, it has also been an interesting and fun time that I am extremely grateful for. It would, however, never have been possible without the help of various people and I would like to thank these people.

I thank my supervisors prof. Christos Georgakis and prof. Rune Brincker for supporting, supervising, pushing, and believing in me and my ideas. I very much appreciate this opportunity for a Ph.D. position and I thank both of you for all the wisdom and knowledge that you have shared throughout this project. I am grateful for the concern and calming words from prof. Christos Georgakis when I was stressed out halfway through the Ph.D. project and when I had to work from home due to the coronavirus while taking care of my daughter. Furthermore, I send my regards to prof. Rune Brincker for inviting me to stay at the Technical University of Denmark (DTU).

I thank my colleagues at Aarhus University (AU) in random order; Michael Vigsø, Thomas Kabel, Julie Carøe Kristoffersen, Lubomír Matejíčka, Jannick Balleby Hansen, Martin Juul, Anders Skaftø, and Peter Olsen. I am grateful for your help, discussions, collaborations, words of encouragement, bad jokes, and insight throughout the Ph.D. project. I think fondly of our coffee breaks, beers on Fridays, the growing and tasting of chilli in the office, the random rebuses on the whiteboard, and our competitions to guess the first natural frequency of different structures. Furthermore, an acknowledgement is needed to my collaborators at the Technical University of Denmark (DTU); Tobias Friis and Bruna Nabuco. I appreciate your prompt help over mail, our many long Skype/phone meetings, and your courtesy and kindness whenever I visited DTU desperately looking for assistance. Additionally, I thank all the inspirational people that I have been so fortunate to meet at conferences and other research events around the world. Your comments and suggestions have helped to progress my project. Furthermore, I thank assoc. prof. Rubén Boroschek from the University of Chile for sharing his knowledge on rotating/tilting accelerometers and I thank Ulf Tyge Tygesen from Ramboll for his collaboration on strain estimation of the Valdemar platform.

I acknowledge the funding received from the Centre for Oil and Gas - DTU/Danish Hydrocarbon Research and Technology Centre (DHRTC). Without DHRTC, this Ph.D. thesis would never have seen the light of day and I am grateful for this opportunity.

I have been stressed and absent-minded in periods of the Ph.D. project and I thank my family and friends for their support through these periods. I am particularly grateful for the help and support that I received while the coronavirus swept across the world and I had to stay home with my daughter for five weeks while I wrote this thesis. Especially, I am grateful for the patience and support of my wife and daughter.

Thank you,
Marius Tarpø

Publications

Throughout the Ph.D. project, the research has been presented to the research community in written and oral presentations.

Appended papers

The following papers are deemed representable of the main research conducted during the Ph.D. and they are appended in the dissertation as the main body of work.

- Paper 1 *The statistical errors of the estimated correlation function matrix for operational modal analysis*
M. Tarpø, T. Friis, C. Georgakis, & R. Brincker
Journal of Sound and Vibrations, 2019
- Paper 2 *Automated reduction of statistical errors in the estimated correlation function matrix for operational modal analysis*
M. Tarpø, T. Friis, P. Olsen, M. Juul, C. Georgakis, & R. Brincker
Mechanical Systems and Signal Processing, 2019
- Paper 3 *Modal truncation in experimental modal analysis*
M. Tarpø, M. Vigsø, & R. Brincker
Conference proceedings of the International Modal Analysis Conference, IMAC 2018
- Paper 4 *Expansion of experimental mode shape from operational modal analysis and virtual sensing for fatigue analysis using the modal expansion method*
M. Tarpø, B. Nabuco, C. Georgakis, & R. Brincker
International Journal of Fatigue in a special issue on Fatigue in Structural Integrity of Offshore Energy Industry, 2020
- Paper 5 *Full-field strain estimation of subsystems within time-varying and nonlinear systems using modal expansion*
M. Tarpø, T. Friis, C. Georgakis, & R. Brincker
Under review at Mechanical Systems and Signal Processing, November 2019
- Paper 6 *Tilt errors of linear accelerometers attached to dynamic systems with tilt motion caused by the system response*
M. Tarpø, B. Nabuco, R. Boroschek, & R. Brincker
Submitted to Journal of Sound and Vibrations
- Paper 7 *Preliminary study: Quasi-static strain estimation above water for an offshore tripod structure in the North Sea*
M. Tarpø, B. Nabuco, U.T. Tygesen, C. Georgakis, & R. Brincker
Unpublished paper

Other papers

The following papers were published or written during the Ph.D. project but they are excluded from the Ph.D. thesis. The reader is referred to Appendix A for a brief summary of these papers.

Main author

- *Experimental determination of structural damping of a full-scale building with and without tuned liquid dampers*
M. Tarpø, C. Georgakis, A. Brandt, & R. Brincker
Submitted to Structural Control and Health Monitoring, summer 2020
- *The effect of operational modal analysis in strain estimation using the modal expansion*
M. Tarpø, B. Nabuco, C. Geargakis, & R. Brincker
Conference proceedings of the International Operational Modal Analysis Conference, IOMAC 2019
- *Statistical error reduction for correlation-driven operational modal analysis*
M. Tarpø, P. Olsen, M. Juul, S. Amador, T. Friis, & R. Brincker
Conference proceedings of the International Conference on Noise and Vibration Engineering, ISMA 2018
- *Operational modal analysis based stress estimation in friction systems*
M. Tarpø, T. Friis, B. Nabuco, S. Amador, E. Katsanos, & R. Brincker
Conference proceedings of the International Modal Analysis Conference, IMAC 2018
- *On minimizing the influence of the noise tail of correlation functions in operational modal analysis*
M. Tarpø, P. Olsen, S. Amador, M. Juul, & R. Brincker
Procedia Engineering 199, 1038-1043
- *Operational modal analysis based prediction of actual stress in an offshore structural model*
M. Tarpø, B. Nabuco, A. Skafte, J. Kristoffersen, J. Vestermark, S. Amador, & R. Brincker
Procedia Engineering 199, 2262-2267

Co-author

- *Best linear approximation of nonlinear and nonstationary systems using Operational Modal Analysis*
T. Friis, **M. Tarpø**, E. Katsanos, & R. Brincker
Mechanical Systems and Signal Processing
- *Fatigue Stress Estimation of an Offshore Jacket Structure Based on Operational Modal Analysis*
Bruna Nabuco, **M. Tarpø**, U. T. Tygesen, & R. Brincker
Shock and Vibration in a special issue on Dynamics and Vibration Analysis of Oil and Gas Equipment, 2020
- *Automated operational modal analysis using sliding filters and time domain identification techniques*
P. Olsen, **M. Tarpø**, M. Juul, & R. Brincker
Submitted to Mechanical Systems and Signal Processing, spring 2020
- *Equivalent linear systems of nonlinear systems*
T. Friis, **M. Tarpø**, E. Katsanos, & R. Brincker
Journal of Sound and Vibrations, 2020
- *Operational modal analysis based linear system identification of systems with elasto-perfectly-plastic non-linear behaviour*
T. Friis, **M. Tarpø**, E. Katsanos, & R. Brincker
Conference proceedings of the International Operational Modal Analysis Conference, IOMAC 2019
- *Operational modal analysis and fluid-structure interaction*
M. Vigsø, T. Kabel, **M. Tarpø**, R. Brincker, & C. Georgakis
Conference proceedings of the International Conference on Noise and Vibration Engineering, ISMA 2018

- *Output-only damping estimation of friction systems in ambient vibrations*
T. Friis, E. Katsanos, **M. Tarpø**, S. Amador, & R. Brincker
Conference proceedings of the International Conference on Noise and Vibration Engineering, ISMA 2018
- *Nonlinear strain estimation based on linear parameters*
B. Nabuco, T. Friis, **M. Tarpø**, S. Amador, E. Katsanos, & R. Brincker
ASME 2018 37th International Conference on Ocean, Offshore and Arctic Engineering
- *Scenario based approach for load identification*
M. Vigsø, **M. Tarpø**, J.B. Hansen, C.T. Georgakis, & R. Brincker
Conference proceedings of the International Modal Analysis Conference, IMAC 2018
- *Reliability Analysis of Offshore Structures Using OMA Based Fatigue Stresses*
B. Nabuco, **M. Tarpø**, A. Aïssani, & R. Brincker
ASME 2017 36th International Conference on Ocean, Offshore and Arctic Engineering

Oral presentations

The research of this thesis was been orally presented at the following events:

- Eurodyn 2017, Rome, Italy
Operational modal analysis based prediction of actual stress in an offshore structural model
- Eurodyn 2017, Rome, Italy
On minimizing the influence of the noise tail of correlation functions in operational modal analysis
- DHRTC Technology Conference 2017, Kolding, Denmark
OMA-based strain estimation of friction systems
- International Modal Analysis Conference, IMAC 2018, Orlando, United States
Operational Modal Analysis based Stress Estimation in Friction Systems
- International Modal Analysis Conference, IMAC 2018, Orlando, United States
Modal Truncation in Experimental Modal Analysis
- International Conference on Noise and Vibration Engineering, ISMA 2018, Leuven, Belgium
Statistical error reduction for correlation-driven operational modal analysis
- International Operational Modal Analysis Conference, IOMAC 2019, Copenhagen, Denmark
The effect of operational modal analysis in strain estimation using the modal expansion
- DHRTC Technology Conference 2019, Kolding, Denmark, presented by prof. Rune Brincker due to illness
Stress estimation for nonlinear structures

Contents

| | |
|---|------------|
| Declaration of authorship | iii |
| Abstract | v |
| Resumé | vii |
| Acknowledgements | ix |
| Publications | xi |
| | |
| I Preliminaries | 1 |
| 1 Introduction | 3 |
| 1.1 Background | 3 |
| 1.2 Motivation | 4 |
| 1.3 Aim of Ph.D. project | 6 |
| 1.4 Outline of Ph.D. thesis | 6 |
| 2 Basic theory | 9 |
| 2.1 Structural dynamics | 9 |
| 2.2 Operational modal analysis | 10 |
| 2.3 Mechanics of material | 11 |
| 2.4 Fatigue | 12 |
| 3 Narrative literature review of stress/strain estimation | 15 |
| 3.1 Introduction to virtual sensing and stress/strain estimation | 15 |
| 3.2 History | 17 |
| 3.3 System model | 22 |
| 3.4 Physical sensors | 26 |
| 3.5 Process models | 26 |
| 3.6 Discussion | 30 |
| 3.7 Conclusion | 36 |
| 3.8 Planning and framing the Ph.D. project | 37 |
| | |
| II Contributions | 43 |
| 4 Paper 1 - The statistical errors in the estimated correlation function matrix for operational modal analysis | 45 |
| 4.1 Introduction | 45 |
| 4.2 Contribution | 45 |
| 4.3 Main findings | 45 |
| 4.4 Reflections | 46 |
| 4.5 Appended paper | 47 |

| | | |
|-----------|---|------------|
| 5 | Paper 2 - Automated reduction of statistical errors in the estimated correlation function matrix for operational modal analysis | 81 |
| 5.1 | Introduction | 81 |
| 5.2 | Contribution | 81 |
| 5.3 | Main findings | 81 |
| 5.4 | Reflection | 82 |
| 5.5 | Appended paper | 83 |
| 6 | Paper 3 - Modal truncation in experimental modal analysis | 101 |
| 6.1 | Introduction | 101 |
| 6.2 | Contribution | 101 |
| 6.3 | Main findings | 101 |
| 6.4 | Reflection | 102 |
| 6.5 | Appended paper | 103 |
| 7 | Paper 4 - Expansion of experimental mode shape from operational modal analysis and virtual sensing for fatigue analysis using the modal expansion method | 111 |
| 7.1 | Introduction | 111 |
| 7.2 | Contribution | 111 |
| 7.3 | Main findings | 111 |
| 7.4 | Reflections | 112 |
| 7.5 | Appended paper | 113 |
| 8 | Paper 5 - Full-field strain estimation of subsystems within time-varying and nonlinear systems using modal expansion | 131 |
| 8.1 | Introduction | 131 |
| 8.2 | Contribution | 131 |
| 8.3 | Main findings | 132 |
| 8.4 | Reflections | 132 |
| 8.5 | Appended paper | 133 |
| 9 | Paper 6 - Tilt errors of linear accelerometers attached to dynamic systems with tilt motion caused by the system response | 153 |
| 9.1 | Introduction | 153 |
| 9.2 | Contribution | 153 |
| 9.3 | Main findings | 153 |
| 9.4 | Reflections | 154 |
| 9.5 | Appended paper | 155 |
| 10 | Paper 7 - Preliminary study: Quasi-static strain estimation above the sea for an offshore tripod structure in the North Sea | 169 |
| 10.1 | Introduction | 169 |
| 10.2 | Contribution | 169 |
| 10.3 | Main findings | 170 |
| 10.4 | Reflections | 170 |
| 10.5 | Appended paper | 171 |
| 11 | Conclusion | 193 |
| 12 | Future works | 197 |
| A | Other publications | 199 |
| A.1 | Main author | 199 |
| A.2 | Co-author | 201 |

Part I

Preliminaries

Chapter 1

Introduction

“

Success is a science; if you have the conditions, you get the result

”

Oscar Wilde

This chapter is an introduction to the background, motivation, aim, and outline of the Ph.D. project.

1.1 Background

The sea is a harsh and hostile environment for offshore structures that must withstand the severe forces of the environment for the entirety of their service life, as shown in Fig. 1.1. Offshore structures are subjected to an irregular load history of fluctuating environmental and operational forces. These forces cause initiation and propagation of cracks in the structure, meaning, offshore structures accumulate fatigue damage. This eventually leads to fatigue failure if a structure remains unchecked. Consequently, the fatigue design along with an operational lifetime and planned inspections of the integrity should prevent fatigue failures and ensure safe operations so an offshore structure meets its intended functions throughout its lifetime.

From a design perspective, the load history of an offshore structure is, however, difficult to predict and therefore quite uncertain. The practical design of offshore structures allows for these uncertainties by considering the load as a stochastic process. The calculation of the load history is based on precautionary norms and standards and it represents a simplified version of the reality. The entire design process of offshore structures is based on risk assessments due to high levels of uncertainties related to the environmental conditions and the material properties. Generally, fatigue life assessments entail significant uncertainties [1]. These uncertainties accumulate during the design phase and they affect the estimated lifetime of the structure [1, 2]. To ensure safety during operation, offshore structures have to be inspected regularly [1]; however, subsea inspections are expensive and dangerous. Visual inspections are limited since they are unable to detect “root cracks” in welded joints before the cracks have grown through the weld.

Furthermore, the numerical model applied in the design process is an approximation of the structure under the actual conditions. The structure is made from materials with inherent errors of unknown levels and the boundary condition must be estimated before construction. This approximation of the actual structure creates uncertainty in the fatigue design.

A great deal of effort has been put into the field of structural health monitoring through the last three decades [3, 4]. Unfortunately, there are several issues that complicate the monitoring of offshore structures [3, 4]. The hostile environments make the platforms abstruse and this hinders inspections. The corrosive salt water damages subsea sensors and platform machinery introduces noise, which causes a non-stationary structural response. Furthermore, the system changes over time due to, for instance, ingress of water, marine growth, fluid storage levels, and soil properties. The offshore platforms are often connected with bridges, which introduce friction and nonlinear behaviour to the structures, and the fuel tanks on the topside might act as liquid dampers.



Figure 1.1: Operational offshore platform, L09-BF 2007, Dutch continental shelf, NAM and Shell UK Ltd, ©Aarhus University, Department of Engineering, Structural Dynamics and Monitoring Group

1.2 Motivation

The motivation for this Ph.D. project hails from the lifetime extension of existing structures since many offshore platforms in the North Sea are reaching the end of their design lifetime. These oil platforms are expensive structures and the owners are faced with a potential loss of profit by either abandoning an oil reservoir or building a new platform. Thus, there is a potential profit if the lifetime is increased. The actual integrity of these structures is, however, largely unknown since the lifetime is based on norms, standards, and visual inspections that are precautious and hold a high safety consideration. Due to these precautions, there could be a significant reserve of fatigue lifetime that would enable a lifetime extension. In other words, the actual fatigue damage could be lower than the nominal fatigue damage calculated in the fatigue design. Here, monitoring of the actual conditions of the environment and the structural integrity could access the fatigue damage and enable lifetime extension. There is a potential value in virtual sensing, which is the research field of extending physical sensors through a system model to quantities or measurements (virtual sensors) in unmeasured locations. Virtual sensing is applicable for an estimation of the full-field stress history of an offshore structure, see Fig. 1.2, and this stress estimation enables a fatigue assessment of the structure. A review of virtual sensing with respect to stress/strain estimation is given in Chapter 3.

The principle of lifetime extension with virtual sensing is illustrated in Fig. 1.3. The designed lifetime, T , of the structure is estimated based on the given risk assessment for the structure. We start monitoring the structure at a certain time and we begin estimating the stress history of the structure. Based on these stresses, we calculate the fatigue damage for the monitoring period. An appropriate forecasting model is created to predict the accumulated fatigue damage so the expected lifetime will increase to T_1 . The actual damage is assumed to be lower than the nominal damage. We assume the stresses are related to the environmental conditions; therefore we develop a correlation model from the actual fatigue damage and environmental conditions during our monitoring period. Based on past environmental conditions, we estimate the actual damage at the start of our monitoring period and we combine the two forecasting models of past and future to obtain a new predicted lifetime, T_2 .

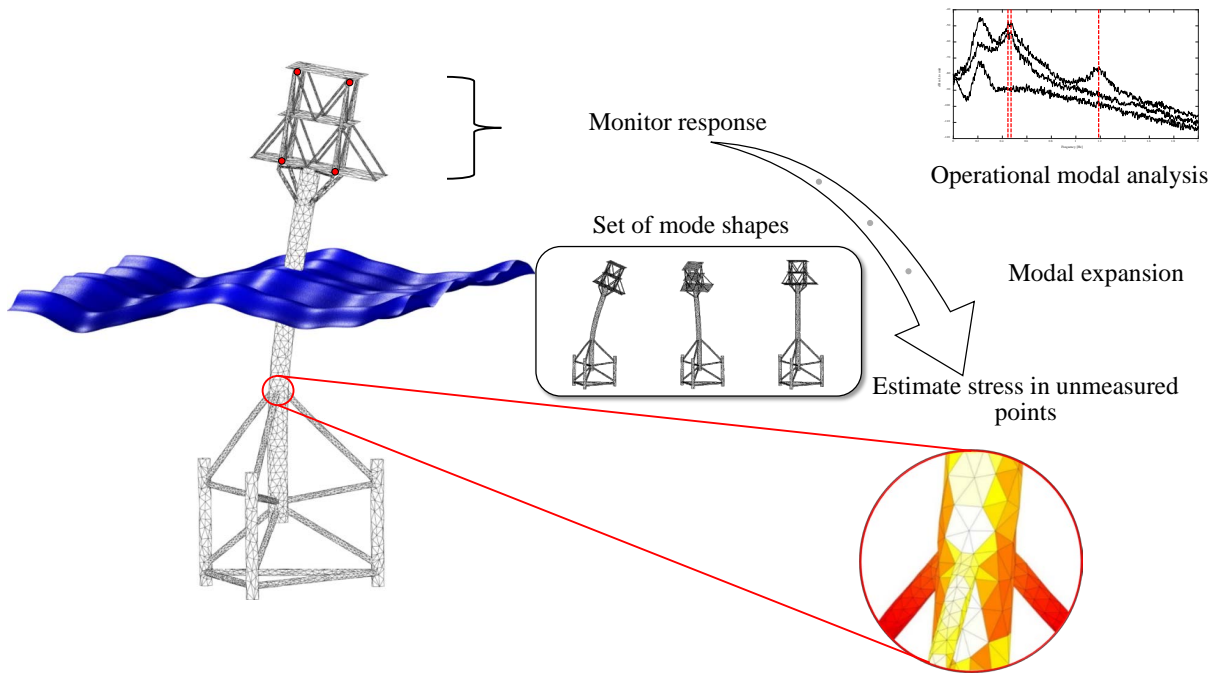


Figure 1.2: The principle of stress/strain estimation studied in this Ph.D. thesis

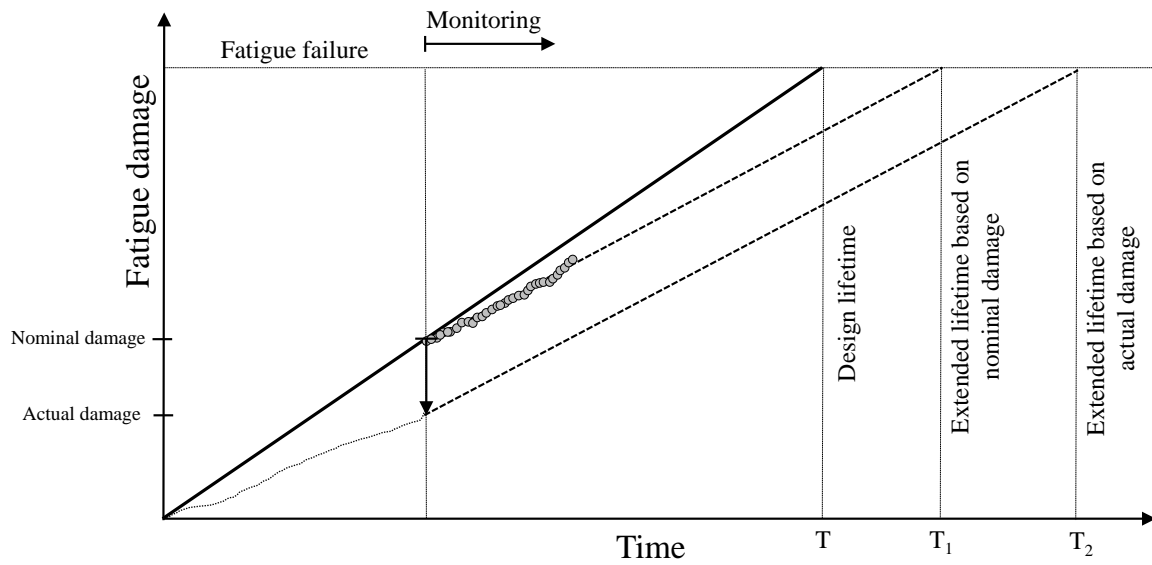


Figure 1.3: The principle of life extension using Palmgren-Miner rule for fatigue damage

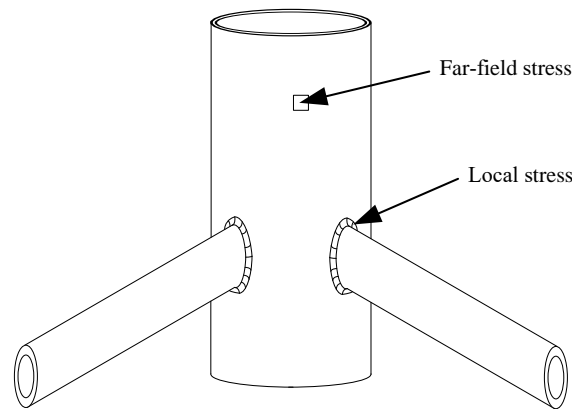


Figure 1.4: Definition of local stresses and far-field stresses (the target of this Ph.D. project)

1.3 Aim of Ph.D. project

Unsolved issues still exist for stress/strain estimation that must be addressed before lifetime extensions can be realised. Therefore, this Ph.D. project is created to study selected issues for virtual sensing intended for the lifetime extensions of offshore structures.

The Centre for Oil and Gas - DTU/Danish Hydrocarbon Research and Technology Centre (DHRTC) funded this Ph.D. project, which is a part of a larger project. This Ph.D. project is performed in collaboration with the Technical University of Denmark (DTU), where the author, Marius Tarpø, collaborated with fellow PhD student, Bruna Nabucco - DTU, as part of the "Stress Estimation" group. This Ph.D. student, Marius Tarpø, researches operational modal analysis and stress estimation (virtual sensing).

In this project, we focus on virtual sensing to estimate the stress/strain history of offshore structures. By installing a network of sensors above water, virtual sensing estimates the stress/strain history of the entire structure. Ideally, this enables us to perform fatigue analysis of any fatigue-critical location without sensors at the given location. The goal is not to obtain a perfect stress history but rather to reduce the uncertainty compared to the fatigue life from the design process. It should be noted that we limited the project to global structural stresses and not localised stresses. In other words, the project is limited to far-field stress estimation and not local stresses (such as stress concentrations near welds), as illustrated in Fig. 1.4.

This Ph.D. project has two research topics: 1) operational modal analysis for the estimation of reliable modal parameters to update the system models, 2) virtual sensing for stress estimation of the structure.
ja

1.4 Outline of Ph.D. thesis

The first part of the thesis relates to the preliminaries, literature review, and the state of the art. The second part includes the main research contribution conducted by the author during the Ph.D. project and it is organised as appended papers whereby each chapter is dedicated to a scientific paper. Each chapter introduces the reader to the topic/scientific problem, which the paper addresses, and it explains its affiliation to the Ph.D. project. The following sections outline the contributions by the author to the paper, summarise the main findings of the paper, and, finally, reflect on the contribution to the overall Ph.D. project. Then each paper is appended in the end of the chapter where they appear identical to the published/submitted versions - except for the page layout. The appended papers are intended to stand alone outside the context of this thesis.

The research presented in this thesis is original and the results have been communicated to the research community in the form of peer-reviewed articles in relevant international journals along with conference papers and presentations of these papers at international conferences.

References

- [1] DNVGL-RP-C203: Fatigue design of offshore steel structures. Recommended practise. Technical report, 2016.
- [2] I. Lotsberg, S. Fines, and G. Foss. Reliability of calculated fatigue lives of offshore structures. *Fatigue 84 : proceedings of the 2nd International Conference on Fatigue and Fatigue Thresholds*, pages 1565 – 1575, 1984.
- [3] C. R. Farrar and K. Worden. *Structural Health Monitoring: A Machine Learning Perspective*. John Wiley and Sons, Ltd, Chichester, West Sussex, UK, 2013.
- [4] O. Loland and C. J. Dodds. Experiences in developing and operating integrity monitoring systems in the north sea. *Proceedings of Offshore Technology Conference*, 2:313–320, 1976.

Chapter 2

Basic theory

“The essence of math is not to make simple things complicated, but to make complicated things simple”

Stanley Gudder

In this chapter, we introduce the fundamental theory of structural dynamics and operational modal analysis used throughout the Ph.D. thesis. We do not base this chapter on any appended papers but it is based on established and well-documented theory. For more extensive explanations of the theory, the reader is referred to textbooks on structural dynamics [1, 2], operational modal analysis [3, 4], and fatigue [5–7].

2.1 Structural dynamics

The dynamic response of a linear and stationary system is calculated by the equation of motion (an ordinary second-order differential equation) [1, 2].

$$\mathbf{M}\ddot{\mathbf{y}}(t) + \mathbf{C}\dot{\mathbf{y}}(t) + \mathbf{K}\mathbf{y}(t) = \mathbf{x}(t) \quad (2.1)$$

where $\mathbf{M} \in \mathbb{R}^{N \times N}$, $\mathbf{C} \in \mathbb{R}^{N \times N}$, and $\mathbf{K} \in \mathbb{R}^{N \times N}$ are the mass, damping, and stiffness matrix, $\mathbf{y}(t) \in \mathbb{R}^N$, $\dot{\mathbf{y}}(t) \in \mathbb{R}^N$, and $\ddot{\mathbf{y}}(t) \in \mathbb{R}^N$ are displacement, velocity, and acceleration of the system, $\mathbf{x}(t) \in \mathbb{R}^N$ is the external load/excitation vector, and N is the total degrees-of-freedom (DOF) of the system.

In the case of proportional damping, we use the undamped equation of motion to set up an eigenvalue problem.

$$\mathbf{M}^{-1}\mathbf{K}\boldsymbol{\phi}_i = \omega_i^2\boldsymbol{\phi}_i \quad (2.2)$$

where ω_i is the angular frequency of the i^{th} mode and $\boldsymbol{\phi}_i \in \mathbb{R}^N$ is the undamped mode shape (normal mode) for the i^{th} mode.

N eigenvalues and linearly independent eigenvectors exist [8] if the mass and stiffness matrices are symmetric and *semi-positive definite* matrices with full rank [2]. Thus, the modal matrix, $\boldsymbol{\Phi} = [\boldsymbol{\phi}_1, \boldsymbol{\phi}_2, \dots, \boldsymbol{\phi}_N] \in \mathbb{R}^{N \times N}$, span \mathbb{R}^N [2] and it is a basis of eigenvector for \mathbb{R}^N [8]. Therefore, any response, $\mathbf{y}(t)$, in \mathbb{R}^N is a linear combination of these mode shapes and this is called the modal superposition.

$$\begin{aligned} \mathbf{y}(t) &= \sum_{i=1}^N \boldsymbol{\phi}_i q_i(t) \\ &= \boldsymbol{\Phi} \mathbf{q}(t) \end{aligned} \quad (2.3)$$

where $\mathbf{q}(t) \in \mathbb{R}^N$ is the modal coordinate (linear combination) of the modes and $\boldsymbol{\Phi}$ is the modal matrix containing the mode shapes as column vectors. This is a linear coordinate transformation from the physical space into the modal space. These mode shapes decorrelate the equation of motion if we insert Eq. (2.3) into Eq. (2.1) and premultiply with the transposed modal matrix, and apply the orthogonal properties of the modal matrix to the mass and stiffness matrix [1, 2].

$$\ddot{\mathbf{q}}(t) + [2\zeta_i\omega_i] \dot{\mathbf{q}}(t) + [\omega_i^2] \mathbf{q}(t) = \left[\frac{1}{m_i} \right] \boldsymbol{\Phi}^T \mathbf{x}(t) \quad (2.4)$$

This enables us to calculate the response as a superposition of independent modal coordinates. We can use the Duhamel integral to calculate each modal coordinate [1, 2]

$$q_i(t) = \int_0^t h_i(t-\tau) \boldsymbol{\phi}_i^\top \mathbf{x}(\tau) d\tau \triangleq h_i(t) * \boldsymbol{\phi}_i^\top \mathbf{x}(t) \quad (2.5)$$

Thus, the total response is given as:

$$\mathbf{y}(t) = \sum_{i=1}^N \boldsymbol{\phi}_i \boldsymbol{\phi}_i^\top \int_0^t h_i(t-\tau) \mathbf{x}(\tau) d\tau \quad (2.6)$$

where $h_i(t) \in \mathbb{R}^1$ is the impulse response function for mode i^{th} .

We set up the impulse response function matrix, $\mathbf{H}(t) \in \mathbb{R}^{N \times N}$.

$$\mathbf{H}(t) = \sum_{i=1}^N \boldsymbol{\phi}_i h_i(t) \boldsymbol{\phi}_i^\top \quad (2.7)$$

Finally, the response of the entire system is the convolution of the impulse response function matrix and the load.

$$\mathbf{y}(t) = \int_0^t \mathbf{H}(t-\tau) \mathbf{x}(\tau) d\tau \triangleq \mathbf{H}(t) * \mathbf{x}(t) \quad (2.8)$$

2.2 Operational modal analysis

Operational modal analysis is an analysis of the random response of a system under operational conditions and it enables an extraction of the modal parameters. Operational modal analysis is a multidisciplinary research field that combines different fields: structural/mechanical dynamics, linear algebra, statistics, and signal processing. We will focus on correlation-driven operational modal analysis where we use the correlation function matrix of the response as free decays corresponding to the modes in the system. In operational modal analysis, we assume that the excitation is white noise and the system is linear and time invariant [3]. We have a finite time length of the random vibrations so the extraction estimates the modal parameters [9] since all statistical properties have some uncertainty due to the finite amount of data.

2.2.1 Correlation function matrix

The correlation function matrix is defined as [9]

$$\mathbf{R}_{yy}(\tau) \triangleq \mathbb{E} [\mathbf{y}(t) \mathbf{y}^\top(t+\tau)] \quad (2.9)$$

where $\mathbf{R}_{yy}(\tau) \in \mathbb{R}^{N \times N}$ is the correlation function matrix of the response.

We insert the response from the Duhamel integral, Eq. (2.8).

$$\begin{aligned} \mathbf{R}_{yy}(\tau) &= \mathbb{E} \left[\int_0^t \int_0^t \mathbf{H}(t-\alpha) \mathbf{x}(\alpha) \mathbf{x}(\beta)^\top \mathbf{H}^\top(t-\beta) d\alpha d\beta \right] \\ &= \int_0^t \int_0^t \mathbf{H}(t-\alpha) \mathbb{E} [\mathbf{x}(\alpha) \mathbf{x}(\beta)^\top] \mathbf{H}^\top(t-\beta) d\alpha d\beta \end{aligned} \quad (2.10)$$

Thus, we have the general theorem that describes the relationship between correlation function matrix of input and output for multiple degree-of-freedom systems.

$$\mathbf{R}_{yy}(\tau) = \mathbf{H}(-\tau) * \mathbf{R}_{xx}(\tau) * \mathbf{H}^\top(\tau) \quad (2.11)$$

where $\mathbf{R}_{xx}(\tau) \in \mathbb{R}^{N \times N}$ is the correlation function matrix of the excitation, $\mathbf{x}(t)$.

Brincker [10] calculated the analytical correlation function matrix for general damping.

$$\mathbf{R}_{yy}(\tau) = 2\pi \sum_{i=1}^N \left(\gamma_i \boldsymbol{\phi}_i^\top e^{\lambda_i \tau} + \gamma_i^* \boldsymbol{\phi}_i^H e^{\lambda_i^* \tau} \right), \tau \geq 0 \quad (2.12)$$

where $\gamma_i \in \mathbb{C}^N$ is the modal participation vector, $\phi_i \in \mathbb{C}^N$ is the complex mode shape due to non-proportional damping, and λ_i is the modal pole for i^{th} mode. Therefore, the correlation function matrix is equivalent to multiple free decays of the system.

2.3 Mechanics of material

2.3.1 Strain and stress

Stress is a measure of the internal forces within a material while strain is a relative deformation of the system caused by the stress [11]. In general, the relationship between stress and strain is material dependent and the stress-strain curve/diagram displays this by experimental material studies, see Fig. 2.1.

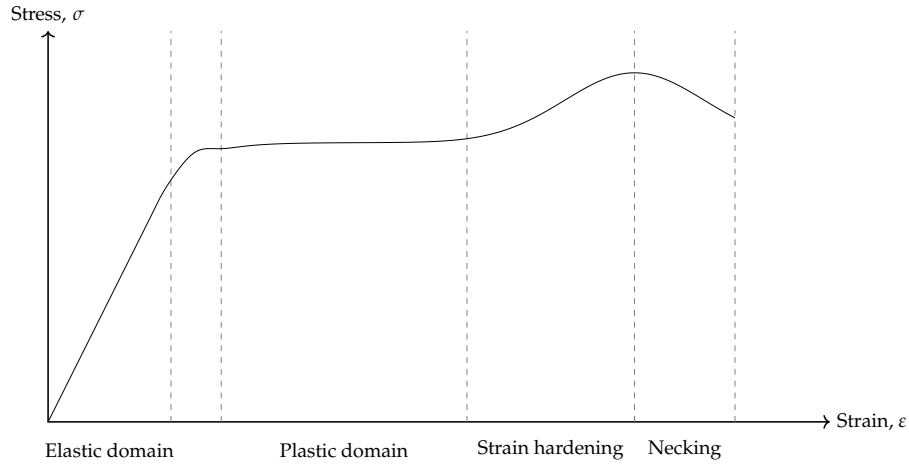


Figure 2.1: Stress-strain curve/diagram of typical structural steel

In the elastic domain at low levels of deformation, a linear relationship exists between stress and strain through the modulus of elasticity, E , - called Hooke's law [11].

$$\sigma = E\varepsilon \quad (2.13)$$

where σ is the stress and ε is the strain.

2.3.2 Dynamic strain/stress

Since strain is a measure of the deformation of a material, a linear relationship exists between the vibrations and the strain response of a system.

$$\varepsilon(t) = \mathbf{B}\mathbf{y}(t) \quad (2.14)$$

where $\varepsilon(t) \in \mathbb{R}^n$ is the strain response vector, $\mathbf{B} \in \mathbb{R}^{n \times N}$ is the displacement-to-strain transformation matrix, and n is the number of DOFs for stress/strain in the system.

Next, we insert Eq. (2.3) into Eq. (2.14)

$$\varepsilon(t) = \mathbf{B}\Phi\mathbf{q}(t) \quad (2.15)$$

We see that both the response, Eq. (2.3), and strain, Eq. (2.15), include the modal coordinates. Therefore, we can find a basis for the strain response with the same linear combination as for the response. This basis is called the strain mode shapes, Φ_ε , where each strain mode shape is the static strain caused by a deflection of a mode shape.

$$\Phi_\varepsilon = \mathbf{B}\Phi \quad (2.16)$$

With the strain mode shape, we have a similar modal decorrelation for the strain response as for the displacement.

$$\varepsilon(t) = \Phi_\varepsilon\mathbf{q}(t) \quad (2.17)$$

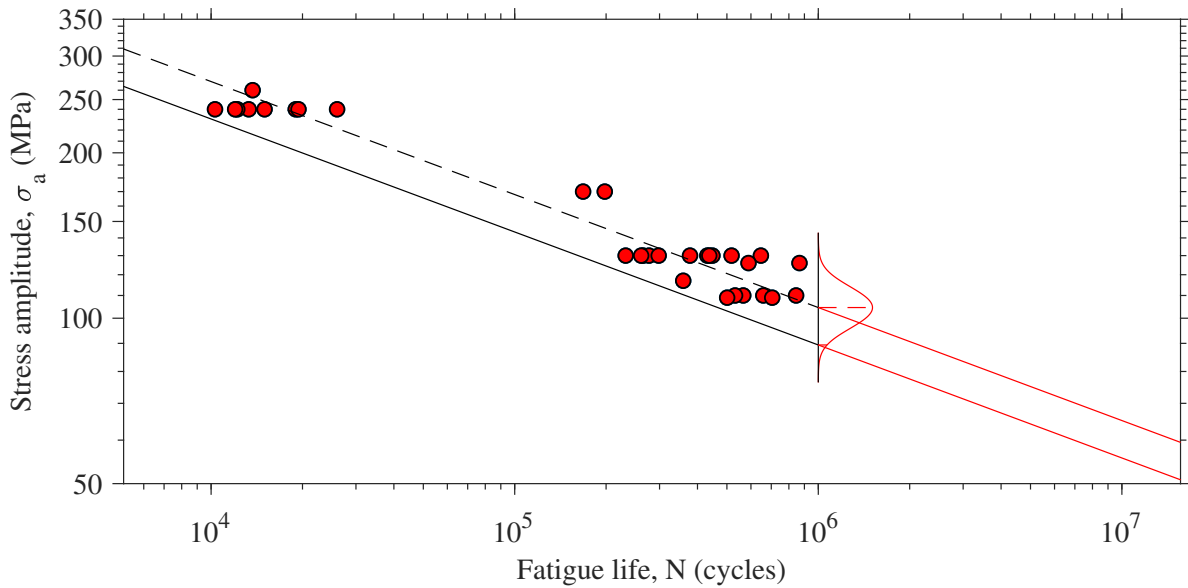


Figure 2.2: An example of a derived SN curve based on experimental data [12]. The assumption of log-normal distribution for the SN curve is illustrated to show how the 97.7% survival probability is obtained for the design fatigue strength.

2.4 Fatigue

This section will give a brief introduction to fatigue in materials science and the reader is referred to [5, 6] for further elaboration on the topic. We refer to [6, 7] for extensive information on the recommended practices for fatigue design of offshore steel structures.

The fluctuating stress, internally in a material, causes fatigue due to a fatigue action. In general, a fatigue action is a load that causes fatigue in the material [7]. Often, a single fatigue action does not cause yielding of the material but these actions are repetitive and cause fluctuating stress. In fatigue, we deal with two phases: the crack initiation and the crack propagation. In the first phase, microcracks are formed at the surface and they continuously propagate. In the end, fatigue failure occurs if crack propagation is allowed. Fatigue failure is a fracture of a material caused by the cracks. The number of stress cycles at fatigue failure is called the fatigue life and it primarily depends on the stress amplitude (or stress range) and the mean stress [5]. The total fatigue life, N_{total} , equals the number of cycles in the crack initiation phase, N_i , and the crack propagation phase, N_p .

$$N_{total} = N_i + N_p \quad (2.18)$$

The fatigue design must ensure that the structure fulfils its intended functions in the entire fatigue life in a safe manner. Furthermore, the calculated fatigue life forms the inspection plans for the structure [7].

There are different fatigue analysis methods [5, 6]. In the offshore industry, the stress-life method is the recommended practice for fatigue analysis [7], so we will focus on the stress-life method, where we utilise the so-called SN curves for the fatigue analysis. Alternatively, we apply fracture mechanics to the fatigue analysis when it is deemed appropriate [7]. In the SN curve, the fatigue life is expressed as the following function

$$N_i \sigma_i^m = C \quad (2.19)$$

where N_i is the fatigue life for the given stress amplitude, σ_i , m is the "slope" of the SN curve, and C is the fatigue capacity (or intercept on the N -axis at a stress amplitude of one).

The design SN curves are derived from fatigue tests where we assume that each fatigue life is log-normal distributed to obtain 97.7% probability of survival, see Fig. 2.2.

For fatigue damage, the Palmgren-Miners rule defines partial damage as a consumption of the fatigue life caused by a single stress cycle [5].

$$D_i = \frac{1}{N_i} \quad (2.20)$$

where D_i is the partial fatigue damage and N_i is the number of endurable cycles before fatigue failure for the given stress range, $\Delta\sigma_i$, and mean stress, $\sigma_{m,i}$ of the stress cycle.

2.4.1 Variable amplitude loading

For offshore structures, the amplitude of the fatigue actions varies; thus, we must apply cycle counting [5] such as *rainflow counting* [13]. For fatigue, the range or amplitude of the stress cycles is of bigger importance than the frequency/period of the cycle.

The Palmgren-Miner rule states that the accumulated fatigue damage is a summation of all partial damage caused by each stress cycle.

$$D = \sum_{i=1}^{n_{cycles}} D_i = \sum_{i=1}^{n_{cycles}} \frac{1}{N_i} \quad (2.21)$$

where n_{cycles} is the number of cycles.

We can also divide the stress cycles into n_{bin} bins and calculate the fatigue damage.

$$D = \sum_{i=1}^{n_{bin}} \frac{n_i}{N_i} \quad (2.22)$$

where n_i is the number of cycles in the stress range corresponding to the given bin. Generally, we will assume fatigue failure at $D = 1$ but there is high uncertainty regarding this value [5].

Additionally, we can rewrite the fatigue damage, from either Eq. (2.21) or (2.22), so the fatigue damage is a function of the strain amplitudes by inserting Eqs. (2.13) and (2.19).

$$D = \sum_{i=1}^N \frac{1}{N_i} = \sum_{i=1}^N \frac{\sigma_i^m}{C} = \sum_{i=1}^N \frac{E^m}{C} \varepsilon_i^m \quad (2.23)$$

References

- [1] R. W. Clough and J. Penzien. *Dynamics of structures*. CSI Computers & Structures, Inc., Berkeley, Calif., 2nd revised edition, 2003.
- [2] A.K. Chopra. *Dynamics of Structures: Theory and Applications to Earthquake Engineering*. Prentice Hall International Series in Civil Engineering And. Pearson/Prentice Hall, 2007.
- [3] Rune Brincker and Carlos Ventura. *Introduction to operational modal analysis*. John Wiley and Sons, Inc., Chichester, West Sussex, UK, 2015.
- [4] Carlo Rainieri and Giovanni Fabbro. *Operational modal analysis of civil engineering : an introduction and guide for applications*. Springer Science+Business, New York, USA, 2014.
- [5] M.M. Pedersen. Introduction to metal fatigue - concepts and engineering approaches. Technical report, Department of Engineering, Aarhus University, 2018.
- [6] A. Almar-Naess. *Fatigue Handbook: Offshore Steel Structures*. Tapir Academic Press, Trondheim, Norway, 3rd edition, 1985.
- [7] DNVGL-RP-C203: Fatigue design of offshore steel structures. Recommended practise. Technical report, 2016.
- [8] Erwin Kreyszig, Herbert Kreyszig, and Edward J. Norminton. *Advanced engineering mathematics*. John Wiley And Sons Ltd, Hoboken, NJ, 10th edition, 2011.
- [9] Julius S. Bendat and Allan G. Piersol. *Random data: analysis and measurement procedures*. Wiley-Blackwell, Hoboken, N.J., USA, 4th edition, 2010.
- [10] Rune Brincker. On the application of correlation function matrices in oma. *Mechanical Systems and Signal Processing*, 87:17–22, 2017.
- [11] J.M. Gere and B.J. Goodno. *Mechanics of materials*. Cengage Learning, 7th edition, 2009.
- [12] Gary Marquis and Jussi Solin. *Long-life fatigue design of GRP 500 nodular cast iron components*. Number 2043 in VTT Tiedotteita - Meddelanden - Research Notes. VTT Technical Research Centre of Finland, Finland, 2000.
- [13] C. Amzallag, J.P. Gerey, J.L. Robert, and J. Bahuaud. Standardization of the rainflow counting method for fatigue analysis. *International Journal of Fatigue*, 16(4):287 – 293, 1994.

Chapter 3

Narrative literature review of stress/strain estimation

“
It's not enough to be up to date, you have
to be up to tomorrow”

David Ben-Gurion

In this chapter, we review the literature on stress/strain estimation, create a new terminology for virtual sensing, and discuss issues related to stress/strain estimation. This work is summarised in a baseline that we have used for planning and framing the Ph.D. project.

3.1 Introduction to virtual sensing and stress/strain estimation

Stress or strain estimation is known by many names and terms: stress/strain prediction, reconstruction of unmeasured stress/strain, fatigue prediction/estimation, hybrid modal analysis, full-strain fields, full-field stress/strain estimation, full-field stress/strain distribution, virtual sensing, soft sensing, full-state estimation, etc.. Generally, there is a lack of consensus and common terminology in the field. In this chapter, we will use the term stress/strain estimation.

Stress/strain estimation is a subsection of virtual/soft/inferential sensing, which is the science of extending physical measurements to unmeasured locations [1–5]. We will use the term "virtual sensing" but the reader should note that the two terms "virtual sensing" and "virtual sensors" are used interchangeably in the literature. Virtual sensing is a state observer and it has similarities to regression and extrapolation, prediction, and forecasting analyses. A virtual sensor is an alternative to a physical sensor, which directly measures a desired quantity of a system. We should, however, only apply virtual sensing when it is advantageous in comparison to its alternative. Put simply, virtual sensing is advantageous when we desire measurements of a quantity at a given location but the installation of physical sensors is restricted and/or expensive or the quantity is undeterminable by direct measurements. Virtual sensing creates virtual sensors, which indirectly measure/estimate this desired quantity by converting the physical sensors. Furthermore, virtual sensing is either model-based (analytical), data-based (empirical), or any combination of the two.

Unfortunately, a common definition and terminology of virtual sensing are not widely accepted in the literature. In the context of this Ph.D. project, we use the terminology from [1, 2] as baseline for the

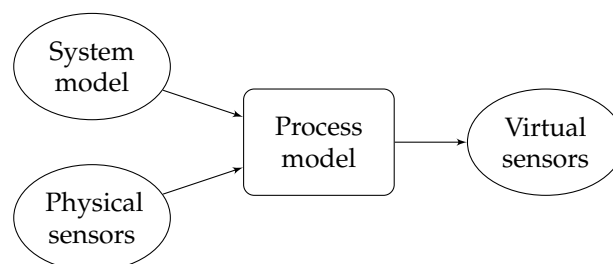


Figure 3.1: Flowchart of virtual sensing

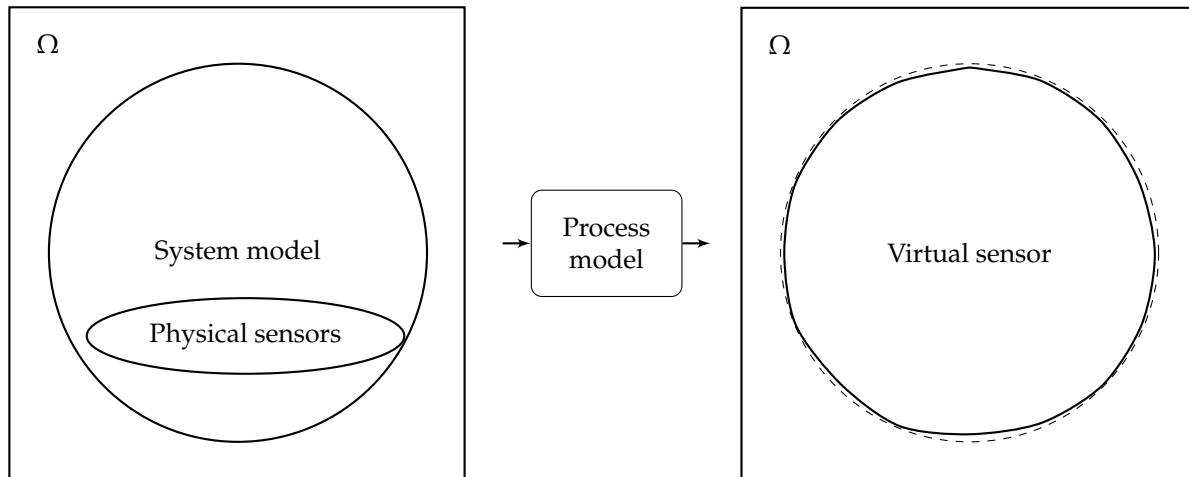


Figure 3.2: Venn diagrams of virtual sensing

one created and applied in this chapter. In this terminology, we need three components to create virtual sensors that we term: system model, physical sensors, and process model, as outlined in Fig. 3.1. The system model could have any form and format but the model contains information on the system and the sensors. In the terms of control theory, the model holds the different states, which the system can be in. We describe the system model in section 3.3. The physical sensors measure physical quantities and the term includes processing of the measurements, see section 3.4. The process model is a state estimator that estimates the full-state of the system based on both the measurements from the physical sensors and the system model. Here, the full-state is a set of state variables or principal components, which describe the entire system. Through the full-state, virtual sensors are available for any desired quantity in the entire system, see section 3.5 for process models in stress/strain estimation. Fig. 3.2 illustrates virtual sensing in terms of Venn diagrams where the system model and the physical sensors each contain a subset of states of the full set, Ω , and the process model estimates the full union of the system model and sensors to enable virtual sensors. We should note that the term "virtual sensing techniques" is often used interchangeably with the term "process model" in the literature.

In stress/strain estimation, the virtual sensing provides virtual sensors (strain gauges) in any location of the system, thus, it enables full-field stress/strain estimation of a system. Stress/strain estimation differs from many other applications of virtual sensing in one challenging aspect. The consequences of errors are dire since they ultimately lead to an unexpected fatigue failure with potentially fatal implications. Thus, the margin of error is small compared to other applications.

In this chapter, we will review a wide range of literature on the topic of stress/strain estimation to provide the state of the art, with a focus on the time period of 1995 to 2019. We, however, exclude response estimation from this literature review even though stress/strain estimation closely relates to this. Likewise, we neglect the different statistical methods for extreme stress prediction. The reader should note that this review is a non-systematic/narrative literature review [6] since many papers use their own terms. It was impossible to set up a few search keywords that cover the entire body of literature on stress/strain estimation. Hence, it has been impossible to conduct a systematic review. Therefore, the author continuously gathered the literature throughout the entire Ph.D. project, as new terms and studies for stress/strain estimation were uncovered. The lack of consensus in the field indicates a need for a literature review in the field. This review might, however, be incomplete due to a potential lack of relevant articles but it has been performed to the best of the author's ability.

We organise the chapter as follows: Section 3.2 sets out the history of stress/strain estimation. Then the following three sections relate to the terminology of virtual sensing, see Fig. 3.1. Section 3.3 summarises the system models, section 3.4 lists some of the most commonly utilised sensors, and section 3.5 introduces the most popular process models applied to stress/strain estimation. Finally, we point out and discuss different problems for virtual sensing in section 3.6.

3.2 History

In the literature of virtual sensing, stress/strain estimation is successfully applied on a wide range of mechanical and civil structures. In this section, we will summarise the history of stress/strain estimation.

3.2.1 The beginning - 1950s to 1980s

Stress/strain estimation had its tentative beginnings during the 1950s when analytic relationships between response and strain for beams or plates were investigated. In this era, the researchers primarily focused on analytic techniques under specific excitation [7]. At this time fatigue problems arose due to broad-banded random vibration in the aerospace industry [7]; hence, analytical expressions and relationships between vibrations, stress/strain, and fatigue life were investigated [8]. In 1960, F. V. Hunt [9] found that the strain response is proportional to the velocity for any elastic body and Stephen H. Crandall [10] extended this relation between strain and velocity in 1962. The same year, Eric E. Ungar [11] derived expressions on the relationship between maximum stress and modal displacement or modal loadings for beams and plates vibrating at resonance. In 1970, S.M. Stearn [12] derived expressions and relationships for the likely variance of mean square stress, strain, and acceleration. The included articles merely form a small section of the literature from this era regarding the analytic expressions.

3.2.2 1990s

In 1995, an early version of the modal expansion was introduced for strain estimation by Okubo and Yamaguchi [13] where it was called displacement-to-strain transformation. It used a projection or transformation matrix that projects and transforms the response to the strain response. Although the formulation is different to the later transformation termed "modal expansion", it works in a similar way - through pseudo inverse matrices. In 1995, Koss and Karczub [14] used the analytic bending wave solution for beams along with the frequency response function to estimate strain in beams. D. Karczub [7] wrote a Ph.D. thesis on the prediction of dynamic strain in 1996 where he focused on analytic expressions for the estimation process. In 1998, Seo et al. [15] applied the displacement-to-strain transformation in a manner close to modal expansion. In 1999, Karczub and Norton [16] applied finite difference methods to predict dynamic strain for a clamped beam and clamped plate in the laboratory.

3.2.3 2000s

In 2001, N. Sehlstedt, [17] proposed a method - hybrid modal analysis - for calculating the dynamic strain tensor field that resembles the modal expansion technique in the frequency domain. Here, the modal coordinates are called the Fourier coefficients.

In 2005, Hjelm et al. and Graugaard-Jensen et al. [18, 19] presented a full-field strain estimation technique using the modal expansion and applied it to a laboratory structure and a lattice tower under operational conditions using a finite element model (system model) and operational modal analysis. This formulation of modal expansion is the first version of the algorithm used today. Furthermore, Hjelm et al. [20] showed - for risk-based inspections - that the number of planned inspections depends on the uncertainty of the load history and that stress estimation reduced the number of inspections by 50% for the given case study.

In 2007, G. M. Lee [21] calculated the displacement-to-strain transformation matrix by the frequency-response-function between the excitation force and the response on simulated data. Thus, the technique requires information on the excitation. In 2009, Pelayo et al. [22] applied modal expansion to a cantilever beam under random excitation in the laboratory using a finite element model (system model) and operational modal analysis where they showed that updating the system model corrected the amplitude of the strain estimation.

3.2.4 2010s

As the first researchers to do so, Papadimitriou et al. [23] applied the Kalman filter to strain estimation in numerical simulations in 2011. In a series of similar papers, Pingle et al. [24–27] applied modal expansion to numerical studies to study the effect of the number of mode shapes and the number of sensors for stress/strain estimation. They found that the set of mode shapes should span the majority of the response, the number of sensors should allow for the least-squares minimisation process, and the

position of sensors should result in a linearly independent set of truncated mode shapes (corresponding to the position of sensors).

In 2012, Avitabile and Pingle [28] estimated the strain response on a test specimen in the laboratory. Aenlle et al. [29] applied strain estimation on a scale model of a two-storey building in 2013. The same year, Papadimitriou et al. [30] used the Kalman filter in the modal domain to estimate the strain response of a steel beam in the laboratory. They found drift in the estimated displacement caused by the numerical integration of the measured acceleration from accelerometers inside the Kalman filter. The drift was, however, successfully removed by a high-pass filter. Avitabile et al. [31] used modal expansion and strain estimation for damage detection in a numerical case study.

In 2014, Ren and Zhou [32] applied the Kalman filter on a simulated truss structure to estimate the strain response. Erazo and Hernandez [33] proposed a model-based observer for state and stress estimation (an adaptive filter) that resembles the Kalman filter in the modal domain. Jo and Spencer [34] applied the Kalman filter with multi-metric (sensor fusion) to estimate the strain response of a numerical truss structure.

In 2015, Palanisamy et al. [35] studied strain estimation in a numerical simulation using the Kalman filter for non-zero mean excitation. They showed the potential of multimetric sensor networks where tilt sensors and accelerometers were the best combination. Furthermore, they found that accelerometers are inappropriate for the estimation of the quasi-static response near 0 Hz from the non-zero mean excitation. In the same year, Maes et al. [36] applied a Kalman filter to the strain estimation of offshore monopile wind turbines in the Belgian North Sea with high precision. This was one of the first times the Kalman filter was applied to an actual structure outside a laboratory. In 2015, Pelayo et al. [37] applied modal expansion on laboratory tests using expanded experimental mode shapes from an operational modal analysis. Gevinski et al. [38] applied modal expansion in the frequency domain to a test plate in the laboratory but they used the term hybrid modal analysis. Baqersad et al. [39] used modal expansion with 3D point tracking to estimate the full-field dynamic strain on a wind turbine rotor in the laboratory. They found that the set of mode shapes is a critical part of modal expansion. In a similar paper, Baqersad et al. [40] applied stereophotogrammetry as the physical sensor for modal expansion on the same test specimen. J. Kullaa [41] combined empirical and analytical virtual sensing for stress/strain estimation using minimum square error estimation and modal expansion in a numerical study.

In 2016, Maes et al. [42] compared dynamic strain estimation using the Kalman filter, the joint input-state estimation algorithm (an adaptive filter technique similar to the Kalman filter), and the modal expansion on an offshore monopile wind turbine in the Belgian North Sea and applied data fusion to combine accelerometers and strain gauges. They concluded that the three techniques are competitive and interchangeable while the inclusion of strain gauges - sensor fusion - has minor improvements. In the same year, J. Kullaa [43] applied dynamic substructuring in the system model for virtual sensing in three numerical simulations. Due to the substructuring, only a part of the structure is needed, thus, reducing the potential for modelling errors in the system model. Iliopoulos et al. [44] used three frequency regions for modal expansion to estimate the strain response of an offshore wind turbine. For the quasi-static response, they performed a static calculation of the deflection shape by a representative load. To estimate the fatigue damage, Dertimanis et al. [45] integrated the dual Kalman filter with the unscented Kalman filter and applied it on a numerical case study. Dertimanis et al. [46] applied an augmented implementation of the unscented Kalman filter for fatigue estimation on a numerical case study.

In 2017, in order to study strain estimation on a wave-induced structure, Skafte et al. [47] applied modal expansion with Ritz vectors (static deflection shapes) to account for the quasi-static response caused by waves and estimated the strain response on a scale model of an offshore platform excited with shakers mimicking a wave spectrum. Similarly and simultaneously, Iliopoulos et al. [48] applied a multi-banded modal expansion on an offshore monopile wind turbine including the quasi-static strain contributions from thrust loads by combining accelerometers and strain gauges. Palanisamy et al. [49] studied multimetric sensor network (sensor fusion) for the Kalman filter using a simulated case study. Ren and Zhou [50] compared the augmented Kalman filter and modal expansion technique on a simulated truss structure. In this study, the modal expansion gave "*more satisfactory results*" [50]; however, Ren and Zhou concluded that the techniques are competitive and their performances are interchangeable. In the work of Aenlle et al. [51], modal expansion is applied to a fatigue test of a cantilever beam. Giagopoulos et al. [52] proposed a framework for the estimation of fatigue damage using the known input/load and a high-fidelity finite element model, although, the paper revolves more around finite element updating than stress/strain estimation. In a numerical study, J. Kullaa [53] used Bayesian empirical virtual sensing to reduce noise from the physical sensors and modal expansion to estimate the strain response.

In 2018, Lu et al. [54] used pattern recognition (machine learning algorithms) for stress estimation on the Shenzhen Bay Stadium. Stress values from a finite element were used to build the pattern library and testing library while actual stress measurements from the structure were used for the observed library. Thus, this virtual sensing technique requires training data to build up a library. The same year, Noppe et al. [55] compared modal expansion with multiple frequency band-pass filters and the Kalman filter on an offshore wind turbine from the wind farm Belwind. Both virtual sensing techniques have similar strain estimates in the time domain but in the frequency domain the modal expansion technique has a better correlation to the measured strain response than the Kalman filter. Luthe et al. [56] applied modal expansion for strain estimation on a cantilever beam in the laboratory. Chen et al. [57] used modal expansion for a test specimen submersed in a water tank with success. Lagerblad et al. [58] applied Kalman filters to a full-scale fatigue test of a truck chassis in the laboratory. Here, the estimated fatigue damage differed to the measured fatigue damage by 25% and they contributed this to modelling errors of the complex truck component and tuning errors of the filters. Roberts et al. [59] used modal expansion on a test specimen in the laboratory for strain estimation. Baqersad and Bharadwaj [60] used modal expansion with strain gauges as physical sensors to estimate the full strain field of a cantilever beam in both a numerical study and a laboratory test.

In 2019, Deng et al. [61] applied learning to modal expansion by machine learning. The technique used the data from binocular cameras and strain gauges to self-learn the mode shapes of the structure and they subsequently validated the technique with the same strain gauges. J. Kullaa [62] applied Bayesian empirical (data-driven) virtual sensing to modal expansion to reduce measurement noise on sensors and the technique was validated by simulations. Furthermore, Nabiyan et al. [63] applied the modal expansion technique on a simulated wind turbine. Risaliti et al. [64] applied the augmented extended Kalman filter to nonlinear mechanical systems by the means of the implicit equation of motion. The process model was validated on a suspension test rig in the laboratory. Henkel et al. [65] applied modal expansion with multiple frequency bands to estimate the strain response of the subsoil part of an offshore wind turbine in the Belgian North Sea with good accuracy for wind velocities of 4-9 m/s. In 2019, Pedersen et al. [66] compared the modal expansion with two adaptive filter algorithms - the Kalman filter and the joint input-state estimation algorithm - where they studied the effect of the number of sensors. Based on their laboratory test, the modal expansion was the preferred technique when the number of sensors exceeds the number of applied modes, while the joint input-state estimation algorithm was the preferred method when this was not the case. Bharadwaj et al. [67] used a transformation matrix for strain estimation using digital image correlation to extract strain mode shapes. They found that the set of mode shapes depends on the loading. Papadimitriou et al. [68] discussed a framework for the remaining fatigue lifetime prognosis using stress/strain estimation. In two papers, Giagopoulos et al. [69, 70] proposed a framework for updating the system model by applying a covariance matrix adaptation evolution strategy to update a high-fidelity finite element model applied to fatigue damage estimation. Utilising the updated finite element model and the known input/load, Giagopoulos et al. [69, 70] calculated the strain of structure. Palanisamy et al. [71] applied the Kalman filter and a buffering technique with sensor fusion to estimate the strain response of bottom-fixed offshore structures with quasi-static and non-stationary excitation in a numerical and laboratory study with a circulating water channel setup.

3.2.5 Discussion

Stress/strain estimation started with analytic expressions, then the displacement-to-strain transformation matrix started to gain momentum. In 2005, Hjelm et al. [18, 20] and Graugaard-Jensen et al. [19] extended the transformation matrices into the formulation of modal expansion used today. Since Papadimitriou et al. [23] introduced the Kalman filter to stress/strain estimation in 2011, many contributions have been made to the field using adaptive filters [33, 72–74]. In recent years, machine learning has been introduced to stress/strain estimation. In the literature, the Kalman filter and the modal expansion have been proven to be competitive and interchangeable in terms of performance [42, 50, 55, 66]. Fig. 3.3 shows the timeline of the literature in stress/strain estimation from 1995 to 2019 while Fig. 3.4 illustrates the number of publications in the same time period. Based on the number of articles, the research activity in the field has increased in the last decade.

The general formulation and theory of modal expansion are unchanged since the introduction in 2005 [18–20]. Ever since, however, the literature has introduced new, advanced, and complex process models for stress/strain estimation and these include adaptive filters and machine learning techniques. At the time of writing, they are not superior to modal expansion and, at best, these new process models are

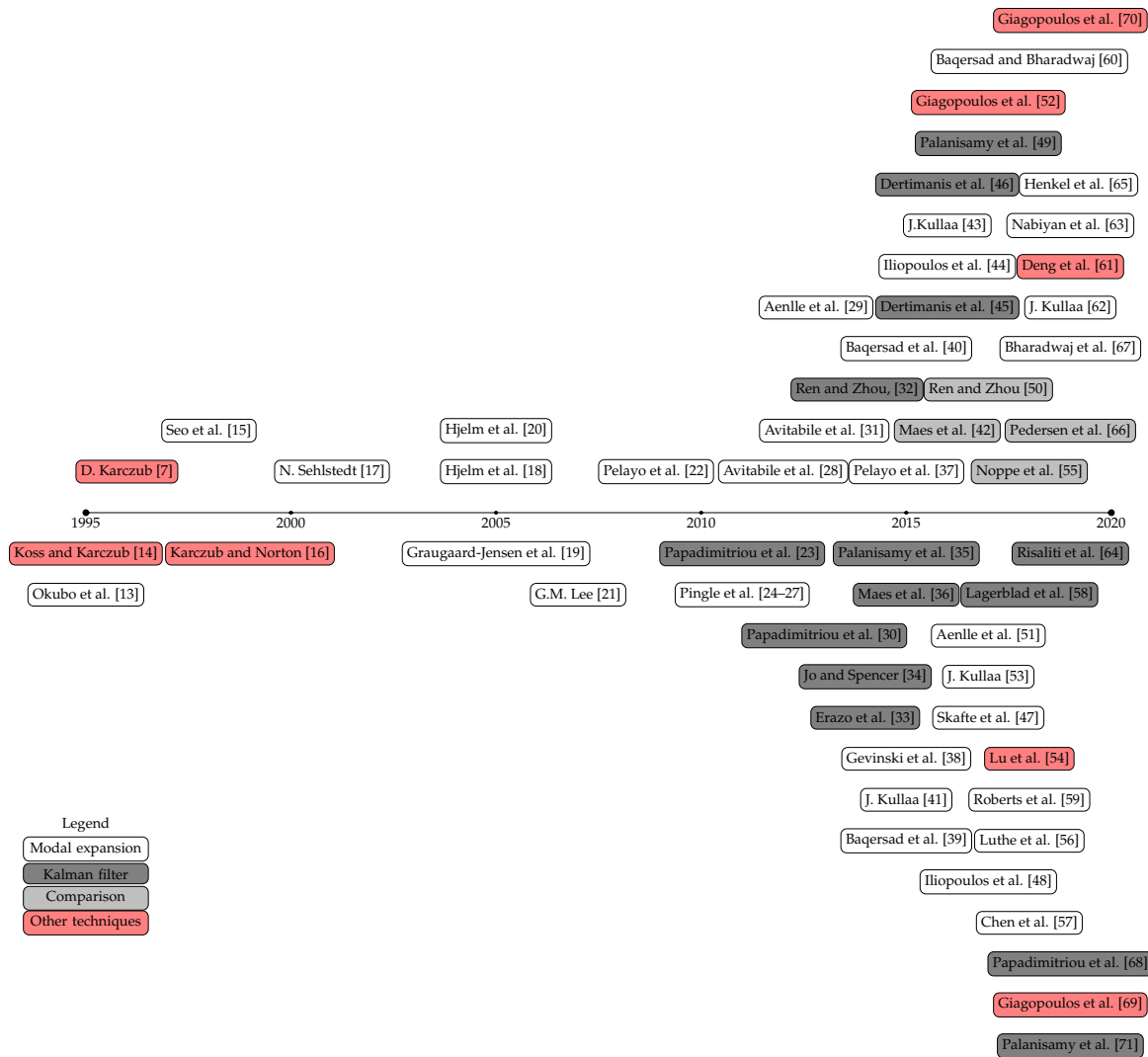


Figure 3.3: Timeline of literature for stress/strain estimation reviewed in this chapter from 1995 to 2019

competitive and interchangeable, performance-wise, to the modal expansion from 2005 [42, 50, 55, 66]. For stress/strain estimation, the accuracy of the process model is largely the same today as in 2005. Thus, despite the increasing research activity in the field, stress/strain estimation has seen little progress since 2005 in terms of accuracy in the process model.

Generally, there is little consensus in the literature for stress/strain estimation and many papers use their own terminology. Unfortunately, some papers do not acknowledge or reference the previous relevant literature on the subject or they claim to be the first to propose a stress/strain estimation technique. This could be attributed to the many different terms and the general lack of consensus in the research field. This results in independent and separated subfields that revolve around the same research topic: stress/strain estimation. Moreover, this yields many similar articles that repeat or revise already published research.

In the past two decades, stress/strain estimation has been successfully applied to a wide range of test specimens and research has proven the feasibility under a controlled environment. We have analysed the distribution of application in the case studies in Fig. 3.5 and grouped the articles depending on the application: numerical, laboratory, and operational (applications under actual conditions outside the laboratory). Fig. 3.6 a) illustrates the distribution of all applications in the reviewed articles. Most research relies on test specimens in a laboratory to validate and evaluate stress/strain estimation under a controlled environment. The second biggest group is the numerical simulations, where all conditions are modelled and controlled. These two groups of applications are highly controlled, hence, an evaluation of stress/strain estimation misses the achievability and practicality of the techniques. Merely 13% of the reviewed articles include applications on systems in operation under the actual conditions where

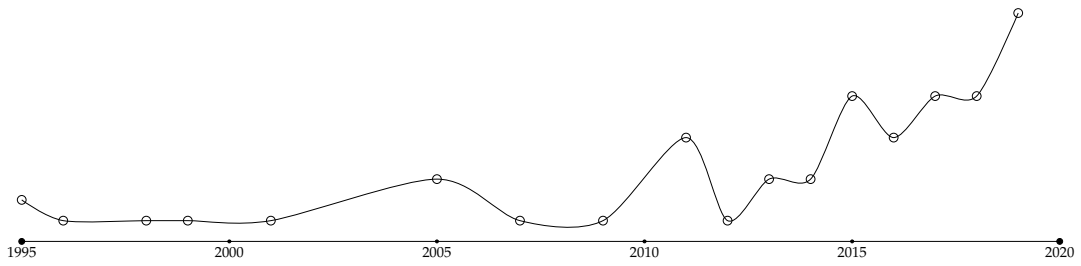


Figure 3.4: The number of publications as function of time for stress/strain estimation reviewed in this chapter from 1995 to 2019

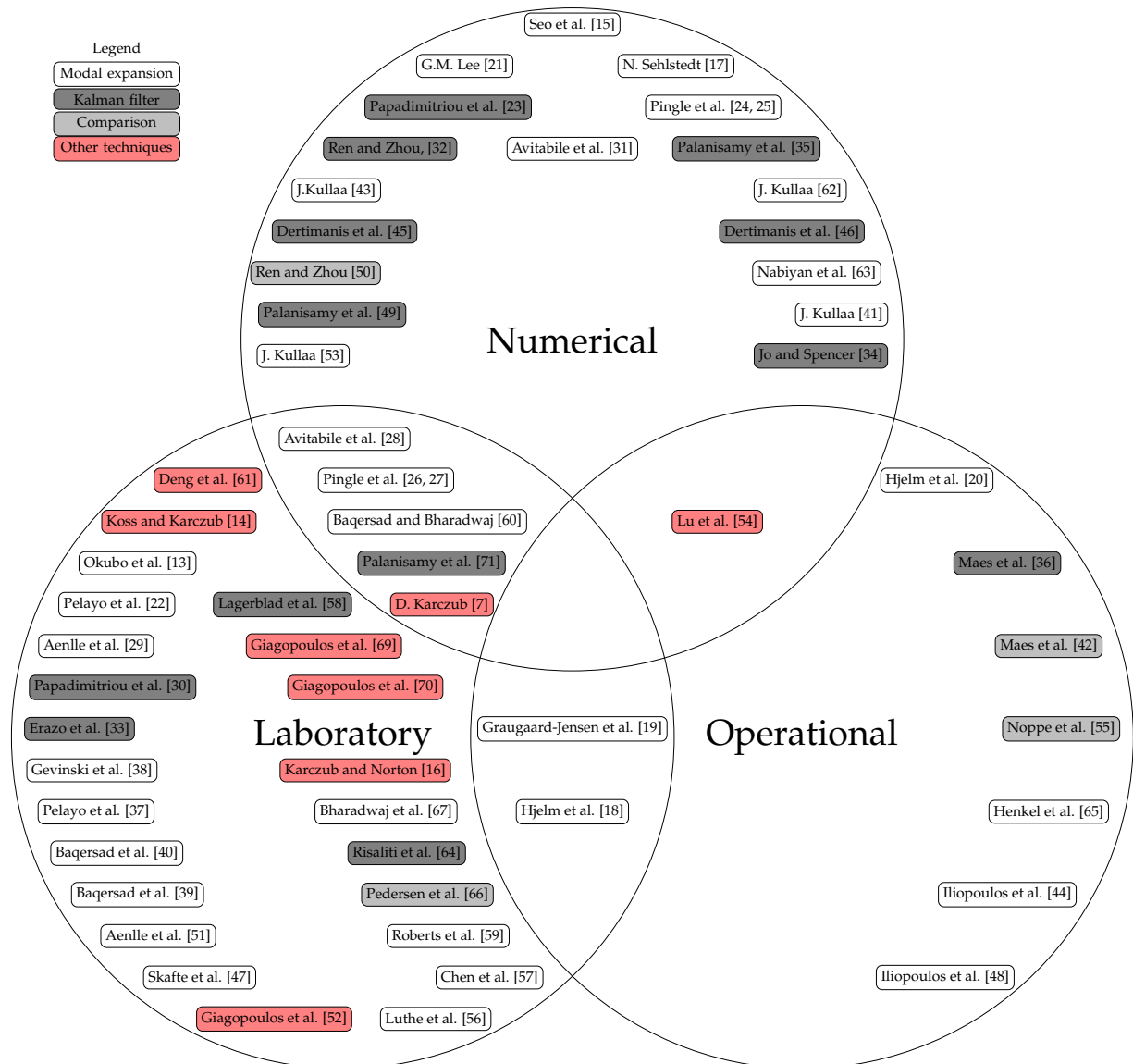


Figure 3.5: Distribution of the application of stress/strain estimation reviewed in this chapter in the time period of 1995 to 2019

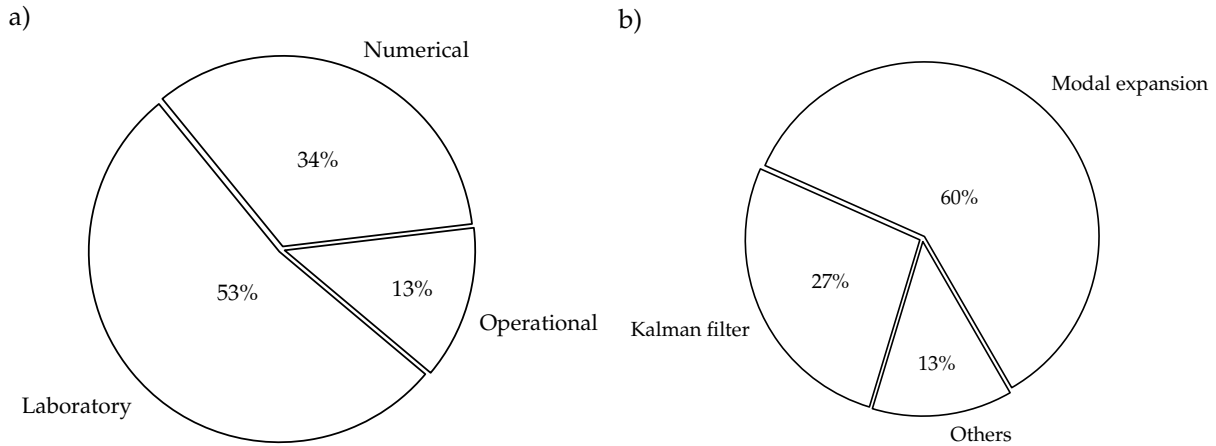


Figure 3.6: Categorisations and distribution of the reviewed articles from 1995 to 2019 in pie charts. a) The distribution of all applications, and b) the distribution of process model

the complexity tends to increase. Here, most articles involves wind turbines from the Belgian North Sea while other real-world applications include a lattice tower and the Shenzhen Bay Stadium in China. These applications test the achievability and practicality of the applied stress/strain estimation technique. At the technology readiness level of stress/strain estimation (at the time of writing), numerical simulation and laboratory testing of linear and stationary systems add little value to the research field. Based on this literature review, the readiness level of stress/strain estimation calls for real application in an operational environment.

We have analysed the distribution of applied process models in Fig. 3.6 b). In the literature, the most commonly applied process model is the modal expansion with 60% of applications while the various versions of Kalman filters take up 27%. Thus, we will introduce and discuss these two process models in section 3.5.

3.3 System model

Common for all virtual sensing techniques is that we need to add information regarding the measurements and the system to the process model. The process models, however, might require different information depending on the formulation and theory of the process model. Generally, this information is called the system model, mathematical model, or digital twin. The system model describes the system using mathematical expressions (variables, functions, and/or equations) [75] and it holds the state variables of the system. This model contains the general assumptions of the system and we term the process of setting up this model as "mathematical modelling". For virtual sensing, a system model relates the spatial-limited network of sensors to the system. Thus, it contains the geometrical information of the system and sensors while the system model holds all essential physical properties of the system required for the particular application and it could include information on the excitation. Furthermore, the configuration of the system model depends on the implementation of the process model.

For stress/strain estimation, the most common system model is the finite element model of the system, but it could take any form. It must, however, contain the necessary information required by the process model. For example, the system model could consists of mathematical shape functions [76].

In the following subsections, we will introduce some key concepts for system models.

3.3.1 Model evaluation and calibration

The accuracy of the system model is essential to the success of virtual sensing. A system model, which perfectly emulates the actual system, provides the optimal basis. Unfortunately, all mathematical models are approximations of the actual system. These approximations result in modelling errors in the system models that influence the quality of virtual sensing. We can apply model evaluation (validation) to access the level of modelling errors where the evaluation criteria depend on the application of virtual sensing.

To reduce modelling errors, we must calibrate and update the system model to better resemble the actual properties of the system. For stress/strain estimation, these properties are often modal parameters

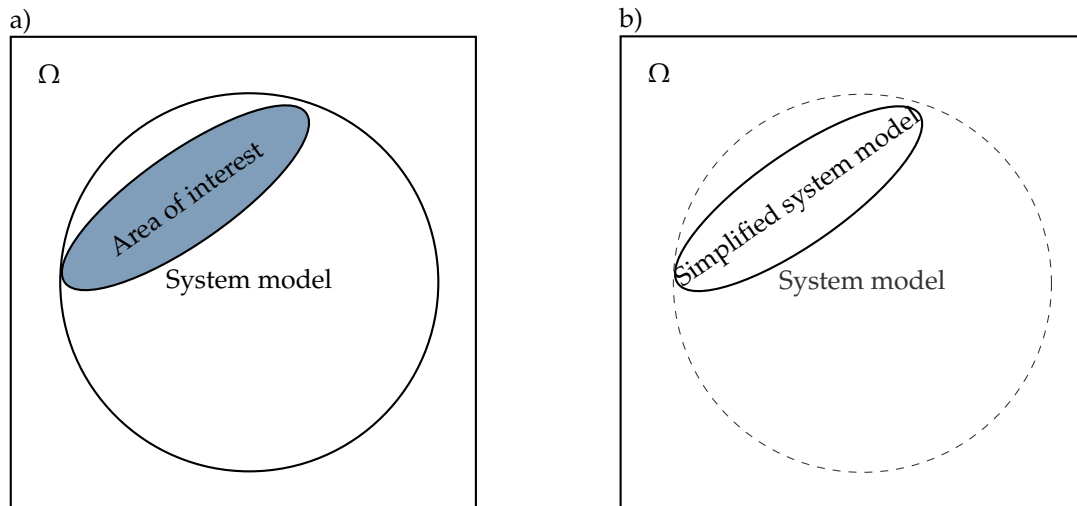


Figure 3.7: Venn diagram of model simplification, a) the full system model with redundant information and area of interest for the virtual sensing application, and b) simplified system model with the essential information for the particular application

from modal analysis: either experimental modal analysis [77] or operational modal analysis [78]. See [69, 70, 79, 80] for more on model updating using modal parameters as regards finite element models.

3.3.2 Model simplification

We merely need the essential information of the system in the system model for a successful application of virtual sensing. This essential information is the smallest possible set of state variables, which describes the desired behaviour of the system for the particular application. Therefore, we can apply model simplification, which is the identification and removal of the redundant information in the system model for the particular application. Thus, it reduces the set of possible states for the system. Fig. 3.7 illustrates this simplification of the system model in a Venn diagram. There is, however, a trade-off between the simplicity and accuracy of a model. Due to the model simplification, we have an error that is the absolute complement of the simplified system model.

A common model simplification is modal truncation, where the system is reduced to the contribution of a few modes (principal components). It uses the modal superposition, Eq. (2.3) page 9, to reduce the system model using different reduction techniques such as the System Equivalent Reduction-Expansion Process (SEREP) [81]. The modal expansion technique is another example of modal truncation since it requires this specific model simplification where the system model is simplified to a subset of mode shapes.

Example 3.1 - Modal truncation on offshore platform

We create a finite element model of an offshore tripod platform in Ansys using shell elements so that the model includes 57,456 DOFs. Let us say that we are interested in the global response. We simplify the model to a cantilever beam with an angular mass at the end so the simplified system contains five DOFs (neglecting the translational DOF along the beam): The two translational and three rotational DOFs describe the response of the simplified system and they roughly correspond to the first five modes. Here, the five mode shapes contain similar information regarding the system response as the five DOFs. Thus, we reduce the finite element model to these five modes (principal components). This system simplification - modal truncation - is illustrated in Fig. 3.8. Due to this simplification, we neglect the local behaviour of the structure.

3.3.3 State-to-measurement, sensitivity, and observability

In virtual sensing, a process links the physical measurements to the system model so that the process model is able to estimate the state of the system. In this chapter, we call this the "state-to-measurement-process". Here, the system model is reduced to the active DOFs corresponding to the number and position of the physical sensors. In mathematical terms, this reduced system model is the intersection of

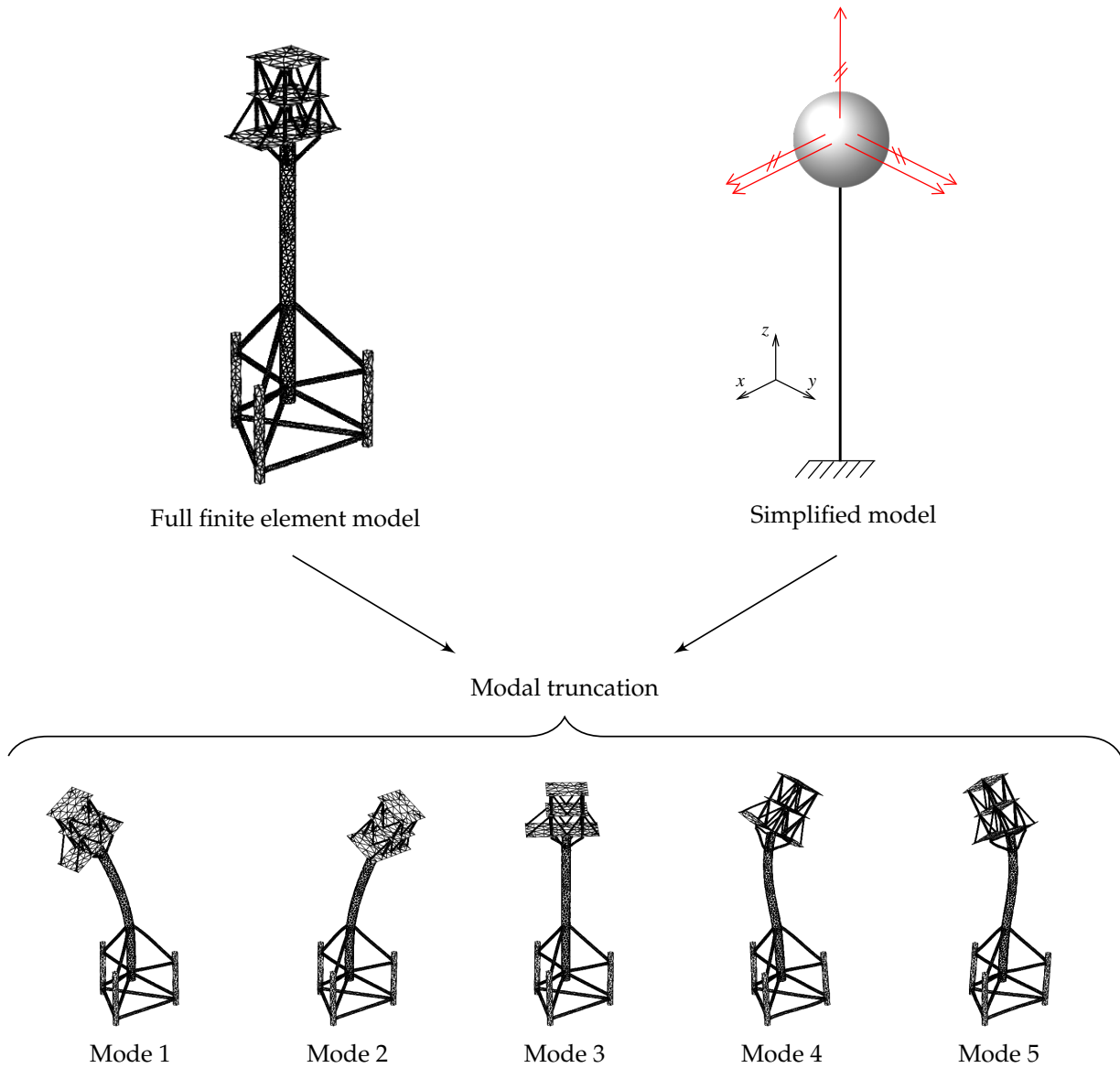


Figure 3.8: Example 3.1 - Modal truncation on offshore platform: The principle of modal truncation of a system model

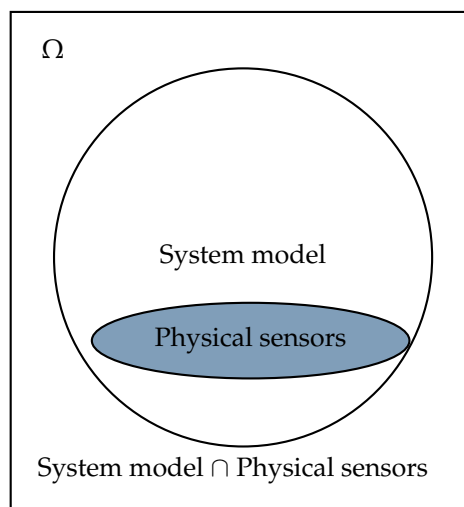


Figure 3.9: Venn diagram of the reduced system model in the state-to-measurement-process. Here, the reduced system model is the intersection of the system model and the physical sensors.

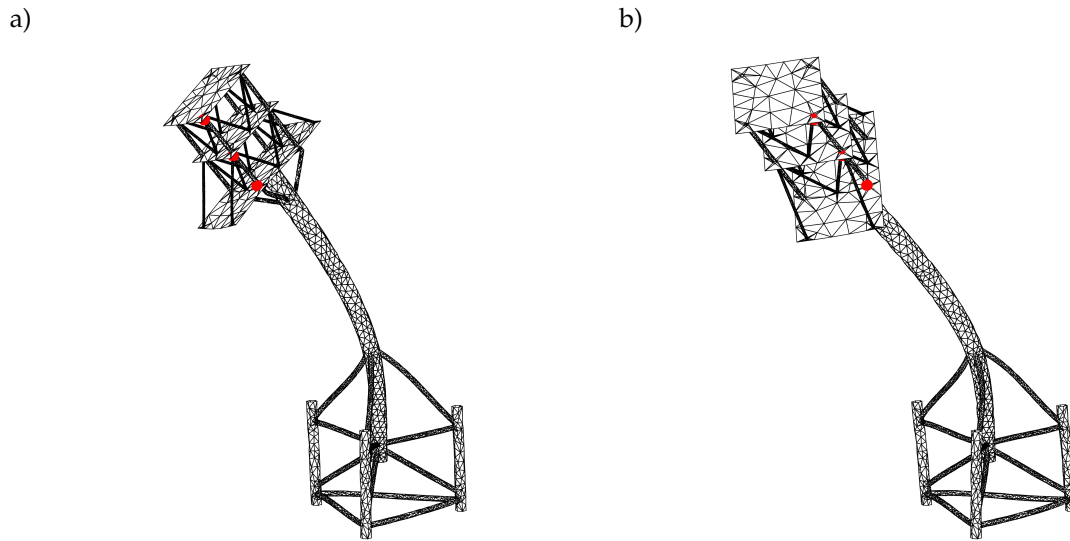


Figure 3.10: Example 3.2 - Sensitivity of reduced offshore platform: The principle of sensitivity of system model where a network of sensors (*red dots*) results in a sensitive reduced system model of nine degree-of-freedom: two iterations of added noise of low levels to the sensors and the corresponding estimated deflection shapes. The sensors have same position in a) and b) but the estimated deflection shapes are different.

the system model and the physical sensors (system model \cap physical sensors), see Fig. 3.9. The process makes the reduced system model sensitive where the position and number of the physical sensors determine the sensitivity of the system model in the state-to-measurement-process. Here, we apply the term "sensitivity" from linear algebra to describe how well the reduced system model distinguishes between states of the system in the presence of noise. The term "observability" is, however, utilised in control theory and it provides us with an indication of the state variables that we can observe in the measurements [82]. In an unstable, reduced system model, the system is ill-conditioned and several states are equally likely or noise might dominate so we are unable to correctly estimate the full set of state variables. In such a case, the system is unobservable and tiny amounts of noise can completely change the estimated states. Thus, it is important that the intersection of the system model and physical sensors exhibits all the relevant and essential state variables for the given application.

Therefore, the level of sensitivity for a system model is essential for the accuracy and reliability of the virtual sensors. A sensitive, reduced system model is easily corrupted or dominated by noise in the process model so the virtual sensors become erroneous. In contrast a stable system model is less inclined to result in erroneous estimation caused by noise. Given an unstable, reduced system model, the actual state of the system is indistinguishable based on the measurement from the physical sensors. The reader should, however, note that each process model deals differently with the sensitivity of the reduced system model.

Example 3.2 - Sensitivity of reduced offshore platform

In this example, we will illustrate the sensitivity of a reduced system model. We will use the system model from example 3.1 in section 3.3.2. We simplify the system model to the five mode shapes, see Fig. 3.8. Let us say we have a network of sensors that measure nine translational DOFs in three nodes of the finite element model, as seen in Fig. 3.10 a). The position of sensors, however, results in an unstable, reduced system model where we are largely incapable of estimating the third (torsional) mode. Here, the condition number of the reduced modal matrix is 490.12, which indicates the instability of the reduced system model. Furthermore, we calculate the rank of the reduced modal matrix to four by a tolerance of E^{-4} , thus, the matrix is near deficient rank.

We give the model a deflection shape and estimate this shape based on the first five modes and the sensor with additive white Gaussian noise in two iterations. This results in two widely different deflection shapes, see Fig. 3.10. The position of sensors in Fig. 3.10 a) and b) is the same albeit with a tiny error due to the added noise but the estimated deflection shapes are vastly different.

To increase the stability of the system model, we could exclude the third mode from the model so the condition number decreases to 5.7 - consistent with the near rank deficiency of the reduced modal matrix. This indicates that third mode is unobservable for the given network of sensors.

3.3.4 Data-driven (empirical) system model

We can base the system model on the available data of the system where we have either fully data-driven (empirical) system models or partial data-assisted system models [83, 84]. Data-driven system models build relationships in the data while the data calibrate and assist the mathematical modelling for the data-assisted system model. The hypothesis of these system models is that they contain less modelling errors since they are based on the data of the system. The reader should note that the fully data-driven system model is limited by the data upon which it is based. Thus, we are unable to extend the system model beyond the data without adding information to the system model.

In the literature, the expansion of experimental mode shapes is applied to stress/strain estimation [85]. Essentially, this is a data-assisted system model since it calibrates the system model where the expanded experimental mode shapes are a calibration of the spatial solution of the system model. The calibration, however, depends on the accuracy of the mode shape expansion. We refer the reader to chapter 7 page 111 for more on expansion of experimental mode shapes.

3.4 Physical sensors

In this Ph.D. thesis, the term "physical sensors" for virtual sensing includes both the sensor and signal processing of these sensors. In this section, we list and analyse the most commonly applied physical sensors in the literature of stress/strain estimation. This section is intended as a brief introduction to these sensors and we refer the reader to [86] for more extensive details and information on the sensors and to [87] for signal processing.

Generally, physical sensors are capable of measuring the observable and physical quantities (such as displacement, deformation, weight, and so forth) of a test specimen while they are incapable of directly measuring the external load or internal stress. Some sensors, however, transform these physical quantities into other quantities (e.g. load or stress) through transfer functions under specific assumptions [86].

We evaluate all physical sensors in terms of range (also dead band), sensitivity (or resolution), repeatability, accuracy, and errors caused by misalignment and calibration [86]. Some errors, such as calibration errors, lead to erroneous amplitude of the measurement while other sources of errors, like misalignment of the sensors, blend the desirable quantity with an undesirable component.

The accelerometer is the most commonly applied sensor for stress/strain estimation. These sensors measure the acceleration and they are beneficial for dynamic stress/strain estimation but they have limitations at low-frequency, where they are largely insensitive. Furthermore, these sensors are incapable of measuring the true Direct Current (DC) acceleration and they are prone to tilt (the effect of gravity) [78], see chapter 9 page 153. In stress/strain estimation, the measured acceleration must be numerically integrated into displacements and this introduces drift into the displacement.

The strain gauges are applied in stress/strain estimation as both the primary sensor and reference sensor, where we apply the latter to access and verify the virtual sensors. The sensors are passive transducers and they transform relative change in resistance to strain response by a proportional relationship between the relative change of resistance and the strain of the specimen. Unfortunately, a misalignment of a strain gauge causes the sensor to measure a combination of the desired and the transverse strain response, and thus we measure an erroneous strain response. Additionally, the strain gauge has a high noise floor and a limited lifespan. Furthermore, the fibre Bragg grating sensor is applicable as strain gauges and it is a fibre optic sensor.

There are other sensors applied to stress/strain estimation, although to a lesser degree than accelerometers and strain gauges. The geophone measures velocity through voltage while the gyroscope measures the orientation and the angular velocity. The Global Positioning System (GPS) measures position in time using a satellite-based radio-navigation system. There are also the optical sensors: digital image correlation [28, 67] or 3D point tracking [39, 40].

3.5 Process models

The process model estimates the state of the system based on the physical sensors and the system model. Therefore, the accuracy of the estimated state depends on the physical sensors, system model, and process model. For stress/strain estimation, there are various process models available, where the modal expansion technique and the Kalman filter are the most popular process models, see Fig. 3.6 b).

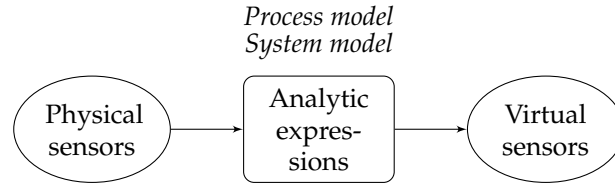


Figure 3.11: Flowchart of the analytic expressions as virtual sensing

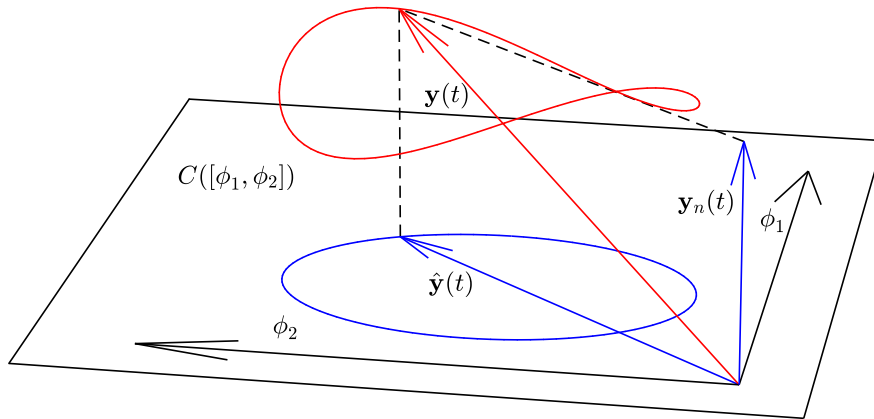


Figure 3.12: The principle of modal expansion illustrated in \mathbb{R}^3 with a two-dimensional subspace: We project the response, $\mathbf{y}(t)$, onto the subspace spanned by the mode shapes, ϕ_1 and ϕ_2 , and obtain the truncated response, $\hat{\mathbf{y}}(t)$, where all of the response orthogonal to the subspace, $\mathbf{y}_n(t)$, are removed

3.5.1 Analytic expressions

There are wide range of analytic expressions for the relationship between displacement and stress/strain [7–9, 9, 11, 12] that can be used for stress/strain estimation. Many of these are based on the well-known theory of differential equations for beams and plates. Here, the system and process model blend together since the process model is based directly on a known system and the corresponding theory, see the flowchart of the analytic expressions as virtual sensing in Fig. 3.11.

3.5.2 Transformation matrices and modal expansion

Transformation matrices transform the response into the strain response through matrix calculations as the process model. These techniques use least-square regression and/or linear algebra [82, 88] to create virtual strain gauges. These techniques compress the system model into this transformation matrix where the system model is reduced to the column space of the transformation matrix.

In the modern versions, the transformation matrix is estimated based on a subset of spatial limited base functions (vectors), which approximately span the response of the system. The system model contains the base functions and we reduced the model to the active DOFs corresponding to the position of physical sensors. The technique uses a linear transformation that projects the response onto the subspace of the reduced system model spanned by the base functions [88]. This enables an expansion of the measured response using the full spatial base functions. Thus, these transformation techniques work as a subspace reduction that removes any noise or response perpendicular to the new subspace of the base functions. Fig. 3.12 illustrates this subspace reduction with mode shapes as base functions (modal expansion). The transformation techniques must avoid an ill-posed inverse problem so they require a redundant sensor network - more physical sensors than base functions. In other words, transformation techniques require an overdetermined reduced system model. This limitation could be bypassed by separating the response into frequency bands with a reduced subset of the base functions for each band

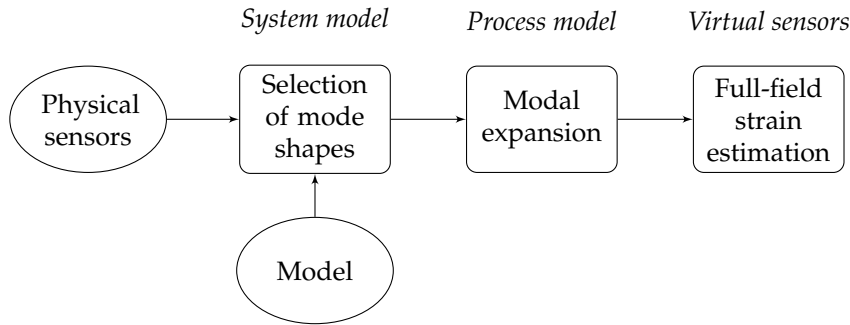


Figure 3.13: Flowchart of the modal expansion as virtual sensing

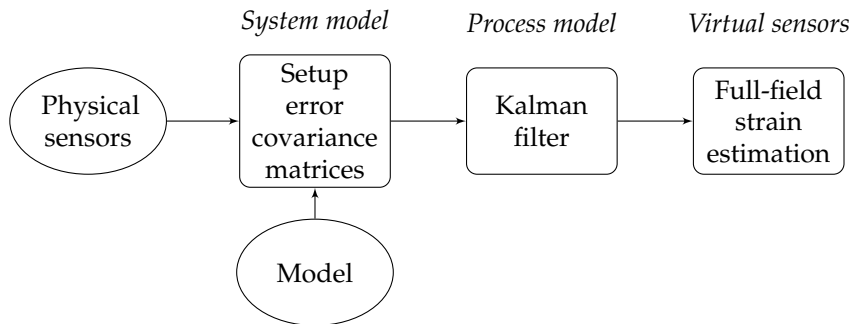


Figure 3.14: Flowchart of the Kalman filter as virtual sensing

[47, 48, 89]. Similar to least-square regression, the base functions should be linearly independent (or distinguishable) in the fitting domain to avoid rank deficiency of the transformation matrix for the pseudo inversion [82, 88]. These techniques have two main assumptions: the base functions span the system response of interest and there is a linear relationship between strain and displacement of the system. There is, however, no assumption regarding excitation.

For modal expansion, the base functions are a subset of spatial limited mode shapes [90, 91]. This technique utilises the aspect that the mode shapes of a linear system form the vector basis for the response in \mathbb{R}^N , hence, the response is a linear combination (called modal coordinates) of these mode shapes. We truncate the number of mode shapes to avoid an ill-posed inverse problem so their column space spans the majority of the system response. Thus, we apply model simplification to the system model in the form of modal truncation, see section 3.3.2. Fig. 3.13 outlines the flowchart of modal expansion. A thorough description of modal expansion given in chapter 7 page 111.

3.5.3 Adaptive filters

The adaptive filters emerge from control theory, which uses a state-space model of the system [92]. A common argument for the adaptive filters is that they are (probabilistic) optimal estimation algorithms and they have the potential to overcome both modelling errors and measurement noise. These filters are actually algorithms but they have similarities to low pass filters [93]. Thus, the adaptive filters remove noise while they estimate the full-state of the system. The most well-known of these adaptive filters is the Kalman filter. There are many different adaptive filters that resemble the Kalman filter in the literature: the dual Kalman filter [72], the augmented Kalman filter [74], the joint input-state estimator [73], the model-based observer for state and stress estimation [33], the extended Kalman filter [93], unscented Kalman filter [93, 94], and so forth. In this chapter, we refer to all these different filters as Kalman filters for simplicity. The flowchart of virtual sensing is outlined for the Kalman filter in Fig. 3.14 and the flow scheme of the Kalman filter as a process model is illustrated in Fig. 3.15. The statistical background of the Kalman filter is found in [92, 95] while an introduction for civil engineering is given in [96] and a practical introduction to the Kalman filter is given in [93].

The Kalman filter is an adaptive filter that utilises Bayesian filtering for linear state-space models using the discrete state equation and the observation equation [92, 95]. It uses measurements and a system model of a linear system to predict the next stage of the system. The main assumption of the Kalman filter is that the system model has some uncertainties and the measurements contain noise. The Kalman

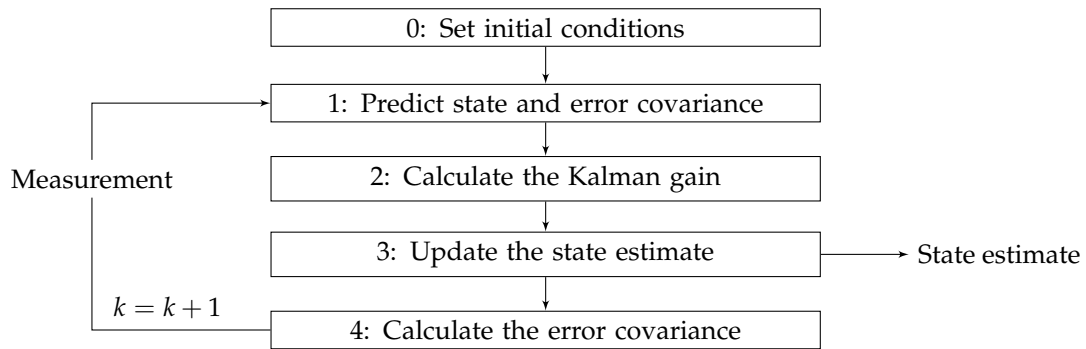


Figure 3.15: Flowchart of the Kalman filter as process model

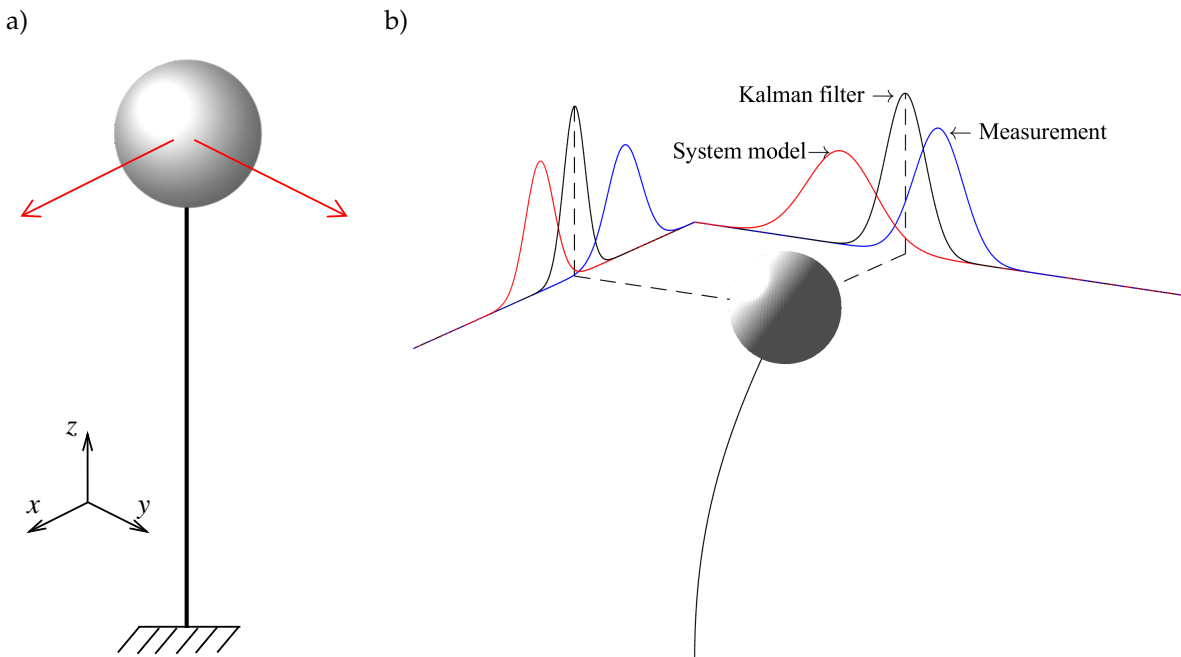


Figure 3.16: Example 3.3 - Simple example of the Kalman filter: the principle behind the Kalman filter illustrated for the simple system in a). In b), the probability density functions of the system model and the measurements fuse into a new probability density function for the Kalman filter. The expected value from Kalman filter is the optimal prediction of the state of system given the probability density functions of both the system model and the measurements.

filter assumes that these noise sources are white Gaussian noise with zero mean so we compute error covariance matrices for both noise sources [92, 95]. For Kalman filters, the system models include these error covariance matrices that the designer of the filter has to set up and it is a non-trivial task. Essentially, a Kalman filter uses multivariate Gaussian distributions to compute the conditional probability density function of the next state from the state equation of the linear system, given the probability of the current step. This probability density function is a new Gaussian distribution [95]. The same process is performed with the measurements from the observation equation. Given the Gaussian distributions of the two noise sources, the Kalman filter finds the best estimate for the state and observation equation in a closed-form solution. Hence, the Kalman filter finds the best fit given these noise sources and it is an optimal predictor.

Example 3.3 - Simple example of the Kalman filter

In this example, we want to illustrate the simplified concept behind the Kalman filter. Let us consider the two-DOF system in Fig. 3.16 a). We measure the system response with noise and we have a system model with modelling errors. The observation equation uses the measurements and the state equation applies the system model. Based on the previous data point, each equation estimates the new response. Here, the measurement of the system response is a stochastic process and system response based on the system model is another stochastic process. Each process is Gaussian distributed with a mean and a variance and the Kalman filter fuses the distributions and calculates the best estimate of

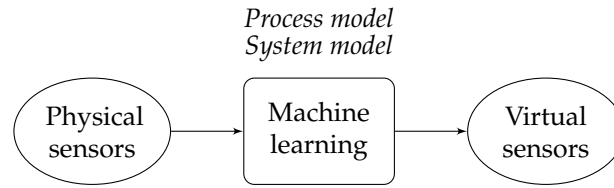


Figure 3.17: Flowchart of fully data-driven machine learning as virtual sensing

the response, see Fig. 3.16 b). The relative relationship between the variance or co-variance matrix of two processes determines the best estimate of the Kalman filter. Put simply, it finds a weighted mean given noisy measurements and a system model with modelling errors.

The accuracy of the Kalman filter, however, depends on the system model (including the error covariance matrices). Thus, the most important part of the design of a Kalman filter is an accurate system model. To sum up, the Kalman filter requires all modal parameters - in the form of the mass, damping, and stiffness matrix - while it requires the error covariance matrices.

The Kalman filter applies a state-to-measurement matrix to reduce the system model to the DOF corresponding to the physical sensors [96]. This matrix directly allows for sensor fusion - the use of different physical sensors - inside the Kalman filter. Unlike the modal expansion, the Kalman filter works with fewer sensors than the principal components in system model.

3.5.4 Other techniques

Recently, machine learning and pattern recognition have been applied to stress/strain estimation [54, 61]. These process models are data-driven (empirical) or data-assisted techniques so the system model blends somewhat into the process model where they automatically build the system and process models, see the flowchart of machine learning as virtual sensing in Fig. 3.17. These learning techniques require data from training sets and they enable stress/strain estimation in any point where a sensor trained the technique. Thus, fully data-driven techniques are incapable of full-field stress/strain estimation since they are limited to the locations of sensors from the training sets. To obtain full-field stress/strain estimation, we apply data-assisted techniques that require mathematical modelling aided by data. Machine learning from one system does, however, not necessarily transfer directly to another system. This topic falls under transfer learning. For complex and unique systems, learning algorithms require reference sensors since it is difficult to base the learning libraries on other systems so we must build a unique library for these systems. This is particularly the case for civil engineering, where structural designs are rarely repeated. Machine learning has potential in stress/strain estimation for systems produced in vast quantities where the model is directly transferable. Furthermore, we can apply machine learning to systems with temporary strain gauges, which measure the strain response in the desired locations, in the training sets. For more on machine learning see [95, 97].

Statistical predictions have also been applied to estimate the stress/strain response but these are not actual virtual sensing techniques. These techniques often focus on extreme stress (the maximum stress measured in a time period) [98, 99] instead of the stress/strain time history. Therefore, we excluded them from the literature review.

3.6 Discussion

In this section, we discuss important topics, challenges, and issues for stress/strain estimation.

3.6.1 Evaluation of virtual sensors

In the literature and/or industry, no rules or guidelines exist for the evaluation of virtual sensors. In this section, we will discuss the evaluation of virtual sensors for stress/strain estimation.

Similar to physical sensors, we should evaluate virtual sensors in terms of range, repeatability, sensitivity, and accuracy. Unlike physical sensors, the performance of virtual sensors depends on the combination of physical sensors, system model, and process model, which complicates an evaluation of a virtual sensor. Hence, we should consider a complex network of potential errors, which affect the performance,

such as measurement errors, modelling errors, sensitivity of the reduced system model, processing errors, and violations of the assumptions for the system and process model. In the literature, stress/strain estimation is evaluated by reference sensors where various quality measurements quantify the virtual sensors. We refer to the next subsection for an explanation of quality measurements. Thus, the virtual sensing is solely evaluated for the accuracy of the final output - the virtual sensor.

Any virtual sensing technique provides the perfect virtual sensors under ideal conditions. The achievement of these conditions might, however, be difficult in practice. Thus, an evaluation of the different virtual sensor techniques should account for the achievability and practicality of the conditions, assumptions, and tuning of the techniques that will provide the best estimation. This strengthens the argument for more operational applications under the actual conditions.

Quality measurements

Stress/strain estimation is often evaluated through quality measurement/metrics, which all have different strengths and weaknesses.

The Time Response Assurance Criterion (TRAC) [28] and Frequency Response Assurance Criterion (FRAC) [100] are popular quality measurements for stress/strain estimation. These metrics calculate a correlation between a reference signal and an estimated signal but they do not account for amplitude difference. Amplitude differences are, however, very important in fatigue analysis and an amplitude error in the estimation of stress leads to an erroneous estimation of the fatigue damage, see section 3.6.2. The two metrics are defined in a similar manner to the Modal Assurance Criterion (MAC).

$$TRAC_i = \frac{\left(\mathbf{\epsilon}_{t,i}^\top \hat{\mathbf{\epsilon}}_{t,i}\right)^2}{\left(\mathbf{\epsilon}_{t,i}^\top \mathbf{\epsilon}_{t,i}\right) \left(\hat{\mathbf{\epsilon}}_{t,i}^\top \hat{\mathbf{\epsilon}}_{t,i}\right)}, \quad FRAC_i = \frac{\left(\mathbf{\epsilon}_{f,i}^\top \hat{\mathbf{\epsilon}}_{f,i}\right)^2}{\left(\mathbf{\epsilon}_{f,i}^\top \mathbf{\epsilon}_{f,i}\right) \left(\hat{\mathbf{\epsilon}}_{f,i}^\top \hat{\mathbf{\epsilon}}_{f,i}\right)} \quad (3.1)$$

where $\mathbf{\epsilon}_{t,i}$ is the entire measured strain response for sensor i arranged in a column vector, and similarly, $\hat{\mathbf{\epsilon}}_{t,i}$ is the estimated strain response at the same location in the time domain. Additionally, $\mathbf{\epsilon}_{f,i}$ is the Fourier transform of the measured strain response for the i^{th} strain gauge arranged in a column vector, and similarly, $\hat{\mathbf{\epsilon}}_{f,i}$ is the frequency estimation of strain response in the same position.

Mean Square Error (MSE) and Mean Absolute Error (MAE) [101] are two popular metrics for evaluating the error of stress/strain estimation. These metrics are a measurement of the error in the signal but they are independent of the variance of the reference signal. Therefore, they do not indicate the signal-to-noise-ratio but only the error. In the literature, these two metrics are often normalised with the variance/maximum of the reference signal.

$$MSE_i = \mathbb{E} \left[(\varepsilon_i(t_k) - \hat{\varepsilon}_i(t_k))^2 \right], \quad MAE_i = \mathbb{E} \left[|\varepsilon_i(t_k) - \hat{\varepsilon}_i(t_k)| \right] \quad (3.2)$$

where $\varepsilon_i(t)$ is the measured strain response (reference signal) in the i^{th} strain gauge, $\hat{\varepsilon}_i(t)$ is the estimated strain response at the same location, and $\mathbb{E}[\cdot]$ denotes the expected value.

When the mean square error is normalised with the variance of the reference signal, it is equivalent to the coefficient of determination, R^2 or r^2 , from statistics and modal validation [88, 102]. This metric accounts for both amplitude differences and the general correlation between the signals. This metric should not be confused with the Pearson correlation coefficient.

$$R_i^2 = 1 - \frac{\mathbb{E} \left[(\varepsilon_i(t_k) - \hat{\varepsilon}_i(t_k))^2 \right]}{\text{Var} \left[\varepsilon_i(t_k) \right]} = 1 - \frac{\mathbb{E} \left[(\varepsilon_i(t_k) - \hat{\varepsilon}_i(t_k))^2 \right]}{\mathbb{E} \left[(\varepsilon_i(t_k) - \mathbb{E}[\varepsilon_i(t_k)])^2 \right]} \quad (3.3)$$

where $\text{Var}[\cdot]$ denotes the variance.

3.6.2 Stress/strain amplitude or range

In this section, we will illustrate how small amplitude differences in stress/strain estimation are amplified in the estimated fatigue damage. As stated in section 2.4.12, the stress amplitude (or stress range) and mean stress are the most influential parameters for the fatigue life whereas the frequencies of the fatigue stress are of minor importance (neglecting the number of cycles associated with the frequency). Therefore, the correct amplitude of the estimated stress/strain response is essential for fatigue analyses and we must attach great importance to the amplitude in stress/strain estimation.

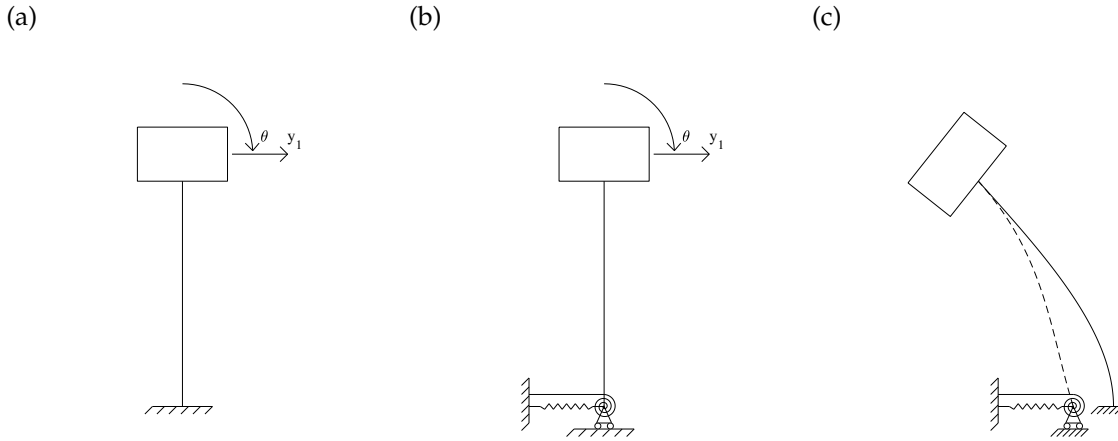


Figure 3.18: Example 3.4 - Amplitude difference due to erroneous boundary conditions of offshore structures: a beam with mass in the end with two different boundary conditions: a) fix support, and b) spring supports. In c), we apply the same displacement, y_1 and rotation, θ , for the mass and calculate the deflection of each boundary condition.

When we have an amplitude difference in our stress/strain estimation, this introduces an error in the estimated fatigue damage using the stress-life method. Let us say we have estimated the stress amplitude with a general amplitude error, $\hat{\sigma}_i = a\sigma_i$. We calculate the fatigue damage based on Palmgren-Miner rule, Eq. (2.23) page 13, with the estimated stress amplitude.

$$\begin{aligned}
 D_{est} &= \sum_{i=1}^N \frac{(a\sigma_i)^m}{C} \\
 &= a^m \sum_{i=1}^N \frac{\sigma_i^m}{C} \\
 &= a^m D
 \end{aligned} \tag{3.4}$$

Thus, a general amplitude error of a in the stress/strain estimation results in an amplified error in the fatigue damage of a^m . The correct amplitude in stress/strain estimation is an important factor for an accurate assessment of the fatigue damage. The estimated amplitude is, however, sensitive to both modelling error in the system model and calibration error and misalignment of the physical sensors. In this case, we intend stress/strain estimation for a fatigue analysis using the stress-life method, then it is crucial to evaluate the virtual sensor in terms of fatigue damage since this makes the effect of any amplitude differences in the estimation clear.

Example 3.4 - Amplitude difference due to erroneous boundary conditions of offshore structures

In this example, we will illustrate a potential cause for an amplitude difference in stress/strain estimation. The boundary conditions of offshore structures are not completely fixed since the soil has stiffness and damping properties. Generally, even small changes in boundary conditions will change the strain response of the system even though the displacement response is largely the same. Furthermore, soil properties change over time [97], see section 3.6.7. The soil properties pose a problem for calibrating a system model. Hence, modelling errors are likely to occur to some extent in the system model. Thus, it is important to consider boundary conditions in the calibration of the system model otherwise it might lead to an amplitude error in the stress/strain estimation.

Let us say that we apply stress/strain estimation to a cantilever beam with mass in the end, see Fig. 3.18 a), where we measure the displacement, y_1 , and rotation, θ , of the mass. Unfortunately, the actual system has supports with stiffness, Fig. 3.18 b). Mathematically, it is possible to obtain two sets of mass and stiffness matrices for these two systems that provide the same natural frequencies and mode shapes for the two DOFs of the mass for the first two modes.

Thus, we could erroneously estimate the strain response where Fig. 3.18 c) shows two excessive deflection shapes based on the same displacement and rotation of the mass. The stiffness of supports decreases the curvature of the beam near the bottom of the beam. Thus, we have an amplitude difference in our stress/strain estimation.

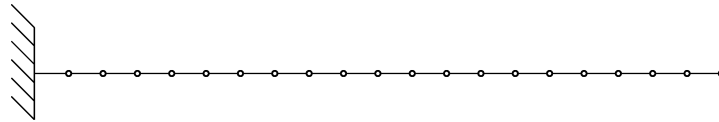


Figure 3.19: Example 3.5 - Position of sensors using modal expansion: Numerical cantilever beam with 20 Euler-Bernoulli beam elements

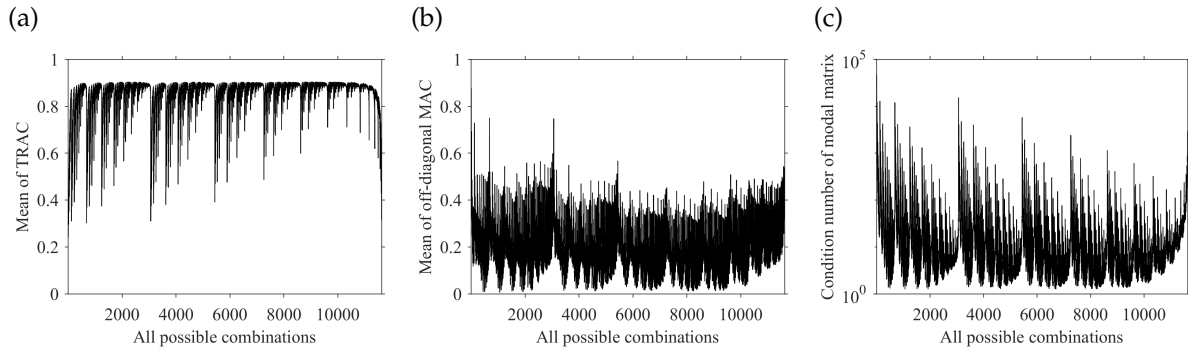


Figure 3.20: Example 3.5 - Position of sensors using modal expansion: a) the mean Time Response Assurance Criterion (TRAC) value as a function of the position of sensors, b) the mean of the off-diagonal values of the Modal Assurance Criterion (MAC) matrix as function of the position of sensors, and c) the conditional number of the reduced modal matrix as function of the position of sensors.

3.6.3 Number and position of sensors

A considerable volume of research has been conducted on the optimal position and number of sensors [24, 25, 103] since the position and number of the sensors are important for the performance of virtual sensing. This relates to the sensitivity of the reduced system model, see section 3.3.3. The reduced system model must be stable before we consider the virtual sensors to be accurate and reliable since the stability of the system model is transferred to the virtual sensors. In general, the number of sensors depends on the position of the sensors, the system, and the excitation.

Pingle and Avitabile [24, 25] found for modal expansion that the number of sensors should allow for the least-squares minimisation process, and the position of sensors should result in a linearly independent set of truncated mode shapes (corresponding to the position of sensors). A. Iliopoulos [104] proposed using the off-diagonals of the Modal Assurance Criterion (MAC) between the truncated mode shapes to validate the position of sensors for virtual sensing. These arguments are alternative formulations of the necessity for stable reduced system models.

In the framework of modal expansion, this author recommends applying the condition number of the truncated modal matrix (matrix holding the set of mode shapes) as a metric for the number and position of sensors. The reduced modal matrix corresponds to the reduced system model. The condition number relates to the sensitivity of matrix [75]; thus, in this case, the sensitivity of the system model reduced to the number and position of sensors.

Example 3.5 - Position of sensors using modal expansion

In this example, we will study the position of sensors in regards to strain estimation of a cantilever beam for modal expansion, see Fig. 3.19. We will evaluate the estimated strain response and check the relationship to the MAC values and the condition number. The beam is made in 2D with 20 Euler-Bernoulli beam elements. We simulate the response using the Fourier transformed method [78] with white noise excitation. We will use the first four mode shapes and five translational DOFs (corresponding to sensors) in all possible combinations to estimate the strain response in the entire beam. Then we will study the mean value of TRAC values, Eq. (3.1), mean of the off-diagonal values of the Modal Assurance Criterion (MAC) matrix, and the conditional number of the reduced modal matrix for each combination of sensors, see Fig. 3.20.

The off-diagonal values are not an ideal quantity to validate the quality of stress estimation. We obtain MAC values of 0.45 on the off-diagonal entries but we still obtain good TRAC values for the stress estimation, see Fig 3.21. The MAC values are only well correlated with the condition number as long as the mean off-diagonal MAC value is below 0.1. The condition number of the truncated modal matrix with the active DOFs is a better metric for stress/strain estimation. As stated in section

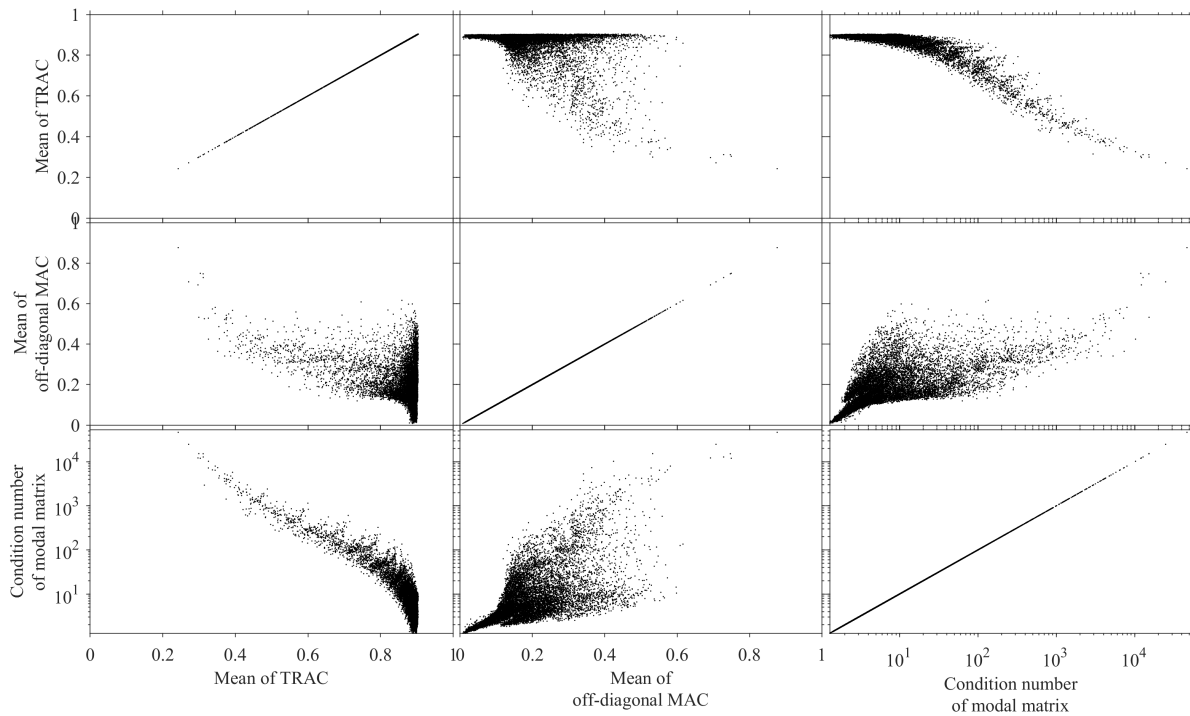


Figure 3.21: Example 3.5 - Position of sensors using modal expansion: scatter plot matrix of Time Response Assurance Criterion (TRAC), Modal Assurance Criterion (MAC), and condition number of modal matrix

3.5.2, the system model for modal expansion is truncated to a set of spatially limited mode shapes in a modal matrix. The condition number of this modal matrix shows the sensitivity of the system model. Therefore, this is a good indicator for the quality of the position of sensors.

3.6.4 Sensor fusion

The addition of sensors can decrease the sensitivity of the system model. Furthermore, a network of different and disparate sensors with individual strengths and weaknesses might decrease the sensitivity. We can combine the data and information of the disparate sensors so the resulting data holds less uncertainty than any of the individual sensors. This combination of disparate sensors is called sensor fusion. The research field of sensor fusion can benefit virtual sensing.

We can apply the Kalman filter [92] to sensor fusion so that we can obtain a new set of measurements. An example is accelerometers fused with GPSs or gyroscopes to reduce the drift caused by the numerical integration of acceleration into displacement. Optionally, we can apply complementary filters to two different sensors [93]. The idea of complementary filters is to apply filters that complements each other. An example is the fusion of two different sensors measuring the same quantity by applying a high-pass filter to one sensor and a low-pass filter to the other. The summation of two both filtered sensors gives the fused data.

We should note that the adaptive filters for virtual sensing already have sensor fusion incorporated into their process model [49, 71], while other techniques require manipulation or sensor fusion to account for different physical sensors. Additionally, the weighted least-square regression allows for regression for sensors with different levels of measurement errors where the diagonal weight matrix is the inverted covariance matrix of the measurement error for the sensors [62].

3.6.5 Modal truncation

It is critical that the system model spans the vector space of the response for an accurate stress/strain estimation. As stated in section 3.3.2, the system model is often truncated to only include contribution from a few modes. In the literature, many studies have been performed regarding the sufficient number of modes that we are able to truncate the system to, see [24–27, 67].

A system can have static effects from higher modes that are located away (in terms of frequency content) from the excitation frequency due to the spatial distribution of the excitation [105–110]. Therefore, describing the response by a limited number of lower modes causes a modal truncation error. The errors of modal truncation are studied in the numerical simulation of structures and structural computation [106–113]. In these fields, a truncation of modal superposition is applied to reduce the computation of the structural response. This, however, introduces a modal truncation error, which depends on the load and modes. For example, the spatial distributions of waves on an offshore structure creates contributions from higher modes [107]. In these fields, it is stated that the structural response can be calculated as a combination of the dynamic responses of the lower modes and a correction term based on the residual modes. Two types of corrections are created; static residual and residual vectors. The static residual uses static correction terms to adjust for the modal truncation, while the other method makes use of residual modes, also called “assumed modes” or “pseudo modes”, combined with the mode shapes [113].

Through this literature review, the concepts of the modal truncation error are rarely applied in an experimental setting. In stress/strain estimation, most research is based on the frequency content of the loading and the structure. Reintroducing the theory behind static correction to virtual sensing could, thus, benefit stress/strain estimation.

3.6.6 Nonlinearity, nonstationarity, and general damping

In an ideal world, all mechanical and structural systems are linear and stationary with proportional damping. This is, however, seldom the case in reality where some level of nonlinearity, nonstationarity, and general damping exists in a system. For insignificant levels, the linear and time-invariant assumptions are valid. When the level, however, increases, the validity decreases. In such a case, the traditional theories of dynamics and modal analysis are inapplicable and we have an issue for virtual sensing where solutions are needed for the nonlinear and nonstationary system with general damping. Stress/strain estimation for nonlinear systems is only studied in [64].

3.6.7 Offshore environment

In the literature, stress/strain estimation is often applied to offshore structures [36, 42, 44, 47, 48, 55, 65] and there are a few reasons for this. For these structures, fatigue is a significant factor of the design process so estimation of the stress history could lead to lifetime extensions. Furthermore, the sea makes up a harsh and hostile environment so the offshore structures are abstruse while the corrosive water corrupts and damages subsea sensors [97, 114]. Any network of sensors should be located above water in safe and accessible locations so virtual sensing could enable subsea measurements. Due to the importance of fatigue in the lifetime extension and the inaccessible subsea conditions, virtual sensing is often deemed to be beneficial for offshore structures.

Offshore structures have a unique set of issues for virtual sensing. An offshore platform has operating machinery and a wind turbine has rotating rotors that result in a nonstationary environment and excitation. Generally, offshore structures have strong variations in the modal properties based on the environmental and operational conditions, for instance: ingress of water, marine growth, fluid storage levels, subsidence, and soil properties [97]. Any changes in soil stiffness, soil damping, scour, and sediment transport at the seabed are critical for the fatigue damage [115]. Additionally, hydrodynamic damping of the surrounding water introduces nonlinearity to the offshore structure. The offshore platforms are often connected with bridges that introduce friction and nonlinear behaviour. The fuel tanks on the topside of the platform potentially act as tuned liquid dampers¹. Additionally, wave-induced structures have an influential quasi-static response since the wave load has a fixed spatial distribution and frequency content below the first structural mode [107, 109]. This means that we have an issue with modal truncation error for offshore structures, see section 3.6.5. A successful virtual sensing technique must include mitigations to these problems.

3.6.8 Quasi-static response and low frequency response

In this section, we will analyse and discuss the literature for stress/strain estimation for quasi-static response and low-frequency response. This relates to modal truncation, see section 3.6.5.

¹This was expressed as a concern by Maersk Oil and Gas (then)/Total (now), DUC, and DHRTC in initial talks to apply structural health monitoring

In the literature on stress/strain estimation, Skafte et al. [47] used Ritz vectors (static deflection shapes) to account for modal truncation in the quasi-static domain and Iliopoulos et al. [48] used strain gauges instead of the accelerometers in the quasi-static domain. Furthermore, Palanisamy et al. [35] found that accelerometers are ineffective for estimation of the quasi-static response near 0 Hz. This is due to the numerical drift and tilt of accelerometers. The drift is low-frequency noise that is caused by the numerical integration, which is an approximation, of acceleration signal to displacement. Furthermore, the numerical integration amplifies any noise near DC and the noise content depends on the type of accelerometer. The tilt of accelerometers and the noise on accelerometers near DC are issues and concerns for acceleration measurements [48, 78].

To summarise, there are several problems for stress/strain estimation for low-frequency content below the first structural mode. These include the structural-dynamics-related problem of the quasi-static effects and the drift and tilt of accelerometers. These problems must all be solved for successful stress/strain estimation for low frequencies.

3.7 Conclusion

In this chapter, we reviewed and presented the literature for virtual sensing of full-field stress/strain estimation using a narrative literature review. We summarised the history of the reviewed literature on virtual sensing related to stress/strain estimation and we found it to be a growing research field with an increasing number of published articles each year for the last decade. In this chapter, we introduced a terminology for stress/strain estimation and we analysed the system models, physical sensors, and process models frequently applied to stress/strain estimation. In the last section, we discussed different topics, challenges, and issues encountered in the application of stress/strain estimation and the evaluation of virtual sensors.

Stress/strain estimation started during the 1950s where the research was primarily focused on analytic techniques based on the theory of beams and plates. During the 1990s, the focus shifted towards projection and transformation techniques that used a fit between the response and the strain response to transform the measured response to strain. This allowed for strain estimation on more complex structures. The modal expansion techniques evolved from these projection techniques and they gained focus and popularity in the research field of stress/strain estimation. The analytic expressions for strain estimation using beam, plate, or shell theory are mostly neglected by the 2000s.

In 2005, Hjelm et al. [18, 20] and Graugaard-Jensen et al. [19] introduced the modern formulation of modal expansion. Since then only a few additions have been made to the modal expansion technique to overcome specific problems to a given application - such as overcoming the quasi-static response of wave-induced structures [47, 48]. Most literature on the modal expansion for stress/strain estimation relates to application and case studies in the laboratory. The actual development of the technique is, however, limited.

In the 2000s, the adaptive filters - such as the Kalman filter - was applied to strain estimation. Since then the adaptive filters have been commonplace in the literature where new versions have been introduced. The theory behind the adaptive filters is more complex than the modal expansion technique and the manual tuning of error covariance matrices requires expertise to ensure the proper setup of these filters. In recent years, machine learning has begun its entry into stress/strain estimation. To date, these techniques have, however, not been shown to be superior to the modal expansion. Therefore, the accuracy of stress/strain estimation today is largely the same as in 2005 where the modern version of the modal expansion was introduced for stress/strain estimation. Put simply, little progress has been made to stress/strain estimation since 2005 in direct contradiction to the increasing number of research articles.

Generally, there is a lack of consensus of the terminology in stress/strain estimation. This results in parallel subfields that research the same topic without acknowledging, incorporating, or building on the research of the other subfields. Thus, some papers introduce the same or similar research under different names and terms and do little to progress the overall research field. Most articles are applications and case studies of numerical simulations and laboratory tests. Applications are scarcely applied to real-world applications in operational environments. These applications would test the achievability and practicality of the conditions, assumptions, and tuning of the techniques. The readiness levels of stress/strain estimation point toward evaluation under operational conditions.

There are some common issues for virtual sensing. Stress/strain estimation is barely applied to non-linear and nonstationary systems. A successful technique should account for the level of nonstationarity and nonlinearity in the given application. For offshore structures, we must account for the quasi-static

response while removing the drift of the numerical integration of accelerometers and the tilt error on the accelerometers.

3.8 Planning and framing the Ph.D. project

We applied this review to set the course of this Ph.D. project. To focus and limit the research, we have had to make some choices regarding physical sensors, system models, and process model.

As stated by Loland and Dodds [114], a physical monitoring system should be restricted to being mounted above sea. In this Ph.D. thesis, we will focus on accelerometers located above water as the main sensors since the offshore industry primarily focuses on these sensors for structural health monitoring [97].

As the primary system model, we focus on the finite element model, which is also the most commonly applied system model in stress/strain estimation. As stated in this chapter, accuracy of stress/strain estimation depends on a well-calibrated system model. We see operational modal analysis and mode shape expansion of experimental mode shapes as a means to update a system model. Therefore, a significant part of this Ph.D. project relates to operational modal analysis and mode shape expansion. Furthermore, we want to study modal truncation errors since the set of mode shapes is critical for the success of stress/strain estimation. In this Ph.D. project, we want to apply the knowledge from the research fields of numerical simulation and structural computation.

As regards the process model, the exact excitation is unknown for offshore structures in operation so a successful virtual sensing technique must remain independent of the exact excitation. Additionally, a versatile technique supports different system models so its application covers the wide range of offshore structures. Therefore, the analytic expressions are neglected in this Ph.D. project. The harsh environment hinders machine learning techniques since the installation of sensors at the critical fatigue locations is difficult and makes it hard to train the algorithm properly. We are left with a choice between the Kalman filters and the modal expansion. This choice largely comes down to personal preferences. The modal expansion is the simplest process model and it merely requires the mode shapes compared to the Kalman filter, which requires the system matrices and tuned error covariance matrices. We restricted our research to the modal expansion as process model.

In this Ph.D. thesis, we will focus on the issues of nonlinearity and nonstationarity, quasi-static response, and modal truncation for stress/strain estimation. We have chosen to leave the other issues from section 3.6 for future research.

References

- [1] L. Liu, S. M. Kuo, and M. Zhou. Virtual sensing techniques and their applications. In *2009 International Conference on Networking, Sensing and Control*, pages 31–36, March 2009.
- [2] Haorong Li, Daihong Yu, and James E. Braun. A review of virtual sensing technology and application in building systems. *HVAC&R Research*, 17(5):619–645, 2011.
- [3] Shima Khatibisepehr, Biao Huang, and Swanand Khare. Design of inferential sensors in the process industry: A review of bayesian methods. *Journal of Process Control*, 23(10):1575 – 1596, 2013.
- [4] Bao Lin, Bodil Recke, Jørgen K.H. Knudsen, and Sten Bay Jørgensen. A systematic approach for soft sensor development. *Computers & Chemical Engineering*, 31(5):419 – 425, 2007. ESCAPE-15.
- [5] Herman Van der Auweraer, Tommaso Tamarozzi, Enrico Risaliti, Mathieu Sarrazin, Jan Croes, Bart Forrier, Frank Naets, and Wim Desmet. Virtual sensing based on design engineering simulation models. 07 2017.
- [6] Rossella Ferrari. Writing narrative style literature reviews. *Medical Writing*, 24:230–235, 12 2015.
- [7] Denis Gordon Karczub. *The prediction of dynamic stress and strain in randomly vibrating structures using vibrational velocity measurements*. PhD thesis, The University of Western Australia, 1996.
- [8] Alan Powell. On the fatigue failure of structures due to vibrations excited by random pressure fields. *The Journal of the Acoustical Society of America*, 30(12):1130–1135, 1958.
- [9] F. V. Hunt. Stress and strain limits on the attainable velocity in mechanical vibration. *The Journal of the Acoustical Society of America*, 32(9):1123–1128, 1960.
- [10] Stephen H. Crandall. Relation between strain and velocity in resonant vibration. *The Journal of the Acoustical Society of America*, 34(12):1960–1961, 1962.

- [11] Eric E. Ungar. Maximum Stresses in Beams and Plates Vibrating at Resonance. *Journal of Manufacturing Science and Engineering*, 84(1):149–155, 02 1962.
- [12] S.M. Stearn. Spatial variation of stress, strain and acceleration in structures subject to broad frequency band excitation. *Journal of Sound and Vibration*, 12(1):85 – 97, 1970.
- [13] N. Okubo and K. Yamaguchi. Prediction of strain distribution under operating condition by the use of modal analysis. *Proceedings of the International Modal Analysis Conference XIII*, 210(5):91–96, 1995.
- [14] L.L. Koss and D. Karczub. Euler beam bending wave solution predictions of dynamic strain using frequency response functions. *Journal of Sound and Vibration*, 184(2):229 – 244, 1995.
- [15] S.-W. Seo, K.-J. Kim, and B.-K. Bae. Estimation of operational strains from vibration measurements: An application to lead wires of chips on printed circuit board. *Journal of Sound and Vibration*, 210(5):567 – 579, 1998.
- [16] D.G. Karczub and M.P. Norton. Finite differencing methods for the measurement of dynamic bending strain. *Journal of Sound and Vibration*, 226(4):675 – 700, 1999.
- [17] N. SEHLSTEDT. Calculating the dynamic strain tensor field using modal analysis and numerical differentiation. *Journal of Sound and Vibration*, 244(3):407 – 430, 2001.
- [18] Henrik P. Hjelm, Rune Brincker, Jesper Gaugaard-Jensen, and Kasper Munch. Determination of stress histories in structures by natural input modal analysis. *Proceedings of IMAC XXIII International Modal Analysis Conference*, 12:838–844, 2005.
- [19] J. Graugaard-Jensen, Rune Brincker, H. P. Hjelm, and K. Munch. Modal based fatigue monitoring of steel structures. *Structural Dynamics EUROODYN 2005: Proceedings of 6th International Conference on Structural Dynamics*, pages 305–310, 2005.
- [20] *Reduction in Inspection Costs for Dynamic Sensitive Steel Structures by Modal Based Fatigue Monitoring*, volume 24th International Conference on Offshore Mechanics and Arctic Engineering: Volume 2 of International Conference on Offshore Mechanics and Arctic Engineering, 06 2005.
- [21] Gun-Myung Lee. Prediction of strain responses from the measurements of displacement responses. *Mechanical Systems and Signal Processing*, 21(2):1143 – 1152, 2007.
- [22] F. Pelayo, M. Aenlle, R. Brincker, and A. Fernández-Canteli. Stress estimation in structures using operational model analysis. *Third International Operational Modal Analysis Conference (IOMAC)*, page 675–682, 2009.
- [23] C. Papadimitriou, C.P. Fritzen, P. Kraemer, and E. Ntotsios. Fatigue predictions in entire body of metallic structures from a limited number of vibration sensors using kalman filtering. *Structural Control and Health Monitoring*, 18(5):554–573, 2011.
- [24] Pawan Pingle and Peter Avitabile. Prediction of full field dynamic stress/strain from limited sets of measured data. In Tom Proulx, editor, *Structural Dynamics, Volume 3*, pages 883–895, New York, NY, 2011. Springer New York.
- [25] Pawan Pingle and Peter Avitabile. Full field dynamic stress/strain from limited sets of measured data. In Tom Proulx, editor, *Linking Models and Experiments, Volume 2*, pages 187–200, New York, NY, 2011. Springer New York.
- [26] Pawan Pingle, Christopher Niezrecki, and Peter Avitabile. Full field numerical stress-strain from dynamic experimental measured data. pages 2068 – 2076. Proceedings of the 8th International Conference on Structural Dynamics, EUROODYN 2011, 07 2011.
- [27] Pawan Pingle and Peter Avitabile. Limited experimental displacement data used for obtaining full-field dynamic stress strain information. In Tom Proulx, editor, *Linking Models and Experiments, Volume 2*, pages 201–217, New York, NY, 2011. Springer New York.
- [28] Peter Avitabile and Pawan Pingle. Prediction of full field dynamic strain from limited sets of measured data. *Shock and Vibration*, 19(5):765–785, 2012.
- [29] Manuel López Aenlle, Lutz Hermanns, Pelayo Fernández, and Alberto Fraile. Stress estimation in a scale model of a symmetric two story building. page 9, 2013.
- [30] C. Papadimitriou, E.-M. Lourens, G. Lombaert, G. De Roeck, and K. Liu. Prediction of fatigue damage accumulation in metallic structures by the estimation of strain from operational vibrations. page 304–310, 2013.
- [31] Peter Avitabile, Eric Harvey, and Justin Ruddock. Comparison of full field strain distributions to predicted strain distributions from limited sets of measured data for shm applications. In *Damage Assessment of Structures X*, volume 569 of *Key Engineering Materials*, pages 1140–1147. Trans Tech

- Publications Ltd, 10 2013.
- [32] P. Ren and Z. Zhou. Strain response estimation for fatigue monitoring of an offshore truss structure. *Pacific Science Review*, 16(1):29–35, 2014.
- [33] Kalil Erazo and Eric M. Hernandez. A model-based observer for state and stress estimation in structural and mechanical systems: Experimental validation. *Mechanical Systems and Signal Processing*, 43(1):141 – 152, 2014.
- [34] B. F. Spencer Jr. Hongki Jo. Multi-metric model-based structural health monitoring, 2014.
- [35] Rajendra Prasath Palanisamy, Soojin Cho, Hyunjun Kim, and Sung-Han Sim. Experimental validation of kalman filter-based strain estimation in structures subjected to non-zero mean input. *Smart Structures and Systems*, 15:489–503, 2015.
- [36] K. Maes, G. De Roeck, G. Lombaert, A. Iliopoulos, D. Van Hemelrijck, C. Devriendt, and P. Guillaume. Continuous strain prediction for fatigue assessment of an offshore wind turbine using kalman filtering techniques. In *2015 IEEE Workshop on Environmental, Energy, and Structural Monitoring Systems (EESMS) Proceedings*, pages 44–49, July 2015.
- [37] Fernández P., A. Skafté, M. L. Aenlle, and R. Brincker. Modal analysis based stress estimation for structural elements subjected to operational dynamic loadings. *Experimental Mechanics*, 55(9):1791–1802, Nov 2015.
- [38] Jakerson Gevinski and Robson Pederiva. Dynamic strain prediction using modal parameters. *Journal of the Brazilian Society of Mechanical Sciences and Engineering*, 38, 06 2015.
- [39] Javad Baqersad, Christopher Niezrecki, and Peter Avitabile. Extracting full-field dynamic strain on a wind turbine rotor subjected to arbitrary excitations using 3d point tracking and a modal expansion technique. *Journal of Sound and Vibration*, 352:16 – 29, 2015.
- [40] Javad Baqersad, Christopher Niezrecki, and Peter Avitabile. Full-field dynamic strain prediction on a wind turbine using displacements of optical targets measured by stereophotogrammetry. *Mechanical Systems and Signal Processing*, 62-63:284 – 295, 2015.
- [41] J. Kullaa. Combined empirical and analytical virtual sensing in structural dynamics for uncertainty reduction. pages 443–466, 01 2015.
- [42] K. Maes, A. Iliopoulos, W. Weijtjens, C. Devriendt, and G. Lombaert. Dynamic strain estimation for fatigue assessment of an offshore monopile wind turbine using filtering and modal expansion algorithms. *Mechanical Systems and Signal Processing*, 76-77:592–611, 2016.
- [43] Jyrki Kullaa. Virtual sensing of structural vibrations using dynamic substructuring. *Mechanical Systems and Signal Processing*, 79:203 – 224, 2016. Special Issue from ICEDyn 2015.
- [44] Alexandros Iliopoulos, Wout Weijtjens, Danny Van Hemelrijck, and Christof Devriendt. Full-field strain prediction applied to an offshore wind turbine. In Sez Atamturktur, Tyler Schoenherr, Babak Moaveni, and Costas Papadimitriou, editors, *Model Validation and Uncertainty Quantification, Volume 3*, pages 349–357, Cham, 2016. Springer International Publishing.
- [45] Vasilis Dertimanis, Eleni Chatzi, Saeed Eftekhar Azam, and Costas Papadimitriou. Output-only fatigue prediction of uncertain steel structures. page 11, 07 2016.
- [46] Vasilis Dertimanis, Eleni Chatzi, Saeed Eftekhar Azam, and Costas Papadimitriou. Fatigue assessment in steel railway bridges using output only vibration measurements and partial structural information. volume 110, 01 2016.
- [47] A. Skafté, J. Kristoffersen, J. Vestermark, U. T. Tygesen, and R. Brincker. Experimental study of strain prediction on wave induced structures using modal decomposition and quasi static ritz vectors. *Engineering Structures*, 136:261–276, 4/1 2017.
- [48] Alexandros Iliopoulos, Wout Weijtjens, Danny Van Hemelrijck, and Christof Devriendt. Fatigue assessment of offshore wind turbines on monopile foundations using multi-band modal expansion. *Wind Energy*, 20(8):1463–1479, 2017.
- [49] Rajendra Prasath Palanisamy, Wonsul Kim, Sung-Han Sim, and Jin-Hak Yi. Reconstruction of unmeasured strain responses in bottom-fixed offshore structures by multimetric sensor data fusion. *Procedia Engineering*, 188:96 – 101, 2017.
- [50] Peng Ren and Zhi Zhou. Strain estimation of truss structures based on augmented kalman filtering and modal expansion. *Advances in Mechanical Engineering*, 9(11):1–10, 2017.
- [51] M. Aenlle, F. Pelayo, and A. Fernandez-Canteli. Fatigue damage detection and prediction of fatigue life on a cantilever beam. *International Journal of Structural Integrity*, 10:648–655, 2017.

- [52] Dimitrios Giagopoulos, Alexandros Arailopoulos, V. Dertimanis, Costas Papadimitriou, Eleni Chatzi, and Konstantinos Grompanopoulos. Computational framework for online estimation of fatigue damage using vibration measurements from a limited number of sensors. *Procedia Engineering*, 199:1906 – 1911, 2017. X International Conference on Structural Dynamics, EUROODYN 2017.
- [53] Jyrki Kullaa. Bayesian virtual sensing for full-field dynamic response estimation. *Procedia Engineering*, 199:2126 – 2131, 2017. X International Conference on Structural Dynamics, EUROODYN 2017.
- [54] Wei Lu, Jun Teng, Qiushi Zhou, and Qiexin Peng. Stress prediction for distributed structural health monitoring using existing measurements and pattern recognition. *Sensors*, 18(2), 2018.
- [55] N. Noppe, K. Tatsis, E. Chatzi, C. Devriendt, and W. Weijtjens. Fatigue stress estimation of offshore wind turbine using a kalman filter in combination with accelerometers. page 9, 2018.
- [56] Johannes Luthe, Andreas Schulze, Roman Rachholz, János Zierath, and Christoph Woernle. Acceleration-based strain estimation in a beam-like structure. Lisboa, Portugal, 07 2018. The 5th Joint International Conference on Multibody System Dynamics.
- [57] Yuanchang Chen, Dagny Joffre, and Peter Avitabile. Underwater Dynamic Response at Limited Points Expanded to Full-Field Strain Response. *Journal of Vibration and Acoustics*, 140(5), 05 2018.
- [58] L. Lagerblad, H. Wentzel, and A. Kulachenko. Fatigue damage prediction based on the strain field estimates using a smoothed kalman filter and sparse measurements. *Proceedings of ISMA2018 and USD2018*, pages 2805–2817, 2018.
- [59] Callum Roberts, Sophie Isbister, Cameron Murphy, Calvin Nisbet, Paul Sweeney, Dmitri Tcherniak, and David García Cava. Strain estimation using a modal expansion approach via virtual sensing for structural asset management. 1st International Conference on Structural Integrity for Offshore Energy Industry, 09 2018.
- [60] Javad Baqersad and Kedar Bharadwaj. Strain expansion-reduction approach. *Mechanical Systems and Signal Processing*, 101:156 – 167, 2018.
- [61] Huaxia Deng, Haicong Zhang, Jun Wang, Jin Zhang, Mengchao Ma, and Xiang Zhong. Modal learning displacement–strain transformation. *Review of Scientific Instruments*, 90(7):075113, 2019.
- [62] J. Kullaa. Bayesian virtual sensing in structural dynamics. *Mechanical Systems and Signal Processing*, 115:497 – 513, 2019.
- [63] Mansure Nabiyan, Hamed Ebrahimian, Babak Moaveni, and Faramarz Khoshnoudian. Structural identification for dynamic strain estimation in wind turbine towers. In Shamim Pakzad, editor, *Dynamics of Civil Structures, Volume 2*, pages 239–245, Cham, 2019. Springer International Publishing.
- [64] Enrico Risaliti, Tommaso Tamarozzi, Martijn Vermaut, Bram Cornelis, and Wim Desmet. Multi-body model based estimation of multiple loads and strain field on a vehicle suspension system. *Mechanical Systems and Signal Processing*, 123:1 – 25, 2019.
- [65] Maximilian Henkel, Wout Weijtjens, and Christof Devriendt. Validation of virtual sensing on sub-soil strain data of an offshore wind turbine. *8th International Operational Modal Analysis Conference - IOMAC' 19*, page 10, 2019.
- [66] Mathias W. Pedersen, Emil K. Andersen, Martin D. Ulriksen, and Lars Damkilde. Estimation of modal expansion and kalman filtering techniques for vibration estimation. page 675–682, 2019.
- [67] Kedar Bharadwaj, Azadeh Sheidaei, Arash Afshar, and Javad Baqersad. Full-field strain prediction using mode shapes measured with digital image correlation. *Measurement*, 139:326 – 333, 2019.
- [68] Costas Papadimitriou, Eleni N. Chatzi, Saeed Eftekhar Azam, and Vasilis K. Dertimanis. Fatigue monitoring and remaining lifetime prognosis using operational vibration measurements. In Robert Barthorpe, editor, *Model Validation and Uncertainty Quantification, Volume 3*, pages 133–136, Cham, 2019. Springer International Publishing.
- [69] Dimitrios Giagopoulos, Alexandros Arailopoulos, Vasilis Dertimanis, Costas Papadimitriou, Eleni Chatzi, and Konstantinos Grompanopoulos. Structural health monitoring and fatigue damage estimation using vibration measurements and finite element model updating. *Structural Health Monitoring*, 18(4):1189–1206, 2019.
- [70] Dimitrios Giagopoulos, Alexandros Arailopoulos, and Sotirios Natsiavas. A model-based fatigue damage estimation framework of large-scale structural systems. *Structural Health Monitoring*, 0(0):1475921719871953, 2019. Special Issue: APWSHM-2018.

- [71] Rajendra prasath Palanisamy, B.-J Jung, Sung-Han Sim, and Jin-Hak Yi. Quasi real-time and continuous non-stationary strain estimation in bottom-fixed offshore structures by multimetric data fusion. *Smart Structures and Systems*, 23:61–69, 01 2019.
- [72] S. E. Azam, E. Chatzi, and C. Papadimitriou. A dual kalman filter approach for state estimation via output-only acceleration measurements. *Mechanical Systems and Signal Processing*, 60-61:866–886, 2015.
- [73] K. Maes, A.W. Smyth, G. De Roeck, and G. Lombaert. Joint input-state estimation in structural dynamics. *Mechanical Systems and Signal Processing*, 70-71:445 – 466, 2016.
- [74] E. Lourens, E. Reynders, G. De Roeck, G. Degrande, and G. Lombaert. An augmented kalman filter for force identification in structural dynamics. *Mechanical Systems and Signal Processing*, 27:446 – 460, 2012.
- [75] Erwin Kreyszig, Herbert Kreyszig, and Edward J. Norminton. *Advanced engineering mathematics*. John Wiley And Sons Ltd, Hoboken, NJ, 10th edition, 2011.
- [76] Yuanchang Chen, P. Logan, P. Avitabile, and Jacob Dodson. Non-model based expansion from limited points to an augmented set of points using chebyshev polynomials. *Experimental Techniques*, 43:521–543, 2019.
- [77] Anders Brandt. *Noise and vibration analysis : signal analysis and experimental procedures*. Wiley, Chichester, UK, 1st edition, 2011.
- [78] Rune Brincker and Carlos Ventura. *Introduction to operational modal analysis*. John Wiley and Sons, Inc., Chichester, West Sussex, UK, 2015.
- [79] N A Z Abdullah, M S M Sani, M M Rahman, and I Zaman. A review on model updating in structural dynamics. *IOP Conference Series: Materials Science and Engineering*, 100:012015, dec 2015.
- [80] J.E. Mottershead and M.I. Friswell. Model updating in structural dynamics: A survey. *Journal of Sound and Vibration*, 167(2):347 – 375, 1993.
- [81] J.C. O’Callahan, P.A. Avitabile, and R. Riemer. System equivalent reduction expansion process (serep). *Proceedings of the 7th International Modal Analysis Conference*, 1989.
- [82] John L. Crassidis and John L. Junkins. *Optimal Estimation of Dynamic Systems, Second Edition (Chapman & Hall/CRC Applied Mathematics & Nonlinear Science)*. Chapman & Hall/CRC, 2nd edition, 2011.
- [83] Eliz-Mari Lourens, Edwin Reynders, Geert Lombaert, Guido De Roeck, and Geert Degrande. Dynamic force identification by means of state augmentation: a combined deterministic-stochastic approach. pages 2069–2080. Sas, P, KATHOLIEKE UNIV LEUVEN, DEPT WERKTUIGKUNDE, 2010.
- [84] Jui-Jung Liu, Chin-Kao Ma, I-Chung Kung, and Dong-Cherng Lin. Input force estimation of a cantilever plate by using a system identification technique. *Computer Methods in Applied Mechanics and Engineering*, 190(11):1309 – 1322, 2000.
- [85] Anders Skaftø. *Applications of Expansion Techniques in Operational Modal Analysis*. PhD thesis, Aarhus University, DK, 2016.
- [86] Jacob Fraden. *Handbook of Modern Sensors: Physics, Designs, and Applications*. Springer International Publishing, London, UK, 2016.
- [87] R. G. Lyons. *Understanding digital signal processing*. Prentice Hall, Upper Saddle River, N.J., USA, 3rd. edition, 2011.
- [88] Per Christian Hansen, Víctor Pereyra, and Godela Scherer. *Least squares data fitting with applications*. Johns Hopkins University Press, Baltimore, MD, USA, 2013.
- [89] A. Iliopoulos, R. Shirzadeh, W. Weijtjens, P. Guillaume, D. V. Hemelrijck, and C. Devriendt. A modal decomposition and expansion approach for prediction of dynamic responses on a monopile offshore wind turbine using a limited number of vibration sensors. *Mechanical Systems and Signal Processing*, 68-69:84–104, 2016.
- [90] D.C. Kammer. Test-analysis model development using an exact modal reduction. *International Journal of Analytical and Experimental Modal Analysis*, 2:174–179, 1987.
- [91] Daniel Kammer. Estimation of structural response using remote sensor locations. *Journal of Guidance, Control and Dynamics*, 20:1379–1385, 05 1997.
- [92] R.E. Kalman. A new approach to linear filtering and prediction problems. *Journal of Basic Engineering*, 82:35–45, 1960.

- [93] Phil Kim and Lynn Huh. *Kalman filter for beginners : with MATLAB examples*. CreateSpace, United States, 2011.
- [94] S. J. Julier, J. K. Uhlmann, and H. F. Durrant-Whyte. A new approach for filtering nonlinear systems. *Proceedings of 1995 American Control Conference - ACC'95*, 3:1628–1632, 1995.
- [95] Kevin P. Murphy. *Machine learning : a probabilistic perspective*. MIT Press, Cambridge, Mass., 2012.
- [96] Carlo Rainieri and Giovanni Fabbro. *Operational modal analysis of civil engineering : an introduction and guide for applications*. Springer Science+Business, New York, USA, 2014.
- [97] C. R. Farrar and K. Worden. *Structural Health Monitoring: A Machine Learning Perspective*. John Wiley and Sons, Ltd, Chichester, West Sussex, UK, 2013.
- [98] Xueping Fan. Bridge extreme stress prediction based on bayesian dynamic linear models and non-uniform sampling. *Structural Health Monitoring*, 16(3):253–261, 2017.
- [99] Yuefei Liu and Xueping Fan. Bayesian prediction of bridge extreme stresses based on dltn and monitoring coupled data. *Structural Health Monitoring*, 0(0):1475921719853171, 0.
- [100] W. Heylen and S. Lammens. Frac: a consistent way of comparing frequency response functions. *Proceedings of the Conference on Identification in Engineering Systems*, pages 48–57, 1996.
- [101] Julius S. Bendat and Allan G. Piersol. *Random data: analysis and measurement procedures*. Wiley-Blackwell, Hoboken, N.J., USA, 4th edition, 2010.
- [102] Charles L. Lawson and Richard J. Hanson. *Solving least squares problems*. Prentice-Hall, Englewood Cliffs, USA, 1974.
- [103] C.D. Zhang and Y.L. Xu. Optimal multi-type sensor placement for response and excitation reconstruction. *Journal of Sound and Vibration*, 360:112 – 128, 2016.
- [104] Alexandros Iliopoulos. *Virtual sensing techniques for response estimation and fatigue assessment of offshore wind turbines*. PhD thesis, Vrije Universiteit Brussel, 2017.
- [105] A.K. Chopra. *Dynamics of Structures: Theory and Applications to Earthquake Engineering*. Prentice Hall International Series in Civil Engineering And. Pearson/Prentice Hall, 2007.
- [106] D.C. Lui, H.L. Chung, and W.M. Chang. The errors caused by modal truncation in structure dynamic analysis. *IMAC XVIII – 18th International Modal Analysis Conference*, pages 1455–1460, 2000.
- [107] P. Léger, J. M. Ricles, and L. J. Robayo. Reducing modal truncation error in wave response analysis of offshore structures. *Communications in applied numerical methods*, 6(1):7–16, 1990.
- [108] J. H. Vugts, I. M. Hinesm, R. Nataraja, and W. Schumm. Modal superposition vs. direct solution techniques in the dynamic analysis of offshore structures. *BOSS'79, Proceedings of the Second International Conference on Behaviour of Off-Shore Structures*, pages 23–29, 1979.
- [109] O. E. Hansteen and K. Bell. On the accuracy of mode superposition analysis in structural dynamics. *Earthquake Engineering and Structural Dynamics*, 7:405–411, 1979.
- [110] P. Léger and E. L. Wilson. Generation of load dependent ritz transformation vectors in structural dynamics. *Engineering Computations*, 4(4):309–318, 1987.
- [111] N. R. Maddox. On the number of modes necessary for accurate response and resulting forces in dynamic analysis. *Journal of Applied Mechanics ASME*, 42(2):516–517, 1975.
- [112] J. M. Dickens, J. M. Nakagawa, and M. J. Wittbrodt. A critique of mode acceleration and modal truncation augmentation methods for modal response analysis. *Computers & Structures*, 62(6):985–998, 1997.
- [113] N. Roy and A. Girard. Impact of residual modes in structural dynamics. *Proceedings of the European Conference on Spacecraft Structure, Materials and Testing*, 2005.
- [114] O. Loland and C. J. Dodds. Experiences in developing and operating integrity monitoring systems in the north sea. *Proceedings of Offshore Technology Conference*, 2:313–320, 1976.
- [115] M. Damgaard, L.V. Andersen, and L.B. Ibsen. Dynamic response sensitivity of an offshore wind turbine for varying subsoil conditions. *Ocean Engineering*, 101:227 – 234, 2015.

Part II

Contributions

Chapter 4

Paper 1 - The statistical errors in the estimated correlation function matrix for operational modal analysis

“

I do not have empathy for damping

”

Carmelo Gentile

Status

- Published in Journal of Sound and Vibration
- Available here: <https://doi.org/10.1016/j.jsv.2019.115013>

4.1 Introduction

Unbiased modal parameters with low uncertainty are important for stress/strain estimation since they are used to update and calibrate the system model. To obtain the estimated modal parameters with reduced bias and random errors, the first step is to understand the errors involved in operational modal analysis and the identification process. There are many different sources of errors, including:

- Measurement setups
- Identification process
- Statistical process
- Violation of the core assumptions in operational modal analysis

We focused on the statistical errors in correlation-driven operational modal analysis to provide a better theoretical framework for this problem. The statistical errors stem from the estimation process of the correlation function matrix due to the finite set of data. To the best of this author's knowledge, the theory of the erratic behaviour in the tail region of the correlation function matrix, due to estimation process, has been left largely untouched in the literature on operational modal analysis.

4.2 Contribution

The author came up with the idea, made all mathematical derivations, performed the data analysis for the case studies, and wrote the paper.

4.3 Main findings

The statistical errors are found to cause the noise tail at the end of the correlation function matrix. The envelope of the modal auto-correlation function is Rice distributed; thus, it is biased and it is the reason

for the phenomenon of the noise tail. The errors cause bias on the zero crossings of the modal auto-correlation function but they cause random error of the zero crossings that increases linearly in the noise tail. The statistical errors affect the subspace of the correlation function matrix with insignificant errors, leading to the conclusion that statistical errors are primarily located within the subspace spanned by the mode shapes. Thus, in an identification process of modal parameters, the statistical errors have minor effects on the mode shapes while they cause random errors on the frequency estimates and this results in both random and biased error for the damping estimate.

4.4 Reflections

In this paper, we studied the statistical error in the estimation of the correlation function matrix to better understand the error. This provides a better understanding of the correlation-driven operational modal analysis and the identified modal parameters used to calibrate the system model (digital twin).

The statistical errors in the estimated correlation function matrix for operational modal analysis

Marius Tarpø^a, Tobias Friis^b, Christos Georgakis^a, Rune Brincker^b

^aAarhus University, Department of Engineering, Inge Lehmanns Gade 10, Aarhus, Denmark

^bTechnical University of Denmark, Department of Civil Engineering, Brovej B.118, Kgs. Lyngby, Denmark

Abstract

Given the random vibration of a linear and time-invariant system, the correlation function matrix is equivalent to free decays when the system is excited by Gaussian white noise. Correlation-driven Operational Modal Analysis utilises these properties to identify modal parameters from systems in operation based on the response only. Due to the finite length of the system response, the correlation function matrix must be estimated and this introduces statistical errors. This article focuses on the statistical errors due to this estimation process and the effect it has on the envelope and zero crossings of the estimated correlation function matrix. It is proven that the estimated correlation function matrix is a Gaussian stochastic process. Furthermore, it is proven that the envelope of the modal correlation function matrix is Rice distributed. This causes the tail region of the correlation function to become erroneous - called the noise tail. The zero crossings are unbiased, but the random error related to the crossings increases fast in the noise tail. The theory is tested on a simulated case and there is a high agreement between theory and simulation. A new expression for the minimal time length is introduced based on the bias error on the envelope.

Keywords: Uncertainty, operational modal analysis, envelope, zero crossings, Rice distribution

4.6 Introduction

In operational modal analysis or output-only modal analysis, we use the random response of a system in its ambient environment to identify the modal parameters [1, 2]. A common practice is the use of a correlation function matrix in a two-stage modal identification process - the correlation-driven operational modal analysis. Firstly, we calculate the correlation function matrix of the measured random system response. Secondly, we apply an identification technique to identify the modal parameters since we interpret the correlation function matrix as transposed free decays of the linear and time-invariant system, assuming white Gaussian noise as excitation [3, 4]. This is the idealised and exact statistical properties of the random system response, and it is based on a system response with an infinite time length. Exact properties of random data, however, are inaccessible from sampled data and they must be estimated instead. Thus, in operational modal analysis, we calculate an estimated correlation function matrix based on a measured system response with a finite time length. This introduces statistical errors into the estimated correlation function matrix [5, 6]. Hence, in practice, the statistical properties of the estimated correlation function are a stochastic process.

In the literature, the statistical errors in the correlation function matrix are system and time-dependent [5, 6]. Furthermore, it is well-known that the statistical errors result in an erroneous and erratic tail region of the correlation function matrix - the noise tail [6–8]. Whereas the beginning of the estimated correlation matrix is more persistent despite the statistical errors, generally, the length of the "persistent" properties is called the "*correlation time*" of the correlation function. The noise tail causes biased errors in the identification of the modal parameters [8] and it is common practice to disregard this region and utilise the correlation time of the correlation function matrix in an identification process. To the best of the authors' knowledge, however, the theory behind this erratic tail region is scarcely studied in the literature. Bendat and Piersol [5] show the introduction of statistical errors in the estimation of a correlation function. Orlowitz and Brandt [9] study the random errors in the estimated correlation function in operational modal analysis numerically. Giampellegrini [6] derives an analytic expression of the random error in the auto-correlation function of a single-of-degree (SDOF) system that illustrates the system and time dependency of the random error. Tarpø et al. [7] introduce an algorithm for the automatic detection of the correlation time or the noise tail. Furthermore, Tarpø et al. [10] introduce an algorithm for reduction of statistical errors by applying windows to the noise tail of each modal auto-correlation function.

They found that the estimated damping ratios were biased due to the statistical errors and a reduction of the statistical errors reduces the biased and random errors.

To account for the statistical errors, different studies exist on the optimal or required time length of measured system response [8, 11] since the time length relates to the statistical errors in the identification of modal parameters where an increase of time length decreases the statistical errors [5]. Damping estimates are often biased, but an increase in the time length results in a decrease in both random and biased errors in the damping estimates. Generally, different recommended time lengths exist for operational modal analysis [1, 2, 5, 12–14]. Most of these are based on calculation of the spectral density function [2, 5] while others are based on experience. [14] sets up a rule of thumb saying the time length should be 1,000 to 2,000 times the fundamental period.

Another approach is uncertainty quantifications that set up uncertainty bonds for the estimated modal parameters [15, 16]. For Bayesian operational modal analysis, the analytic expressions of the uncertainty for modal parameters are calculated for a frequency approach [12, 17].

This article will study the statistical errors in the estimated correlation function matrix used in correlation-driven operational modal analysis, and it adds novel information to the field. To illustrate the effect of statistical errors in this article, we will use two different recommended time lengths from Brincker and Ventura [1] & ANSI 2.47 [13]. This article will show that the length of the correlation function matrix - the correlation time - is an equally important parameter as the time length. To access the statistical errors of the estimated correlation function matrix, we will base this article on the following assumptions:

- The system is linear and time-invariant
- The excitation is stationary white Gaussian noise
- The system is lightly damped with orthogonal modes
- The time length of the measured system response is long compared to the time lags of the estimated correlation function matrix

In this article, the term "*statistical errors*" includes all random and biased errors, which affect the estimated correlation function matrix due to the estimation process. Thus, we exclude the effect of measurement noise on the correlation function matrix in this study, see [18] for more on this subject. We assess the random errors by the variance and any biased errors by the difference between the analytic and the expected value [5]. The term "*statistical errors*", however, exclude all errors in the identified modal parameter caused by any identification techniques. Likewise, we disregard eventual errors caused by violations of the core assumptions of operational modal analysis - linear and time-invariant system excited by white Gaussian noise.

We organise the remainder of this article in the following manner. In Section 4.7, we derive an expression for the random errors in the estimated correlation function matrix. Section 4.8 proves that the modal auto-correlation function has a biased envelope by applying the theory of peak probability density functions. Section 4.10 presents a new expression of the required time length based on the statistical errors in the correlation function matrix. Finally, in Section 4.11, we validate the analytic expressions of errors in the correlation function matrix from the previous sections by a simulation study.

4.7 Statistical errors in the correlation function matrix

In this section, we will go through the general statistical errors in the correlation function matrix. We will show that we can express the statistical errors as system dependent errors in each modal auto-correlation function.

4.7.1 Correlation function matrix

In operational modal analysis, we consider random vibrations from linear systems that are excited by white Gaussian noise. We measure the spatial limited system response, $\mathbf{y}(t)$, at a finite number degrees-of-freedom. In the correlation-driven operational modal analysis, the correlation function matrix, $\mathbf{R}(\tau)$, for the system response is equivalent to free decays corresponding to the modal parameters of the system [3, 4].

$$\mathbf{R}(\tau) \triangleq \mathbb{E} [\mathbf{y}(t)\mathbf{y}^\top(t + \tau)] \quad (4.1)$$

where $(\cdot)^\top$ denotes the transpose and τ is the time lag.

We can use the modal decomposition to transform the system response into the modal domain.

$$\begin{aligned}\mathbf{y}(t) &= \sum_{i=1}^N \boldsymbol{\Phi}_i q_i(t) \\ &= \boldsymbol{\Phi} \mathbf{q}(t)\end{aligned}\quad (4.2)$$

where $\boldsymbol{\Phi}_i$ is the mode shape for the i^{th} mode, $q_i(t)$ is the modal coordinates for the i^{th} mode, N is the total number of modes in the system, $\boldsymbol{\Phi}$ is the modal matrix containing mode shapes as columns, and $\mathbf{q}(t)$ is the modal coordinate vector with the modal coordinates in the rows.

We use the modal decomposition to decorrelate the correlation function matrix into the modal correlation function matrix by inserting Eq. (4.2) in Eq. (4.1) [1].

$$\mathbf{R}(\tau) = \boldsymbol{\Phi} \mathbf{R}_q(\tau) \boldsymbol{\Phi}^\top \quad (4.3)$$

where $\mathbf{R}_q(\tau)$ is the modal correlation function matrix. Each modal auto-correlation function corresponds to a single-degree-of-freedom (SDOF) system and a free decay of the given mode [19]. When white Gaussian noise excites a linear and time-invariant system with lightly damped and orthogonal modes, the modal coordinates are independent and the modal correlation function matrix is diagonal [1, 19]. Thus, we rewrite the equation of the correlation function matrix as a summation of the modal auto-correlation function.

$$\mathbf{R}(\tau) \approx \sum_{i=1}^N \boldsymbol{\Phi}_i \boldsymbol{\Phi}_i^\top R_{q_i}(\tau) \quad (4.4)$$

where $R_{q_i}(\tau)$ is the modal auto-correlation function for the i^{th} mode.

Clough and Penzien [19] made an expression for the correlation function for an SDOF system excited by white Gaussian noise that we will use to describe the modal auto-correlation functions analytically.

$$R_{q_i}(\tau) = \frac{\pi \omega_0 S_0}{2k^2 \zeta} e^{-\omega_0 \zeta |\tau|} \left(\cos(\omega_d \tau) + \frac{\zeta}{\sqrt{1 - \zeta^2}} \sin(\omega_d |\tau|) \right) \quad (4.5)$$

where ω_0 is natural cyclic frequency, ω_d is natural damped cyclic frequency, ζ is the damping ratio, S_0 is the loading-constant from the white Gaussian noise in the frequency domain, and k is the modal stiffness of the i^{th} mode. We omit the index for the given mode on all modal parameters to improve readability of the equations. Based on this equation, we have an expression for the variance of the modal coordinates.

$$\sigma_{q_i}^2 = \frac{\pi \omega_0 S_0}{2k^2 \zeta} \quad (4.6)$$

The Hilbert transformation is often used to find the (Hilbert) envelope by the absolute value of the analytic signal [20].

$$\text{env}(X(t)) = \sqrt{X(t)^2 + \mathcal{H}[X(t)]^2} \quad (4.7)$$

where $X(t)$ is an arbitrary function and \mathcal{H} denotes the Hilbert transformation.

We calculate the envelope of the modal auto-correlation function, Eq. (4.5), using the Hilbert transformation.

$$e_{q_i}(\tau) = \text{env}(R_{q_i}(\tau)) = \sigma_{q_i}^2 e^{-\omega_0 \zeta |\tau|} \sqrt{1 + \frac{\zeta^2}{1 - \zeta^2}} \quad (4.8)$$

For simplicity, we will assume that the system has low damping.

$$e_{q_i}(\tau) = \sigma_{q_i}^2 e^{-\omega_0 \zeta |\tau|} \quad (4.9)$$

4.7.2 Estimated correlation function matrix

Since the system response is ergodic, we use *time averaging* instead of *ensemble averaging*. The length of the signal, however, must tend towards infinite if the *time averaging* should equal the expected value [5].

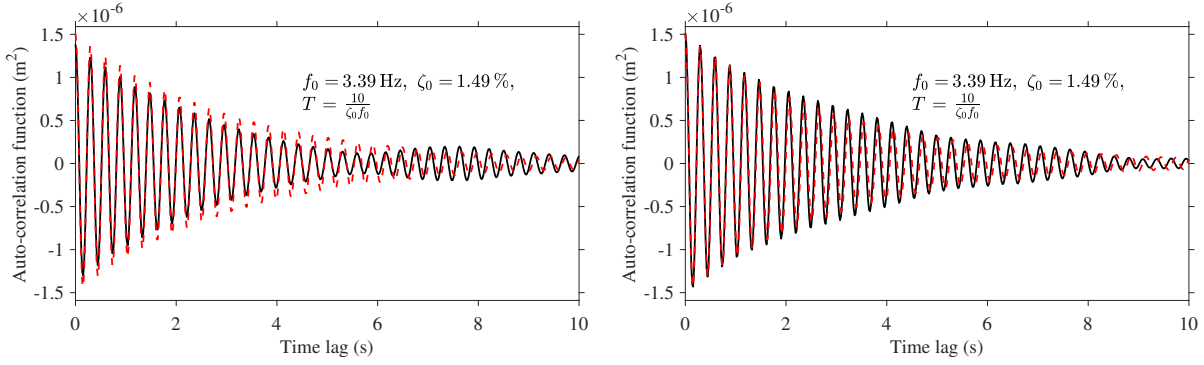


Figure 4.1: Correlogram with two realisations of the same estimated correlation function (*black solid line*) and the corresponding theoretical correlation function, Eq. (4.5), (*red dashed line*)

$$\mathbf{R}(\tau) = \lim_{T \rightarrow \infty} \frac{1}{T} \int_0^T \mathbf{y}(t) \mathbf{y}^\top(t + \tau) dt \quad (4.10)$$

where T is the time length of the measured system response. The measured system response has a finite time length, meaning, we have to estimate the correlation function matrix and this introduces statistical errors. This is illustrated in Fig. 4.1 where two estimated correlation functions are plotted next to the theoretical correlation function. Therefore, the estimated correlation function matrix is a stochastic process.

Different estimators exist for the correlation function [5]. The unbiased estimator has a higher variance as we increase the time lag, τ , whereas the biased error of the biased estimator increases with increasing time lags. The biased estimator has a biased envelope and this biased error transfers into the identified damping ratios. In operational modal analysis, however, the time length is often longer than the maximum time lag, $T \gg \tau$, thus the difference between the estimators is small. Since we use the correlation function matrix to identify modal parameters, then an unbiased estimator is preferable.

$$\tilde{\mathbf{R}}(\tau) = \frac{1}{T - \tau} \int_0^{T - \tau} \mathbf{y}(t) \mathbf{y}^\top(t + \tau) dt, \quad 0 \leq \tau < T \quad (4.11)$$

By increasing the time length of the recording, the variance of the estimated correlation function matrix decreases.

$$\lim_{T \rightarrow \infty} \tilde{\mathbf{R}}(\tau) \rightarrow \mathbf{R}(\tau) \quad (4.12)$$

4.7.3 Probability density function of the estimated correlation function matrix

Next, we will find the probability density function of the estimated correlation function matrix. We consider a linear and stationary multi-degree-of-freedom system excited by white Gaussian noise. In linear structural dynamics, we apply the modal decorrelation/modal superposition, Eq. (4.2), to decorrelate this system into multiple SDOF systems describing each mode [19]. The response of each SDOF system is a convolution of the excitation and the impulse response function of the given mode [19]. The (convolution) integral is defined as the limit of a summation and - according to the Central Limit Theorem - the summation of many random variables tends toward a normal distribution [1, 5]. Thus, the modal coordinates are normal distributed, $q_i(t) \sim \mathcal{N}(0, \sigma_{q_i}^2)$, if the time length, T , is large, $T \gg 0$, see Appendix 4.A. The modal decomposition is a linear transformation of normal random vectors [21] so the system response is a multivariate Gaussian variable, $\mathbf{y}(t) \sim \mathcal{N}(\mathbf{0}, \mathbf{\Phi}[\sigma_{q_i}^2] \mathbf{\Phi}^\top)$ where $\mathbf{0}$ is a zero vector [1, 5].

The estimated modal auto-correlation functions are approximately Gaussian distributed, $\tilde{R}_{q_i}(\tau) \sim \mathcal{N}(R_{q_i}(\tau), \text{Var}[\tilde{R}_{q_i}(\tau)])$, see Appendix 4.A. Therefore, the estimated correlation function matrix follows a multivariate Gaussian distribution, $\tilde{\mathbf{R}}(\tau) \sim \mathcal{N}(\mathbf{R}(\tau), \text{Cov}[\tilde{\mathbf{R}}(\tau)])$, see Appendix 4.B. Thus, the expected value of the estimated correlation function matrix is given by

$$\begin{aligned}\mathbb{E} \left[\widetilde{\mathbf{R}}(\tau) \right] &= \mathbf{R}(\tau) \\ &\approx \sum_{i=1}^N \boldsymbol{\Phi}_i \boldsymbol{\Phi}_i^\top R_{q_i}(\tau)\end{aligned}\quad (4.13)$$

Let us turn to the variance - or statistical error - of each entry of the correlation function matrix using Eq. (4.4).

$$\text{Var} \left[\widetilde{\mathbf{R}}_{j,k}(\tau) \right] \approx \text{Var} \left[\sum_{i=1}^N \boldsymbol{\Phi}_{j,i} \boldsymbol{\Phi}_{k,i} \widetilde{R}_{q_i}(\tau) \right] \quad (4.14)$$

We can express the variance as a summation of the covariances of all products in the summation.

$$\text{Var} \left[\widetilde{\mathbf{R}}_{j,k}(\tau) \right] = \sum_{i=1}^N \left(\boldsymbol{\Phi}_{j,i} \boldsymbol{\Phi}_{k,i} \right)^2 \text{Var} \left[\widetilde{R}_{q_i}(\tau) \right] + \sum_{i=1}^N \sum_{\substack{m=1 \\ m \neq i}}^N \boldsymbol{\Phi}_{j,i} \boldsymbol{\Phi}_{k,i} \boldsymbol{\Phi}_{j,m} \boldsymbol{\Phi}_{k,m} \text{Cov} \left[\widetilde{R}_{q_i}(\tau), \widetilde{R}_{q_m}(\tau) \right] \quad (4.15)$$

When we are dealing with orthogonal modes, the covariance between modal auto-correlation functions is much smaller than the variance of each modal auto-correlation function. This enables us to approximate the statistical errors in the entire matrix as a summation of the variance of each modal auto-correlation function (a similar expression is derived in [6]).

$$\text{Var} \left[\widetilde{\mathbf{R}}_{j,k}(\tau) \right] \approx \sum_{i=1}^N \left(\boldsymbol{\Phi}_{j,i} \boldsymbol{\Phi}_{k,i} \right)^2 \text{Var} \left[\widetilde{R}_{q_i}(\tau) \right] \quad (4.16)$$

Each product of mode shapes, $(\boldsymbol{\Phi}_{j,i} \boldsymbol{\Phi}_{k,i})^2$, is a linear transformation from the variance of the modal auto-correlation function to the contribution of the i^{th} modes' contribution of variance of the estimated correlation function matrix. Thus, the mode shapes distribute the statistical errors from the modal auto-correlation functions to the entire correlation function matrix. The statistical errors exist within the vector space spanned by the mode shapes of the system and this vector space of the estimated correlation function matrix is independent of the statistical errors, at least for systems with low damping and orthogonal modes. Thus, in correlation-driven operational modal analysis, an identification of the mode shapes is almost independent of the statistical errors.

To express the statistical errors in the estimated correlation function matrix, we have to derive an expression for the variance of the estimated modal auto-correlation functions. Bendat and Piersol [5] derived an expression for the variance of the cross-correlation function by assuming Gaussian distributed data as input in the correlation function matrix - here written for the unbiased auto-correlation function for the modal coordinates.

$$\text{Var} \left[\widetilde{R}_{q_i}(\tau) \right] = \frac{1}{T-\tau} \int_{-T+\tau}^{T-\tau} \left(1 - \frac{|r|}{T-\tau} \right) \left(R_{q_i}(r)^2 + R_{q_i}(r+\tau)R_{q_i}(r-\tau) \right) dr \quad (4.17)$$

Bendat and Piersol [5] further simplified the variance of the estimated correlation function by assuming a large record length, $T \gg 0$.

$$\text{Var} \left[\widetilde{R}_{q_i}(\tau) \right] \approx \frac{1}{T-\tau} \int_{-\infty}^{\infty} \left(R_{q_i}^2(r) + R_{q_i}(r+\tau)R_{q_i}(r-\tau) \right) dr \quad (4.18)$$

Giampellegrini [6] calculated the variance of the estimated correlation functions using this integral, Eq. (4.18), by assuming small damping.

$$\text{Var} \left[\widetilde{R}_{q_i}(\tau) \right] \approx \frac{\sigma_{q_i}^4}{2(T-\tau)\omega_0\zeta} \left(1 + e^{-2\omega_0\zeta\tau} \left(\cos(2\omega_d\tau)(1 + 2\zeta\omega_0\tau) - \sin(2\omega_d\tau) \frac{4\omega_0\zeta^2\tau}{\sqrt{1-\zeta^2}} \right) \right) \quad (4.19)$$

Thus, the statistical errors are non-stationary while they are system and time-dependent. By increasing the time length, T , the statistical errors decrease. Figs. 4.2 and 4.3 illustrate this time dependence. The statistical errors tend to become approximately stationary as the time lags increase, see Fig. 4.3.

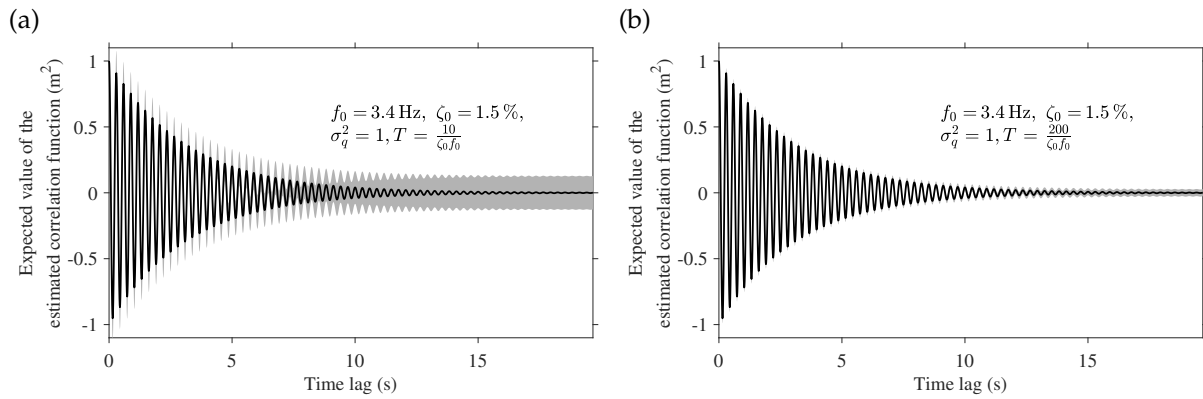


Figure 4.2: Correlogram with probability density function of the estimated correlation function for an arbitrary system plotted for two different time lengths, (a) Brincker and Ventura [1], (b) ANSI [13], the expected value (black solid line) and the interquartile range (grey)

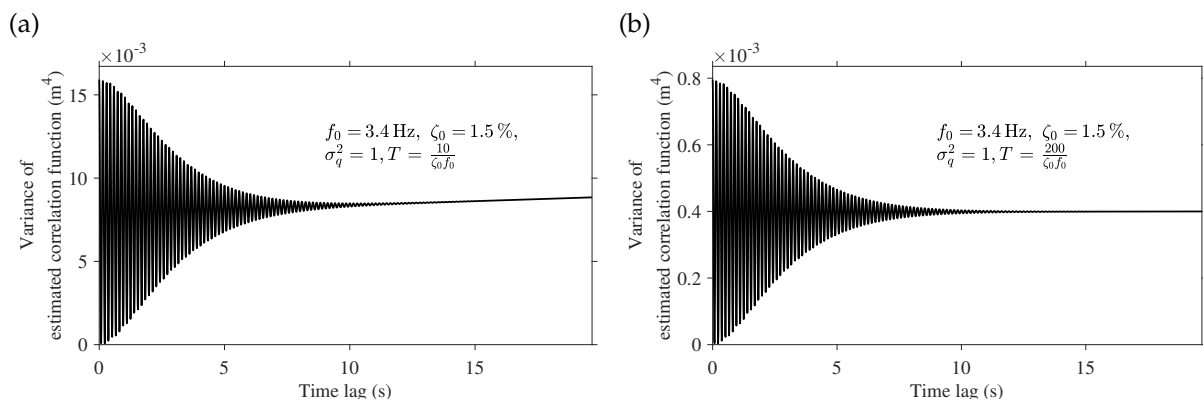


Figure 4.3: Variance of the estimated correlation function, Eq. (4.19), for an arbitrary system plotted for two different time lengths, (a) Brincker and Ventura [1], (b) ANSI [13]

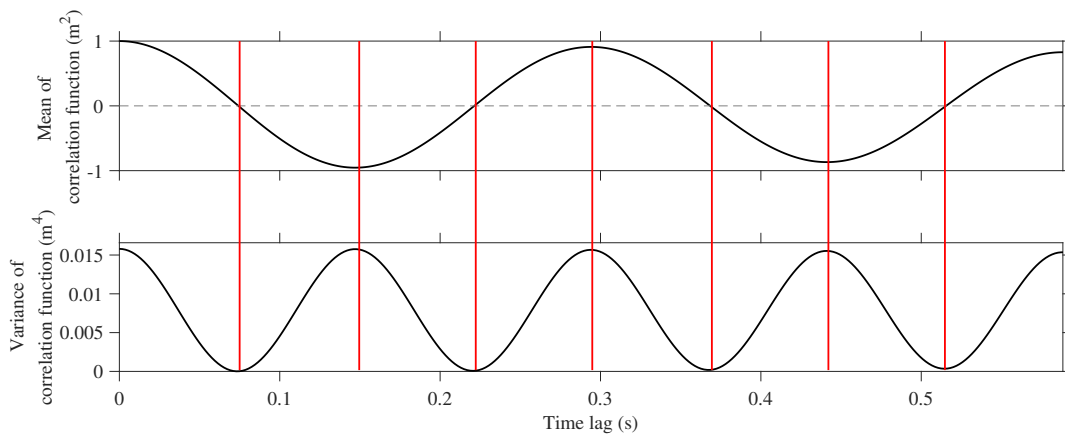


Figure 4.4: The relationship between the analytic correlation function, Eq. (4.5), (top) and the variance of the estimated correlation function, Eq. (4.19), (bottom)

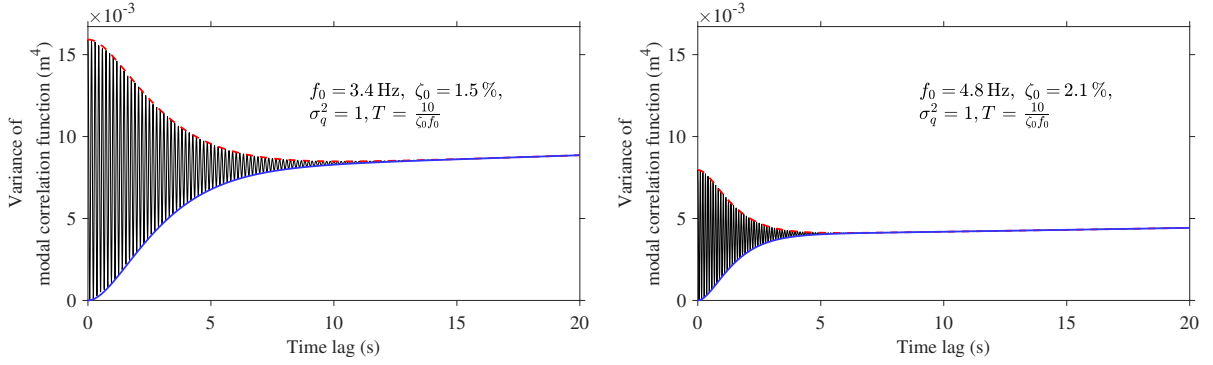


Figure 4.5: The variance of the estimated correlation function for two arbitrary systems with the upper and lower envelopes, the variance, Eq. (4.19), (black solid line), upper envelope, Eq. (4.20), (red dashed line), and lower envelope, Eq. (4.20), (blue solid line)

The minima of the variance of the correlation function give the variance at zero crossings or axis crossings and the maxima give the variance at the peaks [6], see Fig. 4.4. We want to find the envelopes of the variance, Eq. (4.18), since this converts the variance to either the zero crossings or the peaks of the modal auto-correlation function, similarly to an interpolation. By assuming small damping and removing all terms with ζ to the power of minimum 2, the variance at the peaks and zero crossings of the estimated correlation function is given by

$$\text{Var} \left[\widetilde{R}_{q_i}(\tau) \right]^{\pm} \approx \sigma_{q_i}^4 \frac{1 \pm e^{-2\omega_0\zeta\tau} (2\omega_0\zeta\tau + 1)}{2(T - \tau)\omega_0\zeta} \quad (4.20)$$

where \pm denotes the upper (+) or lower (-) envelope of the variance from Eq. (4.18).

Fig. 4.5 illustrates the variance and its envelopes for two SDOF systems. For the second SDOF system, we double the frequency-damping product, $f_0\zeta$, of the first system. Generally, the variance drops for the second system and it decays faster. Hence, for multi-degree-of-freedom systems, the mode with the lowest frequency-damping product has the highest level of statistical errors.

On their own, these expressions of variance do not explain the erratic behaviour in the tail region of the estimated correlation function, as seen in Fig. 4.7. We have to apply the theory of Peak Probability Density Functions and Level Crossing to obtain an expression of the density function of the envelope, see section 4.8, and the zero crossings, see section 4.9.

4.7.4 Error of the estimated modal auto-correlation functions

In this section, we will study the random error of the modal auto-correlation function, Eq. (4.20). Two special cases of this equation are worth mentioning. First, for variance at time lag zero, $\tau = 0$, the random error becomes

$$\text{Var} \left[\widetilde{R}_{q_i}(0) \right]^+ \approx \sigma_{q_i}^4 \frac{1}{T\omega_0\zeta} \quad , \quad \text{Var} \left[\widetilde{R}_{q_i}(0) \right]^- \approx 0 \quad (4.21)$$

While for large time lags, $\tau \gg 0$, and time length much larger than the time lag, $T \gg \tau$, the random error is

$$\text{Var} \left[\widetilde{R}_{q_i}(\tau) \right]^{\pm} \approx \sigma_{q_i}^4 \frac{1}{2(T - \tau)\omega_0\zeta}, \quad \tau \gg 0, \quad T \gg \tau \quad (4.22)$$

For both cases, we decrease the random error by increasing the frequency-damping product or the time length, see Fig. 4.5.

In the literature, the normalised random error, $\frac{\sigma}{\mu}$, is often used. This is inversely proportional to the signal-to-noise ratio, $\frac{\mu}{\sigma}$.

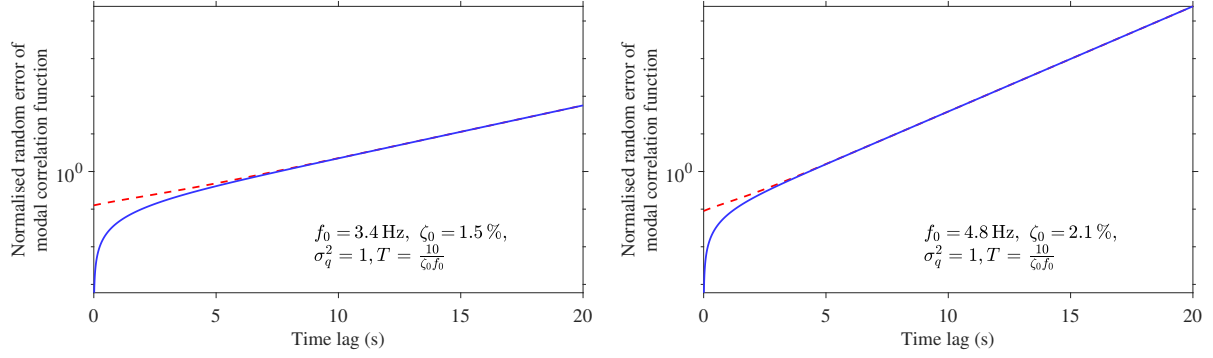


Figure 4.6: The normalised random error of the estimated correlation function, Eq. (4.23), for two arbitrary systems, normalised random error for the upper envelope, $\epsilon(\tau)^+$, (red dashed line) and normalised random error for the lower envelope, $\epsilon(\tau)^-$, (blue solid line)

$$\begin{aligned} \epsilon(\tau)^\pm &= \frac{\sqrt{\text{Var} [\widetilde{R}_{q_i}(\tau)]^\pm}}{e_{q_i}(\tau)} \\ &= \sqrt{\frac{1}{T-\tau} \frac{e^{2\omega_0\zeta\tau} \pm (2\omega_0\zeta\tau + 1)}{2\omega_0\zeta}} \end{aligned} \quad (4.23)$$

This is identical to the results in [6], who looked at the normalised random error by converting the envelope of the variance function for the biased auto-correlation function, $\tau = n \frac{\pi}{\omega_d}$, where n is the discrete number of each peak of the modal auto-correlation function.

Let us have a look at Eq. (4.23). Let us say that we increase the frequency-damping product, then we increase the slope of the normalised random error. Thus, the normalised random error of modes with high frequency-damping products increases rapidly compared to modes with low frequency-damping products, see Fig. 4.6. This is, however, due to the normalisation process. The random errors are inversely proportional to the frequency-damping product and the time length, see Eqs. (4.20), (4.21), and (4.22). Thus, modes with low frequency-damping products have higher random errors than modes with higher frequency-damping products, as seen in Fig. 4.5.

This concludes this section. So far we have shown that the finite time length of measurement introduces statistical errors to the correlation function matrix. It was shown that the non-stationary statistical errors are system and time-dependent, and they are introduced in each modal auto-correlation function (for lightly damped and orthogonal modes). The auto-correlation function for the statistical errors and expression for the variance (statistical errors) are presented in the next section.

4.8 Statistical errors in the envelope of the modal auto-correlation function

In this section, we will go into more detail regarding the statistical errors in the envelope and the correlation time. Let us focus on the errors regarding the envelope of each modal auto-correlation function by applying the theory of Peak Probability Density Functions [5, 22].

4.8.1 Noise tail

The noise tail is a non-persistent feature in the estimated correlation function matrix where we have erratic behaviour in the tail region, see Fig. 4.7. This happens when the statistical errors dominate the correlation function and introduce a biased error in the envelope of the estimated correlation function. As seen in Fig. 4.7, the noise tail looks different for each realisation of the same system. We must neglect the notion that the estimated correlation function is a free decay in this tail region. This section will prove this phenomenon analytically by studying the (Hilbert) envelope of the estimated modal auto-correlation function and compare it with the theoretical envelope, Eq. (4.9).

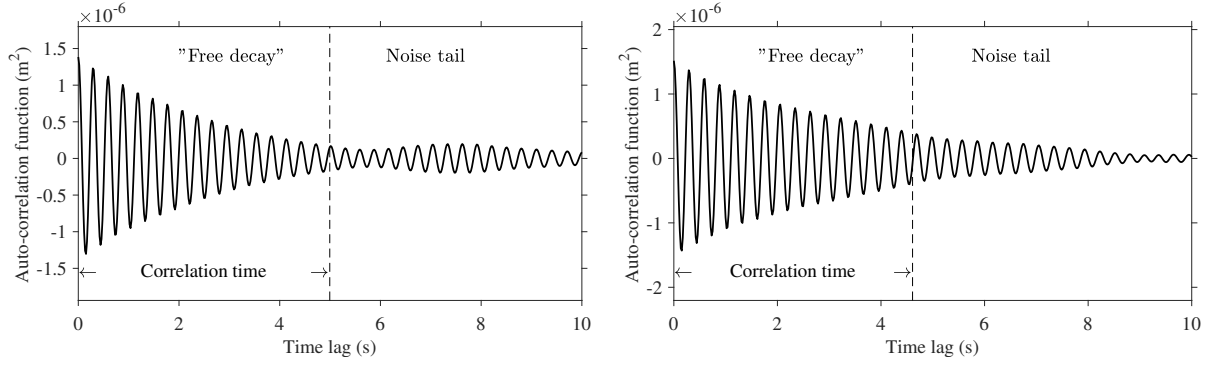


Figure 4.7: Correlogram with two example of the noise tail in a correlation function based on two realisations of the same estimated correlation function

$$\text{env}(\widetilde{R}_{q_i}(\tau)) = \sqrt{\widetilde{R}_{q_i}(\tau)^2 + \mathcal{H}[\widetilde{R}_{q_i}(\tau)]^2} \quad (4.24)$$

4.8.2 Probability density function of the Hilbert envelope

In this section, we will derive the general probability density function for the Hilbert envelope of a normal distributed random variable, $X \sim \mathcal{N}(\mu, \sigma^2)$. The Hilbert envelope of X is given by: $\text{env}(X) = \sqrt{X^2 + \mathcal{H}[X]^2}$. We look at the probability density of the Hilbert transformed variable, $\mathcal{H}[X]$. By a linear combination of the standard normal distribution, $M \sim \mathcal{N}(0, 1)$, we write the normal distributed random variable as: $X = \sigma M + \mu$. Then we apply the Hilbert transformation to this linear combination and use the fact that the Hilbert transformation of a constant is zero.

$$\begin{aligned} \mathcal{H}[X] &= \mathcal{H}[\sigma M + \mu] \\ &= \sigma \mathcal{H}[M] \end{aligned} \quad (4.25)$$

Thus, the Hilbert transformation creates a modified normal distribution with an expected value of zero and the same variance, $\mathcal{H}[X] \sim \mathcal{N}(0, \sigma^2)$. So we have two normal variables with the same variance but different expected values. Hence, the Hilbert envelope has a Rice distribution [22], which is a special case of the non-central chi-square distribution with two degrees of freedom and non-centrality parameter $(\frac{\mu}{\sigma})^2$. A variable, $R \sim \text{Rice}(|\mu_1^2 + \mu_2^2|, \sigma)$, is Rice distributed when it is comprised of two normal variables, $Z \sim \mathcal{N}(\mu_1, \sigma^2)$ and $Y \sim \mathcal{N}(\mu_2, \sigma^2)$, in the following way, $R = \sqrt{Z^2 + Y^2}$ [23]. Thus, the general Hilbert envelope of a normal distributed random variable, $X \sim \mathcal{N}(\mu, \sigma^2)$, is Rice distributed, $\text{env}(X) \sim \text{Rice}(\mu, \sigma)$.

The probability density function of the Rice distributed variable is given by

$$f_e(x, \mu, \sigma) \triangleq \frac{x}{\sigma^2} \exp\left(-\frac{x^2 + \mu^2}{2\sigma^2}\right) I_0\left(\frac{\mu x}{\sigma^2}\right) \quad (4.26)$$

where $I_0(\cdot)$ is the modified Bessel function of the first kind with order zero [24].

Then we find the expected value of the Hilbert envelope as a function of the original expected value, μ , and variance, σ^2 , of the normal distributed variable X .

$$\mu_m(\mu, \sigma) = \sqrt{\frac{\pi}{2}} \sigma L_{1/2}\left(-\frac{\mu^2}{2\sigma^2}\right) \quad (4.27)$$

where $L_{1/2}(\cdot)$ is a Laguerre polynomial for case $q = \frac{1}{2}$ [22, 24]. Likewise, we find the variance of the Hilbert envelope.

$$\begin{aligned} \sigma_m^2(\mu, \sigma) &= 2\sigma^2 + \mu^2 - \frac{\pi\sigma^2}{2} L_{1/2}\left(-\frac{\mu^2}{2\sigma^2}\right)^2 \\ &= 2\sigma^2 + \mu^2 - \mu_m(\mu, \sigma)^2 \end{aligned} \quad (4.28)$$

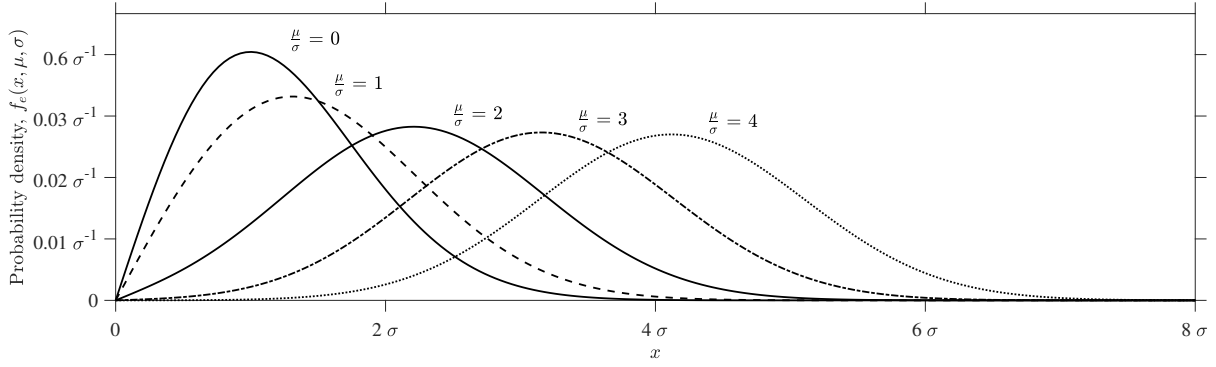


Figure 4.8: The probability density function of the Rice distribution, Eq. (4.26), for different values of μ while σ is constant

The Rice distribution changes shape depending on the signal-to-noise ratio, $\frac{\mu}{\sigma}$, see Fig. 4.8. When this ratio tends towards infinite, the envelope becomes normal distributed, and the envelope gets a Rayleigh distribution when the ratio tends towards zero [22, 23]. In practice, the distribution is approximately normal distributed when the ratio is above 3 [25].

4.8.3 Probability density function of the envelope for the estimated correlation function

We insert the expected value and variance of the underlying normal distribution into the general Rice distribution for the envelope, Eq. (4.26). Here we use the analytic envelope of the modal auto-correlation function, Eq. (4.9), and the upper envelope of the variance, Eq. (4.20).

$$f_i(x, \tau) = f_e \left(x, e_i(\tau), \text{Var} [\widetilde{R}_{q_i}(\tau)]^+ \right) \quad (4.29)$$

The shape of the Rice distribution depends on the signal-to-noise ratio or the relationship between the analytic envelope, $e_i(\tau)$, and the statistical errors at the peaks, $\text{Var}[\widetilde{R}_{q_i}(\tau)]^+$.

We find the expected value of the Hilbert envelope using Eq. 4.27.

$$\mu_{m_i}(\tau) = \sqrt{\frac{\pi}{2}} \sigma_{q_i}^2 \sqrt{\frac{1 + e^{-2\omega_0 \zeta \tau} (2\omega_0 \zeta \tau + 1)}{2(T - \tau)\omega_0 \zeta}} L_{1/2} \left(\frac{(\tau - T)\omega_0 \zeta}{e^{2\omega_0 \zeta \tau} + 2\omega_0 \zeta \tau + 1} \right) \quad (4.30)$$

Likewise, we find the variance of the Hilbert envelope using Eq. 4.28.

$$\sigma_m^2(\tau) = \sigma_{q_i}^4 \frac{1 + e^{-2\omega_0 \zeta \tau} (2\omega_0 \zeta \tau + 1)}{2(T - \tau)\omega_0 \zeta} \left(2 - 2 \frac{(\tau - T)\omega_0 \zeta}{e^{2\omega_0 \zeta \tau} + 2\omega_0 \zeta \tau + 1} - \frac{\pi}{2} L_{1/2} \left(\frac{(\tau - T)\omega_0 \zeta}{e^{2\omega_0 \zeta \tau} + 2\omega_0 \zeta \tau + 1} \right)^2 \right) \quad (4.31)$$

Fig. 4.9 shows the expected value and the interquartile range of the envelope for the modal auto-correlation function. In the beginning, the expected value follows the analytic envelope but it diverts as the signal-to-noise ratio decreases in the tail region, see Eq. (4.30). Hence, the expected envelope is biased in this region of the modal auto-correlation function since it tends toward a constant value due to the statistical errors. This explains the erratic noise tail in the estimated correlation function matrix.

The variance of the envelope is displayed in Fig. 4.10 for two different time lengths, and the shape and amplitude of the variance depend on the time length and frequency-damping product, see Eq. (4.31). The excitation level is related to the amplitude of the variance.

4.8.4 First part of the envelope - free decay

We want to look at the first part of the modal auto-correlation function that has low levels of statistical errors. In this region, the analytic envelope is much bigger than the variance, $e_i(\tau) \gg \text{Var}[\widetilde{R}_{q_i}(\tau)]$, and the length of this region is the correlation time. Then we have a limit of the Rice distribution where it is an approximated normal distribution with the expected value of $\sqrt{\mu^2 + \sigma^2}$ and variance of σ^2 [25]. The expected value of the envelope of a modal auto-correlation function is

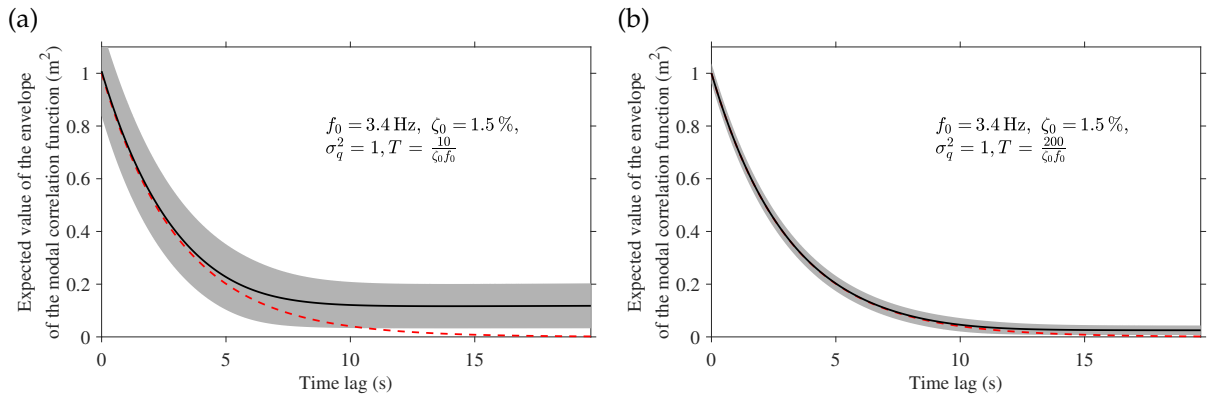


Figure 4.9: Expected value and variance of the envelope of the estimated correlation function for an arbitrary system plotted for two different time lengths, (a) Brincker and Ventura [1], (b) ANSI [13], the expected value, Eq. (4.30), (black solid line), the interquartile range (grey fill), and the analytic envelope, Eq. (4.9), (red dashed line)

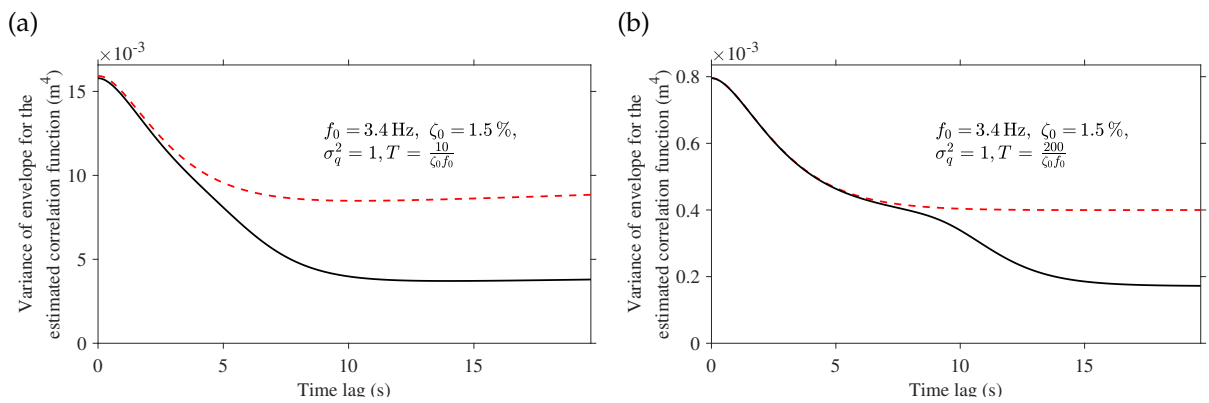


Figure 4.10: Variance of the envelope of the estimated correlation function for an arbitrary system plotted for two different time lengths, (a) Brincker and Ventura [1], (b) ANSI [13], the variance of the envelope, Eq. (4.31), (black solid line) and the general variance of modal auto-correlation function, Eq. (4.20), (red dashed line)

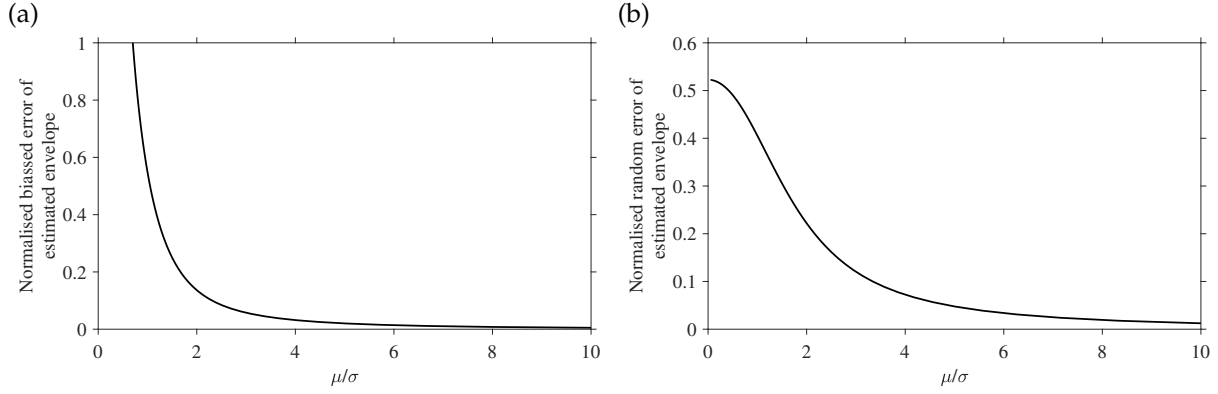


Figure 4.11: (a) The normalised biased error as a function of $\frac{\mu}{\sigma}$, (b) the normalised random error as a function of $\frac{\mu}{\sigma}$

$$\mathbb{E} [\tilde{e}_i(\tau)] = \sqrt{e_i(\tau)^2 + \text{Var} [\widetilde{R}_{q_i}(\tau)]^+}, \quad e_i(\tau) \gg \text{Var} [\widetilde{R}_{q_i}(\tau)] \quad (4.32)$$

The variance of this region of the envelope yields

$$\text{Var} [\tilde{e}_i(\tau)] = \text{Var} [\widetilde{R}_{q_i}(\tau)]^+, \quad e_i(\tau) \gg \text{Var} [\widetilde{R}_{q_i}(\tau)] \quad (4.33)$$

4.8.5 Last part of envelope - noise tail

We will look at the part of the correlation function where the noise tail appears. As the analytic envelope tends towards zero, $e_i(\tau) \approx 0$, the density function of the Hilbert envelope changes to another special case of the Rice distribution; the Rayleigh distribution [22, 23]. Then we calculate the expected value of the envelope in the noise tail region of the correlation function.

$$\mathbb{E} [\tilde{e}_i(\tau)] = \sqrt{\frac{\pi}{2}} \sqrt{\text{Var} [\widetilde{R}_{q_i}(\tau)]^+}, \quad e_i(\tau) \approx 0 \quad (4.34)$$

We calculate the variance of the envelope in this region of the modal auto-correlation function.

$$\text{Var} [\tilde{e}_i(\tau)] = \left(2 - \frac{\pi}{2}\right) \text{Var} [\widetilde{R}_{q_i}(\tau)]^+, \quad e_i(\tau) \approx 0 \quad (4.35)$$

The envelope depends only on the statistical errors in the noise tail. Therefore, the estimated modal auto-correlation function is no longer a free decay since it is independent of the analytic envelope of the modal auto-correlation function in this region. The noise tail violates the core assumption in the correlation-driven operational modal analysis: that the correlation function matrix consists of free decays. Therefore, it is crucial that we exclude the noise tail from an identification process.

4.8.6 Errors of the estimated envelope

Let us look at the biased and random errors to understand the statistical errors and their effect on the envelope. We start with the normalised biased error as a function of the signal-to-noise ratio, see Fig. 4.11 A).

$$\begin{aligned} \varepsilon_m \left(\frac{\mu}{\sigma} \right) &= \frac{\mu_m}{\mu} - 1 \\ &= \sqrt{\frac{\pi}{2}} \frac{\sigma}{\mu} L_{1/2} \left(-\frac{\mu^2}{2\sigma^2} \right) - 1 \end{aligned} \quad (4.36)$$

We insert the equation for the envelope, Eq. (4.9) and the equation for the variance related to the peaks of the correlation function, Eq. (4.20), into Eq. (4.36).

$$\varepsilon_m(\tau) = \sqrt{\frac{\pi}{4}} \sqrt{\frac{e^{2\omega_0\zeta\tau} + 2\omega_0\zeta\tau + 1}{(T - \tau)\omega_0\zeta}} L_{1/2} \left(\frac{(\tau - T)\omega_0\zeta}{e^{2\omega_0\zeta\tau} + 2\omega_0\zeta\tau + 1} \right) - 1 \quad (4.37)$$

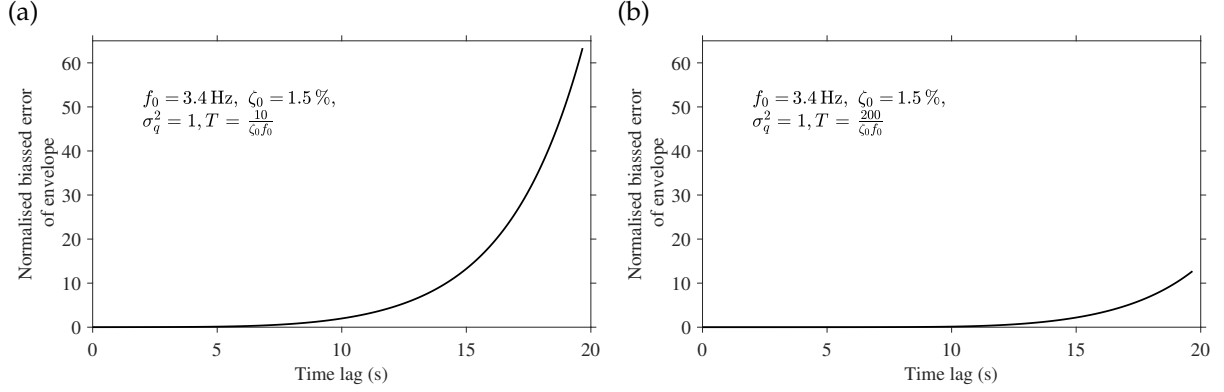


Figure 4.12: The normalised biased error of the envelope, Eq. (4.37), for two different time lengths, (a) Brincker and Ventura [1], (b) ANSI [13]

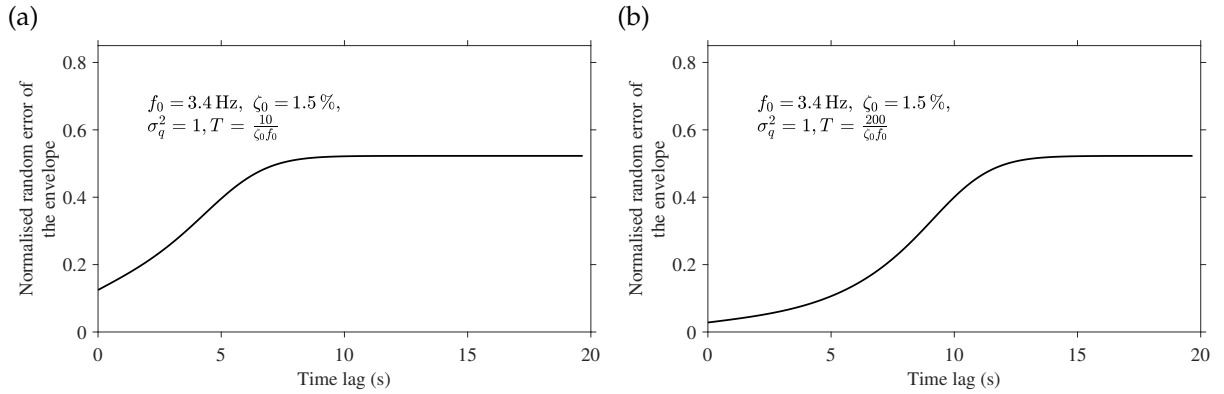


Figure 4.13: The normalised random error of the envelope, Eq. (4.38), for two different time lengths, (a) Brincker and Ventura [1], (b) ANSI [13]

Fig. 4.12 shows the normalised biased error of the envelope of an estimated modal auto-correlation function for two different time lengths.

We turn to the normalised random error, sometimes called the coefficient of variation, see Fig. 4.11 B).

$$\begin{aligned} \epsilon_m \left(\frac{\mu}{\sigma} \right) &= \frac{\sigma_m}{\mu_m} \\ &= \frac{\sqrt{2 + \frac{\mu^2}{\sigma^2} - \frac{\pi}{2} L_{1/2} \left(-\frac{\mu^2}{2\sigma^2} \right)^2}}{\sqrt{\frac{\pi}{2} L_{1/2} \left(-\frac{\mu^2}{2\sigma^2} \right)}} \end{aligned} \quad (4.38)$$

The normalised random error is illustrated in Fig. 4.13. In the physical part of the envelope (high value of signal-to-noise ratio) the normalised random error of the envelope is approximately equal to the normalised random error of the estimated correlation function, Eq. (4.23). In the noise tail region, we calculate the normalised random error by tending $\frac{\mu}{\sigma}$ toward zero.

$$\lim_{\frac{\mu}{\sigma} \rightarrow 0} \epsilon_m \left(\frac{\mu}{\sigma} \right) = \sqrt{\frac{4}{\pi} - 1} \quad (4.39)$$

Both expressions of the error for each mode are independent of the excitation level. Therefore, the effect of the statistical errors depends on the modal parameters, time lag, and the total time length. Both the modal auto-correlation function and its variance have the same relative contribution from the excitation.

In this section, we have proven that the envelope of the estimated correlation function matrix is Rice distributed. Therefore, the envelope becomes increasingly biased as the signal-to-noise ratio decreases to a point where the expected envelope becomes almost constant, thus explaining the phenomenon of

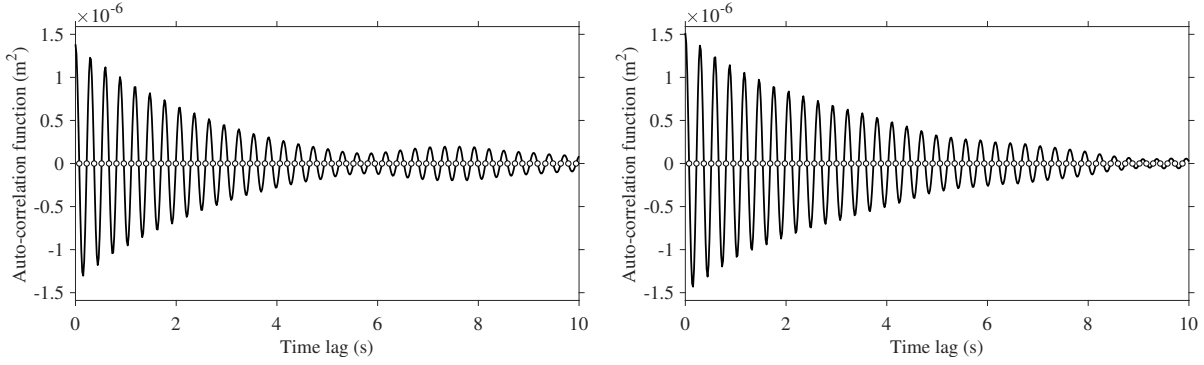


Figure 4.14: Correlogram with two realisations of the same estimated correlation function and the zero crossings

the noise tail. Hence, in operational modal analysis, this biased envelope introduces a biased error in the identified damping ratio.

4.9 Statistical errors in zero crossings of the modal auto-correlation function

In this section, we will study the zero crossings from the modal auto-correlation function, see Fig. 4.14. The statistical properties of zero crossings for a stochastic process are, however, largely unsolved and there is no closed-form solution for the probability density function for the level crossing of a stochastic process [5, 22, 26–30]. Level and zero crossings are studied in [5, 22, 27–29] for a sine wave with ergodic white Gaussian noise. The estimated modal auto-correlation function is an exponential decaying cosine with non-stationary Gaussian non-white noise, thus, we simplify the problem due to this complexity. Therefore, we will study the zero crossing in the noise tail region where the statistical errors dominate and where they are approximately stationary when the time length is much larger than the time lag, $T \gg \tau$.

4.9.1 Expected zero crossing

Rice [22] states that level crossing is given by the joint probability function, $p(\alpha, \beta)$, of a stationary and narrow banded random variable, α , and its derivative, β . The expected zero crossing is then given by

$$N_0 = \int_{-\infty}^{\infty} |\beta| p(0, \beta) d\beta \quad (4.40)$$

For a Gaussian process with zero means, it simplifies to [5]

$$N_0 = \frac{\sqrt{1 - \rho_{\alpha, \beta}^2} \sigma_{\beta}}{\pi \sigma_{\alpha}} \quad (4.41)$$

where σ_{α} and σ_{β} are the standard deviation of α and β respectively, and $\rho_{\alpha, \beta}$ is the population correlation coefficient between α and β .

4.9.2 Variance of the derivative of the modal auto-correlation function

In this section, we will find the variance of the derivative of the estimated modal auto-correlation function with respect to the time lag, τ .

The correlation function has the following properties regarding the first and second derivative with respect to time lag [1, 5, 19]

$$-R_{\dot{x}, x}(\tau) = R_{x, \dot{x}}(\tau) = \frac{d}{d\tau} R_{x, x}(\tau) = \dot{R}_{x, x}(\tau) \quad (4.42)$$

$$R_{\dot{x}, \dot{x}}(\tau) = -\frac{d^2}{d\tau^2} R_{x, x}(\tau) = -\ddot{R}_{x, x}(\tau) \quad (4.43)$$

Thus, the derivative, with respect to time lag, of the modal auto-correlation function equals the cross-correlation function between the modal coordinate and its derivative in time, $\frac{d}{d\tau}R_{q_i}(\tau) = R_{q_i, \dot{q}_i}(\tau)$. We assume a large time length, T , and use the variance expression for a cross-correlation function [5] and we apply the properties of the correlation function from Eqs. (4.42) and (4.43) to rewrite it.

$$\begin{aligned} \text{Var} [\tilde{R}_{q_i, \dot{q}_i}(\tau)] &\approx \frac{1}{T-\tau} \int_{-\infty}^{\infty} (R_{q_i, \dot{q}_i}(r)R_{\dot{q}_i, q_i}(r) + R_{q_i, \dot{q}_i}(r+\tau)R_{\dot{q}_i, q_i}(r-\tau)) dr \\ &\approx \frac{1}{T-\tau} \int_{-\infty}^{\infty} (-R_{q_i}(r)\dot{R}_{q_i}(r) - \dot{R}_{q_i}(r+\tau+)\dot{R}_{q_i}(r-\tau)) dr \end{aligned} \quad (4.44)$$

We calculate the first derivative of the modal auto-correlation function, Eq. (4.5), with respect to τ .

$$\dot{R}_{q_i}(\tau) = -\frac{\omega_0}{\sqrt{1-\zeta^2}}\sigma_{q_i}^2 e^{-\omega_0\zeta|\tau|} \sin(\omega_d\tau) \quad (4.45)$$

Clough and Penzien [19] calculated the second derivative of the auto-correlation function of an SDOF system with respect to τ .

$$\ddot{R}_{q_i}(\tau) = -\omega_0^2\sigma_{q_i}^2 e^{-\omega_0\zeta|\tau|} \left(\cos(\omega_d\tau) + \frac{\zeta}{\sqrt{1-\zeta^2}} \sin(\omega_d|\tau|) \right) \quad (4.46)$$

We can see that $\omega_0^2 R_{q_i}(\tau) = -\ddot{R}_{q_i}(\tau)$. So we simplify again.

$$\text{Var} \left[\frac{d}{d\tau} \tilde{R}_{q_i}(\tau) \right] \approx \frac{1}{T-\tau} \int_{-\infty}^{\infty} (\omega_0^2 R_{q_i}(r)^2 - \dot{R}_{q_i}(r+\tau+)\dot{R}_{q_i}(r-\tau)) dr \quad (4.47)$$

This is similar to Eq. (4.18) but the first term, $\omega_0^2 R_{q_i}(r)^2$, is multiplied by ω_0^2 . We insert Eqs. (4.5) and (4.46) into Eq. (4.47) and calculate the integral by assuming small damping.

$$\text{Var} \left[\frac{d}{d\tau} \tilde{R}_{q_i}(\tau) \right] \approx \omega_0^2 \frac{\sigma_{q_i}^4}{2(T-\tau)\omega_0\zeta} (1 - e^{-2\omega_0\zeta\tau} \cos(2\omega_d\tau)(1 + 2\zeta\omega_0\tau)) \quad (4.48)$$

4.9.3 Auto-correlation of statistical errors

The statistical dependency of the correlation function matrix is another important statistical property of the correlation function. Since we calculate the estimated correlation function matrix for all time lags from the same realisation of the system response, then the matrix - at different time lags - is statistically dependent. Hence, the statistical errors in the estimated correlation function matrix are correlated. In this subsection, we will study this correlation since it relates to the zero crossings.

The estimated modal auto-correlation function is Gaussian distributed so the statistical errors are additive Gaussian noise, $s(\tau) \sim \mathcal{N}(0, \text{Var}[\tilde{R}_{q_i}(\tau)])$, in each estimated modal auto-correlation function.

$$\tilde{R}_{q_i}(\tau) = R_{q_i}(\tau) + s(\tau) \quad (4.49)$$

We will look at the non-stationary and auto-correlation function of the statistical errors in each estimated modal auto-correlation function. This is equivalent to the covariance function of the estimated modal auto-correlation function.

$$\begin{aligned} R_{s,s}(\tau, v) &= \mathbb{E} [s(\tau)s(\tau+v)] \\ &= \mathbb{E} \left[\left(\tilde{R}_{q_i}(\tau) - R_{q_i}(\tau) \right) \left(\tilde{R}_{q_i}(\tau+v) - R_{q_i}(\tau+v) \right) \right] \\ &= \text{Cov}[\tilde{R}_{q_i}(\tau), \tilde{R}_{q_i}(\tau+v)] \end{aligned} \quad (4.50)$$

Priestley [31] derives an expression of the covariance function of the estimated correlation function, see Appendix 4.C for a similar derivation of the expression of the auto-correlation function of the statistical errors.

$$R_{s,s}(\tau, v) \approx \frac{1}{T-\tau} \int_{-\infty}^{\infty} (R_{q_i}(r)R_{q_i}(r+v) + R_{q_i}(r+v+\tau)R_{q_i}(r-\tau)) dr \quad (4.51)$$

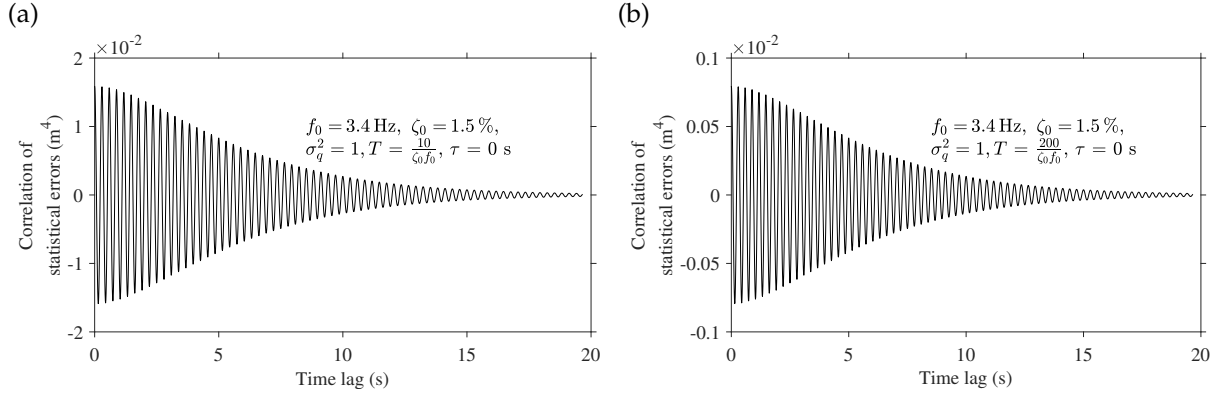


Figure 4.15: Correlogram of statistical errors, Eq. (4.52), for time lag zero, $\tau = 0$, plotted for two different time lengths, (a) Brincker and Ventura [1], (b) ANSI [13]

Giampellegrini [6] calculates the covariance function of the estimated correlation functions using this integral, Eq. (4.51), by assuming small damping. In this article, we calculate the auto-correlation function of the statistical errors based on the work in [6].

$$R_{s,s}(\tau, v) \approx \frac{\sigma_{q_i}^4}{2(T-\tau)\omega_0\zeta} \cdot \left(e^{-\omega_0\zeta|v|} \left(\cos(\omega_d v)(1 + |v|\omega_0\zeta) + \sin(\omega_d |v|) \frac{2\omega_0\zeta^2|v|}{\sqrt{1-\zeta^2}} \right) + e^{-\omega_0\zeta(2\tau+v)} \left(\cos(\omega_d(2\tau+v))(1 + (2\tau+v)\omega_0\zeta) + \sin(\omega_d(2\tau+v)) \frac{2\omega_0\zeta^2(2\tau+v)}{\sqrt{1-\zeta^2}} \right) \right) \quad (4.52)$$

For $v = 0$, the covariance function, Eq. (4.52), simplifies to the variance of the modal correlation function, Eq. (4.19). Fig. 4.15 shows the correlation function of the statistical errors. The statistical errors are a narrow banded process since it - for any value of τ - oscillates with the damped frequency, ω_d , of the given mode.

We will study two special instances: at time lag zero, $\tau = 0$, and high time lags, $\tau \gg 0$.

$$R_{s,s}(0, v) \approx \frac{\sigma_{q_i}^4}{T\omega_0\zeta} e^{-\omega_0\zeta|v|} \left(\cos(\omega_d v)(1 + |v|\omega_0\zeta) + \sin(\omega_d |v|) \frac{2\omega_0\zeta^2|v|}{\sqrt{1-\zeta^2}} \right) \quad (4.53)$$

Fig. 4.7 shows this phenomenon with two examples of the estimated modal auto-correlation function.

$$R_{s,s}(\tau, v) \approx \frac{\sigma_{q_i}^4}{2(T-\tau)\omega_0\zeta} e^{-\omega_0\zeta|v|} \left(\cos(\omega_d v)(1 + |v|\omega_0\zeta) + \sin(\omega_d |v|) \frac{2\omega_0\zeta^2|v|}{\sqrt{1-\zeta^2}} \right), \quad \tau \gg 0 \quad (4.54)$$

This case studies the statistical errors in the noise tail where each estimated modal auto-correlation function oscillates with its damped natural frequency in the tail region of the correlation function. Furthermore, given a large time length compared to the time lag, $T \gg \tau$, the statistical errors are approximately stationary.

4.9.4 Expected zero crossing for the modal auto-correlation function

We focus on the noise tail where the expected value, \widetilde{R}_{q_i} , is approximated zero and the variance is approximately stationary given that the time length is much larger than the time lag, $T \gg \tau$. Therefore, the variance of the modal auto-correlation function and its derivative obtain the following relationship.

$$\text{Var} \left[\frac{d}{d\tau} \widetilde{R}_{q_i}(\tau) \right] \approx \omega_0^2 \text{Var} \left[\widetilde{R}_{q_i}(\tau) \right], \quad \tau \gg 0 \quad (4.55)$$

We have the estimated modal auto-correlation function, $\widetilde{R}_{q_i} \sim \mathcal{N}(0, \text{Var}[\widetilde{R}_{q_i}(\tau)])$, and its derivative, $\frac{d}{d\tau}\widetilde{R}_{q_i}(\tau) \sim \mathcal{N}(0, \omega_0^2 \text{Var}[\frac{d}{d\tau}\widetilde{R}_{q_i}(\tau)])$. Since the statistical errors dominate, $\widetilde{R}_{q_i}(\tau) = s(\tau)$, we can write the correlation coefficient between the estimated modal auto-correlation function and its derivative as

$$\rho_{s,\dot{s}}(\tau) = \frac{R_{s,\dot{s}}(\tau, 0)}{\sqrt{\text{Var}[\widetilde{R}_{q_i}(\tau)]}\sqrt{\text{Var}[\frac{d}{d\tau}\widetilde{R}_{q_i}(\tau)]}}, \quad \tau \gg 0 \quad (4.56)$$

For stationary data, the cross-correlation function between a random process and its derivative is zero at time lags zero, $R_{x,\dot{x}}(0) = 0$, [5]. Hence, the cross-correlation, $R_{s,\dot{s}}(\tau, v)$, between the statistical errors and its derivative approach zero in the noise tail for $v = 0$. Thus, the correlation coefficient is approximately zero in the noise tail.

$$\rho_{s,\dot{s}}(\tau) \approx 0, \quad \tau \gg 0 \quad (4.57)$$

We apply Eq. (4.41) and calculate the expected zero crossing in the noise tail region.

$$N_0(\tau) \approx \frac{\omega_0}{\pi}, \quad \tau \gg 0 \quad (4.58)$$

This corresponds well with the findings in Section 4.9.3, however, here the oscillating frequency is not the damped frequency. This is due to the assumptions of narrow banded in Rice [22], Eq.(4.41), for zero crossings. Since the statistical errors are approximately stationary in the noise tail region and they are narrow banded with the same frequency, ω_0 , as the given mode, then the expected zero crossing should be twice this frequency. Hence, the zero crossings of the estimated modal auto-correlation function are an unbiased process. In the noise tail, the expected number of zero crossings as a function of τ is given by

$$\mathbb{E}[N(\tau)] = \int_0^\tau N_0 d\tau = \frac{\omega_0}{\pi}\tau + \frac{1}{2}, \quad \tau \gg 0 \quad (4.59)$$

4.9.5 Variance of zero crossings for the modal auto-correlation function

As previously stated, no closed-form solution exists for the probability density function of the periods of zero crossings. Thus, it is difficult to express the exact variance of each zero crossing.

Cobb [29] shows that the periods of zero crossings from a sine wave with additive Gaussian noise are normal distributed for high signal-to-noise ratios.

$$\text{Var}[N(\tau)] = \frac{2(1 + \rho_1)}{\pi^2 a^2}, \quad \mu \ll \sigma \quad (4.60)$$

where $a = \frac{1}{\varepsilon(\tau)}$, Eq. (4.23), and ρ_1 is the normalised correlation function for noise alone at the value $T = 1$.

It illustrates that the variance of the zero crossings depends on the signal-to-noise ratio at the beginning of the modal auto-correlation function.

Raninal [28] proves that the variance of the number of zero crossings in a time length, t , increase linearly for low signal-to-noise ratios and high time lags.

$$\text{Var}[N(\tau)] = N_0\tau, \quad \mu \gg \sigma \quad (4.61)$$

This indicates that the variance of zero crossings is much higher and increases linearly in the noise tail.

This concludes this section on zero crossings. We have shown that the statistical errors on each modal auto-correlation function are a non-stationary process but they are narrow banded with the same frequency as the damped natural frequency of each mode. We found that the expected zero crossings are unbiased but the variance of the zero crossings increase linearly in the noise tail. Thus in operational modal analysis, the identified natural frequencies are unbiased regardless of the noise tail but we should disregard the noise tail to reduce the uncertainty of the identification process.

4.10 Noise tail relationship / time length and correlation time relationship

In this section, we will study the relationship between the time length of data and the correlation time of the modal auto-correlation functions. The correlation time is, however, a stochastic process that describes the gradual transition from a persistent physical part to the erratic noise tail. So we will have to express the relationship between the time length and correlation time with some stochastic expression of error. We will set up a simplified relationship between the time length, correlation time, and the modal parameters based on the biased error since Eq. (4.37) is non-trivial to solve. Both the biased and random error of the envelope depend on the signal-to-noise ratio or the normalised random error, Eq. (4.23), of the peaks of the estimated correlation function.

We know from Sections 4.7.3 and 4.7.4 that the mode with the lowest frequency-damping product has the highest level of statistical errors. Thus, we should use the mode with the lowest frequency-damping product to find the required time length or correlation time.

In operational modal analysis, the excitation is unknown so we must use the relative expression of the statistical errors since these are unrelated to the excitation levels.

We want to solve the equation for the biased error of the envelope, Eq. (4.36), to find an expression for the signal-to-noise ratio as a function of this biased error. We use the asymptotic expansion of the Laguerre polynomial for the case $\frac{1}{2}$ for negative values [23].

$$L_{1/2}(-x) = \frac{2\sqrt{x}}{\sqrt{\pi}} + \frac{1}{2\sqrt{\pi x}} + \frac{1}{16\sqrt{\pi x^3}} + \mathcal{O}\left(x^{-\frac{5}{2}}\right) \quad (4.62)$$

We insert this into the normalised biased error, Eq. (4.36), and solve it for the signal-to-noise ratio, $\frac{\mu}{\sigma}$.

$$SNR(\varepsilon_m) = \sqrt{\frac{\sqrt{2\varepsilon_m + 1} + 1}{4\varepsilon_m}} \quad (4.63)$$

where $SNR(\varepsilon_m)$ is the approximated signal-to-noise ratio, $\frac{\mu}{\sigma}$, as a function of the normalised biased error. Since we based it on an asymptotic expansion, it only works for a small normalised biased error.

We know that the signal-to-noise ratio is inversely proportional to the normalised random error. Thus, we can equal the approximated signal-to-noise ratio, Eq. (4.63), to the normalised random error, Eq. (4.23), that we derived in Section 4.7.4.

$$\frac{1}{SNR(\varepsilon_m)} = \sqrt{\frac{1}{T - \tau} \frac{e^{2\omega_0\zeta\tau} + 2\omega_0\zeta\tau + 1}{2\omega_0\zeta}} \quad (4.64)$$

Since the normalised biased error is based on the biased error relative to the envelope, we will express the correlation time relative to the decay of the correlation function, $a = e^{-\omega_0\zeta|\tau_0|}$. We simplify Eq. (4.64) by removing the smallest terms of the normalised random error and we insert Eq. (4.63).

$$T_{min}(\varepsilon_m, f_0\zeta, a) = \frac{\sqrt{2\varepsilon_m + 1} + 1}{4\varepsilon_m} \frac{a^{-2}}{4\pi f_0\zeta} \quad (4.65)$$

where τ_0 is the correlation time for the given mode.

This new expression adds novel information on the relationship between the normalised biased error of the envelope, ε_m , the frequency-damping product, $\omega_0\zeta$, the time length of the recording, T , and the correlation time of the correlation function matrix, τ_0 . For this expression, we should use the mode with the lowest frequency-damping product since it has the highest level of statistical errors as previously stated. We can use this expression to find an appropriate time length, T_{min} , based on a given time lag, biased error, and correlation time. Or we can find the correlation time, τ_{max} , for a given time length if we have the desired level of normalised biased error.

We will show the application of Eq. (4.65) with an example. Let us say that we want to find the time length of a measurement setup meant for operational modal analysis. We have an initial estimate of the modal parameters of the first fundamental mode. Now we must specify how much correlation time, a , we need for the identification process, e.g. $a = 10\%$. In practice, the authors find that the noise tail seems to begin at 10% normalised biased error of the envelope. Thus, we need a time length of approximately $T_{ex} \approx \frac{42}{f_0\zeta}$.

4.10.1 Comparison to other required time lengths

By applying Eq. (4.65), we will study two minimum required time lengths, Brincker and Ventura [1] and ANSI 2.47 [13]. These two expressions recommend minimum time lengths with a difference of 2,000%.

$$T_{Brincker} = \frac{10}{f_0 \zeta} \quad (4.66)$$

$$T_{ANSI} = \frac{200}{f_0 \zeta} \quad (4.67)$$

The required time length from Brincker and Ventura, Eq. (4.66), assumes that the lowest frequency of the system defines the longest correlation time. It uses spectral density functions as the basis for this time length requirement [5]. The correlation function for the lowest mode must decay to an amplitude of 4% and we need 20 data segments with 50% overlap and 40 frequency averages [1]. We want to compare this time length requirement with Eq. (4.65). We know from Eq. (4.66) that we must have $a = 4\%$. We equal Eq. (4.65) to Eq. (4.66), $T_{min}(\varepsilon_m, f_0 \zeta, 0.04) = T_{Brincker}$, and solve for the normalised biased error, ε_m , which is approximately 440%. Since ε_m was based on an asymptotic expansion of the Laguerre polynomial for negative values, it is inaccurate for large values of normalised biased error. The normalised biased error is, however, still so big that we should decrease the correlation time for the given time length. We set the normalised biased error to 10%, so the correlation time ends at an amplitude of approximately 20%. This contradicts the 4% decay of the original derivation.

We turn to the other time length requirement from ANSI 2.47, Eq. (4.67). It uses the first fundamental mode of a system and has a biased error of 4% and a variance error of 10% [13]. We insert a normalised biased error, ε_m , of 4% into Eq. (4.65) and equal it to Eq. (4.67), $T_{min}(0.04, f_0 \zeta, a) = T_{ANSI}$. Then the correlation time should end at an amplitude of 7.1%. If we accept a normalised biased error of 10% then the correlation time ends at an amplitude of approximately 5%.

A normalised biased error at 10% often occurs at the end of the correlation time and the beginning of the noise tail. So, for Brincker and Ventura the noise tail begins when the amplitude drops to $\sim 20\%$ while it begins at an amplitude of $\sim 5\%$ for ANSI 2.47. The increased correlation time from ANSI 2.47, however, comes with a 2,000% increase in the time length. The two recommended time lengths result in widely different levels of error, but Brincker and Ventura provide the more practical of the two recommended time lengths, though the correlation time is shorter.

In this section, we showed that the normalised random error of the estimated correlation function can be used to set up a simple relationship between the normalised biased error, the time length, correlation time, and the system parameters.

4.11 Case study

In this section, we will verify the statistical properties derived in this article of the estimated correlation function matrix based on a simulation and an experimental study. For the discrete estimation of the correlation function matrix, we apply the direct method in the time domain where we compute average products of the sampled data using the toolbox from Brincker and Ventura [1].

$$\hat{\mathbf{R}}(k) = \frac{1}{N-k} \sum_{n=0}^{N-k} \mathbf{y}(n) \mathbf{y}^\top(n+k), \quad 0 \leq k < N \quad (4.68)$$

where $\hat{\mathbf{R}}(k)$ is the discrete estimated correlation function matrix, N is the total number of samples, $T = N\Delta t$, k is the discrete time lag, $\tau = k\Delta t$, and Δt is the sampling interval. For more information on the discrete estimation of the correlation function matrix, we refer to [1, 5].

4.11.1 Simulation study

We simulate the response of a three degree-of-freedom system corresponding to masses in series supported in one end, see the system in Fig. 4.16. To model a system with closely spaced and orthogonal modes, we modify the system so the third mode has the similar natural frequency as the second mode but shifted upwards with 0.05 Hz, see the modal parameters in Table 4.1. The time length of each simulation was 13 minutes. Thus, the correlation time corresponds to a decay of 6.7% of the original amplitude

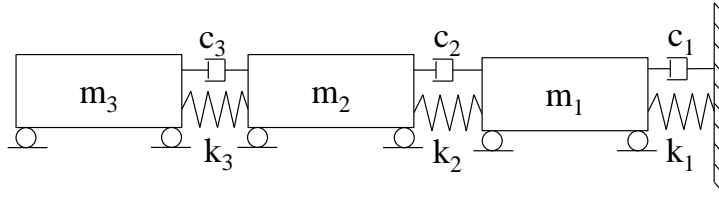


Figure 4.16: The system used in the case study

while the normalised error is below 25% according to Eq. (4.65). We run 100,000 simulations of the system response by generating white Gaussian noise as excitation and use the Fourier transformed modal superposition to simulate the linear system [1]. For each simulation of the response, we calculate the estimated correlation function matrix and use the analytic mode shapes of the system to decorrelate each estimated correlation function matrix into the modal auto-correlation functions, similar to Eq. (4.4). We estimate the envelope of each modal auto-correlation function using the Hilbert transformation [20].

Table 4.1: Modal parameters of the numerical system

| | Mode 1 | Mode 2 | Mode 3 |
|-------------------|--------|--------|--------|
| Frequency (Hz) | 3.39 | 10.01 | 10.06 |
| Damping Ratio (%) | 1.49 | 1.34 | 5.00 |

Figs. 4.17 and 4.18 show the expected value, Eq. (4.13), and variance, Eq. (4.16), respectively, of the correlation function matrix next to sampled values of all estimated correlation function matrices from the simulation. Fig. 4.19 compares the expected value, Eq. (4.5), and the variance, Eq. (4.19), of the estimated modal auto-correlation functions, $\widetilde{R}_{q_i}(\tau)$, to the sample mean and sample variance of the decorrelated estimated correlation function matrix from the Monte Carlo simulations. There is a high correlation between the theoretical and the simulated statistical properties.

In Fig. 4.20, we move to the envelope and compare the analytic expressions of the expected value, Eq. (4.30), and the variance, Eq. (4.31), of the envelope to sample mean and variance from the Monte Carlo simulation. The sample mean and analytic expression of the expected envelope are identical while the sample variance is almost equivalent to the analytic variance of the envelope. Fig. 4.21 illustrates the normalised biased and random error of the Hilbert envelope.

Fig. 4.22 illustrates the correlation function of the statistical errors in each modal correlation function at two time lags, τ , by comparing the analytic expression, Eq. (4.52), with the results from the simulation. The analytic correlation function of the statistical errors matches with the simulation study. Fig. 4.23 shows the zero crossings for each modal auto-correlation function, and the analytic expression is similar to the sample mean zero crossing. The variance of the zero crossings increases rapidly and linearly in the noise tail region while the variance is small for zero crossings located in the correlation time. By comparing it with Fig. 4.21, this growth of variance happens as the biased error exceeds 10%.

The assumption of a sufficient time length is system dependent. For the second and third mode, there is a high correlation between theory and the simulation but the first mode deviates a bit. Thus, the time length must be sufficiently long for the individual modes, see sections 4.7.4 and 4.8.6. Thus, modes with low frequency-damping products require longer time lengths compared to modes with higher products. Therefore in this case study, we should expect the third mode to behave more as the analytic equations from this article than the first mode would.

Thus, based on these findings, we will expect relatively large random and biased errors in the estimated damping ratios, some random errors in the estimated frequency, and only identification errors in the estimated mode shapes in an identification process using correlation-driven operational modal analysis.

The assumptions in this article are mainly based on lightly damped and orthogonal modes. Very closely spaced modes, however, have correlated modal coordinates, and the cross-correlation between the modes is influential. In such a case, the expectation and variance of the estimated correlation function matrix differ from the summation of the expectations and variances of the modal auto-correlation functions. In this case, these summations are more a rule of thumb.

Based on this case study, the statistical properties of the estimated correlation function matrix match well with the analytic expression.

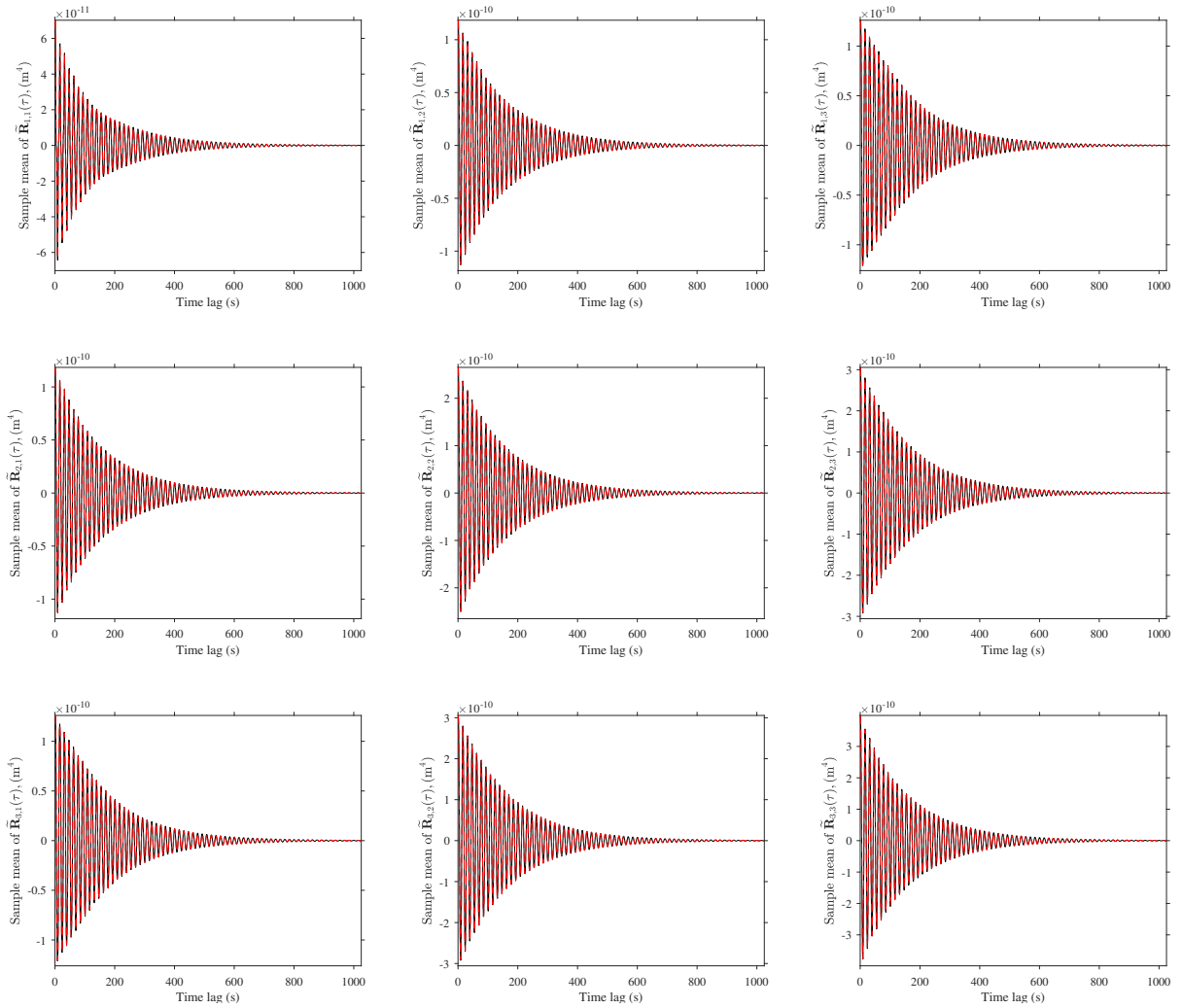


Figure 4.17: Simulation study: Analytic expectation, Eq. (4.13), (red dashed line) against sample mean of the Estimated Correlation Matrix, $\tilde{\mathbf{R}}(\tau)$, based on 100,000 Monte Carlo Simulations (black solid line)

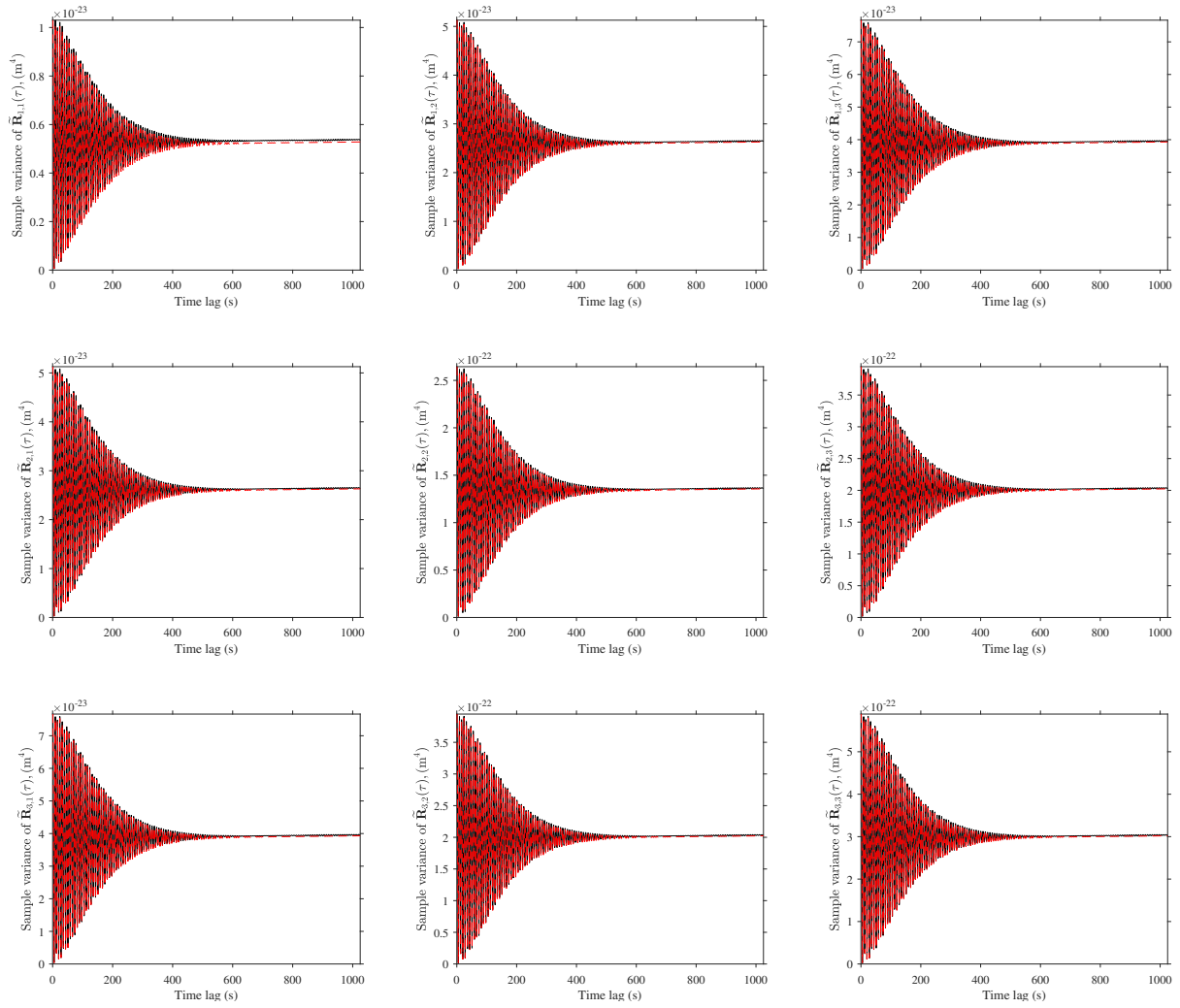


Figure 4.18: Simulation study: Analytic variance, Eq. (4.16), (red dashed line) against sample variance of the Estimated Correlation Function Matrix, $\tilde{\mathbf{R}}(\tau)$, based on 100,000 Monte Carlo Simulations (black solid line)

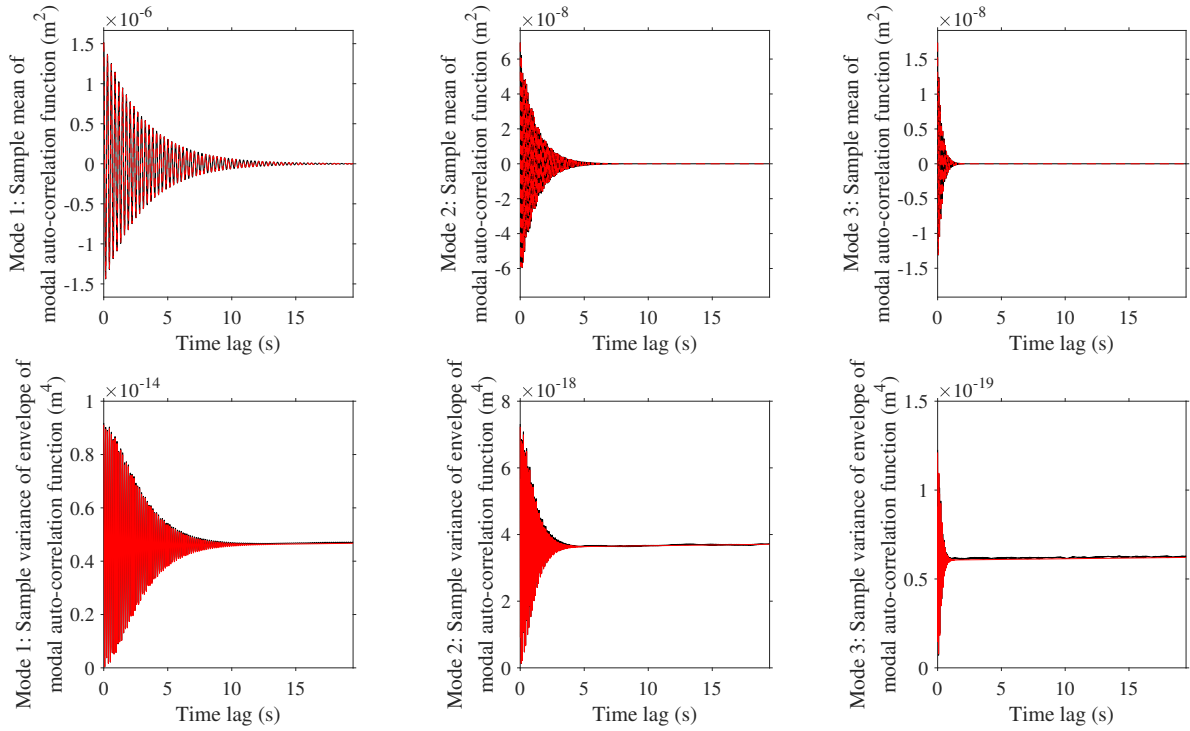


Figure 4.19: Simulation study: Analytic expected value, Eq. (4.5), and analytic variance, Eq. (4.19), (red dashed line) against sample mean and variance of the Estimated Modal Auto-Correlation Function, $\hat{R}_{q_i}(\tau)$, for each mode based on 100,000 Monte Carlo Simulations (black solid line)

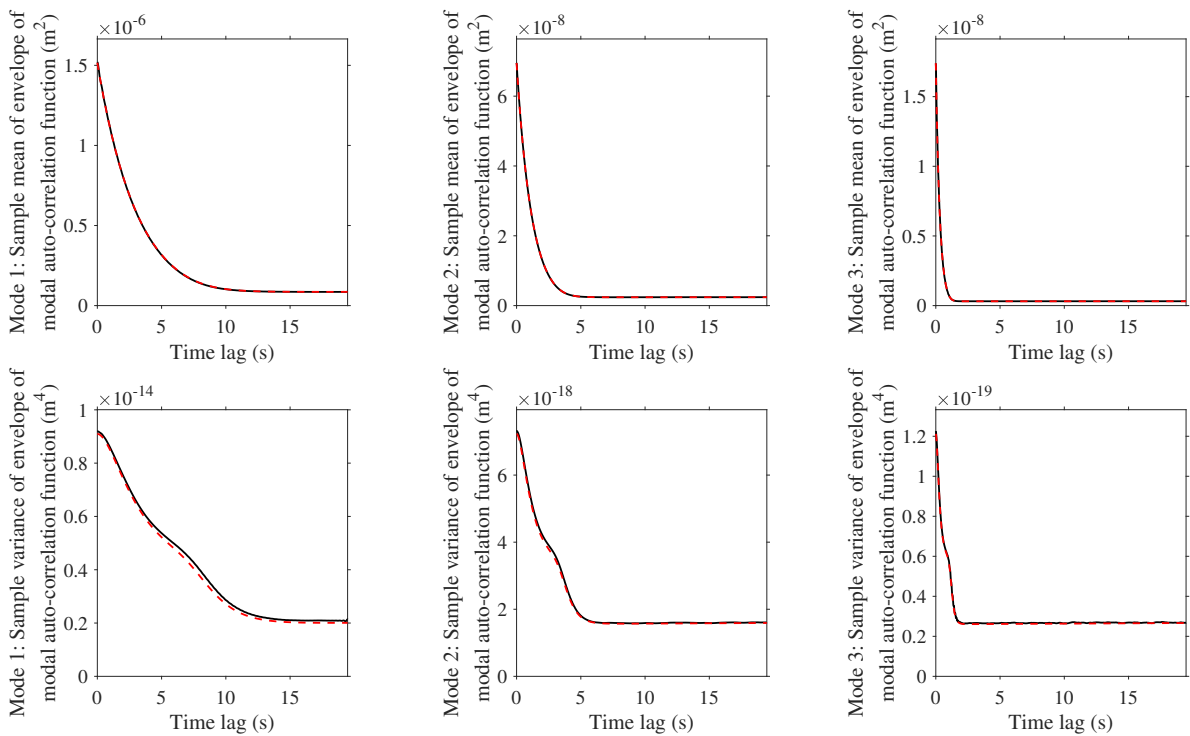


Figure 4.20: Simulation study: Analytic expected value, Eq. (4.30), and variance, Eq. (4.31), of envelope (red dashed line) against sample mean and variance of envelope based on 100,000 Monte Carlo simulations (black solid line)

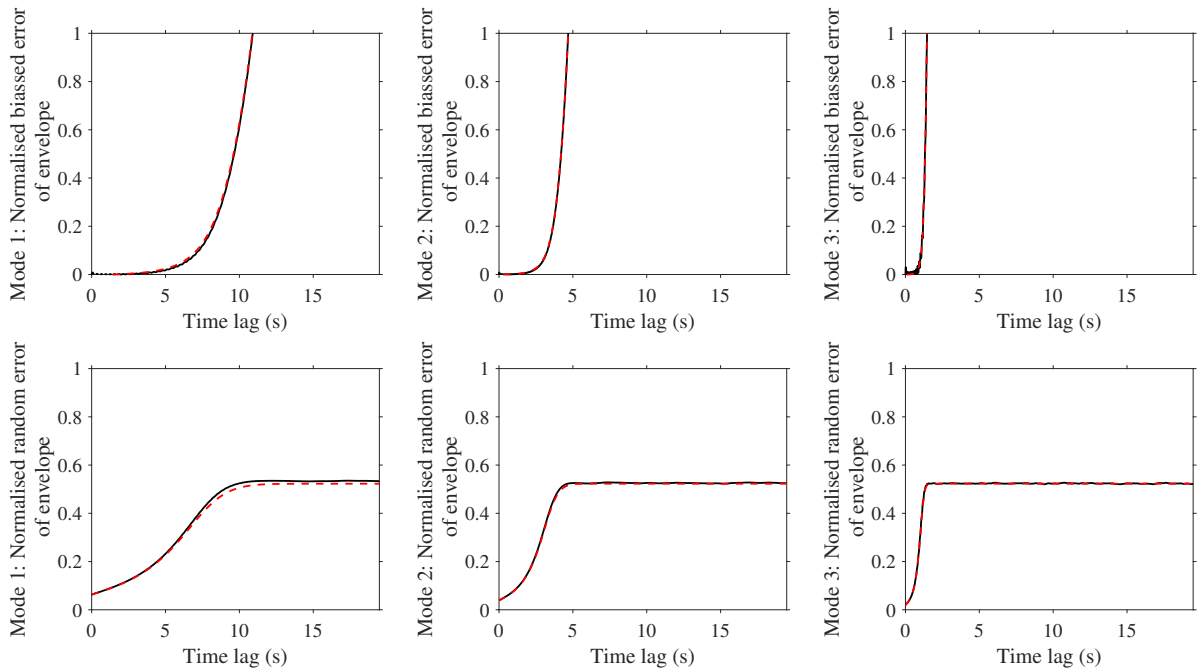


Figure 4.21: Simulation study: The normalised biased error, Eq. (4.37), and normalised random error, Eq. (4.38), (red dashed line) against the sampled versions from 100,000 Monte Carlo simulations (black solid line)

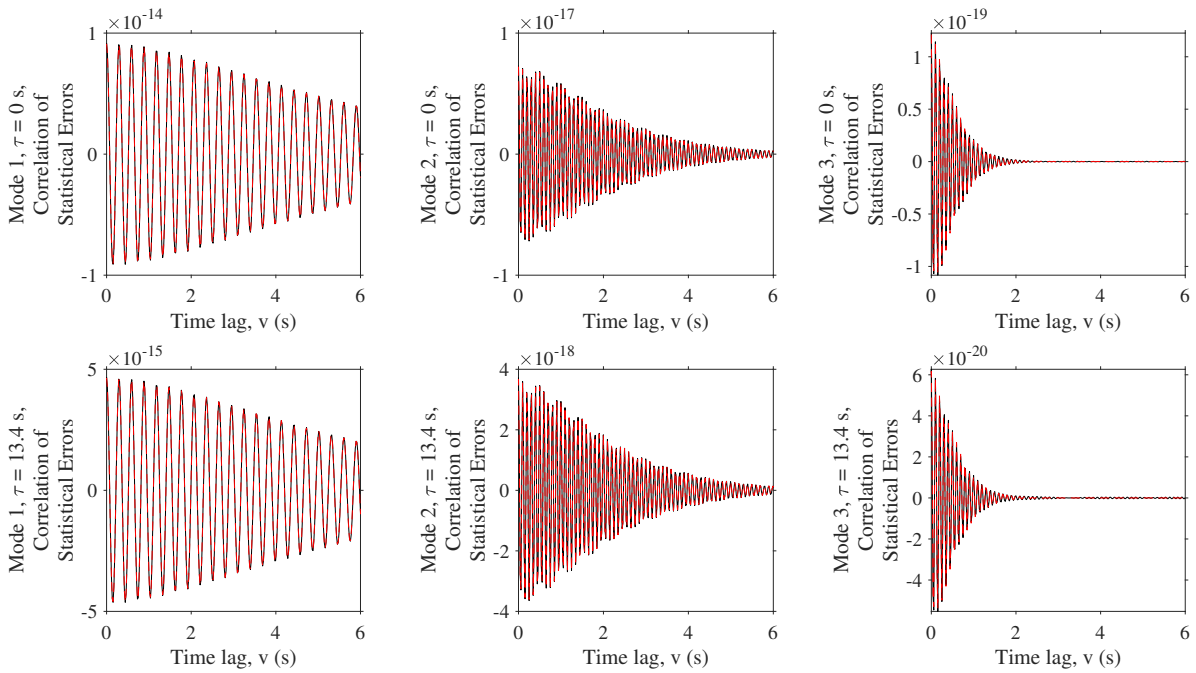


Figure 4.22: Simulation study: Analytic correlation of statistical errors, Eq. (4.52), (red dashed line) against estimated correlation of statistical errors based on 100,000 Monte Carlo simulations (black solid line)

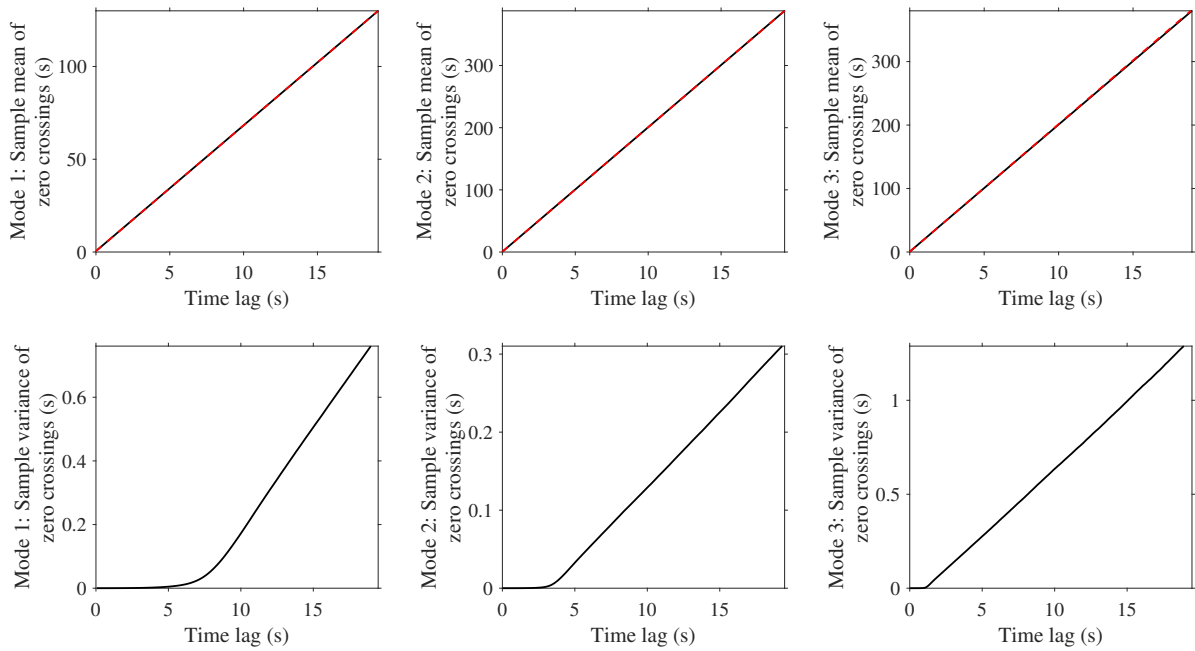


Figure 4.23: Simulation study: Analytic expected zero crossings, Eq. (4.59), (red dashed line) against sample mean and variance of zero crossings based on 100,000 Monte Carlo simulations (black solid line)

4.11.2 Experimental study

In this section, the analytic expressions are verified by an experimental study of a T shaped steel structure with a hollow cross-section, RHS40×40×2, in a laboratory facility, see Fig. 4.24. To verify the statistical properties, we need many data sets measured over a longer period. The fluctuation of the modal parameters is, however, near inevitable due to environmental effects during the recording. Even in a laboratory, it is difficult to obtain complete stationarity and completely remove environmental effects over many data sets, see Fig. 4.26. The variances in temperature and humidity cause slightly non-stationary in the modal parameters over all the data sets. Thus for the experimental study, we have a variance from both the statistical errors and non-stationary modal parameters. This additional variance obstructs the verification of any analytic expression regarding variance; however, we can still verify the analytic expression regarding expected values using the experimental study.

For the measurement-setup, we applied 10 Brüel & Kjær 4508-B-002 uniaxial accelerometers to the structure as seen in Fig. 4.25. The data sets were recorded over the course of four days, primarily at night. We sampled the data at a frequency of 1651 Hz and we used 386 data sets with a time length of 238 seconds. Thus, the correlation time corresponds to a decay of 14.6% given a normalised error of 25% according to Eq. (4.65) using the lowest frequency-damping product. We bandpass filter the data with cut-off frequencies at 5 and 100 Hz to remove noise and higher modes. The Ibrahim time domain technique [32] identified the modal parameters from an arbitrary data set using the correlation function matrix. The identified mode shapes were used to decorrelate the estimated correlation function matrix from each data set. Finally, we identified the modal parameters based on the sample mean of each modal auto-correlation functions using the Ibrahim time domain, see Table 4.2. In this study, only the first three modes are included.

Table 4.2: Modal parameters of the experimental system

| | Mode 1 | Mode 2 | Mode 3 |
|-------------------|--------|--------|--------|
| Frequency (Hz) | 7.30 | 8.91 | 22.8 |
| Damping ratio (%) | 2.47 | 0.392 | 0.237 |

Fig. 4.27 compares the expected value of the estimated modal auto-correlation functions, Eq. (4.5), to the sample mean of the decorrelated estimated correlation function matrix from the experimental study. For the envelope, Fig. 4.28 compares the analytic expressions of the expected value, Eq. (4.30), of the envelope to the sample mean. While Fig. 4.29 shows the expected and sample mean of zero crossings

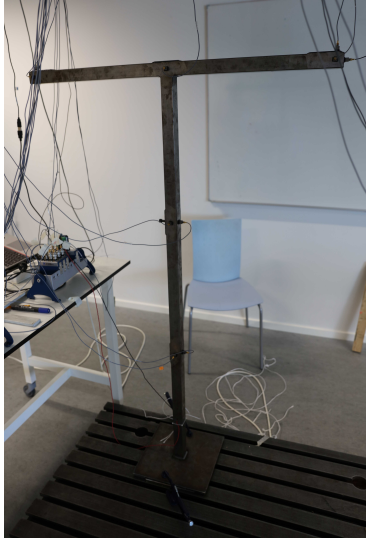


Figure 4.24: Experimental study: Photo of the test specimen in the laboratory

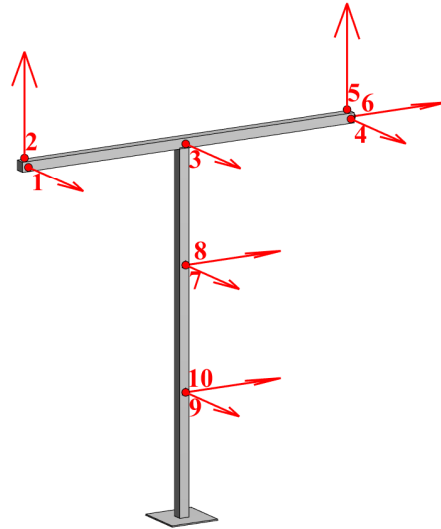
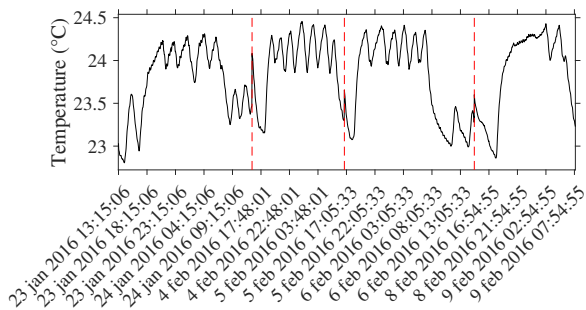


Figure 4.25: Experimental study: Position of sensors on the test specimen, arrows denotes uniaxial accelerometers

(a)



(b)

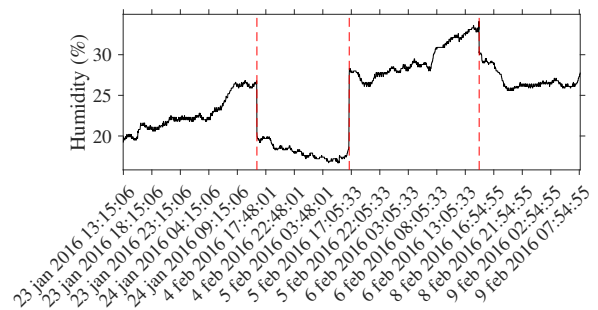


Figure 4.26: Experimental study: The environmental effects during the experimental tests, variance in (a) temperature and (b) humidity

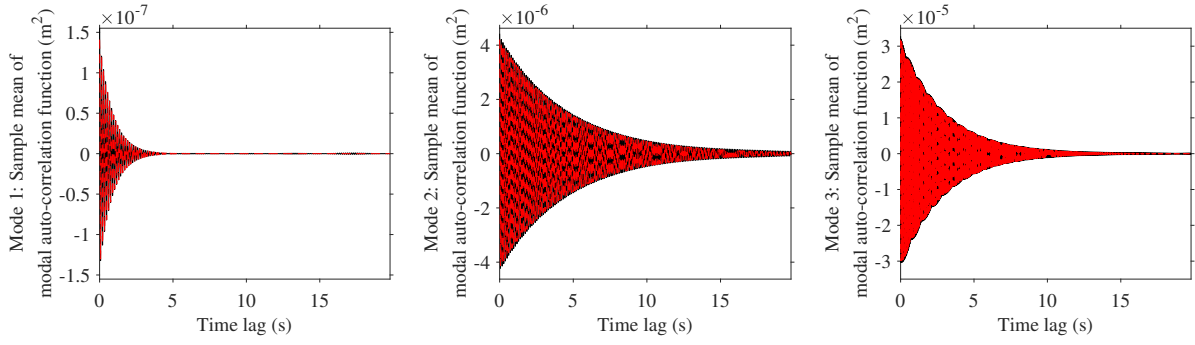


Figure 4.27: Experimental study: Analytic expected value, Eq. (4.5), (red dashed line) against sample mean of the Estimated Modal Auto-Correlation Function, $\widetilde{R}_{q_i}(\tau)$, for each mode based on experimental study (black solid line)

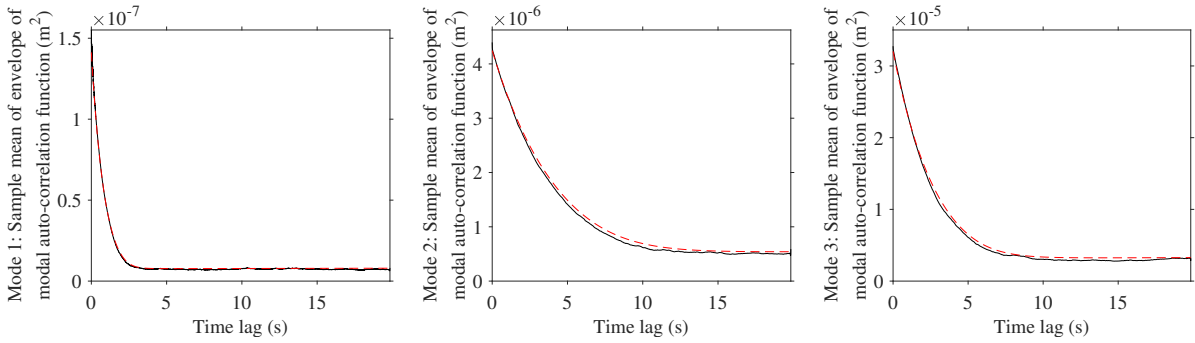


Figure 4.28: Experimental study: Analytic expected value, Eq. (4.30), of envelope (red dashed line) against sample mean of envelope based on experimental study (black solid line)

for each modal auto-correlation function. Generally, the analytic expression correlates well with this experimental study, taking into account, that the uncertainty of the actual modal parameters is a source of error.

Based on this experimental case study, the statistical properties of the estimated correlation function matrix match well with the analytic expression for all expected values.

4.12 Conclusion

In this article, we have studied the estimation of the correlation function matrix in operational modal analysis and the associated statistical errors, which relates to the finite time length of the measured system response. To verify the statistical properties derived in this article, we performed a Monte Carlo simulation of a three DOF system, and generally, these simulations agree well with the analytical expressions from this article. We showed that the statistical errors are non-stationary and additive Gaussian noise in each modal auto-correlation function - for orthogonal modes. The relative statistical errors depend on the system parameters, the time length of the measurements, and time lags (correlation time)

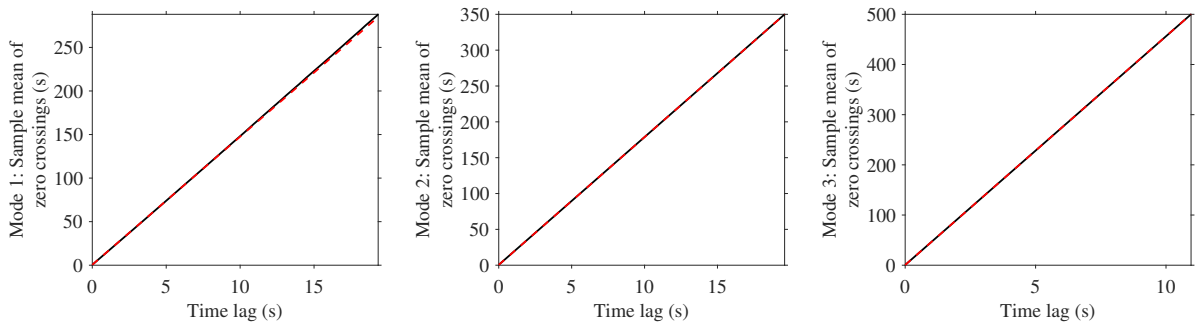


Figure 4.29: Experimental study: Analytic expected zero crossings, Eq. (4.59), (red dashed line) against sample mean of zero crossings based on experimental study (black solid line)

in the estimated correlation function matrix. The statistical errors are narrow banded with the same frequency as the damped frequency of the mode. The zero crossing of each modal auto-correlation function is unbiased.

We have shown that the envelope of the modal auto-correlation function is Rice distributed, meaning it becomes biased as the statistical errors increase in the tail region. We derived an expression for the expected envelope of the modal auto-correlation function. In this article, we call this biased region the *noise tails* of the modal auto-correlation functions, and the correlation function matrix contains a noise tail for each mode in the system. The biased error of the envelope transfers to an identification process and creates a biased error in the estimated modal parameters. Since damping ratios are primarily identified based on the envelope, the estimation of damping is highly affected by the noise tail.

These statistical errors affect identification of modal parameters in operational modal analysis. The mode shapes span the vector space of the estimated correlation function matrix and the statistical errors are located within this space. Thus, for orthogonal modes, there are no statistical errors in the subspace of the estimated correlation function matrix. The frequency estimates are unbiased since the zero crossings of the correlation function matrix are unbiased but the variance increases rapidly in the noise tail. The damping estimates are biased when the correlation function matrix includes parts of the noise tail. Generally, there is a higher variance on the envelopes than the zero crossings, thus, a higher variance is expected for damping estimates than the frequency estimates.

We derived a relationship between the modal parameters, time lags, and the total time length of the recording. The expression is based on the assumption of white Gaussian noise as excitation, a linear and ergodic system, low damping, and a large time length.

For further research, the effect of statistical errors on the identification of modal parameters in the correlation-driven operational modal analysis should be studied. The theory and analytic expressions provided within this article provide the theoretical framework for such a study.

Acknowledgements

The authors acknowledge the funding received from the Centre for Oil and Gas - DTU/Danish Hydrocarbon Research and Technology Centre (DHRTC).

The authors thank Michael Vigsø, Thomas Kabel, Peter Olsen, and Martin Juul from Aarhus University for their helpful discussions and suggestions. Furthermore, the authors thank Sebastian Glavind from Aalborg University for his contribution to the experimental case study.

Appendix 4.A Probability density function of the estimated modal auto-correlation function

We will look at the probability density function of the modal auto-correlation function and we will use the Transformation of Probability Densities, the Central Limit Theorem, and the Moment Generating Function to obtain it [5, 21]. We want to find the distribution of the modal auto-correlation function.

$$R_{q_i}(\tau) = \mathbb{E} [q_i(t)q_i(t + \tau)] \quad (4.69)$$

First, we go back to the equation of motion for a stationary system excited with white Gaussian noise.

$$\mathbf{M}\ddot{\mathbf{y}}(t) + \mathbf{C}\dot{\mathbf{y}}(t) + \mathbf{K}\mathbf{y}(t) = \mathbf{x}(t) \quad (4.70)$$

where \mathbf{M} is the mass matrix, \mathbf{C} is the damping matrix, \mathbf{K} is the stiffness matrix, and $\mathbf{x}(t)$ is the excitation vector. The excitation vector is multivariate normal distributed, $\mathbf{x}(t) \sim \mathcal{N}(\mathbf{0}, \mathbf{\Sigma})$, where $\mathbf{\Sigma}$ is the covariance matrix.

We apply the modal decomposition, Eq. (4.2), for mode i and pre-multiply with the transposed mode shape for mode i to decorrelate the equation of motion into an SDOF system for mode i .

$$\phi_i^\top \mathbf{M} \phi_i \ddot{q}_i(t) + \phi_i^\top \mathbf{C} \phi_i \dot{q}_i(t) + \phi_i^\top \mathbf{K} \phi_i q_i(t) = \phi_i^\top \mathbf{x}(t) \quad (4.71)$$

The response of an SDOF system is a convolution of the modal excitation, $\phi_i^\top \mathbf{x}(t)$, and the impulse response function, $h_i(t)$, [19].

$$q_i(t) = \int_{-\infty}^{\infty} \Phi_i^\top \mathbf{x}(t-\tau) h_i(t) d\tau \quad (4.72)$$

The integral is defined as the limit of a sum and the Central Limit Theorem states that the sum of many random variables tends to be normal distributed [1]. Thus, the modal coordinates, $q_i(t)$, are approximated normal distributed, $q_i(t) \sim \mathcal{N}(0, \sigma_{q_i}^2)$, where $\sigma_{q_i}^2$ is the variance of the modal coordinates. Any time lag of the response is still a normal variable with the same variance due to the time-invariance of the system and the excitation, $q_i(t+\tau) \sim \mathcal{N}(0, \sigma_{q_i}^2)$.

For simplicity, we deal with a single discrete variable, $q_i(t) \rightarrow X \sim \mathcal{N}(0, \sigma^2)$, and the distribution of the estimated auto-correlation coefficient. The auto-correlation function will have similar proof but the number of averaging changes from N to $N-j$ where N is the discrete time length, $T = N\Delta t$, and j is the discrete time lag, $\tau = j\Delta t$. We leave that proof to the reader.

The density function for a normal distribution with zero mean is given by

$$f_x(x, \sigma^2) = \frac{1}{\sqrt{2\pi\sigma^2}} \exp\left(-\frac{x^2}{2\sigma^2}\right) \quad (4.73)$$

Then the correlation coefficient (auto-correlation function at time lag zero) of this normal variable is given by

$$\begin{aligned} \rho_x(\tau) &= \mathbb{E}[X^2] \\ &= \frac{1}{N} \sum_{i=1}^N X_i^2 \end{aligned} \quad (4.74)$$

Firstly, we transform the normal distribution by squaring the random variables, $Y = X^2$, using the Transformation of Probability Densities.

$$g(x) = x^2, \quad g^{-1}(y) = \pm\sqrt{y} \quad (4.75)$$

We calculate the transformed probability density function for Y :

$$\begin{aligned} f_y(y, \sigma^2) &= f_x(g^{-1}(y), \sigma^2) \left| \frac{d}{dy} g^{-1}(y) \right| \\ &= f(\sqrt{y}, \sigma^2) \left| \frac{1}{2\sqrt{y}} \right| + f(-\sqrt{y}, \sigma^2) \left| \frac{1}{2\sqrt{y}} \right| \\ &= \frac{1}{\sqrt{2\pi\sigma^2 y}} \exp\left(-\frac{y}{2\sigma^2}\right) \end{aligned} \quad (4.76)$$

We rewrite the probability density function to a Gamma distribution with shape factor $k = \frac{1}{2}$ and scale factor $\theta = 2\sigma^2$.

$$f_y(y, k, \theta) = \frac{y^{k-1}}{\Gamma(k)(\theta)^k} \exp\left(-\frac{y}{\theta}\right) \quad (4.77)$$

Therefore, we can write the squared normal variable as a Gamma distributed variable, $Y \sim \Gamma(k, \theta) = \Gamma(\frac{1}{2}, 2\sigma^2)$.

Now, we will transform this Gamma distribution by finding the sum of N Gamma variables with the same shape and scale factor, $Z = \sum_{i=1}^N Y_i$. We will use the Moment Generating Function [5] to find the new probability density function. The Moment Generating Function for a Gamma distribution is given by

$$\begin{aligned} M(t) &= \mathbb{E}[\exp(tX)] \\ &= \frac{1}{(1-t\theta)^k} \end{aligned} \quad (4.78)$$

The Moment Generating Function for a summation of random variables equals the product of all the Moment Generating Functions.

$$\begin{aligned}
 M_{\sum_{i=1}^N Y_i}(t) &= \prod_{i=1}^N M_{Y_i}(t) \\
 &= \prod_{i=1}^N \frac{1}{(1-t\theta)^k} \\
 &= \frac{1}{(1-t\theta)^{Nk}}
 \end{aligned} \tag{4.79}$$

The Moment Generating Function for the summation is still valid for a Gamma distribution with a shape factor of Nk . Therefore, we have $Z \sim \Gamma(Nk, \theta) = \Gamma(\frac{N}{2}, 2\sigma^2)$.

Finally, we need to divide with the number of variables, $\rho_x = \frac{Z}{N}$, which is a scaling of a Gamma distribution. We use the Transformation of probability densities.

$$g(z) = \frac{z}{N}, \quad g^{-1}(r) = Nr \tag{4.80}$$

The transformed probability density function for ρ_x is given by

$$\begin{aligned}
 f_r(r, \sigma^2) &= f_z(g^{-1}(r), \sigma^2) \left| \frac{d}{dr} g^{-1}(r) \right| \\
 &= \frac{(Nr)^{Nk-1}}{\Gamma(Nk)(\theta)^{Nk}} \exp\left(-\frac{Nr}{\theta}\right) N \\
 &= \frac{r^{Nk-1}}{\Gamma(Nk)(\frac{\theta}{N})^{Nk}} \exp\left(-\frac{Nr}{\theta}\right)
 \end{aligned} \tag{4.81}$$

Thus, proving that a scaling of a Gamma distribution is another Gamma distribution with a new scale parameter, $\rho_x \sim \Gamma(Nk, \frac{\theta}{N}) = \Gamma(\frac{N}{2}, \frac{2\sigma^2}{N})$.

We rewrite the Gamma distribution as a summation, $\rho_x = \sum_{i=1}^{Nk} \Omega_i$, using the Moment Generating Functions.

$$\begin{aligned}
 M_{\rho_x}(r) &= \frac{1}{\left(1 - r\frac{\theta}{N}\right)^{Nk}} \\
 &= \prod_{i=1}^{Nk} \frac{1}{1 - r\frac{\theta}{N}}
 \end{aligned} \tag{4.82}$$

Thus, we have $\Omega_i \sim \Gamma(1, \frac{\theta}{N})$ [21]. The Central Limit Theorem states that a large sum of random variables is approximately normal distributed [5]. For a long discrete time length, N , the modal auto-correlation function is approximately normal distributed.

Appendix 4.B Probability density function of the estimated correlation function matrix

We will look at the probability density function of the correlation function matrix.

$$\mathbf{R}(\tau) = \mathbb{E}[\mathbf{y}(t)\mathbf{y}(t+\tau)^\top] \tag{4.83}$$

We know from Appendix 4.A that the modal coordinates are uncorrelated normal variables, $q_i(t) \sim \mathcal{N}(0, \sigma_{q_i}^2)$. We stack the modal coordinates in a multivariate normal variable, $\mathbf{q}(t) \sim \mathcal{N}(\mathbf{0}, [\sigma_{q_i}^2])$ where $\mathbf{0}$ is a zero vector and $[\sigma_{q_i}^2]$ is the covariance matrix where the non-diagonal elements are zero.

Let us look at the modal decomposition. It is a linear transformation of Gaussian random vectors or a linear transformation of a multivariate Gaussian variable [21].

$$\mathbf{y}(t) = \Phi \mathbf{q}(t) \tag{4.84}$$

If we assume that the mode shapes are time invariant, we have the multivariate normal variable, $\mathbf{y}(t) \sim \mathcal{N}(\mathbf{0}, \mathbf{\Phi}[\sigma_{q_i}^2]\mathbf{\Phi}^\top)$ [21]. As for the modal coordinates, any time lag of the response is a multivariate normal variable with the same covariance $\mathbf{y}(t + \tau) \sim \mathcal{N}(\mathbf{0}, \mathbf{\Phi}[\sigma_{q_i}^2]\mathbf{\Phi}^\top)$.

We turn to the correlation function matrix and assume uncorrelated modal coordinates [1, 19].

$$\begin{aligned} \mathbf{R}(\tau) &= \mathbf{\Phi} \mathbb{E} [\mathbf{q}(t)\mathbf{q}(t + \tau)^\top] \mathbf{\Phi}^\top \\ &= \sum_{i=1}^N \mathbf{\Phi}_i \mathbf{\Phi}_i^\top R_{q_i}(\tau) \end{aligned} \quad (4.85)$$

Thus, the correlation function matrix is a summation of the product, $\mathbf{\Phi}_i \mathbf{\Phi}_i^\top R_{q_i}(\tau)$. We know from Appendix 4.A that each modal correlation function is approximately normal distributed. Therefore, the correlation function matrix is a summation of linear transformations of multivariate Gaussian variables. Hence, the correlation function matrix is also approximately normal distributed due to the Central Limit Theorem. Thus, the correlation function matrix, $\mathbf{R}(\tau)$, is approximated multivariate normal distributed for a long time series in Operational Modal Analysis.

Appendix 4.C Auto-correlation of statistical errors

The estimated modal auto-correlation function has non-stationary and additive Gaussian noise, $s(\tau) \sim \mathcal{N}(0, \text{Var}[\widetilde{R}_{q_i}(\tau)])$.

$$\widetilde{R}_{q_i}(\tau) = R_{q_i}(\tau) + s(\tau) \quad (4.86)$$

The auto-correlation function of these statistical errors is equivalent to the covariance function of the estimated modal auto-correlation function, $\text{cov}[\widetilde{R}_{q_i}(\tau), \widetilde{R}_{q_i}(\tau + v)]$, and given by

$$\begin{aligned} R_s(\tau, v) &= \mathbb{E} [s(\tau)s(\tau + v)] \\ &= \mathbb{E} \left[\left(\widetilde{R}_{q_i}(\tau) - R_{q_i}(\tau) \right) \left(\widetilde{R}_{q_i}(\tau + v) - R_{q_i}(\tau + v) \right) \right] \\ &= \mathbb{E} \left[\widetilde{R}_{q_i}(\tau)\widetilde{R}_{q_i}(\tau + v) \right] + \mathbb{E} [R_{q_i}(\tau)R_{q_i}(\tau + v)] \\ &\quad - \mathbb{E} \left[\widetilde{R}_{q_i}(\tau)R_{q_i}(\tau + v) \right] - \mathbb{E} [R_{q_i}(\tau)\widetilde{R}_{q_i}(\tau + v)] \end{aligned} \quad (4.87)$$

We arrive at the following equation.

$$R_s(v) = \mathbb{E} \left[\widetilde{R}_{q_i}(\tau)\widetilde{R}_{q_i}(\tau + v) \right] - R_{q_i}(\tau)R_{q_i}(\tau + v) \quad (4.88)$$

The rest of the derivation follows a similar derivation of the variance of the auto-correlation function from [5]. The estimated modal auto-correlation function is defined as (assuming data exist for $T - \tau$).

$$\widetilde{R}_{q_i}(\tau) = \frac{1}{T - \tau} \int_0^{T-\tau} q_i(t)q_i(t + \tau) dt \quad (4.89)$$

We insert the definition of the estimated modal auto-correlation function into Eq. (4.88).

$$R_s(v) = \mathbb{E} \left[\frac{1}{(T - \tau)^2} \int_0^{T-\tau} \int_0^{T-\tau} q_i(t)q_i(t + \tau)q_i(u)q_i(u + \tau + v) dt du \right] - R_{q_i}(\tau)R_{q_i}(\tau + v) \quad (4.90)$$

We use the fourth-order statistical expression of stationary Gaussian processes on the modal coordinates inside the integral [5].

$$\begin{aligned} \mathbb{E} [q_i(t)q_i(t + \tau)q_i(u)q_i(u + \tau + v)] &= R_{q_i}(\tau)R_{q_i}(\tau + v) + R_{q_i}(u - t)R_{q_i}(u + v - t) + \\ &\quad R_{q_i}(u + v - t + \tau)R_{q_i}(u - t - \tau) \end{aligned} \quad (4.91)$$

We insert this back into the integral Eq. (4.90).

$$R_s(\tau, v) = \frac{1}{(T-\tau)^2} \int_0^{T-\tau} \int_0^{T-\tau} (R_{q_i}(u-t)R_{q_i}(u+v-t) + R_{q_i}(u+v-t+\tau)R_{q_i}(u-t-\tau)) dt du \quad (4.92)$$

We rewrite this expression by $r = u - t$.

$$R_s(\tau, v) = \frac{1}{T-\tau} \int_{-T+\tau}^{T-\tau} \left(1 - \frac{|r|}{T-\tau}\right) (R_{q_i}(r)R_{q_i}(r+v) + R_{q_i}(r+v+\tau)R_{q_i}(r-\tau)) dr \quad (4.93)$$

We assume a long time length, T , so we simplify the equation.

$$R_s(\tau, v) \approx \frac{1}{T-\tau} \int_{-\infty}^{\infty} (R_{q_i}(r)R_{q_i}(r+v) + R_{q_i}(r+v+\tau)R_{q_i}(r-\tau)) dr \quad (4.94)$$

References

- [1] Rune Brincker and Carlos Ventura. *Introduction to Operational Modal Analysis*. John Wiley and Sons, Inc., Chichester, West Sussex, UK, 2015.
- [2] Carlo Rainieri and Giovanni Fabbro. *Operational Modal Analysis of Civil Engineering: An Introduction and Guide for Applications*. Springer Science+Business, New York, USA, 2014.
- [3] G. C. James, T. G. Carne, and J. P. Lauffer. The Natural Excitation Technique (NExT) for modal parameter extraction. *The International Journal of Analytical and Experimental Modal Analysis*, 10(4):260–277, 1995.
- [4] Rune Brincker. On the application of correlation function matrices in OMA. *Mechanical Systems and Signal Processing*, 87:17–22, 2017.
- [5] Julius S. Bendat and Allan G. Piersol. *Random Data: Analysis and Measurement Procedures*. Wiley-Blackwell, Hoboken, N.J., USA, 4th edition, 2010.
- [6] Laurent Giampellegrini. *Uncertainty in correlation-driven operational modal analysis*. PhD thesis, University College London, UK, 2007. 64-74.
- [7] Marius Tarpø, Peter Olsen, Sandro Amador, Martin Juul, and Rune Brincker. On minimizing the influence of the noise tail of correlation functions in operational modal analysis. *Procedia Engineering*, 199:1038 – 1043, 2017. X International Conference on Structural Dynamics, EURODYN 2017.
- [8] Brad A. Pridham and John C. Wilson. A study of damping errors in correlation-driven stochastic realizations using short data sets. *Probabilistic Engineering Mechanics*, 18(1):61 – 77, 2003.
- [9] Esben Orlowitz and Anders Brandt. Influence of correlation estimation methods on damping estimates. *5th International Operational Modal Analysis Conference, Guimarães, Portugal*, page 6, 2013.
- [10] Marius Tarpø, Tobias Friis, Peter Olsen, Martin Juul, Christos Georgakis, and Rune Brincker. Automated reduction of statistical errors in the estimated correlation function matrix for operational modal analysis. *Mechanical Systems and Signal Processing*, 132:790 – 805, 2019.
- [11] Etienne Cheynet, Jasna Bogunović Jakobsen, and Jonas Snæbjörnsson. Damping estimation of large wind-sensitive structures. *Procedia Engineering*, 199:2047 – 2053, 2017. X International Conference on Structural Dynamics, EURODYN 2017.
- [12] Siu-Kui Au. Uncertainty law in ambient modal identification—part ii: Implication and field verification. *Mechanical Systems and Signal Processing*, 48(1):34 – 48, 2014.
- [13] ANSI S2.47. *Vibration of buildings—guidelines for the measurement of vibrations and evaluation of their effects on buildings*. Standard, Acoustical Society of America, January 1991.
- [14] R. Cantieni. Experimental methods used in system identification of civil engineering structures. *Proceedings of Workshop Problemi di vibrazioni nelle strutture civili e nelle costruzioni meccaniche*, 2004.
- [15] R. Pintelon, P. Guillaume, and J. Schoukens. Uncertainty calculation in (operational) modal analysis. *Mechanical Systems and Signal Processing*, 21(6):2359 – 2373, 2007.
- [16] Edwin Reynders, Kristof Maes, Geert Lombaert, and Guido De Roeck. Uncertainty quantification in operational modal analysis with stochastic subspace identification: Validation and applications. *Mechanical Systems and Signal Processing*, 66-67:13 – 30, 2016.

- [17] Siu-Kui Au. Uncertainty law in ambient modal identification—part i: Theory. *Mechanical Systems and Signal Processing*, 48(1):15 – 33, 2014.
- [18] Esben Orlovitz and Anders Brandt. Influence of noise in correlation function estimates for operational modal analysis. *Topics in Modal Analysis & Testing, Proceedings of the 36th IMAC*, 9:55–64, 2019.
- [19] R. W. Clough and J. Penzien. *Dynamics of Structures*. CSI Computers & Structures, Inc., Berkeley, Calif., USA, 2nd revised edition, 2003.
- [20] R. G. Lyons. *Understanding Digital Signal Processing*. Prentice Hall, Upper Saddle River, N.J., USA, 3rd. edition, 2011.
- [21] Kevin P. Murphy. *Machine Learning: A Probabilistic Perspective*. MIT Press, Cambridge, Mass., USA, 2012.
- [22] S. O. Rice. Mathematical analysis of random noise. *Bell System Technical Journal*, 24(1):46–156, 1945.
- [23] Santiago Aja-Fernández and Gonzalo Vegas-Sánchez-Ferrero. *Statistical Analysis of Noise in MRI - Appendix A*. Springer International Publishing, Cham, Schweiz, 2016.
- [24] N. N. Lebedev. *Special Functions & Their Applications*. Dover Publications, Mineola, NY, USA, 1972.
- [25] Hákon Gudbjartsson and Samuel Patz. The rician distribution of noisy mri data. *Magnetic Resonance in Medicine*, 34(6):910–914.
- [26] Rita Greco, Giuseppe Carlo Marano, Alessandra Fiore, and Ivo Vanzi. Nonstationary first threshold crossing reliability for linear system excited by modulated gaussian process. *Shock and Vibration*, 2018:17, 2018.
- [27] S. O. Rice. Statistical properties of a sine wave plus random noise. *The Bell System Technical Journal*, 27(1):109–157, Jan 1948.
- [28] J. Rainal. Axis-crossings of the phase of the sine wave plus noise. *The Bell System Technical Journal*, pages 737 – 754, 1967.
- [29] S. Cobb. The distribution of intervals between zero crossings of sine wave plus random noise and allied topics. *IEEE Transactions on Information Theory*, 11(2):220–233, April 1965.
- [30] Afshin Firouzi, Wei Yang, and Chun-Qing Li. Efficient solution for calculation of upcrossing rate of nonstationary gaussian process. *Journal of Engineering Mechanics*, 144(4):04018015, 2018.
- [31] M.B. Priestley. *Spectral Analysis and Time Series*. Academic Press Inc., Fift Avenue, New York, NY, USA, 1982.
- [32] S. R. Ibrahim and E. C. Mikulcik. A method for the direct identification of vibration parameters from the free response. *The Shock and Vibration Inform. Ctr. Shock and Vibration Bull.*, pages 183–198, 1977.

Chapter 5

Paper 2 - Automated reduction of statistical errors in the estimated correlation function matrix for operational modal analysis

“

Stability can only be attained by inactive matter

”

Marie Curie

Status

- Published in Mechanical System and Signal Processing
- Available here: <https://doi.org/10.1016/j.ymssp.2019.07.024>

5.1 Introduction

In the previous chapter, we established the theory of statistical errors in the estimated correlation function matrix. Next, we want to reduce these errors in an identification process of the modal parameters in operational modal analysis. In this way, we could update and reduce the modelling errors in the system model used in stress/strain estimation.

In this paper, we proposed a new algorithm for the reduction of the noise tail and the statistical errors so it reduces the biased part of the correlation function matrix.

5.2 Contribution

The author had the idea to reduce statistical errors by modifying the envelope for the modal auto-correlation functions. The idea of finding the noise tail by fitting two lines to the correlation function was proposed by cosupervisor Rune Brincker. The author performed the data analyses and wrote the paper.

5.3 Main findings

The proposed algorithm increased stability and reduced the biased error in the identification process of modal parameters in operational modal analysis.

5.4 Reflection

To the best of this author's knowledge, this algorithm is the first attempt to reduce statistical errors in the operational modal analysis community. It reduced biased errors - primarily on the damping estimation - and it increased stability in the identification process. This inspires more confidence in an estimation of the modal parameter, which will be used to calibrate and update a system model for stress/strain estimation. Thus, the research results in a better basis for updating the system model for stress/strain estimation.

Automated reduction of statistical errors in the estimated correlation function matrix for operational modal analysis

Marius Tarpø^a, Tobias Friis^b, Peter Olsen^a, Martin Juul^c, Christos Georgakis^a, Rune Brincker^b

^aAarhus University, Department of Engineering, Inge Lehmanns Gade 10, Aarhus, Denmark

^bTechnical University of Denmark, Department of Civil Engineering, Brovej B.118, Kgs. Lyngby, Denmark

^cBrincker & Georgakis, Inge Lehmanns Gade 10, Aarhus, Denmark

Abstract

In operational modal analysis, the correlation function matrix is treated as multiple free decays from which system parameters are extracted. The finite time length of the measured system response, however, introduces statistical errors into the estimated correlation function matrix. These errors cause both random and bias errors that transfer to an identification process of the modal parameters. The bias error is located on the envelope of the modal correlation functions, thus violating the assumption that the correlation function matrix contains multiple free decays. Therefore, the bias error transmits to the damping estimates in operational modal analysis. In this paper, we show an automated algorithm that reduces the bias error caused by the statistical errors. This algorithm identifies erratic behaviour in the tail region of the modal correlation function and reduces this noise tail. The algorithm is tested on a simulation case and experimental data of the Heritage Court Building, Canada. Based on these studies, the algorithm reduces bias error and uncertainty on the damping estimates and increases stability in the identification process.

Keywords: Operational modal analysis, correlation function matrix, uncertainty, bias reduction, estimation error

5.6 Introduction

In operational modal analysis, we use the random vibrations of a linear and time-invariant system, excited by white Gaussian noise, to extract modal parameters. The correlation-driven operational modal analysis uses a two-stage time domain modal identification process [1]. The first step is the calculation of the correlation function matrix by the random vibrations of the system. In the second step, we treat the correlation function matrix as free decays of the system [2, 3] from which we estimate the modal parameters. Unfortunately, exact properties of any random data are inaccessible from sampled data with a finite length thus we must estimate them instead. In operational modal analysis, the finite length of the time series forces us to estimate the correlation function matrix and this introduces statistical errors [4]. The statistical errors are system dependent and they cause the estimated correlation function matrix to become a stochastic process that depends on the modal parameters and the time length. These statistical errors create random errors in the correlation functions [5–8] that increase with the number of time lags.

Recently, it was shown for operational modal analysis that the envelope of the correlation function is Rice distributed [5]. Therefore, the envelope becomes increasingly biased as the random error increases in the estimated correlation function. This bias error results in erratic behaviour in the tail region of the estimated correlation function - referred to as the noise tail - for each mode in the system, see Fig. 5.1. The error depends on the frequency-damping product, the excitation level, and the time length of the measurement. Since the envelope is biased in the noise tail, this introduces bias errors in the modal parameters from an identification process. The bias error is pronounced for the estimated damping ratio since it is located at the envelope. The zero crossings of the correlation function is, however, unbiased [5].

We should exclude the noise tails from an estimation of modal parameters to reduce the bias error in operational modal analysis. Each mode, however, has an individual position of the noise tail [5, 9, 10] and this complicates the matter of choosing a sufficient length of the correlation function matrix when estimating the modal parameters. For instance, modes with a high frequency-damping product need a smaller part of the estimated correlation function than modes with a lower frequency-damping product to obtain a valid estimation [11]. Truncation, however, might lead to erroneous results if the correlation

function has insufficient information about one of the modes for an estimation of the modal parameters [11].

In the literature, there are various methods for dealing with random noise on the system response. We can use singular value decomposition or principle component analysis for subspace reduction to remove noise perpendicular to the reduced subspace [12–14]. Research, however, indicates that a substantial part of the statistical error is located in the subspace of the physical signals [5, 10]. Furthermore, we can remove the first part of the correlation function matrix to reduce the additive and uncorrelated noise [15]. The statistical errors in the correlation function matrix, however, are different than other types of random noise since it increases with time lags [6, 7]. The use of exponential windows or other tapering windows, traditionally used to reduce leakage [16], could be applied to the correlation function matrix to reduce the noise tails [1]. Each mode, however, has a unique noise tail and this complicates the matter of choosing a suitable window (similar to a truncation of the correlation function matrix). Therefore, an exponential window might remove the noise tails from some modes while it tampers the physical response of others and loses information of these modes.

This article presents an algorithm for an automatic reduction of statistical errors in the estimated correlation function matrix while decreasing the chance of an erroneous truncation. This reduction of statistical errors assumes that we can manipulate the noise tail since its envelope is purely made of errors. We change the envelope in the noise tail to mimic that of the physical correlation function by using a least square fit of a negative exponential. The disadvantage of this algorithm is that the system must be overdetermined. So we need fewer modes than measured channels with the system response. We can, however, bypass this problem by applying filtering techniques to the response so the contribution of modes outside the filter is reduced. The algorithm reduces the bias on damping estimates and increases stability and reliability in the identification process of modal parameters.

5.7 Theory

5.7.1 Correlation Function Matrix

In operational modal analysis, we use ambient vibrations for modal analysis by measuring the spatial limited system response, $\mathbf{y}(t)$. We assume that stationary white Gaussian noise excites a linear and time-invariant system [1]. When these assumptions are fulfilled, we can treat the correlation function matrix, $\mathbf{R}_y(\tau)$, as multiple free decays of the system [2, 3].

$$\mathbf{R}_y(\tau) = \mathbf{E} [\mathbf{y}(t)\mathbf{y}^\top(t + \tau)] \quad (5.1)$$

where \mathbf{E} denotes the expectation operator.

Brincker [3] has calculated the analytic expression for the correlation, here written for positive time lags, τ .

$$\mathbf{R}_{y+}(\tau) = 2\pi \sum_{i=1}^N \left(\boldsymbol{\gamma}_i \boldsymbol{\Phi}_i^\top e^{\lambda_i \tau} + \boldsymbol{\gamma}_i^* \boldsymbol{\Phi}_i^H e^{\lambda_i^* \tau} \right) \quad (5.2)$$

where λ_i is the modal pole, $\boldsymbol{\gamma}_i$ is the modal participation vector, and $\boldsymbol{\Phi}_i$ is the mode shape for i^{th} mode.

If we apply the modal decomposition on the correlation function matrix and assume uncorrelated modal coordinates, we can decorrelate it into a diagonal matrix [1] where each diagonal component is a free decay of a single-degree-of-freedom (SDOF) system. The modal decomposition states that the response from a linear system is a linear combination of mode shapes and modal coordinates.

$$\mathbf{y}(t) = \boldsymbol{\Phi} \mathbf{q}(t) \quad (5.3)$$

where $\boldsymbol{\Phi}$ is the mode shape matrix and $\mathbf{q}(t)$ is a vector containing the modal coordinates for all modes. We insert Eq. (5.3) into Eq. (5.1).

$$\mathbf{R}_y(\tau) = \boldsymbol{\Phi} \mathbf{R}_q(\tau) \boldsymbol{\Phi}^\top \quad (5.4)$$

where $\mathbf{R}_q(\tau)$ is the modal correlation function matrix, which is based on the modal coordinates. In the case of uncorrelated modal coordinates, the modal correlation function matrix is a diagonal matrix where modal auto-correlation functions are equivalent to a free decay of a SDOF system of the given mode.

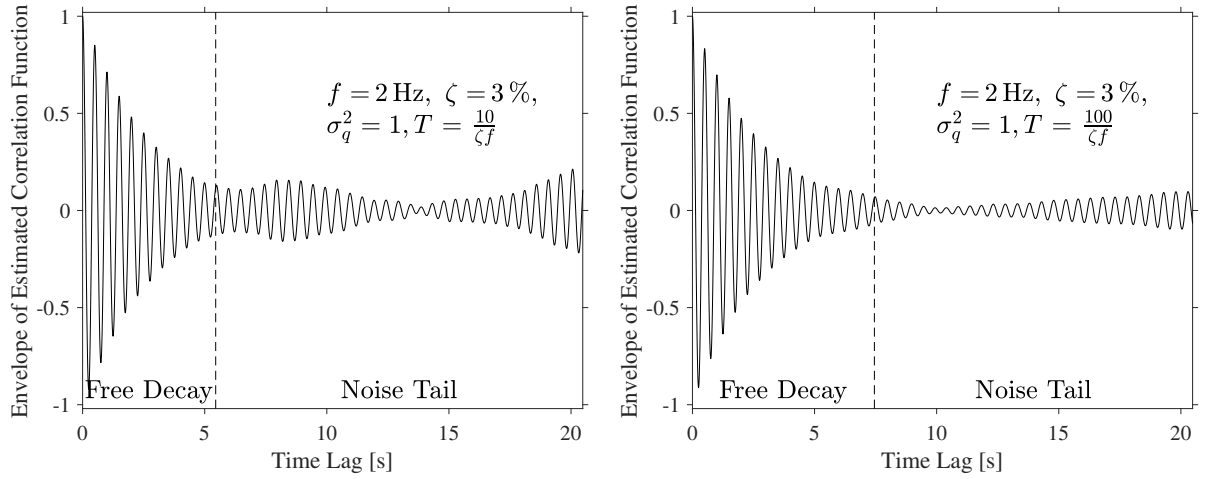


Figure 5.1: Correlogram with random iteration of the estimated correlation function for two different time lengths and the approximated beginning of the noise tail

5.7.2 Estimated Correlation Function Matrix

When we have to calculate the correlation function matrix from measured data, we use *time averaging* instead of *ensemble averaging* since the system response is ergodic. The length of the signal must, however, tend towards infinity for this to be true [4].

$$\mathbf{R}_y(\tau) = \lim_{T \rightarrow \infty} \frac{1}{T} \int_0^T \mathbf{y}(t) \mathbf{y}^\top(t + \tau) dt \quad (5.5)$$

where T is the total time length of the measured system response and \top denotes the transpose.

In reality, however, we measure the system response with a sample time step, Δt , and a finite length of each data set. Therefore we have to estimate the discrete correlation function matrix from a finite sample size, which introduces statistical errors [4].

$$\tilde{\mathbf{R}}_y(k) = \frac{1}{N-k} \sum_{n=0}^{N-k} \mathbf{y}(n) \mathbf{y}^\top(n+k), \quad 0 \leq k < N \quad (5.6)$$

where $\tilde{\mathbf{R}}_y(k)$ is the estimated correlation function matrix, N is the total number of samples, $T = N\Delta t$, k is the discrete time lag, $\tau = k\Delta t$, and Δt is the sampling interval.

This estimated correlation function matrix is a random variable with an expected value equal to the analytic correlation function matrix and a variance caused by the statistical errors which are additive Gaussian noise [4, 5]. Since the finite time length of the recorded signal causes the statistical errors, the variance decreases when the time length increases [5–7]. Furthermore, the estimated correlation function matrix at different time lags is statistically dependent since we calculate the entire function matrix from the same sample. Thus, the statistical errors have cross-correlation.

For simplicity, let us assume that the statistical errors on the mode shapes are small and neglectable compared to the errors on the frequencies and damping ratios of the system. This enables us to decorrelate the statistical errors into individual statistical errors on the modal auto-correlation functions by the use of Eq. (5.4).

$$\tilde{\mathbf{R}}_{q_i}(k) = \boldsymbol{\Phi}_i^\dagger \tilde{\mathbf{R}}_y(k) \left(\boldsymbol{\Phi}_i^\dagger \right)^\top \quad (5.7)$$

where † denotes the pseudo inverse and $\tilde{\mathbf{R}}_{q_i}(k)$ is the estimated modal correlation function.

Now, the variance on each modal auto-correlation function expresses the statistical errors that depend on the modal properties of the system, the excitation, and the duration of the system response [5, 7].

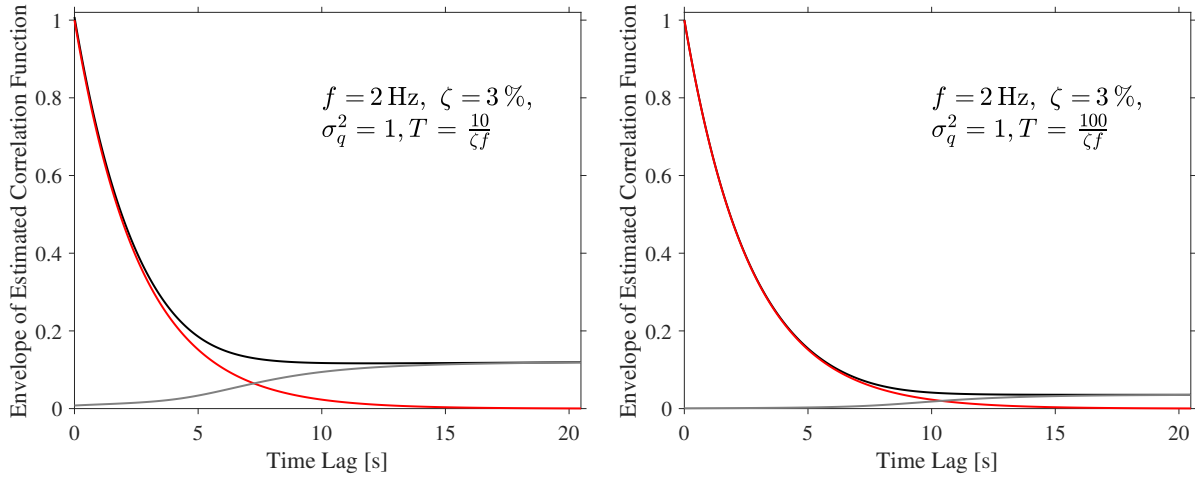


Figure 5.2: The expected value of the envelope of the estimated correlation function (black), the envelope of the correlation function, Eq. (5.2), (black), and the difference between them (the bias error) (grey) for two different time lengths

5.7.3 Noise Tail

As previously mentioned, the statistical errors create erratic behaviour in the tail region of the estimated correlation function matrix - known as the noise tail - as illustrated in Fig. 5.1. This happens when the statistical errors dominate the correlation function [5, 7, 9, 10]. Tarpø et al. [5] showed that the envelope of the estimated modal correlation function is Rice distributed and therefore biased in the tail region, see Fig. 5.2. The discrete expected value of the envelope follows this expression

$$env_i(k) = \sqrt{\frac{\pi}{2}} \sigma_{q_i}^2 \sqrt{\frac{1 + e^{-2\omega_i \zeta_i k \Delta t} (2\omega_i \zeta_i k \Delta t + 1)}{2(N - k) \Delta t \omega_i \zeta_i}} L_{1/2} \left(\frac{(k - N) \Delta t \omega_i \zeta_i}{e^{2\omega_i \zeta_i k \Delta t} + 2\omega_i \zeta_i k \Delta t + 1} \right) \quad (5.8)$$

where $L_{1/2}(\cdot)$ is the Laguerre polynomial for case $\frac{1}{2}$, $\sigma_{q_i}^2$ is the variance of the modal coordinates, ω_i is the natural frequency, and ζ_i is the damping ratio for the i^{th} mode. Fig. 5.2 illustrates the expected envelope of the estimated correlation function, the envelope of the analytic correlation function, and the bias error caused by the statistical errors [5].

Fig. 5.3 shows a random realisation of an estimated correlation function for two different time lengths. The envelope of an analytic free decay is plotted along with the expected value of the envelope from Eq. (5.8). The frequency of the oscillations from the correlation functions is consistent, at least to the eye, in Fig. 5.3 whereas the envelope is obviously biased in the tail region. Therefore, the envelope of an estimated correlation function indicates the level of statistical errors since it diverts from a negative exponential function as the errors increase.

The expected envelope has an increasing bias error as the time lag of the correlation function increases. When the statistical errors are small, the expected envelope is an approximated exponential decay. As the statistical errors start to dominate, the envelope becomes constant and this creates the noise tail - thus violating the assumption that the correlation function matrix consists of free decays. Therefore, it is essential that we reduce the statistical errors in operational modal analysis.

Since statistical errors affect each mode in the correlation function, it creates a noise tail for each mode in the estimated correlation function matrix. As seen in Eq. (5.8), the expected value of the modal envelope will be different for each mode. Therefore, the individual noise tails start at different positions for each mode. This poses a problem when we have to choose the number of time lags to utilise from the correlation function matrix. If we use a small part of the correlation function matrix to remove noise tail for one mode, it might truncate another mode and cause an erroneous identification of that given mode. This problem is further discussed in [11].

5.8 Algorithm

In this section, we will introduce a novel algorithm to minimise the bias error caused by the statistical errors without truncating the correlation function matrix. The algorithm decorrelates the correlation

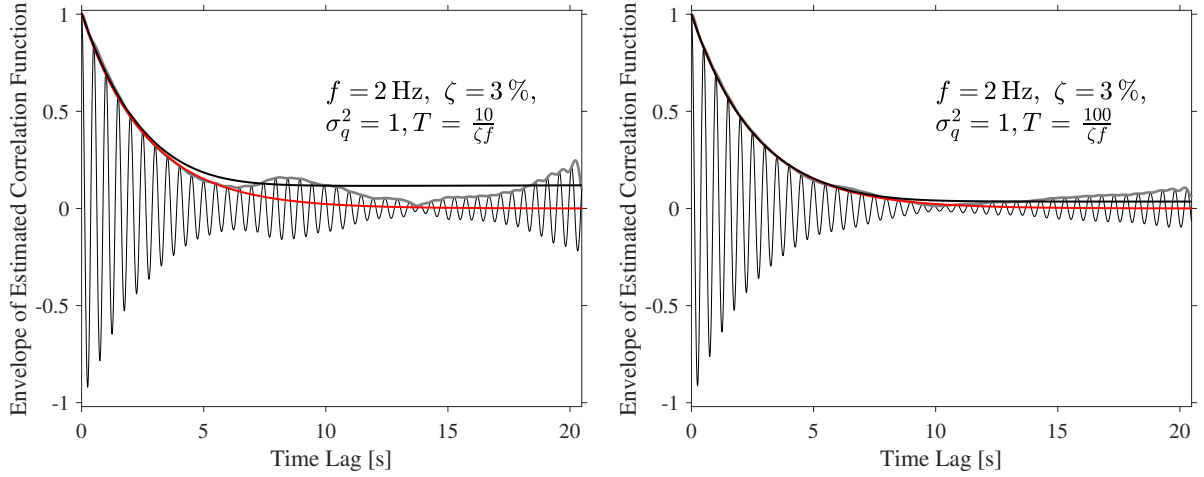


Figure 5.3: Correlogram with random iteration of the estimated correlation function with the expected value of the envelope (black), the estimated envelope (grey), and the envelope of the correlation function, Eq. (5.2), (black) for two different time lengths

function matrix, detects the noise tails, and modifies the envelopes of the decorrelated correlation functions in these regions.

5.8.1 Modal Decorrelation of Correlation Function Matrix

We want to decorrelate the estimated correlation function matrix into an approximated modal correlation function matrix as in Eq. (5.7). This decorrelation is called a similarity transformation. When the transformation matrix contains the eigenvectors as column vectors, the similarity transformation diagonalise the estimated correlation function matrix.

We could use any identification process to identify mode shapes and apply these to decorrelate and equalise the energy in the estimated correlation function matrix. Thus, the algorithm is applicable on previously identified modal parameters to reduce uncertainty of these since we can apply the identified mode shapes in the modal decorrelation of the estimated correlation function matrix. In this article, we automatically estimate the mode shapes using a condensation technique by Olsen et al. [12] combined with a similar identification process as Vold et al. [17] using auto-regression models and a poly reference technique, see Sec. Appendix 5.A.

When we have a transformation matrix, $\tilde{\Phi}$, containing a set of identified mode shape, we decorrelate the estimated correlation function matrix into an approximated modal correlation function matrix, which we will call the decorrelated correlation function matrix.

$$\hat{\mathbf{R}}_q(\tau) = \tilde{\Phi}^\dagger \tilde{\mathbf{R}}_y(\tau) (\tilde{\Phi}^\dagger)^\top \quad (5.9)$$

On the diagonals of this matrix, the correlation functions are decorrelated to auto-correlation functions, which corresponds to free decays of SDOF systems. Since this is an approximated decorrelation, the decorrelated correlation function matrix is a non-diagonal matrix.

5.8.2 Envelope Detection

In Signal Processing we can use the Hilbert transformation as envelope detection [18]. For this algorithm, we want to find the envelopes of the diagonal components of the decorrelated correlation function, Eq. (5.9). These diagonal components, $\hat{R}_{q_i}(k)$, are auto-correlation functions and they each form an approximated free decay of a SDOF system.

When we apply the Hilbert transformation, we obtain a phase shifted signal, $\mathcal{H}[\hat{R}_{q_i}(k)]$. We estimate the envelope of each decorrelated auto-correlation functions using the absolute value of the analytic signal [18].

$$e_i(k) = \sqrt{\hat{R}_{q_i}(k)^2 + \mathcal{H}[\hat{R}_{q_i}(k)]^2} \quad (5.10)$$

where \mathcal{H} denotes the Hilbert transformation. Fig. 5.3 shows two examples of the Hilbert envelope of a decorrelated correlation function. The decorrelated auto-correlation functions are aperiodic functions since they have a discontinuity in the ends due to the noise tail. Therefore, oscillations often exist in the Hilbert envelope at the end of the correlation functions, see Fig. 5.3. These (Gibbs) oscillations must be positioned in the noise tail since they scramble the detection of the real noise tail.

5.8.3 Identifying the location of the Noise Tail

The envelope of the estimated correlation function is a stochastic process that follows a Rice distribution [5]. The analytic expression for the expected envelope is a Laguerre polynomial, Eq. (5.8), and each realization of the stochastic process varies slightly. Generally, the physical part of a modal correlation function resembles an exponential decay while the noise tail has an almost constant envelope with fluctuations. Thus, the logarithmic envelope of the physical part is similar to a straight declining line and the noise tail is the divergence that produces a near constant envelope. This, however, is an approximation since the shift from the physical part to the noise tail is gradual due to the Laguerre polynomial.

We use the updated algorithm of Tarpø et al. [9] to find the position of the noise tail. It fits two lines to the estimated envelope where the transition between the two lines is a variable. The combined model has four parameters for each transition between the two lines, and the best fit of all the possible transitions indicates the beginning of the noise tail. Since the expected envelope is described by a Laguerre polynomial, this combined model is a simplification that locates the noise tail as the statistical error dominates completely.

Firstly, we divide the estimated envelope for a decorrelated auto-correlation function into two vectors for each line as a function of the transition, n .

$$\begin{aligned} \mathbf{m}_1(n) &= \log ([e_i(1) \ e_i(2) \ \dots \ e_i(n)])^\top \\ \mathbf{m}_2(n) &= \log ([e_i(n+1) \ e_i(n+2) \ \dots \ e_i(N)])^\top \end{aligned} \quad (5.11)$$

We use linear regression to fit the two lines to the logarithmic envelope.

$$\mathbf{m}_i(n) = \mathbf{X}_i(n)\mathbf{a}_i(n) \quad (5.12)$$

We set up design matrices, $\mathbf{X}_i(n)$, between the two lines.

$$\mathbf{X}_1(n) = \begin{bmatrix} 1 & 2 & 3 & \dots & n \\ 1 & 1 & 1 & \dots & 1 \end{bmatrix}^\top \quad (5.13)$$

$$\mathbf{X}_2(n) = \begin{bmatrix} n+1 & n+2 & n+3 & \dots & N \\ 1 & 1 & 1 & \dots & 1 \end{bmatrix}^\top \quad (5.14)$$

We find the regression parameters by Least Squares [19]:

$$\hat{\mathbf{a}}_i(n) = \mathbf{X}_i^\dagger(n)\mathbf{m}_i(n) \quad (5.15)$$

So we have the best fit for both lines.

$$\hat{\mathbf{m}}_i(n) = \mathbf{X}_i(n)\hat{\mathbf{a}}_i(n) \quad (5.16)$$

We compile the two estimated lines into one vector.

$$\hat{\mathbf{e}}(n) = \exp \left(\begin{bmatrix} \hat{\mathbf{m}}_1(n) \\ \hat{\mathbf{m}}_2(n) \end{bmatrix} \right) \quad (5.17)$$

We use the Coefficient of Determination [20] for each iteration of n as a quality quantification.

$$r^2(n) = 1 - \frac{\sum_{k=1}^N (e_i(k) - \hat{e}_i(k))^2}{\sum_{k=1}^N (e_i(k) - \mathbb{E}[\mathbf{e}])^2} \quad (5.18)$$

We repeat this process for all possible values of n . The highest value of the Coefficient of Determination indicates the best fit and thereby the start of the noise tail, n_0 .

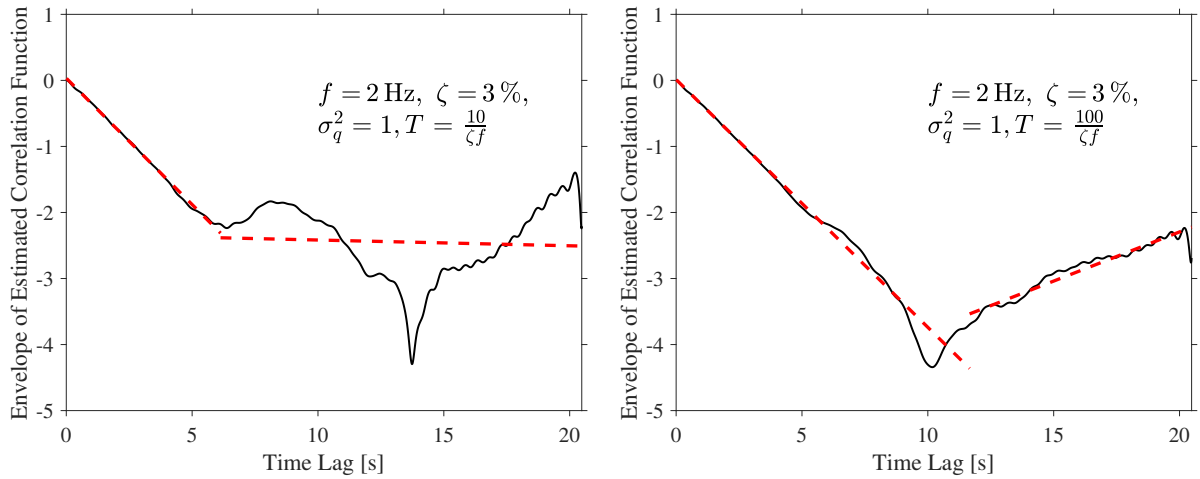


Figure 5.4: Best fit on the analytic mean value of the envelope, the estimated Hilbert envelope of the correlation functions from Fig. 5.3 (black line) and the two fitted models (red) for two different time lengths

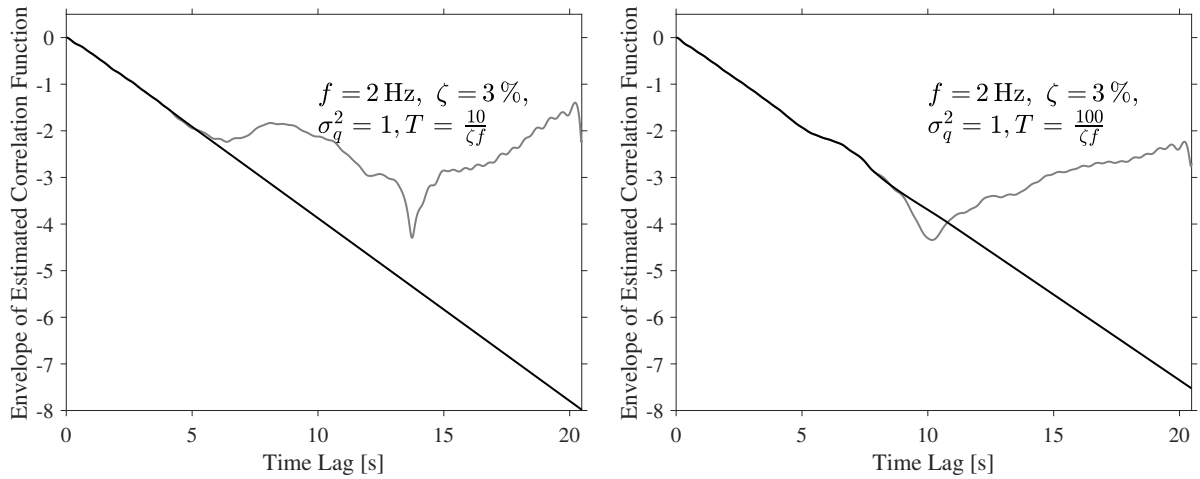


Figure 5.5: Modified Hilbert envelope (black) and the estimated Hilbert envelope (grey) of the correlation functions from Fig. 5.3 in logarithmic scale for two different time lengths

$$r^2(n_0) = \max(r^2(1), r^2(2), r^2(3), \dots, r^2(N)) \quad (5.19)$$

Fig. 5.4 illustrates the best fit of these two models on two different estimated correlation functions based on system responses with different time lengths. Although the piecewise linear fit seems insufficient as a fit of the logarithmic envelope (especially in the noise tail region), it approximates the point of transition into the noise tail well.

Since we estimate the location of the noise tail where the statistical errors dominate, then we have substantial bias error in the part right before the estimated noise tail. In order to reduce this bias error, we say the physical part is located before the noise tail with a transition area between the two. The authors obtained good results with the following expression for the end of the physical part: $n_1 = 0.8n_0$.

5.8.4 Modification of the Noise Tail

We use the envelope of the identified physical part of the correlation functions to modify the envelope of the noise tail. The regression gave the parameters of the line corresponding to the best fit of the physical envelope and we extend this regression line to the envelope of the noise tail by modifying the original envelope. We have two parameters for the line in the physical part, $\hat{\mathbf{a}}_1(n_1)$. We extend the best fit of the free decay into the noise tail. Thereby, we obtain a modified envelope where we only change the envelope of the noise tail based on the best fit of the physical part of the envelope.

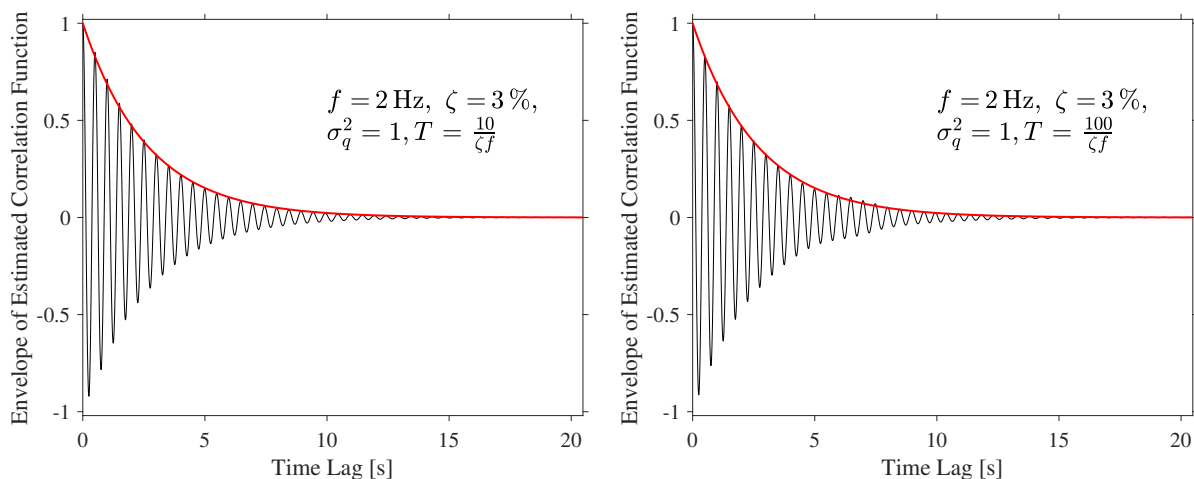


Figure 5.6: Correlogram with the modified estimated correlation function (black) based on the correlation functions from Fig. 5.3 with the analytic envelope of a free decay corresponding to the modal parameters (black) for two different time lengths

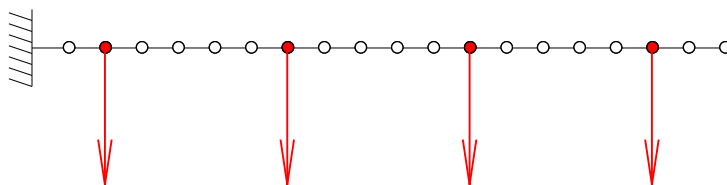


Figure 5.7: Case 1 - Simulated system: Illustration of the cantilever beam used in the simulation study and the position of the sensors (black)

$$\tilde{\mathbf{e}} = \begin{bmatrix} [e_i(1) \ e_i(2) \ \dots \ e_i(n_1)]^\top \\ \exp(\mathbf{X}_2(n_1)\hat{\mathbf{a}}_1(n_1)) \end{bmatrix} \quad (5.20)$$

The transition between the two combined envelopes often has abrupt changes that need to be smoothen since they disrupt the identification process of the modal parameters. We define a transition region, $n_1 \pm \frac{n_1}{6}$, and we apply a monotone piecewise cubic interpolation [21] to replace this region by an interpolation using the rest of the modified envelope, $\tilde{\mathbf{e}}$.

Fig. 5.5 shows two examples of a modified envelope for a decorrelated correlation function based on different time lengths. The modified envelope is identical to the original envelope for discrete time lags below n_1 .

We substitute this modified envelope with the original envelope for each diagonal component in the decorrelated correlation function matrix.

$$\hat{R}_{q_i}^*(k) = \widehat{R}_{q_i}(k) \frac{\tilde{\mathbf{e}}(k)}{\mathbf{e}(k)} \quad (5.21)$$

Finally, we truncate $\hat{R}_{q_i}^*(k)$ so it excludes time lags higher than the detected noise tails. In other words, the noise tail located at the highest time lag determines the truncation. Then we can use this modified correlation function matrix in an identification process. Fig. 5.6 illustrates the modification of a correlation function.

5.9 Case Studies

5.9.1 Case 1 - Simulated Cantilever Beam

We simulate the response of a cantilever beam in 2D, made with 20 Euler-Bernoulli Beam elements, using the Fourier transformed superposition method with all modes implemented in the OMA-toolbox

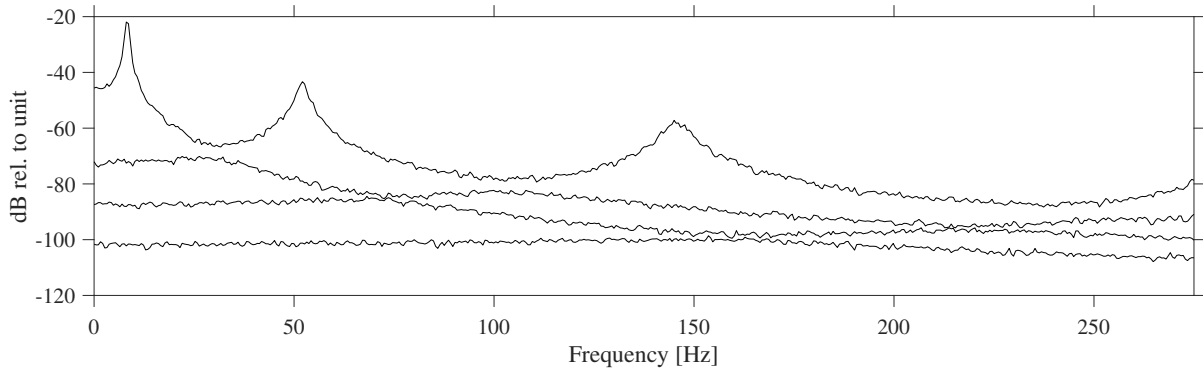


Figure 5.8: Case 1 - Simulated system: Singular values of the spectral density matrix of a random iteration of the Monte Carlo simulation using the Welch technique with 50% overlap

from [1]. To mimic the spatial limited response measured by sensors, we extract the responses of four translational degrees-of-freedom, corresponding to four sensors, see Fig. 5.7. Since we are interested in the first three modes of the system, see Tab. 5.1, we use a sampling frequency of 550 Hz and a time length of 60 seconds, using the recommended time length from [1]. We run 10,000 simulations of the system response excited by white Gaussian noise in all degrees-of-freedom and we calculate the correlation function matrix for each iteration using Eq. (5.6). The singular values of the spectral density matrix are plotted in Fig. 5.8 for a random simulation.

To estimate the modal parameters from an estimated correlation function matrix, we use the Time Domain Poly-reference [17], the Ibrahim Time Domain [22], and the Eigensystem Realization Algorithm [13] from the OMA-toolbox in [1] with two different model orders. For each simulation, we estimate the modal parameters from the original correlation function matrix. We apply the algorithm to reduce the statistical errors of the correlation function matrix automatically and we estimate a new set of modal parameters. Then we choose the estimated modes with modal parameters closest to the three real modes.

The number of included time lags of the correlation function matrix is important for the estimation of modal parameters since the statistical errors increase with increasing number of time lags. These errors create increasing random errors on the estimated correlation functions and increasing bias errors on the estimated envelope [5]. Therefore, the number of time lags is important in an analysis of this algorithm. This complicates the comparison of the normal identification procedure and identification based on this algorithm. So, we test different lengths of the correlation function matrix but we choose 513 discrete time lags (1.03 s) to illustrate the algorithm in the figures.

Table 5.1: Case 1 - Simulated system: Modal parameters of the system

| | Mode 1 | Mode 2 | Mode 3 |
|-------------------|--------|--------|--------|
| Frequency [Hz] | 8.32 | 52.1 | 145.9 |
| Damping Ratio [%] | 2 | 2 | 2 |

Results and discussion

Figs. 5.9 and 5.10 display the estimated modal parameters from the original and the modified correlation function matrix for two different model orders. For the original correlation function matrices, large bias errors and skewness exist in the distribution of modal parameters for all identification techniques with a model order of two. By increasing the model order to three, the estimates of the third mode become approximately Gaussian distributed and the bias error decreases. For the modified correlation function matrix, the distribution is consistently approximately Gaussian and the bias error of the damping estimates is lower regardless of the model order.

The different identification techniques have diverse bias and random errors for the third mode, indicating that the noise tail influences the techniques differently when the model order is low. By increasing the model order, we decrease the skewness of the estimates. So an identification technique with a higher model order is better able to fit with a weakly-excited mode with a large noise tail. All the techniques, however, provide similar results with a low model order when we use the algorithm to reduce the noise

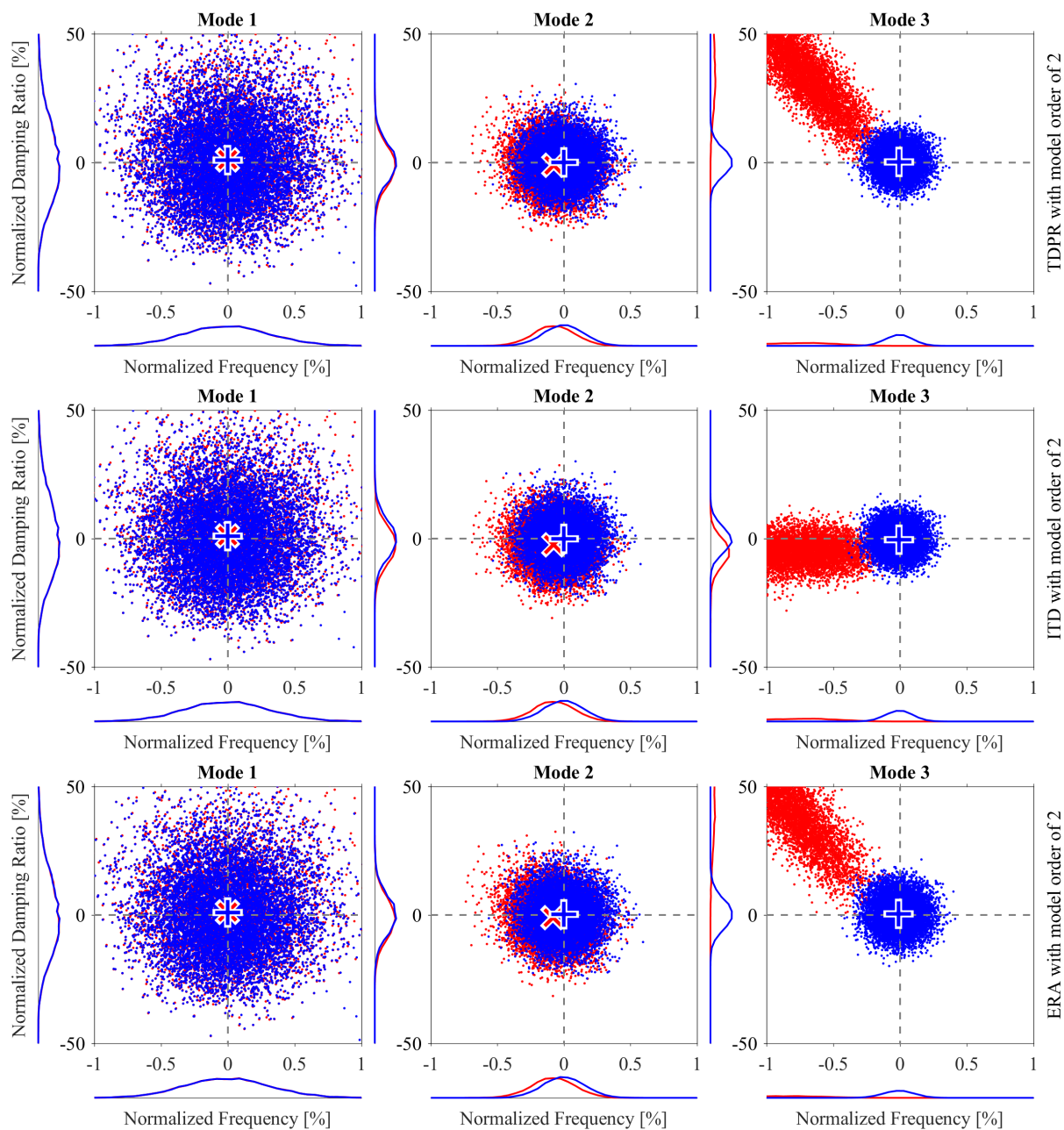


Figure 5.9: Case 1 - Simulated system with 10,000 simulations: Identification of modal parameters from the first 513 time lags from the original correlation function matrix (red) with sample mean (red "x"), and the modified correlation function matrix (blue) with sample mean (blue "+") using Time Domain Poly-reference (TDPR), Ibrahim Time Domain (ITD), and the Eigensystem Realization Algorithm (ERA) for a model order of 2

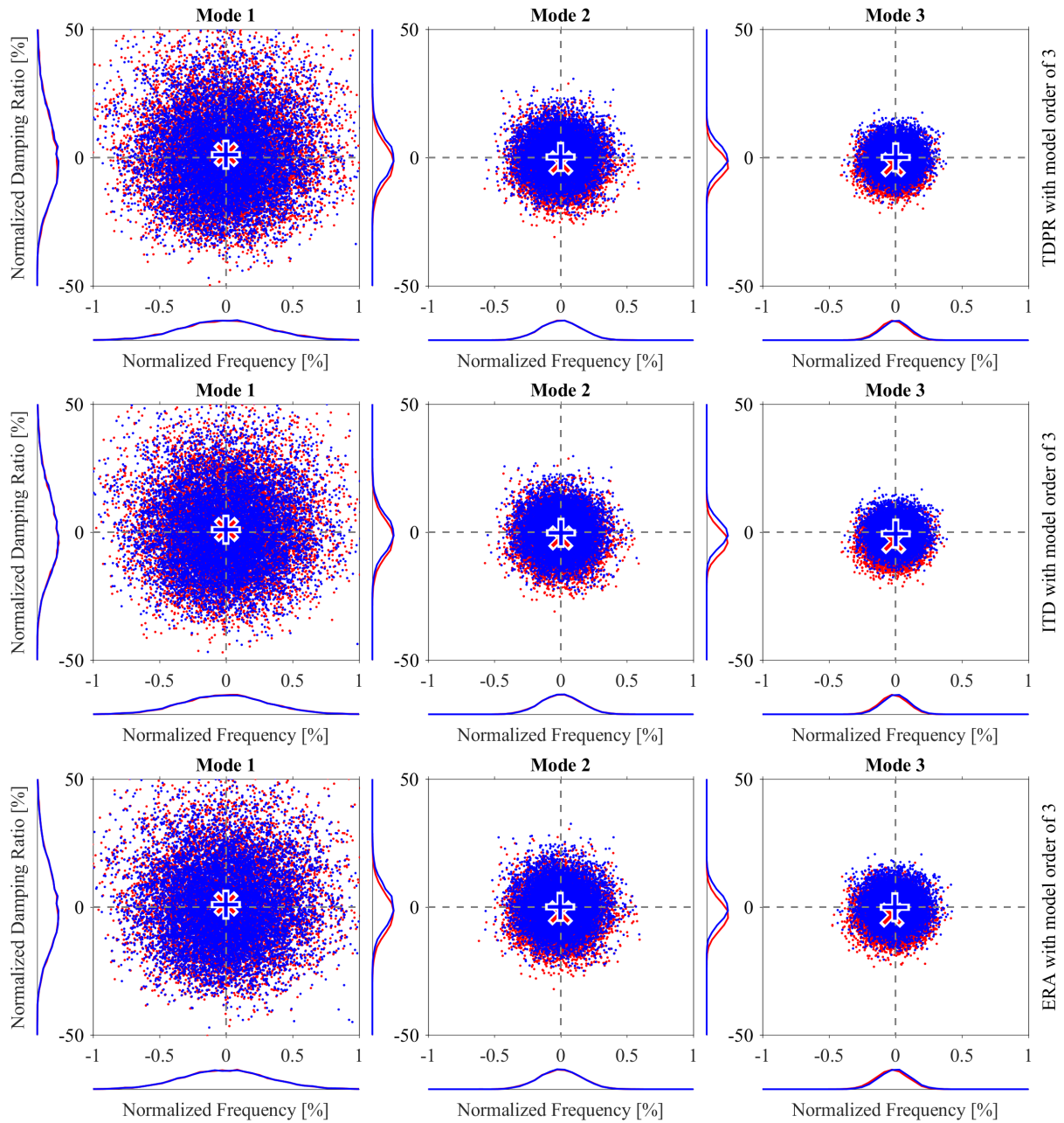


Figure 5.10: Case 1 - Simulated system with 10,000 simulations: Identification of modal parameters from the first 513 time lags from the original correlation function matrix (*red "x"*), and the modified correlation function matrix (*blue "+"*) using Time Domain Poly-reference (TDPR), Ibrahim Time Domain (ITD), and the Eigensystem Realization Algorithm (ERA) for a model order of 3

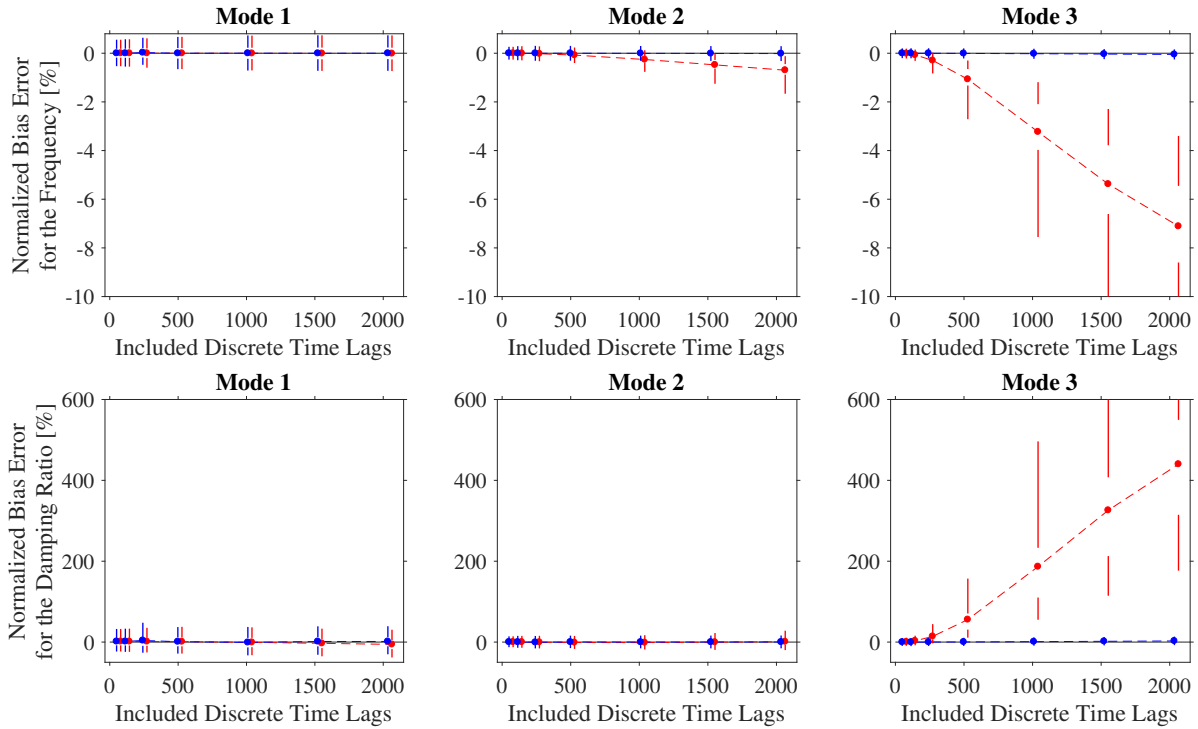


Figure 5.11: Case 1 - Simulated system with 10,000 simulations: (Tuftex) box-plot of the estimated modal parameters using Time Domain Poly-reference a with model order of two [17] for a varying number of included time lags. Estimates based on the original (black) and the modified correlation function matrix (blue). In the (Tuftex) box-plot, the dots mark sample means and the vertical lines mark the 2nd, 25th, 75th, and 98th percentiles.

tail. Furthermore, an identification technique with low model order has lower bias error using the modified correlation function matrix than a technique with a slightly higher model order using the original correlation function. So the algorithm creates stability in terms of the model order in the identification process.

For the first and second mode, the effect of the algorithm is modest with the respective number of time lags of 513. The uncertainty or skewness of the estimation is mostly indifferent to the algorithm. The second mode, however, gets a sample mean of the frequency and damping estimates closer to the real value for the low model order. For the high model order, the algorithm affects the bias on the damping estimates for the second mode. This indicates a general reduction of bias error, regardless of the identification technique and the model order.

In Figs. 5.9 and 5.10, the algorithm has an influence on the estimation of the modal parameters for the third mode. The bias errors reduce when the model order is low. Here a substantial change appears in the distribution of the modal parameters for the third mode. Both damping and frequency estimates have a skewed distribution for the original correlation function matrix, whereas the skewness ceases for the modified correlation function matrix, see Fig. 5.9.

Figs. 5.11 and 5.12 illustrate the results of an identification process with varying number of included time lags. Regardless of the model order, the bias and random errors rise with the increasing inclusion of the noise tails - this is especially apparent for the second and third mode. Evidently, the low model order has increasing estimation errors on the third mode and the Time Domain Poly-reference overestimates the damping ratio and underestimates the natural frequency, see Fig. 5.11. For a model order of three, the identification technique underestimates the damping ratio and natural frequency, see Fig. 5.12. Furthermore, for a small number of included time lags, the identification procedure slightly overestimates the damping ratio for the first mode, indicating truncation errors. The algorithm creates considerably more stable estimates than the original correlation function matrix regardless of the number of included time lags, see Fig. 5.11.

The algorithm has a substantial influence on the bias error in the estimation of modal parameters. Furthermore, it creates a more stable identification process since it, in this study, seems insensitive to the number of included time lags and the model order of the identification technique.

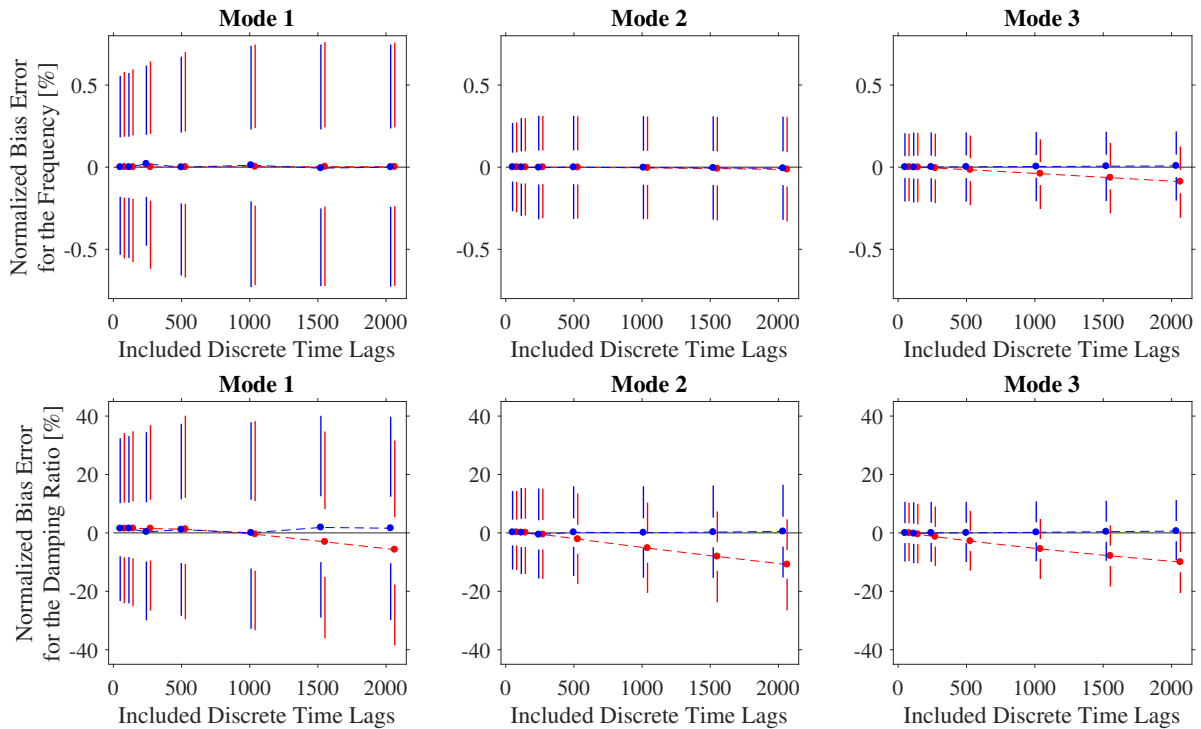


Figure 5.12: Case 1 - Simulated system with 10,000 simulations: (Tufte) box-plot of the estimated modal parameters using Time Domain Poly-reference with a model order of three [17] for a varying number of included time lags. Estimates based on the original (black) and the modified correlation function matrix (blue). In the (Tufte) box-plot, the dots mark sample means and the vertical lines mark the 2nd, 25th, 75th, and 98th percentiles.

5.9.2 Case 2 - Heritage Court Building

We will look at the algorithm applied to a modal analysis of the Heritage Court Tower, dataset 1 [1]. The Heritage Court Building is a 15-story building with a reinforced concrete shear core in Vancouver, British Columbia, Canada, see Fig. 5.13. On April 28th 1998, operational modal tests were carried out to analyse the dynamic properties of the building. A total of eight accelerometers were used in the test where six sensors were rowed while the other two sensors were used as references located on the 14th floor. The vibration measurements have a sampling frequency of 50 Hz and a time length of 326 seconds. This is a relatively short time length so the level of statistical errors will be significant.

For this study, we will focus on the first dataset with a total of six sensors. A band-pass filter is used with cut-off frequencies of 0.95 and 1.75 Hz and roll-off bands of 0.4 Hz.

We use the Eigensystem Realization Algorithm [13] on the correlation function matrix to create a stability diagram by changing the model order (the number of block rows in the Hankel matrices) while we keep the number of extracted modes the same as the number of channels in the measurements. We compare the stability diagram based on the original correlation function matrix with the stability diagram from the modified correlation function matrix where the algorithm reduces the noise tails automatically. For both stability diagrams, the correlation function matrix has 500 discrete time lags and we omit the first ten discrete time lags to remove uncorrelated broadband noise [15].

Results and Discussion

There should be three stable modes at approximately 1.22, 1.28, and 1.45 Hz in the applied frequency range [1]. In the stability diagram, three stable modes stand out as vertical lines for both the original and modified correlation function matrix, see Fig. 5.14. The cluster plot in Fig. 5.15 illustrates the same tendency by three clusters of estimates. Both Fig. 5.14 and Fig. 5.15 contain all identified modal parameters without any validation of the estimates.

The estimated modal parameters from the original correlation function matrix, however, drift slightly as the number of block rows of the Hankel matrix changes whereas the estimates of the modified correlation function matrix are more stable, see Fig. 5.14. In the cluster plot, the clusters of stable modes



Figure 5.13: Case 2 - The Heritage Court Building from two directions

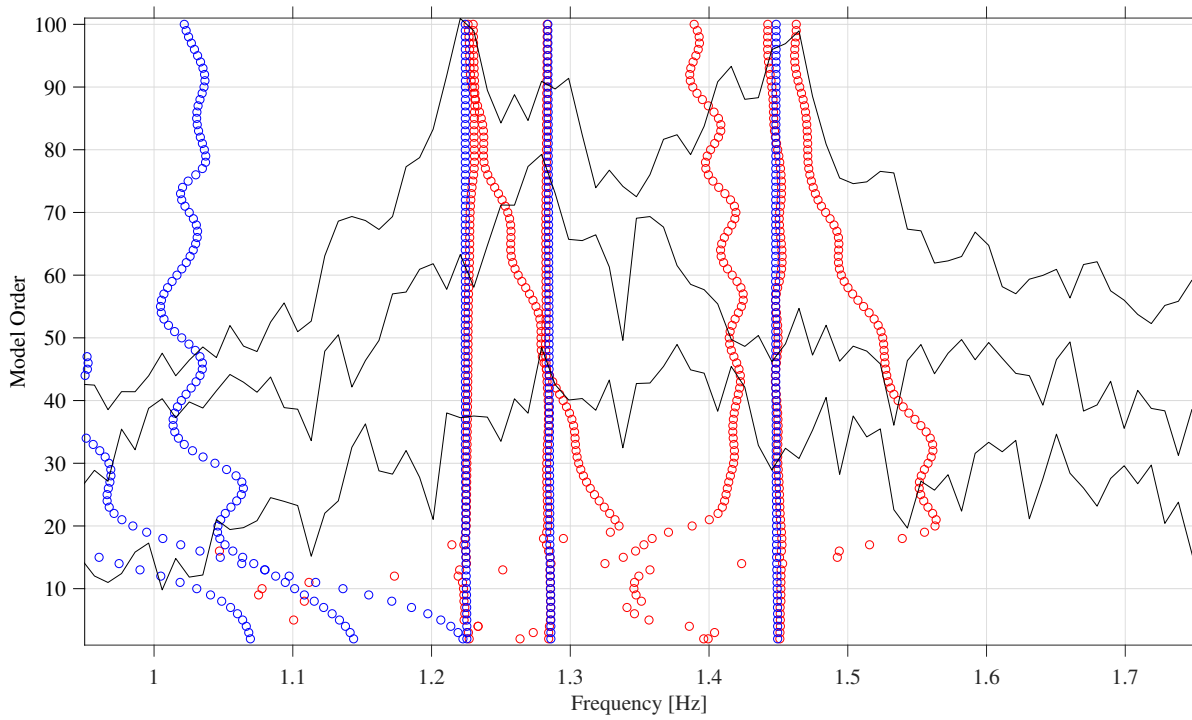


Figure 5.14: Case 2 - Heritage Court Tower, data set 1 [1]: Stability diagram based on the original correlation function matrix (black) and the modified correlation function matrix (blue), both including 500 time lags and disregarding the first ten time lags

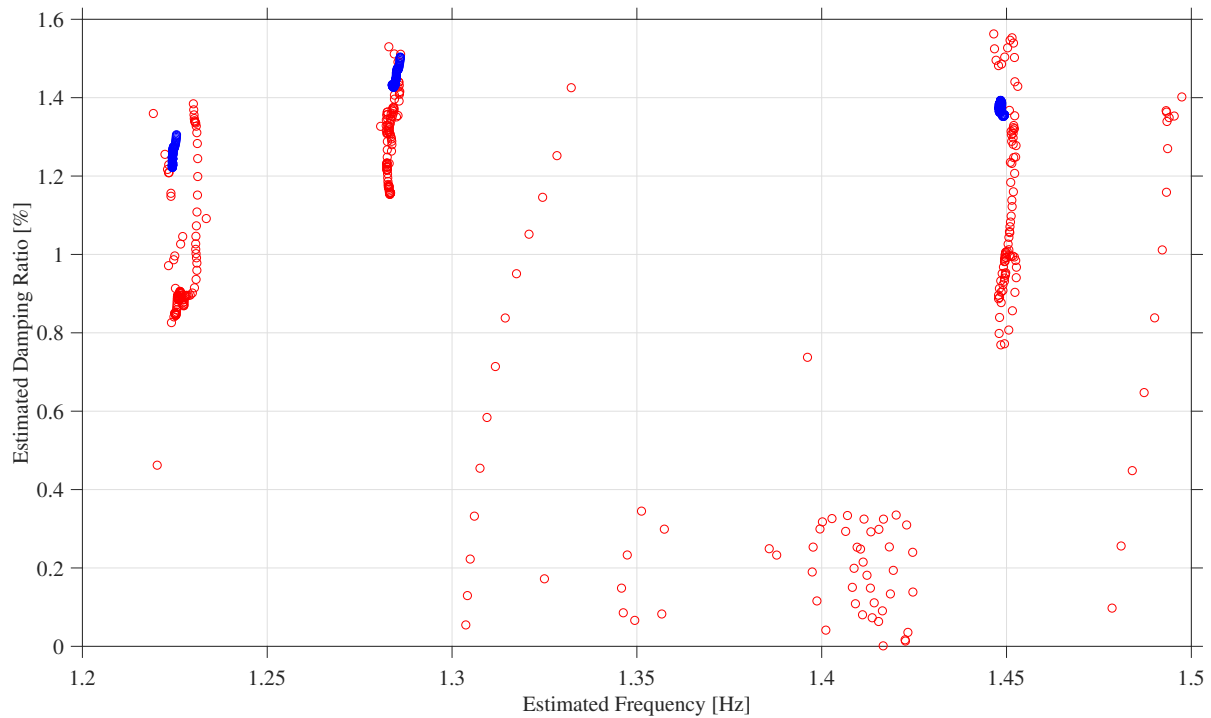


Figure 5.15: Case 2 - Heritage Court Tower, data set 1 [1]: Cluster plot with the natural frequency and damping ratio for estimated modes from the stability diagram based on the original correlation function matrix (*black*) and the modified correlation function matrix (*blue*), both including 500 time lags and disregarding the first ten time lags

are denser and shift when we apply the algorithm to reduce the noise tail, see Fig. 5.15, whereas the damping estimates for the original correlation function matrix are unstable and form scattered clusters.

Since we extract six modes for each model order, there are an additional three modes for each identification as seen in Figs. 5.14 and 5.15. These modes are spurious and instable regardless of the correlation function matrix applied in this identification process. Furthermore, some of these spurious modes have negative damping. The spurious modes from the original correlation function matrix have natural frequencies closer to the three stable modes whereas the natural frequencies of the spurious modes from the modified correlation function reside below.

Based on this study, reducing the noise tail creates more stable estimates that are less dependent on the model order (number of block rows). This indicates that the reduction of statistical errors is essential for a more stable and reliable estimation of the modal parameters using operational modal analysis.

5.10 Conclusion

The finite length of the measured vibrations introduces system dependent statistical errors in operational modal analysis. These errors cause random errors in the estimated correlation function matrix and bias errors in the envelopes of the matrix. The noise tail (erratic behaviour in the tail region of the correlation function matrix) indicates high levels of bias errors. Furthermore, these statistical errors transfer to an identification process of the modal parameters resulting in estimated modal parameters with random and bias errors. Since the bias error relates to the envelope of the correlation function, it mainly affects the damping estimates. Hence, in operational modal analysis, it is essential to reduce the noise tail so we decrease the bias error on damping estimates.

In this article, we introduced an automatic algorithm to reduce the noise tail in the estimated correlation function matrix. The algorithm decorrelates the estimated correlation function matrix through a condensation technique, auto-regression models, and a poly-reference technique. It detects the noise tail of the decorrelated auto-correlation functions by fitting two lines to the Hilbert envelope. Then it modifies the envelope of each noise tail to mimic the physical part using the regression fit. The algorithm reduces the bias error of the statistical errors but random errors still remain in the correlation function matrix.

Based on the studies presented in this article, the statistical errors make identification techniques biased and unstable since the techniques fit a correlation function matrix with both random and bias errors which increase with increasing number of time lags. The number of included time lags of the correlation function matrix and the model order of the identification technique affect this fit and often cause instability - here weakly-excited modes seem to be more unstable. The algorithm reduces the effect of statistical errors on a correlation function matrix. Thereby, it increases the stability and reliability and it reduces the bias error in the identification process of the modal parameters.

Acknowledgements

The authors acknowledge the funding received from the Centre for Oil and Gas - DTU/Danish Hydrocarbon Research and Technology Centre (DHRTC).

The authors thank Michael Vigsø and Thomas Kabel from Aarhus University for their helpful discussions.

Appendix 5.A Automated Modal Decorrelation of Estimated Correlation Function

We use the condensation technique in [12] to decorrelate and equalise the energy for each component in the estimated correlation function matrix. It is a dimensionality reduction based on the Principle Component Analysis using the Singular Value Decomposition [14]. We perform a singular value decomposition on the estimated correlation function matrix at time lag zero.

$$\mathbf{U}\mathbf{S}\mathbf{U}^T = \text{SVD}(\tilde{\mathbf{R}}_y(0)) \quad (5.22)$$

where \mathbf{U} is a unitary matrix holding the singular vectors, $[\mathbf{U}_1, \mathbf{U}_2, \dots, \mathbf{U}_n]$, and \mathbf{S} is a diagonal matrix that holds the descending singular values, $\sigma_1 > \sigma_2 > \dots > \sigma_n \geq 0$.

$$\mathbf{S} = \begin{bmatrix} \sigma_1 & 0 & \dots & 0 \\ 0 & \sigma_2 & \dots & 0 \\ \vdots & \vdots & \ddots & \vdots \\ 0 & 0 & \dots & \sigma_n \end{bmatrix} \quad (5.23)$$

To reduce the dimension, we remove the lower singular values in \mathbf{S} and the corresponding singular vectors in \mathbf{U} and we set up a transformation matrix, \mathbf{T} . In this algorithm, the dimensional reduction is optional and it is mainly applied to reduce the computation time.

$$\mathbf{T} = \mathbf{U}_m \mathbf{S}_m^{\frac{1}{2}} \quad (5.24)$$

where \mathbf{S}_m is the upper left $m \times m$ block of the singular value matrix, and \mathbf{U}_m contains the first m singular vectors. Some identification techniques apply similar dimensionality reduction using the singular value decomposition. These techniques apply this approach to help stabilise the identification process of modal parameters. This implementation of the singular value decomposition has a different objective: We want to create a new correlation function matrix with reduced noise tails that we can use with any identification technique that utilise correlation function matrices. In order to achieve this, we need to decorrelate the estimated correlation function matrix and equalise the energy for each modal auto-correlation function.

This transformation matrix, \mathbf{T} , decorrelates and condenses the correlation function matrix to m components.

$$\mathbf{Y}(k) = \mathbf{T}^+ \tilde{\mathbf{R}}_y(k) (\mathbf{T}^+)^T \quad (5.25)$$

Since the singular vectors are, by definition, orthogonal, it creates some problems when we have a correlation between modes. In such a case, the transformation matrix, Eq. (5.24), is orthogonal and insufficient to decorrelate the correlation function matrix since the mode shapes of the system are non-orthogonal. Therefore, we modify this transformation to decorrelate systems that are more complex. We

use a similar approach as [17] to estimate eigenvectors using auto-regression models and a poly reference technique. First, we set up two block Hankel matrices using Eq. (5.25).

$$\mathbf{H}_1 = \begin{bmatrix} \mathbf{Y}(1)^\top & \mathbf{Y}(2)^\top & \mathbf{Y}(3)^\top & \dots & \mathbf{Y}(K-2)^\top \\ \mathbf{Y}(2)^\top & \mathbf{Y}(3)^\top & \mathbf{Y}(4)^\top & \dots & \mathbf{Y}(K-1)^\top \end{bmatrix} \quad (5.26)$$

$$\mathbf{H}_2 = [\mathbf{Y}(3)^\top \quad \mathbf{Y}(4)^\top \quad \mathbf{Y}(5)^\top \quad \dots \quad \mathbf{Y}(K)^\top] \quad (5.27)$$

We estimate the auto-regression matrices by the use of the block Hankel matrices.

$$[\hat{\mathbf{A}}_2 \quad \hat{\mathbf{A}}_1] = \mathbf{H}_2 \mathbf{H}_1^\dagger \quad (5.28)$$

Then we form the companion matrix.

$$\mathbf{A}_c = \begin{bmatrix} \mathbf{0} & \mathbf{I} \\ \hat{\mathbf{A}}_2 & \hat{\mathbf{A}}_1 \end{bmatrix} \quad (5.29)$$

We perform an eigenvalue decomposition of the companion matrix and obtain the eigenvectors, \mathbf{V} . Then we modify the transformation matrix from Eq. (5.24).

$$\mathbf{Z} = \mathbf{TV} \quad (5.30)$$

Finally, we decorrelate the estimated correlation function matrix into an approximated modal correlation function matrix, which we will call the decorrelated correlation function matrix.

$$\hat{\mathbf{R}}_q(\tau) = \mathbf{Z}^\dagger \tilde{\mathbf{R}}_y(\tau) (\mathbf{Z}^\dagger)^\top \quad (5.31)$$

On the diagonals of this matrix, the correlation functions are decorrelated to auto-correlation functions, which corresponds to free decays of SDOF systems. Since this is an approximated decorrelation, the decorrelated correlation function matrix is a non-diagonal matrix.

References

- [1] Rune Brincker and Carlos Ventura. *Introduction to operational modal analysis*. John Wiley and Sons, Inc., Chichester, West Sussex, UK, 2015.
- [2] G. C. James, T. G. Carne, and J. P. Lauffer. The natural excitation technique (next) for modal parameter extraction. *The International Journal of Analytical and Experimental Modal Analysis*, 10(4):260–277, 1995.
- [3] Rune Brincker. On the application of correlation function matrices in oma. *Mechanical Systems and Signal Processing*, 87:17–22, 2017.
- [4] Julius S. Bendat and Allan G. Piersol. *Random data: analysis and measurement procedures*. Wiley-Blackwell, Hoboken, N.J., USA, 4th edition, 2010.
- [5] Marius Tarpø, Tobias Friis, Christos Georgakis, and Rune Brincker. The statistical errors in the estimated correlation function matrix for operational modal analysis. *Submitted to Journal of Sound and Vibration*, 2019.
- [6] Esben Orlowitz and Anders Brandt. Influence of correlation estimation methods on damping estimates. *5th International Operational Modal Analysis Conference*, 2013.
- [7] Laurent Giampellegrini. *Uncertainty in correlation-driven operational modal analysis*. PhD thesis, University College London, UK, 2007. 64-74.
- [8] Anela Bajrić, Jan Høgsberg, and Finn Rüdinger. Evaluation of damping estimates by automated operational modal analysis for offshore wind turbine tower vibrations. *Renewable Energy*, 116:153 – 163, 2018. Real-time monitoring, prognosis and resilient control for wind energy systems.
- [9] Marius Tarpø, Peter Olsen, Sandro Amador, Martin Juul, and Rune Brincker. On minimizing the influence of the noise tail of correlation functions in operational modal analysis, 2017.
- [10] Marius Tarpø, Peter Olsen, Martin Juul, Sandro Amador, Tobias Friis, and Rune Brincker. Statistical error reduction for correlation-driven operational modal analysis. *Proceedings of ISMA 2018*, 2018.
- [11] Brad A. Pridham and John C. Wilson. A study of damping errors in correlation-driven stochastic realizations using short data sets. *Probabilistic Engineering Mechanics*, 18(1):61 – 77, 2003.

- [12] Peter Olsen, Martin Juul, and Rune Brincker. Condensation of the correlation functions in modal testing. *Mechanical Systems and Signal Processing*, 118:377 – 387, 2019.
- [13] J. N. Juang and R. S. Pappa. An eigensystem realization algorithm for modal parameter identification and model reduction. *Journal of Guidance*, 8(5):620–627, 1985.
- [14] Ian Jolliffe. *Principal component analysis*. Springer Verlag, New York, USA, 2nd revised edition, 2002.
- [15] Esben Orlowitz and Anders Brandt. Influence of noise in correlation function estimates for operational modal analysis. *Topics in Modal Analysis & Testing, Proceedings of the 36th IMAC*, 9:55–64, 2019.
- [16] Anders Brandt. *Noise and vibration analysis : signal analysis and experimental procedures*. Wiley, Chichester, UK, 1st edition, 2011.
- [17] H. Vold, J. Kundrat, G. Rocklin, and R. Russell. A multi-input modal estimation algorithm for mini-computers. *SAE Technical Paper 820194*, page 10, 1982.
- [18] Richard G. Lyons. *Understanding digital signal processing*. Prentice Hall, Upper Saddle River, N.J.,USA, 3rd. edition, 2011.
- [19] Charles L. Lawson and Richard J. Hanson. *Solving least squares problems*. Prentice-Hall, Englewood Cliffs,USA, 1974.
- [20] Per Christian Hansen, Víctor Pereyra, and Godela Scherer. *Least squares data fitting with applications*. Johns Hopkins University Press, Baltimore, MD, USA, 2013.
- [21] F. N. Fritsch and R. E. Carlson. Monotone piecewise cubic interpolation. *SIAM Journal on Numerical Analysis*, 17:238–246, 1980.
- [22] S. R. Ibrahim and E. C. Mikulcik. A method for the direct identification of vibration parameters from the free response. *The Shock and Vibration Inform. Ctr. Shock and Vibration Bull.*, pages 183–198, 1977.

Chapter 6

Paper 3 - Modal truncation in experimental modal analysis

“
*All exact science is dominated by the idea
of approximation*
”

Bertrand Russell

Status

- Published in Topics in Modal Analysis & Testing, Volume 9, as part of the Conference Proceedings of the Society for Experimental Mechanics Series
- Available here: https://doi.org/10.1007/978-3-319-74700-2_15

6.1 Introduction

Modal truncation is a truncation of the modal superposition, which states that the response of a linear system is a linear combination of its mode shapes. Using modal expansion for virtual sensing, we need to truncate the number of included mode shapes so there are less modes than sensors to ensure a overdetermined problem. In the terminology of virtual sensing, this is a model simplification to the relevant information of the system. Any truncation of the modal matrix, however, introduces approximation errors - the modal truncation errors - that depends on the span of the applied mode shapes in relation to the given response. This paper studies modal truncation errors in an experimental setting.

As stated in section 3.6.5, modal truncation is studied in the research fields of numerical simulation and structural computation. Here, they correct the calculated response with a quasi-static contribution from residual modes (modes located in out-of-frequency bands) since they know that higher modes might contribute to the response based on the loading. This knowledge is rarely applied in an experimental setting or stress/strain estimation. Thus, we transfer established knowledge from one research field to experimental analysis. The paper is appended due to the absence of modal truncation in structural health monitoring.

6.2 Contribution

The author came up with the main idea, performed the experiments, made the data analysis, and wrote the paper.

6.3 Main findings

This paper studied modal truncation in an experimental setting. We found that the contribution of each mode depends on the convolution of the impulse response function of the given mode and the temporal variation of the load but, moreover, it depends on the inner vector product between the mode shape of the given mode and the spatial distribution of the load. We prove experimentally that the spatial

distribution of the load is important in modal truncation since it could lead to a quasi-static contribution from residual modes.

6.4 Reflection

We can apply this knowledge of the modal truncation error to stress/strain estimation using modal expansion. We should consider both the frequency and spatial content of the system and excitation when we choose the set of mode shapes for the modal expansion technique. A choice primarily based on frequency might lead to modal truncation errors. Furthermore, we can apply this to the quasi-static response of offshore structures where the spatial content is of great importance.

Modal Truncation in Experimental Modal Analysis

Marius Tarpø^a, Michael Vigsø^a, Rune Brincker^b

^aAarhus University, Department of Engineering, Inge Lehmanns Gade 10, Aarhus, Denmark

^bTechnical University of Denmark, Department of Civil Engineering, Brovej B.118, Kgs. Lyngby, Denmark

Abstract

Some methods in experimental modal analysis rely on a finite set of modes and they neglect the higher modes. However, this approach causes a truncation of the modal decomposition and the modal truncation introduces errors of unknown magnitude. In this paper the effect of modal truncation is investigated on a test specimen in the laboratory. It is found that the system response is dependent of the frequency and the distribution of the load. Modal truncation can introduce significant errors if the set of mode shapes does not efficiently span the spatial distribution of the load.

Keywords: Operational modal analysis, experimental modal analysis, modal truncation, modal decomposition

6.6 Introduction

The modal decomposition describes the structural dynamic response where the mode shapes of the system uncouple the dynamic response into the modal coordinates. When we truncate the modal decomposition to only include the first number of modes, we have a smaller set of modal coordinates to describe the system. This simplifies the structural response and it is frequently used to ease the calculation in structural dynamics. In experimental modal analysis, we identify a number of modes and we use them with experimental techniques for different purposes like; full field response estimation, fatigue analysis, load estimation, damage detection etc..

Normally, the truncated set of mode shapes provides good results however it might result in significant errors in certain instances where omitted modes contribute to the response [1–7]. The gross behaviour of structures is generally captured by the modes that are located in the frequency range of the load [3, 9]. However, higher modes might influence the localised behaviour by their non-trivial contribution. Therefore, a truncation of the modal decomposition can lead to errors of the representation of the response [1, 5, 7, 9]. This is also the case for experimental techniques that uses a truncated set of mode shapes to represent the structural response.

The phenomenon of modal truncation is described in structural computation and finite element modelling. Generally, these fields of research state that we can calculate the response as a combination of the dynamic responses of the lower modes and a correction term, which is based on the quasi static response of the remaining modes. Two types of corrections are created; static residual and residual vectors. The static residual uses static correction terms to adjust for the modal truncation. Whereas the other method make use of residual modes, also called "assumed modes" or "pseudo modes", combined with the mode shapes [8].

This paper showcases the potential problem of the modal truncation in an experimental setting. We find that the required number of modes in a modal decomposition depends on the frequency range and the spatial distribution of the loading.

6.7 Theory

6.7.1 Truncation of the modal decomposition

The modal decomposition says that any response from a linear system is a linear composition of its mode shapes. This means that the response of a linear structure is located in the subspace of its mode shapes.

$$\mathbf{y}(t) = \sum_{i=1}^N \boldsymbol{\phi}_i q_i(t) \quad (6.1)$$

where $\mathbf{y}(t) \in \mathbb{R}^{N \times 1}$ is system response, $\boldsymbol{\phi}_i \in \mathbb{R}^{N \times 1}$ is the mass normalised mode shape, $q_i(t)$ is the modal coordinate for mode i and N is the degree of freedom for the system.

Let us say that we only use K modes in the modal decomposition then we have a smaller set of modes to describe the system. Hence, we have introduced an error in our representation of the structural response due to the modal truncation. This error is often referred to as the residual effect.

$$\boldsymbol{\varepsilon}(t) = \sum_{i=K+1}^N \boldsymbol{\phi}_i q_i(t) \quad (6.2)$$

As long as this error is insignificant then the truncation of the modal decomposition is acceptable. However, it is hard to estimate the magnitude of this error. We will look at the modal coordinates to get a better understanding of the truncation error. We calculate the modal response in the frequency domain.

$$Q_i(\omega) = H_i(\omega) \boldsymbol{\phi}_i^T \mathbf{X}(\omega) \quad (6.3)$$

where $\mathbf{X} \in \mathbb{R}^{N \times 1}$ is the load in the frequency domain, $H_i(\omega)$ is the frequency response function for the i^{th} mode.

$$H_i(\omega) = \frac{1}{m_i (-\omega^2 + j2\zeta_i \omega_i \omega + \omega_i^2)} \quad (6.4)$$

where m_i is the modal mass, ω_i is natural frequency and ζ_i is the damping ratio for mode i .

In the following, we will look at two types of loading: random or fixed spatial distribution of the load. A load with a fixed spatial distribution can be separated like

$$\mathbf{X}(\omega) = \mathbf{F}S(\omega) \quad (6.5)$$

where $\mathbf{F} \in \mathbb{R}^{N \times 1}$ is the spatial distribution of the load and $S(\omega)$ is the scalar function defining the temporal variation of the load. Therefore, we can rewrite the expression for the modal coordinates in the frequency range, eq. 6.3, if the load has a spatial distribution.

$$Q_i(\omega) = H_i(\omega) S(\omega) \boldsymbol{\phi}_i^T \mathbf{F} \quad (6.6)$$

We see that the contribution of each mode is dependent of the scalar product of frequency response function and the frequency range of the load. However, it is also dependent on the inner vector product between the given mode shape and the spatial distribution of the load. This tells us that a modal coordinate is given both by the frequency range and the spatial distribution of the load. But if the load has a random spatial distribution then the modal response only depends on the frequency range of the load. Therefore, the residual effect depends on frequency range and spatial distribution of the load.

Modal Truncation of the Quasi Static Contribution

Often, the omitted modes are located above the frequency range of the load when we truncate the modal decomposition. When the load frequency is located way before the natural frequencies of the modes then the omitted modes act quasi static.

We will show this by an example where the frequency range of the load is restricted and we omit all modes outside this range. Here we assume that the first omitted mode n and all higher modes have much higher natural frequencies, ω_n , than the highest load frequency, ω_x . This means; $\omega_x \ll \omega_n$. So we can rewrite the frequency response function, eq. (6.4), for the truncated modes when we roughly approximate that any term in denominator with ω is insignificant compared with the term ω_n^2 . Then the modal coordinates for truncated modes are

$$\tilde{Q}_n(\omega) \approx \begin{cases} \frac{1}{m_n \omega_n^2} S(\omega) \boldsymbol{\phi}_n^T \mathbf{F} & 0 \leq \omega \leq \omega_x \\ 0 & \omega > \omega_x \end{cases} \quad (6.7)$$

We see on eq. (6.7) that the modal coordinates is no longer a dynamic response but a quasi static response. Therefore, we approximate the residual effect as

$$\tilde{\boldsymbol{\varepsilon}}(t) \approx s(t) \sum_{n=K+1}^N \frac{\boldsymbol{\phi}_n \boldsymbol{\phi}_n^T \mathbf{F}}{m_n \omega_n^2} \quad (6.8)$$

This is a quasi static error, which depends on the inner vector product between the mode shape and spatial distribution of the load and the modal mass and frequency. So a truncation of higher modes might give a amplitude error of the system response because we have removed a quasi static contribution from the residual modes.

6.7.2 Reduction of subspace

We would like to be able to remove the influence of certain modes from a measured system response in order to access the effect of modal truncation. In order to do this we will use a linear transformation, which we base on the modal decomposition. The estimated modal coordinates for K modes is found when we project the system response onto the subspace of the mode shapes.

$$\hat{\mathbf{q}}(t) = \mathbf{\Phi}_K^+ \mathbf{y}(t) \quad (6.9)$$

where $\hat{\mathbf{q}}(t) \in \mathbb{R}^{K \times 1}$ is the estimated modal coordinate matrix and $\mathbf{\Phi}_K \in \mathbb{R}^{N \times K}$ is the truncated modal matrix, which contains the applied mode shape as columns. Then we can find the truncated system response.

$$\hat{\mathbf{y}}(t) = \mathbf{\Phi}_K \hat{\mathbf{q}}(t) \quad (6.10)$$

where $\hat{\mathbf{y}}(t) \in \mathbb{R}^{N \times 1}$ is the truncated system response with a reduced subspace. This transformation projects the response onto the column space of the modal matrix and thereby it reduces the subspace of the response to only include the given modes.

6.7.3 Quality Measurements

It is useful to access the difference between a measured and the equivalent truncated response so we know the errors of a modal truncation. To assess the difference, we utilise the coefficient of determination, $R_{t,i}^2$, from model validation in both time and frequency domain [10].

$$R_{t,i}^2 = 1 - \frac{\sum_{k=1}^N (y_i(t_k) - \hat{y}_i(t_k))^2}{\sum_{k=1}^N (y_i(t_k) - E[y_i(t)])^2} \quad (6.11)$$

$$R_{f,i}^2 = 1 - \frac{\sum_{k=1}^N (|Y_i(f_k)| - |\hat{Y}_i(f_k)|)^2}{\sum_{k=1}^N (|Y_i(f_k)| - E[|Y_i(f)|])^2} \quad (6.12)$$

where $E[X]$ is the expected value of X , $y_i(t)$ & $\hat{y}_i(t)$ are the measured and truncated response for sensor i and $Y_i(f)$ & $\hat{Y}_i(f)$ are the Fourier transformed measured and truncated response for sensor i .

6.8 Case study

We will show the effect of modal truncation on a small structure in the laboratory. The test specimen is a T-shaped steel structure, which is fixed with claps, see Figure 6.1. In this case study, we will assume that we are only interested in the first 100 Hz of the system. We will identify the modes located inside this frequency region and we will project the response onto the column space of the mode shapes using equation (6.10). By projecting the response onto the subspace of the used mode shapes, we remove the contribution of the higher modes and all noise that are perpendicular to this subspace. This is to illustrate the effect of neglecting the contribution of the others modes in an experimental setting.

In this paper, we will call the modes located in given frequency range for the "*dynamic modes*" and we will define the modes located outside this range as "*residual modes*". So we will look at the truncation error by using the dynamic modes that are located in the given frequency range. Then we will add one and then two residual modes to the modal decomposition from outside this frequency range and calculate the truncation error. This is in order to see if modes outside the frequency range will have a contribution to the system response.



Figure 6.1: Photo of the test specimen in the lab

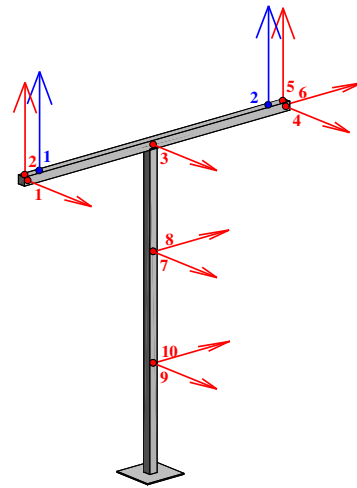


Figure 6.2: Position of sensors, red arrows are for uniaxial accelerometers and blue arrows are the geophones

6.8.1 Set up

Ten uniaxial accelerometers with a sensitivity of 100 mV/g and two geophones are applied to the structure as seen on Figure 6.2. The geophones work as shakers when we apply a current to them. Compressed air excites the structure from 3 directions and this loading creates turbulence around the structure and the excitation resembles white Gaussian noise. One set of data is accuired where the geophones are idle and this data set is used to identify the modal parameters using operational modal analysis [11].

A time length of 300 seconds is used with a sampling frequency of 1651 Hz for each data set. The data is decimated to a new frequency of 825.5 Hz [11]. We bandpass filter the data sets from 5 to 100 Hz, see Figure 6.3. The low frequency cut-off is applied to remove noise from DC.

An Operational Modal Analysis is preformed where the *Frequency Domain Decomposition* is used to identify the modes [12]. We found five dynamic modes in the frequency region and five residual modes outside this range, see Figure 6.3 & 6.4.

6.8.2 Case 1

In this case, the geophones are idle and only compressed air is used as excitation and therefore the load has no defined spatial distribution. The measured response is projected onto the subspace of the five dynamic modes using equation (6.10). Afterwards, we add one and then two residual modes to the modal decomposition. We calculate the coefficient of determination in time and frequency domain for each version of the modal decomposition, see Table 6.1.

Generally, we do not achieve a better representation of the response by adding residual modes to the modal decomposition. The two worst truncated responses are sensor 8 & 10 and the recorded acceleration for these two sensors plotted on Figure 6.5 & 6.6 for the scenario with dynamic modes only.

Table 6.1: Quality Measurements for case 1

| | | Sensor 1 | Sensor 2 | Sensor 3 | Sensor 4 | Sensor 5 | Sensor 6 | Sensor 7 | Sensor 8 | Sensor 9 | Sensor 10 |
|-------------------------------------|---------|----------|----------|----------|----------|----------|----------|----------|----------|----------|-----------|
| Dynamic modes | R_t^2 | 1.0000 | 0.9916 | 0.9990 | 1.0000 | 0.9919 | 0.9958 | 0.9997 | 0.9969 | 0.9977 | 0.9850 |
| | R_f^2 | 1.0000 | 0.9955 | 0.9995 | 1.0000 | 0.9975 | 0.9977 | 0.9998 | 0.9979 | 0.9985 | 0.9866 |
| Dynamic modes + 1 residual mode | R_t^2 | 1.0000 | 0.9924 | 0.9990 | 0.9999 | 0.9917 | 0.9992 | 0.9997 | 0.9986 | 0.9977 | 0.9973 |
| | R_f^2 | 1.0000 | 0.9960 | 0.9995 | 1.0000 | 0.9974 | 0.9995 | 0.9998 | 0.9991 | 0.9985 | 0.9984 |
| Dynamic modes + 2 residual modes | R_t^2 | 1.0000 | 1.0000 | 0.9990 | 1.0000 | 1.0000 | 0.9996 | 0.9997 | 0.9986 | 0.9977 | 0.9978 |
| | R_f^2 | 1.0000 | 1.0000 | 0.9995 | 1.0000 | 1.0000 | 0.9997 | 0.9998 | 0.9991 | 0.9985 | 0.9986 |

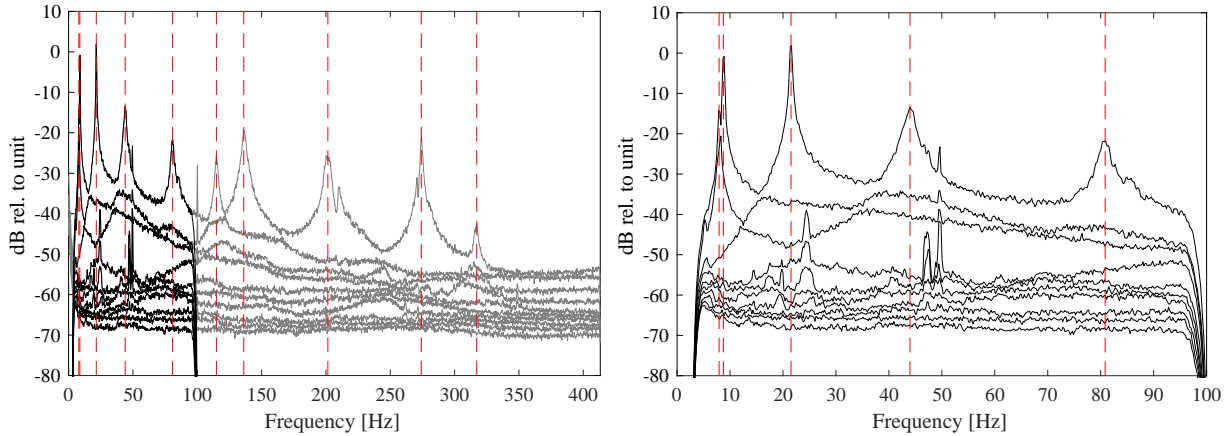


Figure 6.3: Case 1, Singular Value Decomposition of the Spectral Density Matrix

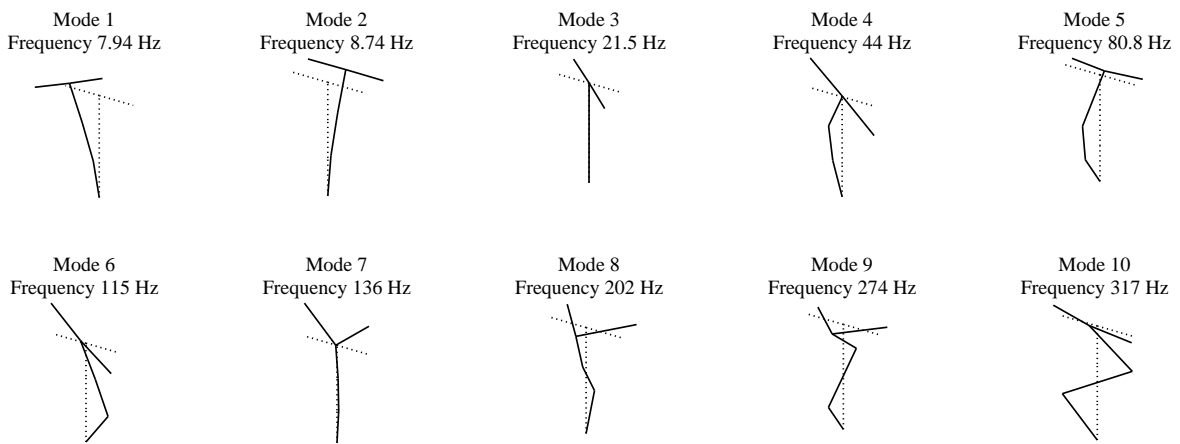


Figure 6.4: Identified Experimental Mode Shapes

6.8.3 Case 2

In the next case, we excite the structure with compressed air. Additional, we apply a current to the second geophone so it excites the structure at a frequency of 64 Hz, see Figure 6.7 for spectral density plot. This means that a significant part of the load has a fixed spatial distribution in this case.

Like in Case 1, the five dynamic mode shapes are used for the projection of the subspace using eq. (6.10). Next, we add one and two residual modes from outside the frequency region. Then the coefficients of determination are calculated for the time and frequency domain, see Table 6.2.

Table 6.2: Quality Measurements for case 2

| | | Sensor 1 | Sensor 2 | Sensor 3 | Sensor 4 | Sensor 5 | Sensor 6 | Sensor 7 | Sensor 8 | Sensor 9 | Sensor 10 |
|-------------------------------------|---------|----------|----------|----------|----------|----------|----------|----------|----------|----------|-----------|
| Dynamic modes | R_t^2 | 0.9999 | 0.9759 | 0.9991 | 0.9999 | 0.9236 | 0.8625 | 0.9991 | 0.9947 | 0.9976 | 0.9745 |
| | R_f^2 | 0.9999 | 0.9759 | 0.9996 | 0.9999 | 0.9227 | 0.8565 | 0.9991 | 0.9947 | 0.9984 | 0.9745 |
| Dynamic modes + 1 residual mode | R_t^2 | 0.9999 | 0.9709 | 0.9991 | 0.9999 | 0.9300 | 0.9718 | 0.9994 | 0.9990 | 0.9977 | 0.9993 |
| | R_f^2 | 0.9999 | 0.9708 | 0.9995 | 1.0000 | 0.9293 | 0.9706 | 0.9995 | 0.9991 | 0.9985 | 0.9994 |
| Dynamic modes + 2 residual modes | R_t^2 | 1.0000 | 1.0000 | 0.9990 | 0.9999 | 1.0000 | 0.9977 | 0.9997 | 0.9989 | 0.9978 | 0.9989 |
| | R_f^2 | 1.0000 | 1.0000 | 0.9995 | 1.0000 | 1.0000 | 0.9977 | 0.9998 | 0.9990 | 0.9985 | 0.9990 |

Generally, the truncated response using only the dynamic mode has a high correlation with the measured response but a few sensors deviate. The two worst channels are for sensor 5 & 6 and the responses for the sensors have wrong amplitudes, see Figure 6.8 & 6.9. By adding residual modes, we see an increase in the quality measurements, which is especially evident for sensor 5 & 6. The quality fit for

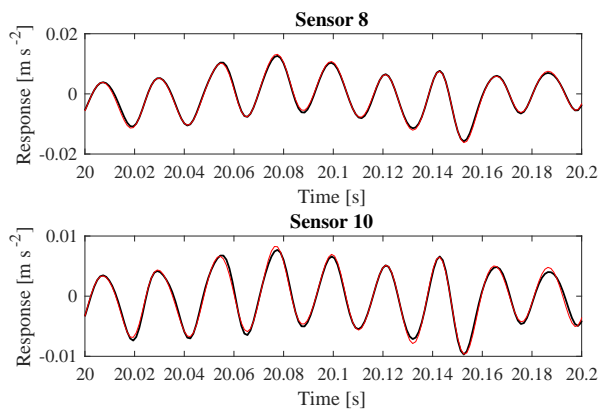


Figure 6.5: Case 1, only dynamic modes: Response of truncated response, black is the measured and red is the truncated response

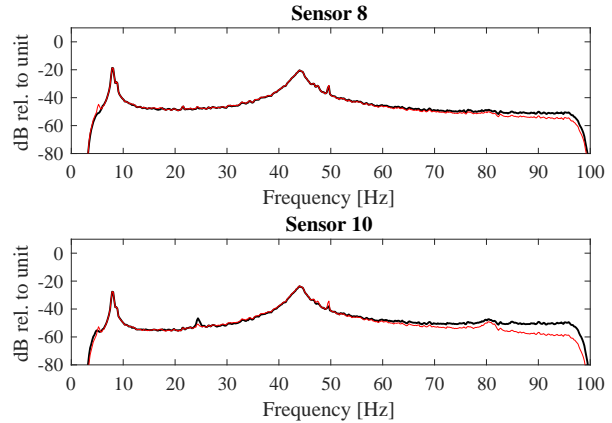


Figure 6.6: Case 1, only dynamic modes: Spectrum of truncated response, black is the measured and red is the truncated response

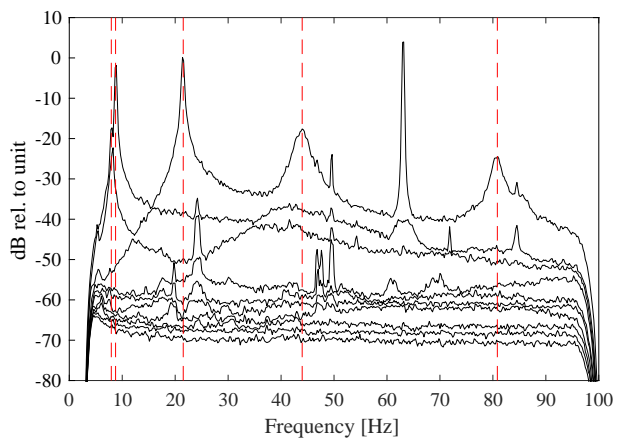
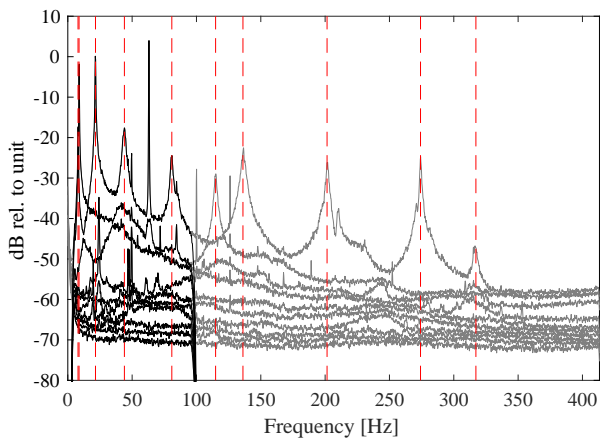


Figure 6.7: Case 2, Singular Value Decomposition of the Spectral Density Matrix

sensor 6 increases with more than 0.1 by adding one residual mode. Whereas, sensor 5 needs two residual modes to have a quality fit above 0.93. The response for sensor 5 & 6 using two residual modes are plotted in Figure 6.10 & 6.11.

6.9 Discussion

First, we should note that the projection onto a fixed number of mode shapes removes noise and modal response alike if their subspaces are orthogonal to the new subspace of the projection. Therefore, we will remove noise and this reduction of noise will affect the quality measurements since we are using a signal with noise as reference. The resolution of the experimental mode shapes also has an influence on the assumption that we can reduce the subspace. However, we will assume that these errors are insignificant.

Overall the modal truncation has a low error and most sensors maintain the same response as measured when we use the five dynamic mode shapes. In Case 1, the first five dynamic mode shapes were sufficient to span the measured response but in Case 2 we needed additional mode shapes to accurately span the measured response for a few of the sensors. Here sensor 5 & 6 are less precise in Case 2 where a part of the load had a defined load pattern. By observing figure 6.2, we can see that the excitation by the second geophone primarily results in responses for sensor 2, 5 & 6. Furthermore, we can observe in figure 6.4 that the first five mode shapes do not span this movement. The sixth and seventh mode shapes add more information to better span the response that is caused by the geophone.

In these tests, we see that an excitation with a fixed spatial distribution has a higher residual effect compared with an excitation with a random load pattern. This is in accordance with the theory of the residual effects. The theory suggests that a fixed spatial distribution of the load causes contributions from modes outside the frequency of load. Therefore, a fixed load pattern seems to activate quasi static

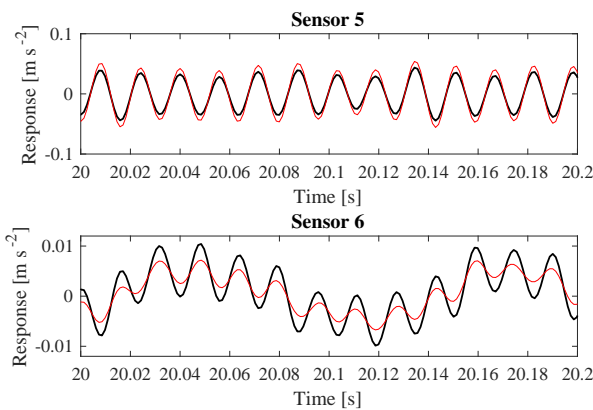


Figure 6.8: Case 2, only dynamic modes: Response of truncated response, black is the measured and red is the truncated response

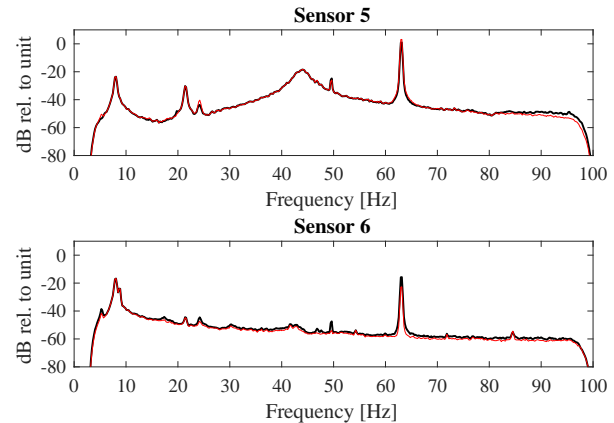


Figure 6.9: Case 2, only dynamic modes: Spectrum of truncated response, black is the measured and red is the truncated response

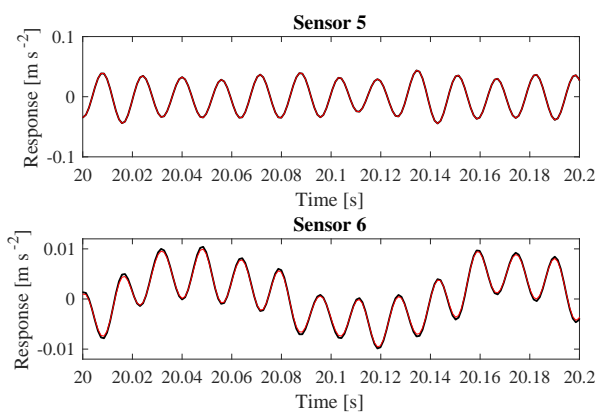


Figure 6.10: Case 2, dynamic modes + 2 residual modes: Response of truncated response, black is the measured and red is the truncated response

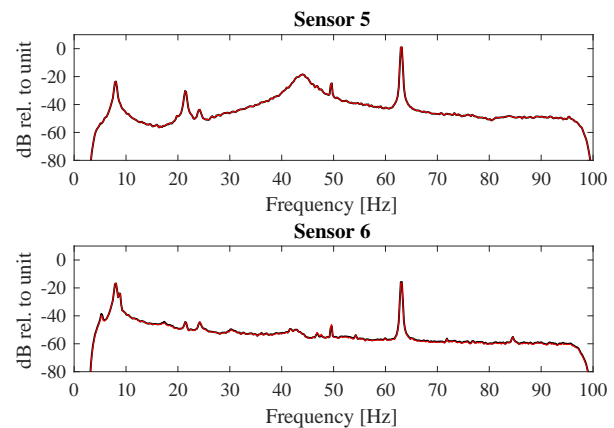


Figure 6.11: Case 2, dynamic modes + 2 residual modes: Spectrum of truncated response, black is the measured and red is the truncated response

response of the higher modes even-though the frequency of the load is located before the natural frequencies of these modes. These modes should be included in the lower frequency region if we want a proper representation of the response for localised behaviour.

6.10 Conclusion

In this paper we have shown the possible errors caused by truncating the modal decomposition in experimental modal analysis. Often this truncation error is insignificant but it is pronounced if a significant part of load has a fixed spatial distribution. The magnitude of the error is hard to estimate but localised structural behaviour seem to be highly affected by this residual effect. This means that experimental techniques that use a truncated set of modes to describe the response might introduce errors in localised behaviour.

To sum up, we cannot rely purely on the frequency range to choose the number of modes in a experimental modal analysis since the combination of higher modes may contribute to the response. Therefore, modal truncation introduces errors in response representation if the set of mode shapes inefficiently span the spatial distribution of the load.

Acknowledgements

The authors acknowledge the funding received from Centre for Oil and Gas - DTU/Danish Hydrocarbon Research and Technology Centre (DHRTC).

A special thanks to Jannick Balleby Hansen for helping with the experimental tests.

References

- [1] D.C. Lui, H.L. Chung, and W.M. Chang. The errors caused by modal truncation in structure dynamic analysis. *IMAC XVIII – 18th International Modal Analysis Conference*, pages 1455–1460, 2000.
- [2] N. R. Maddox. On the number of modes necessary for accurate response and resulting forces in dynamic analysis. *Journal of Applied Mechanics ASME*, 42(2):516–517, 1975.
- [3] J. H. Vugts, I. M. Hinesm, R. Nataraja, and W. Schumm. Modal superposition vs. direct solution techniques in the dynamic analysis of offshore structures. *BOSS'79, Proceedings of the Second International Conference on Behaviour of Off-Shore Structures*, pages 23–29, 1979.
- [4] P. Léger, J. M. Ricles, and L. J. Robayo. Reducing modal truncation error in wave response analysis of offshore structures. *Communications in applied numerical methods*, 6(1):7–16, 1990.
- [5] P. Léger and E. L. Wilson. Generation of load dependent ritz transformation vectors in structural dynamics. *Engineering Computations*, 4(4):309–318, 1987.
- [6] J. M. Dickens, J. M. Nakagawa, and M. J. Wittbrodt. A critique of mode acceleration and modal truncation augmentation methods for modal response analysis. *Computers & Structures*, 62(6):985–998, 1997.
- [7] O. E. Hansteen and K. Bell. On the accuracy of mode superposition analysis in structural dynamics. *Earthquake Engineering and Structural Dynamics*, 7:405–411, 1979.
- [8] N. Roy and A. Girard. Impact of residual modes in structural dynamics. *Proceedings of the European Conference on Spacecraft Structure, Materials and Testing*, 2005.
- [9] P. Avitabile and P. Pingle. Prediction of full field dynamic strain from limited sets of measured data. *Shock and Vibration*, 19(5):765–785, 2012.
- [10] P. C. Hansen, V. Pereyra, and G. Scherer. *Least squares data fitting with applications*. Johns Hopkins University Press, Baltimore, MD, 2013.
- [11] R. Brincker and C. Ventura. *Introduction to operational modal analysis*. John Wiley and Sons, Inc., Chichester, West Sussex, UK, 2015.
- [12] R. Brincker, L. M. Zhang, and P. Andersen. Modal identification of output-only systems using frequency domain decomposition. *Smart Materials and Structures*, 10(3):441–445, 2001.

Chapter 7

Paper 4 - Expansion of experimental mode shape from operational modal analysis and virtual sensing for fatigue analysis using the modal expansion method

“
*One accurate measurement is worth a
 thousand expert opinions*
 ”

Grace Hopper

Status

- Published in International Journal of Fatigue in a Special Issue on Fatigue in Structural Integrity of Offshore Energy Industry, January 2020
- Available here: <https://doi.org/10.1016/j.ijfatigue.2019.105280>

7.1 Introduction

It is quite evident that a perfectly correlated system model (we use finite element models in this thesis) provides the optimal condition for stress/strain estimation. In reality, however, any (mathematical) model is an approximation and this introduces modelling errors. For stress/strain estimation using the modal expansion, the modelling errors are expressed in an incorrect subspace-projection, which are unrepresentative of the actual structure. This inaccuracy of the subspace-projection is investigated in this paper. Furthermore, we examine the expansion of experimental mode shapes as a means for updating a system model and thereby reducing the modelling errors.

7.2 Contribution

The author came up with the idea to study the expansion of experimental mode shape from operational modal analysis, performed the data analysis, and wrote the paper. Both the new "leave- p -out-cross-validation" implementation of the local correspondence principle and the new quality measurement "normalised error of fatigue" were proposed by the author.

7.3 Main findings

Here, we found that expansion of experimental mode shape can decrease modelling errors from a finite element model but the expansion process introduces fitting errors. Thus, we have a trade-off between

modelling and fitting errors that we must balance. Therefore, we must choose an expansion technique with great care and fit it to the application. In this paper, the traditional local correspondence and SEREP techniques, in general, introduced more fitting errors than they reduced the modelling errors. Therefore, the author concluded that expansion of experimental mode shapes should be applied with care.

7.4 Reflections

In this paper, we proved that mode shape expansion provides a tool for optimising the accuracy in stress/strain estimation but it requires expertise to avoid the potential pitfalls of introducing significant levels of fitting errors.

Expansion of experimental mode shape from operational modal analysis and virtual sensing for fatigue analysis using the modal expansion method

Marius Tarpø^a, Bruna Nabuco^b, Christos Georgakis^a, Rune Brincker^b

^aAarhus University, Department of Engineering, Inge Lehmanns Gade 10, Aarhus, Denmark

^bTechnical University of Denmark, Department of Civil Engineering, Brovej B.118, Kgs. Lyngby, Denmark

Abstract

Offshore structures are exposed to fatigue damage due to fluctuating environmental and operational forces. The actual stress history of structures in operation is an important parameter for the remaining fatigue lifetime. Unfortunately, the fatigue critical locations are often difficult to reach for inspection of cracks or installation of sensors and these direct locations lead to corruption of sensors due to the environmental effects. Virtual sensing enables full-field stress/strain estimation that facilitates fatigue analyses of offshore structures in operation. In the literature, various virtual sensing methods exist but this paper focuses on modal expansion. This technique uses the mode shapes (the linear subspace) of the structure to transform the measured system response into the full-field stress/strain response. The applied mode shapes either hail from a finite element model or an expansion of experimental mode shapes from an operational modal analysis. This paper compares the use of mode shapes from a finite element model to the use of expanded experimental mode shapes. Modal expansion is applied to a scaled offshore platform in the laboratory to estimate the strain response using the finite element mode shapes and expanded experimental mode shapes using different expansion techniques: System Equivalent Reduction Expansion Process (SEREP), local correspondence principle, and the new leave- p -out cross validation implementation of the local correspondence principle introduced in this paper. The results are analysed with different metrics and this paper introduces a new quality measurement - the normalised error of fatigue damage - for strain estimation intended for fatigue analysis. Based on this study, expansion of experimental mode shapes has the potential to reduce errors in stress/strain estimation. The expansion is, however, a fitting process and, thus, it contains fitting error dependent on the case. In this study, the finite element mode shapes outperform some of the mode shape expansion techniques due to this fitting errors. Therefore, expansion of experimental mode shapes can improve stress/strain estimation but it should be used with care to avoid an overfit.

Keywords: Stress estimation, mode shape expansion, virtual sensing, fatigue analysis, structural health monitoring

7.6 Introduction

Offshore structures are prone to fatigue failure due to the fluctuating forces, and the stress history of these structures is crucial to access and analyse the remaining fatigue lifetime. The fatigue assessment of existing offshore structures requires information on the strain response from all relevant locations and, therefore, it necessitates sensors at all fatigue critical locations of the structure. Unfortunately, these locations are often inaccessible as well as harmful to the sensors due to the hostile environment [1, 2]. A possible solution is virtual sensing or virtual sensors that convert and extend data from physical sensors to an unmeasured location through some process models [3]. In the literature on stress estimation, the most popular process models are: the modal expansion [4–14] and the Kalman Filter [15–20]. The Kalman filter is an optimal predictor that comes from control theory and it uses a state space model of the system. The modal expansion is a linear transformation that expands the system response based on the mode shapes of the system [21]. The two techniques have been proven to be competitive and interchangeable [15, 17]. This paper focuses on the modal expansion for virtual sensing in preparation for a fatigue analysis. Fig. 7.1 outlines the methodology of modal expansion. Virtual sensing needs information on the system - the system model - and finite element models are the most applied approach for stress estimation.

In the literature of virtual sensing, modal expansion is applied with success on a wide range of mechanical and civil structures. Hjelm et al. [11] presented a full-field strain estimation technique using

the modal expansion and applied it to a laboratory structure and a lattice tower. Avitabile and Pingle [6] estimated the strain response on a test-specimen in the Laboratory while Aenlle et al. [22] applied strain estimation on a scale model of a two-story building. Maes et al. [17] estimated the strain response on an offshore monopile wind turbine and applied data fusion to combine accelerometers and strain gauges. To study strain estimation on wave-induced structure, Skaftø et al. [5] applied modal expansion with Ritz vector to account for the quasi-static response caused by waves and estimated the strain response on a scale model of an offshore platform excited with shakers mimicking a wave spectrum. Similarly, Iliopoulos et al. [7] applied a multi-banded modal expansion on an offshore monopile wind turbine including the quasi-static strain contributions from thrust loads by combining accelerometers and strain gauges. To evaluate strain estimation, Nabuco et al. [9] applied a reliability analysis on the estimated strain response of a scaled offshore platform and showed the relevance of strain estimation compared to the traditional norms and design. Recently, the modal expansion for strain estimation is applied to non-linear structures where Tarpø et al. [8] estimated the strain response with success for a simulated offshore platform with friction in order to test modal expansion for non-linear structures. Furthermore, Nabuco et al. [14] used modal expansion based on parameters determined from a linear case and successfully estimated the strain response of two scaled offshore platforms with a friction coupling.

For modal expansion, researchers divide into two groups: the ones using finite element mode shapes [6, 7, 10, 12, 17] and the ones applying expanded experimental mode shapes [4, 5, 8, 9, 11]. To the best of the authors knowledge, however, the two approaches have never been compared in a study. The hypothesis behind expanding mode shapes is: expanded experimental mode shapes are, essentially, an update of the finite element model and these mode shapes have the potential to reduce modelling errors from the finite element model. The update depends on the accuracy of the mode shape expansion.

In 1965, Guyan [23] introduces the first method for expanding experimental mode shapes and thereafter several researchers contributed to this field. The expansion methods enable a linear relationship between an experimental and analytical model. Generally, the experimental mode shapes have a set of spatially limited Degrees-Of-Freedom (DOF) whereas the analytical models have much larger sets of DOFs. To enable the linear relationship between the two sets of mode shape matrices, we either reduce the analytical model or expand the experimental mode shape. Thus, a close relation exists between reduction and expansion methods, and many of the methods are applicable for both reduction and expansion. Levine-West et al. [24] group the different expanding methods into three main categories: direct, projection, and error methods. The direct methods determine the transformation matrix which maps between the active and full set of DOFs, entirely by the mass and stiffness matrices from the analytical model, e.g. Guyan [23], Kidders dynamic expansion [25], Millers dynamic expansion [26], and Improved Reduced System (IRS) [27]. In the projection methods, the transformation matrix is determined using analytical (and sometimes experimental) mode shapes in different least-squares formulations, e.g. System Equivalent Reduction Expansion Process (SEREP) [28], modal expansion [21], hybrid method [29], perturbed force approach [30], and Procrustes method [31]. The error methods repeat calculations until convergence or minimisation of a cost function, e.g. direct mode shape expansion [32], local correspondence principle [33], and least-squares with quadratic inequality constraints [24].

This paper further develops modal expansion by studying the selection of mode shapes - the use of expanded experimental mode shapes in contrast to the finite element mode shapes. In terms from virtual sensing, this paper studies the system model. In general, expansion of experimental mode shapes and strain estimation are case dependent since they depend on position and number of sensors, measurement noise, modelling errors of the finite element model, and identification errors in the experimental mode shapes. To illustrate the potential benefit for offshore structures, we test the effect on an offshore scale model in the laboratory. The results of this case study suggest that expansion of mode shapes benefits the strain estimation, but it requires low estimation errors in experimental mode shapes and a highly correlated finite element model. The expansion of experimental mode shapes is a fitting procedure and it needs proper tuning to reduce the fitting errors. Overfitting is a risk for mode shape expansion and it results in an erroneous stress estimation. Hence, mode shape expanding has the potential to reduce errors in stress estimation, but it must be handled with care to reduce fitting errors.

Furthermore, this paper introduces a new implementation of the local correspondence principle based on leave- p -out cross-validation in Section 7.7.4 and a new quality measurement for strain estimation with respect to a fatigue analysis called "normalised error of fatigue damage" in Section 7.8.1.

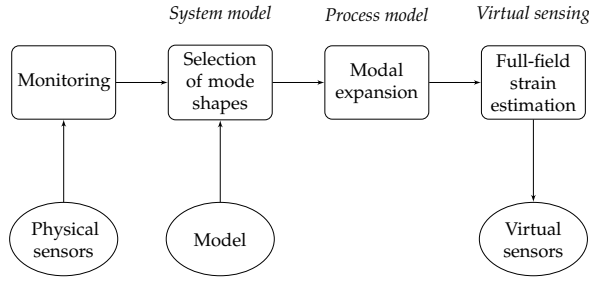
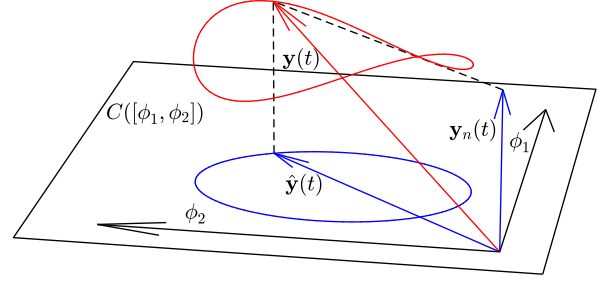


Figure 7.1: The methodology of modal expansion

Figure 7.2: The principle of modal expansion illustrated in \mathbb{R}^3 with a two-dimensional subspace: We project the response, $\mathbf{y}(t)$, onto the subspace spanned by the mode shapes, ϕ_1 and ϕ_2 , and obtain the truncated response, $\hat{\mathbf{y}}(t)$, where all response orthogonal to the subspace, $\mathbf{y}_n(t)$, is removed

This new implementation of the mode shape expansion provides the best fit for the strain estimation.

7.7 Modal expansion for strain estimation

The modal expansion technique is a least square regression and it uses linear algebra to create virtual sensors [21]. The technique uses the modal superposition/modal decorrelation [34] to estimate the response of the entire structure. It is a subspace projection or a linear transformation of the spatial limited response onto the linear subspace (vector space) spanned by the mode shapes, see Fig 7.2.

7.7.1 Modal decorrelation

The response of a linear system is the solution to the differential equation - the equation of motion [34].

$$\mathbf{M}\ddot{\mathbf{y}}(t) + \mathbf{C}\dot{\mathbf{y}}(t) + \mathbf{K}\mathbf{y}(t) = \mathbf{x}(t) \quad (7.1)$$

where $\mathbf{M} \in \mathbb{R}^{N \times N}$, $\mathbf{C} \in \mathbb{R}^{N \times N}$, and $\mathbf{K} \in \mathbb{R}^{N \times N}$ is the mass, damping and stiffness matrix and $\mathbf{y}(t) \in \mathbb{R}^N$, $\dot{\mathbf{y}}(t) \in \mathbb{R}^N$, and $\ddot{\mathbf{y}}(t) \in \mathbb{R}^N$ are displacement, velocity, and acceleration of the system while $\mathbf{x}(t) \in \mathbb{R}^N$ is the load and N is the number of DOFs in the system. For proportional damping, we use the undamped equation of motion to find the mode shapes of the system through the eigenvalue problem.

$$\mathbf{M}^{-1}\mathbf{K} = \Phi [\omega_n^2] \Phi^{-1} \quad (7.2)$$

where $\Phi \in \mathbb{R}^{N \times N}$ is the modal matrix, which contains all mode shapes as column vectors, $\Phi = [\phi_1, \dots, \phi_N]$, and it forms an eigenbasis for \mathbb{R}^N . Thus, the response of a linear structure is located within the vector space spanned by the mode shapes. In terms of linear algebra, the modal matrix defines the column space (also called image or range) of the system response, $C(\Phi) = \text{span}(\phi_1, \dots, \phi_N)$, and it is called the transformation or design matrix. Hence, any response, $\mathbf{y}(t)$, is a linear combination of the mode shapes [34] - this characteristic is called the modal decorrelation.

$$\mathbf{y}(t) = \Phi \mathbf{q}(t) \quad (7.3)$$

where $\mathbf{q}(t) \in \mathbb{R}^N$ contains the modal coordinates.

7.7.2 Modal truncation and spatial limited response

Let us say that we only know K mode shapes, $\tilde{\Phi} = [\phi_1, \dots, \phi_K] \in \mathbb{R}^{N \times K}$, then the column space of this truncated and approximated modal matrix is an approximation of the linear subspace of the system, $C(\tilde{\Phi}) \approx C(\Phi)$. Furthermore, let us assume that we measure the spatial limited system response, $\mathbf{y}_a(t) \in \mathbb{R}^a$, with a sensors. The modal matrix has the same spatial limitation, $\tilde{\Phi}_a \in \mathbb{R}^{a \times K}$.

$$\mathbf{y}(t) = \begin{bmatrix} \mathbf{y}_a(t) \\ \mathbf{y}_d(t) \end{bmatrix}, \quad \tilde{\Phi} = \begin{bmatrix} \tilde{\Phi}_a \\ \tilde{\Phi}_d \end{bmatrix} \quad (7.4)$$

where the subscript $[\cdot]_a$ denotes the active degrees-of-freedom and the subscript $[\cdot]_d$ denotes the inactive degrees-of-freedom.

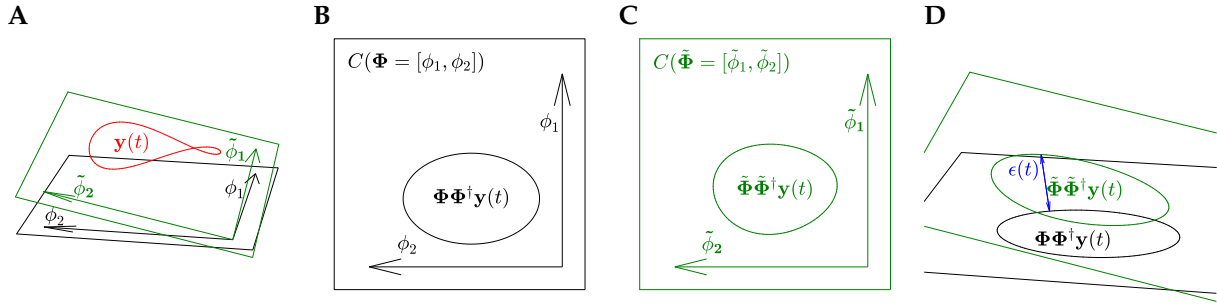


Figure 7.3: The principle of modal expansion with errors in the mode shapes illustrated in \mathbb{R}^3 with a two-dimensional subspace: We have the response, $\mathbf{y}(t)$, and two sets of mode shapes; the correct set ϕ_1 & ϕ_2 and the erroneous set $\tilde{\phi}_1$ & $\tilde{\phi}_2$. **A)** shows the subspaces of these two sets, **B)** and **C)** are the orthogonal view of the subspace and projected response onto this space for the two sets of mode shapes, and **D)** is the error caused by the erroneous subspace

Finally, we add noise to the system response, $\tilde{\mathbf{y}}_a(t) = \mathbf{y}_a(t) + \mathbf{n}(t) \in \mathbb{R}^a$, so the new response locates partially outside the column space of the truncated and spatial limited modal matrix, $\tilde{\mathbf{y}}_a(t) \notin C(\tilde{\Phi}_a)$.

We estimate the modal coordinates by transforming the measured response using the modal decorrelation, Eq. (7.3).

$$\hat{\mathbf{q}}(t) = \tilde{\Phi}_a^\dagger \tilde{\mathbf{y}}_a(t) \quad (7.5)$$

where $[\cdot]^\dagger$ denotes the Moore–Penrose inverse.

Now, we transform the estimated modal coordinates into the physical domain, which is similar to a subspace project of the measured response onto the column space, $C(\tilde{\Phi}_a)$.

$$\hat{\mathbf{y}}_a(t) = \text{proj}_{C(\tilde{\Phi}_a)}(\tilde{\mathbf{y}}_a(t)) = \tilde{\Phi}_a \hat{\mathbf{q}}(t) \quad (7.6)$$

where

$$\begin{aligned} \hat{\mathbf{y}}_a(t) &\in C(\tilde{\Phi}_a) = \text{span}(\phi_{a,1}, \dots, \phi_{a,K}) \\ \hat{\mathbf{y}}_a(t) &\notin C(\tilde{\Phi}_a)^\perp = \text{span}(\phi_{a,K+1}, \dots, \phi_{a,N}) \end{aligned} \quad (7.7)$$

In this way, the modal expansion works as a subspace reduction - called modal filtering [35] - that removes any noise or response orthogonal to the applied subspace. The reader should note that this only holds for the full spatial mode shapes and we always need more sensors than the number of modes, $a > K$, to avoid overfitting. Furthermore, the subspace reduction/modal filtering depends on the truncation, resolution, and the quality of the applied mode shapes and the system response.

It is important that the applied modal matrix spans the response. A truncation of applied mode shapes might lead to modal truncation errors [36] while erroneous mode shapes (caused by modelling errors) introduce errors, see Fig. 7.3. Thus, the column space of the used modal matrix should be close to the actual column space of the system, $C(\tilde{\Phi}) \approx C(\Phi)$.

7.7.3 Modal expansion and strain estimation

For virtual sensing, we expand the estimated response from Eq. (7.6) by replacing the spatial limited mode shape, $\tilde{\Phi}_a$, with the full modal matrix, $\tilde{\Phi}$, containing all DOFs. Thus, we obtain full-field measurements of the system.

$$\hat{\mathbf{y}}(t) = \tilde{\Phi} \hat{\mathbf{q}}(t) \quad (7.8)$$

Similarly, for strain estimation, we use the modal coordinates from Eq. (7.5) to estimate the strain response of the structure since the modal coordinates for strain and displacement are the same [37]. To create virtual strain gauges at any point of the structure, we use the strain mode shapes - mode shapes expressed in strains instead of displacement.

$$\hat{\boldsymbol{\epsilon}}(t) = \tilde{\Phi}_\epsilon \hat{\mathbf{q}}(t) \quad (7.9)$$

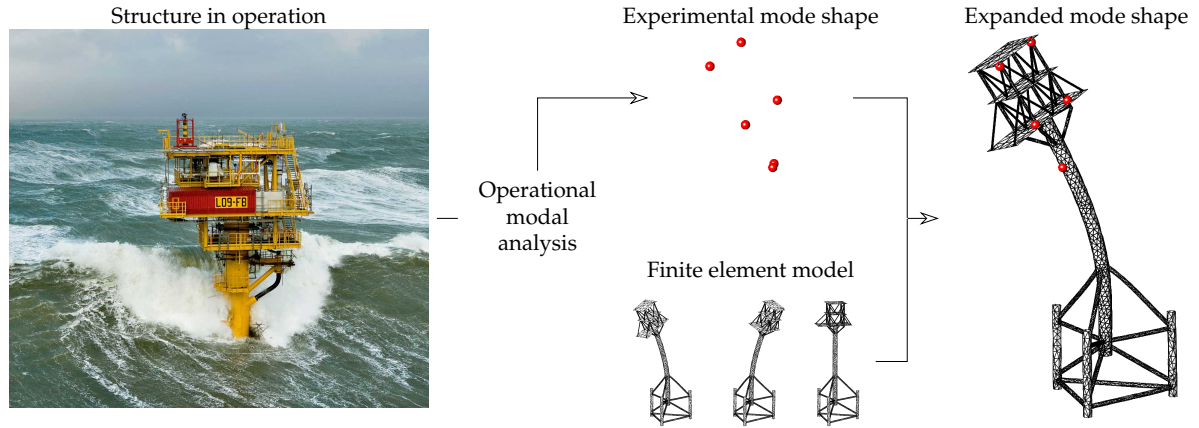


Figure 7.4: Illustration of mode shape expansion

where $\tilde{\Phi}_\varepsilon \in \mathbb{R}^{b \times K}$ is the strain mode shape matrix, $\hat{\boldsymbol{\varepsilon}}(t) \in \mathbb{R}^b$ is the estimated strain response of the entire structure, and b is the number of virtual strain gauges. Each strain mode shape is the static strain caused by a deflection corresponding to each mode shape [38].

$$\tilde{\Phi}_\varepsilon = \mathbf{T}_\varepsilon \tilde{\Phi} \quad (7.10)$$

where $\mathbf{T}_\varepsilon \in \mathbb{R}^{b \times N}$ the displacement-to-strain transformation matrix. Thus, in the case of a dimensionless mode shape matrix, the strain mode shapes have the unit $[m^{-1}]$ since it is a dimensionless displacement relative to a geometric quantity of the structure.

7.7.4 Expansion of experimental mode shapes

We want to apply the modal matrix with a column space closest to the actual system, $C(\Phi)$, and the expansion of experimental mode shapes has the potential to do this. Skaftø [39] and Levine [40] investigate the expansion of experimental mode shapes and we refer the reader to these for further details on the subject. Fig. 7.4 illustrates the process of mode shape expansion for operational modal analysis.

The hypotheses behind mode shape expansion is that experimental mode shapes are more representable of the real structure than a finite element model. Thus, expanded experimental mode shapes are closer to the actual structure than the finite element mode shapes. In other words, we can use expanded experimental mode shapes to reduce modelling errors from the finite element model. As previously stated, different techniques exist for expanding or reducing mode shapes but they might all introduce fitting errors in the attempt to reduce modelling errors.

Generally, mode shape expansion/reduction finds a linear relationship between the mode shapes from experiments, $\Phi_{exp} \in \mathbb{R}^{a \times K}$, and the finite element model, $\Phi_{FE} \in \mathbb{R}^{N \times N}$. Thus, we can transform the experimental mode shapes linearly to the reduced finite element, $\Phi_{FE,a} \in \mathbb{R}^{a \times N}$.

$$\begin{aligned} \Phi_{exp} &= \Phi_{FE,a} \mathbf{T}_1 \\ &= \mathbf{T}_2 \Phi_{FE,a} \end{aligned} \quad (7.11)$$

where $\mathbf{T}_1 \in \mathbb{R}^{N \times K}$ and $\mathbf{T}_2 \in \mathbb{R}^{K \times N}$ are transformation matrices, which hold the linear relationship.

Using the full finite element mode shape matrix, we expand the experimental mode shape to hold all the same DOFs as the finite element model.

$$\begin{aligned} \Phi_{exp,full} &= \Phi_{FE} \mathbf{T}_1 \\ &= \mathbf{T}_2 \Phi_{FE} \end{aligned} \quad (7.12)$$

The reader should note that although the majority of expansion techniques follow the framework in Eqs. (7.11) and (7.12), there are exceptions. These alternative frameworks are outside the scope of this paper.

The linear relationship in Eq. (7.11) is similar to structural modification theory stating that two similar systems have a linear relationship between their mode shape matrices [41]. Let us say that we have a system called A and a perturbed version of this system called B . The mode shapes of system B are a

linear combination of the mode shape of system A , $\Phi_A = \Phi_B \mathbf{T}$, or the other way around. Hence, we can transform the mode shape from one system to the other and this transformation is, essentially, an update from one system to the other.

Given the correct transformation matrix, the expansion of the experimental mode shape is similar to an update of the finite element model. Recently, it has even been applied directly to finite element updating using the mode shape orthogonality equations [42]. The quality of the expansion or finite element update, however, depends on the position and quality of sensors, errors from the identification process of the experimental mode shapes, and their correlation with the finite element model [39, 40].

In this paper, we will apply SEREP [28] and two versions of the local correspondence principle [33].

System Equivalent Reduction Expansion Process (SEREP)

Originally, SEREP was a global mapping technique used to estimate rotational degrees-of-freedom from experimental data [28]. The active DOFs (sensors) of a mode shape matrix relate to the full set of DOFs, hence, it results in a linear transformation of the active DOFs to all DOFs. We will use a similar principle to expand experimental mode shapes by using a reduced finite element model with the same DOF as the experimental mode shape. Furthermore,

$$\Phi_{exp} = \mathbf{T}_{SEREP} \Phi_{FE,a} \quad (7.13)$$

We calculate the transformation matrix, $\mathbf{T}_{SEREP} \in \mathbb{R}^{K \times N}$, using the Moore-Penrose pseudo inverse of the finite element mode shapes.

$$\mathbf{T}_{SEREP} = \Phi_{exp} \Phi_{FE,a}^\dagger \quad (7.14)$$

The linear transformation matrix, \mathbf{T}_{SEREP} , should - preferably - be non-square and we should have less finite element mode shapes for the expansion than active DOFs to minimise the chance of overfitting. When transformation matrices are square, the Moore-Penrose pseudo inverse becomes the general inverse and it is often referred to as SEREPa. Therefore, the number of finite element mode shapes is an important parameter and it relates to the fitting errors.

Local correspondence principle

The local correspondence principle [33] follows the same basic equations as SEREP but it differs in one important aspect: each experimental mode is expanded individually using an optimised subset of finite element modes in an iteration process. The local correspondence principle originates from the mode shape sensitivity equations and it utilises that a change in a mode shape is primarily a linear combination of the surrounding modes (in natural frequency). The local correspondence principle finds an optimised subset of the closest surrounding modes using cross-validation to expand the given experimental mode shape. The i^{th} mode shape is expanded by

$$\phi_{exp,i} = \Phi_{FEP} \mathbf{p}_i \quad (7.15)$$

where $\mathbf{p}_i \in \mathbb{R}^N$ is a projection vector given by

$$\mathbf{p}_i = (\Phi_{FE} \mathbf{S}_i)^\dagger \phi_{exp,i} \quad (7.16)$$

where $\mathbf{S}_i \in \mathbb{R}^{N \times N}$ is a diagonal cluster selection matrix that defines the optimal cluster of finite element mode shapes. To find this optimal subset of finite element modes, \mathbf{S}_i , used for the expansion, Eqs. (7.15) and (7.16) are calculated repeatedly by adding more finite element modes to the subset at each iteration. The optimal subset of finite element modes is chosen as the combination that gives the best correlation between the experimental and expanded mode shape.

The optimisation procedure has two different approaches. In the first, modes are iteratively added to the subset according to their distance in frequency to the corresponding mode, in descending order. The second approach adds modes to the subset according to the highest increment in the correlation between the expanded and experimental mode. In this paper, we will focus on the first approach.

As previously stated, the local correspondence principle uses cross-validation (or leave-one-out) from statistics and machine learning [43] to find the optimal number of mode shapes. In k -fold cross-validation, the data set is split into k subsets that we use either for fitting/training or observation/validation. A fitting set is used to estimate a model - a transformation matrix - and an observation set is

used to check the model to reduce the chance of overfitting. For the local correspondence, the active DOFs from the experimental mode shapes are divided into a fitting, $\boldsymbol{\phi}_{exp,fit,i} \in \mathbb{R}^{a-1}$, and an observation set, $\boldsymbol{\phi}_{exp,obs,i} \in \mathbb{R}^1$, where the observation set has a single DOF that is rowed through all DOFs [33]. This approach corresponds to a repeated leave-one-out cross-validation that is repeated for all combinations. Then, we calculate the transformation matrix for the given cluster of finite element modes.

$$\tilde{\mathbf{p}}_i(m) = \left(\boldsymbol{\Phi}_{FE,fit} \mathbf{S}(m) \right)^\dagger \boldsymbol{\phi}_{exp,fit,i} \quad (7.17)$$

where $\tilde{\mathbf{p}}_i(m) \in \mathbb{R}^N$ is the projection vector as a function of m , which is the number of finite element mode shapes in the cluster, $\mathbf{S}(m) \in \mathbb{R}^{N \times N}$ is the diagonal cluster selection matrix as a function of m , and $\boldsymbol{\Phi}_{FE,fit} \in \mathbb{R}^{(a-1) \times N}$ is the finite element mode shape with fitting DOFs.

Then, we calculate the estimated experimental mode shape, which we call the *smoothed experimental mode shape*.

$$\tilde{\boldsymbol{\phi}}_{exp,i}(m) = \boldsymbol{\Phi}_{FE} \tilde{\mathbf{p}}_i(m) \quad (7.18)$$

Using the observation set, we calculate the Modal Assurance Criterion (MAC) value between the experimental mode shape, $\boldsymbol{\phi}_{exp,obs,i}$, and the estimated mode shape, $\tilde{\boldsymbol{\phi}}_{exp,obs,i}(m)$, to check the quality of the fit.

$$F_{obs,i}(m) = \frac{\left| \tilde{\boldsymbol{\phi}}_{exp,obs,i}(m)^H \boldsymbol{\phi}_{exp,obs,i} \right|^2}{\left(\tilde{\boldsymbol{\phi}}_{exp,obs,i}(m)^H \tilde{\boldsymbol{\phi}}_{exp,obs,i}(m) \right) \left(\boldsymbol{\phi}_{exp,obs,i}^H \boldsymbol{\phi}_{exp,obs,i} \right)} \quad (7.19)$$

The highest MAC value, $F_{obs}(m)$, indicates the optimal number of finite element modes in the cluster, $m_{optimal}$, and we obtain the cluster selection matrix, $\mathbf{S}_i = \mathbf{S}(m_{optimal})$. The cross-validation indicates that the number of modes in a smoothing or expansion process using the local correspondence principle is of minor importance.

To sum up the algorithm:

1. Divide the experimental mode shape into a fitting and observation set of DOFs
2. Rank the finite element mode shapes after their local correspondence to the experimental mode - either in frequency or highest correlation between experimental and finite element mode shapes
3. Make the cluster selection matrix, $\mathbf{S}(m)$, and calculate the transformation matrix, $\tilde{\mathbf{p}}_i(m)$
4. Calculate the quality of the fit for the observation set, Eq. (7.19), between the smoothed and the actual experimental mode shape for each cluster
5. Pick the cluster selection matrix, \mathbf{S}_i , that provides the best quality of the fit

Local correspondence principle - leave- p -out-cross-validation

For this article, we introduce a "leave- p -out-cross-validation" implementation of the local correspondence principle where we specify the value p . Similarly, the active DOFs from the experimental mode shape are divided into two sets: the fitting/training and the observation set. The difference from the original implementation of local correspondence is that the observation sets have p DOFs instead of a single DOF. We calculate all combinations of fitting and observation sets, which results in $\frac{a!}{(a-p)!p!}$ combinations of sets where a is the total number of active DOFs. Alternatively, a random selection of these combinations could be applied to minimise computation time. The median is used for all combinations to obtain $F_{obs}(m)$.

Generally, there are errors in both the fitting/training and the observation set since there is uncertainty in each DOF. Lowering p increases the errors related to the observation set while the errors in the fitting set increase when p increases. Thus, the choice of p is important since a low p increases the observation error while a high p results in higher fitting errors. Generally, low p values - relative to the total number of DOFs - lead to clusters with more finite element mode shapes while high p values result in clusters with fewer finite element mode shapes.

7.8 Case study

We will study the effect of expanding mode shapes using SEREP, the local correspondence principle, and the "leave- p -out-cross-validation" implementation of the local correspondence principle in regard to strain estimation, and compare the results to strain estimation based on the finite element mode shape.

We will have two case studies: with and without frequency bands associated with specific modes. In the literature, frequency bands are used for modal expansion to reduce the chance of overfitting [5, 7].

7.8.1 Quality measurements

Multiple approaches exist for checking the quality of the strain estimation and they have different strengths and weaknesses.

Time Response Assurance Criterion (TRAC) and Frequency Response Assurance Criterion (FRAC)

In the literature, the Time Response Assurance Criterion (TRAC) [6] and the Frequency Response Assurance Criterion (FRAC) [44] are the most popular quality measurements.

$$TRAC_i = \frac{\left(\boldsymbol{\varepsilon}_{t,i}^\top \widehat{\boldsymbol{\varepsilon}}_{t,i}\right)^2}{\left(\boldsymbol{\varepsilon}_{t,i}^\top \boldsymbol{\varepsilon}_{t,i}\right) \left(\widehat{\boldsymbol{\varepsilon}}_{t,i}^\top \widehat{\boldsymbol{\varepsilon}}_{t,i}\right)}, \quad FRAC_i = \frac{\left(\boldsymbol{\varepsilon}_{f,i}^\top \widehat{\boldsymbol{\varepsilon}}_{f,i}\right)^2}{\left(\boldsymbol{\varepsilon}_{f,i}^\top \boldsymbol{\varepsilon}_{f,i}\right) \left(\widehat{\boldsymbol{\varepsilon}}_{f,i}^\top \widehat{\boldsymbol{\varepsilon}}_{f,i}\right)} \quad (7.20)$$

where $\boldsymbol{\varepsilon}_{t,i}$ is the entire discrete time history of the measured strain response for strain gauge i arranged in a column vector, and similarly, $\widehat{\boldsymbol{\varepsilon}}_{t,i}$ is the estimated strain response at the same location in the time domain. Furthermore, $\boldsymbol{\varepsilon}_{f,i}$ is the direct Fourier transformed of the measured strain response for the i^{th} strain gauge arranged in a column vector, and similarly, $\widehat{\boldsymbol{\varepsilon}}_{f,i}$ is the frequency estimation of strain response in the same position. These measurements check the general relationship between two signals where a value of 1 corresponds to perfect correlation while a value of 0 indicates independence between the signals. TRAC and FRAC are, however, independent of amplitude differences.

Mean errors

To account for an amplitude differences, we apply different metrics of the mean error from statistics. The Mean Squared Error (MSE) measures the averaged value of the squared errors between a reference signal and an estimated signal.

$$MSE_i = E \left[(\boldsymbol{\varepsilon}_i(t_k) - \widehat{\boldsymbol{\varepsilon}}_i(t_k))^2 \right] \quad (7.21)$$

where $\boldsymbol{\varepsilon}_i(t)$ is the measured strain response (reference signal) in the i^{th} strain gauge, $\widehat{\boldsymbol{\varepsilon}}_i(t)$ is the estimated strain response at the same location, and $E[\cdot]$ denotes the expected value.

The Mean Absolute Error (MAE) is another measurement of the difference between two signals.

$$MAE_i = E [|\boldsymbol{\varepsilon}_i(t_k) - \widehat{\boldsymbol{\varepsilon}}_i(t_k)|] \quad (7.22)$$

These metrics are independent of the amplitude of the reference signal, therefore, these are often normalised to obtain the relative mean error.

Coefficient of determination, R^2

The coefficient of determination, R_i^2 , is often used in model validation [45] (not to confuse with the Pearson correlation coefficient) and it is the mean squared error normalised with the variance of the reference signal. Thus, it takes into account both amplitude differences and the general amplitude of the reference signal. A coefficient of determination with a value of 1 indicates perfect correlation with the same amplitudes.

$$R_i^2 = 1 - \frac{E \left[(\boldsymbol{\varepsilon}_i(t_k) - \widehat{\boldsymbol{\varepsilon}}_i(t_k))^2 \right]}{\text{Var} [\boldsymbol{\varepsilon}_i(t_k)]} \quad (7.23)$$

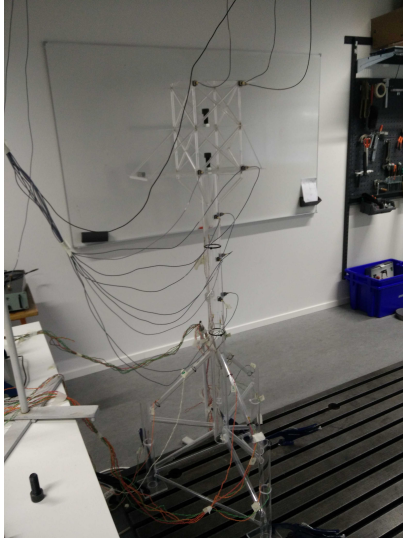


Figure 7.5: Photo of the scale model in the lab

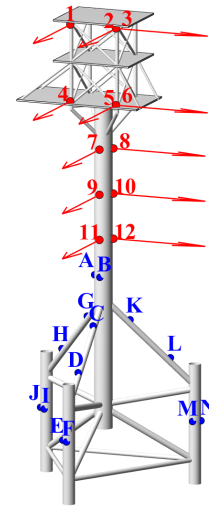


Figure 7.6: Position of sensors on the test specimen, red arrows show Brüel & Kjær 4508-B-002 uniaxial accelerometers and blue dots show HBM 1-LY11-0.3/120 strain gauges measuring along the longitudinal direction of the members

Normalised error of fatigue damage

Strain/stress estimation is intended for a fatigue analysis, hence, it is important to compare the estimated stress with the measured stress in cycle counting since fatigue life depends mainly on the stress ranges [46, 47]. We will set up a new quality measurement based on the SN-curve (excluding the effect of a bilinear SN curve) and the Palmgren-Miners Rule

$$D_i = \sum_{j=1}^{n_{cycles}} \frac{1}{N_j} = \sum_{j=1}^{n_{cycles}} \frac{\Delta\sigma_j^m}{C} = \frac{E^m}{C} \sum_{j=1}^{n_{cycles}} \Delta\varepsilon_j^m \quad (7.24)$$

where D_i is the cumulated fatigue damage in the i^{th} fatigue location, n_{cycles} is the total number of counted cycles, N_j is the number of cycles for fatigue failure at the given stress range, $\Delta\sigma_j$, C is the fatigue capacity (the intercept of $\log(N)$ axis in the SN curve), m is the "slope" of the SN curve, E is the modulus of elasticity, and $\Delta\varepsilon_j$ is the strain range from cycle counting. Thus, the normalised error of fatigue damage between the estimated and the measured fatigue damage is given by

$$\eta_i = \frac{\hat{D}_i - D_i}{D_i} = \frac{\sum_{j=1}^{n_{cycles}} \Delta\hat{\varepsilon}_j^m}{\sum_{j=1}^{n_{cycles}} \Delta\varepsilon_j^m} - 1 \quad (7.25)$$

where $\eta_i = 0$ indicates a perfect estimation of strain, a negative value means an underestimation of fatigue damage, and a positive value indicates an overestimation of fatigue damage.

This quality measurement is independent of the fatigue capacity and modulus of elasticity. It depends on the applied cycle counting algorithm and the "slope", m , from the SN curve, which are the same parameters used in the calculated fatigue damage. Thus, the normalised error of fatigue damage is a measurement of fatigue damage based on the strain response from a reference and an estimated signal. For the remainder of this paper, we will use $m = 3$, which corresponds to welded steel structures [47].

7.8.2 Scale Model of an offshore platform in the laboratory

We will use a 1:50 geometric scale model of a tripod oil platform made of polymethyl methacrylate, see Fig. 7.5 and see Skafte et al. [5] for additional information on the scale model. The entire study ran in a laboratory facility where environmental and operational effects were controlled. Thus, environmental and operational variations for real offshore structures are neglected in this study.

Table 7.1: Modal Parameters

| Mode | | 1 | 2 | 3 | 4 | 5 |
|----------------------------|----------------|------|------|------|-------|-------|
| Finite Element Model | Frequency [Hz] | 10.1 | 10.2 | 24.9 | 65.1 | 71.7 |
| Operational Modal Analysis | Frequency [Hz] | 9.20 | 9.38 | 23.6 | 66.9 | 75.4 |
| Difference | [%] | 9.78 | 8.74 | 5.51 | -2.69 | -4.91 |

We excite the model by brushing the topside with a nylon brush and this loading has a high level of white noise characteristics. Real offshore structures, however, experience some quasi-static response due to the wave and this complicates stress/strain estimation since it introduces modal truncation errors [36]. In this study, the quasi-static response is excluded and we refer to [5, 7] for further information on this topic. The multiple ambient and operational loads of an offshore structure approximate as white noise excitation due to the central limit theorem - a common assumption in operational modal analysis [35]. Thus, in this paper, we study virtual sensing in the dynamic range of the model.

For the measurement-setup, we have 12 Brüel & Kjær 4508-B-002 uniaxial accelerometers with a sensitivity of 100 mV/g on the topside and 14 HBM 1-LY11-0.3/120 strain gauges, with a gauge factor of 2, on the lower part of the model, corresponding to subsea, see Fig. 7.6. No calibration was performed after the installation of the strain gauges. Each strain gauges are applied in Wheatstone bridge circuits using the quarter bridge configuration. The locations of the sensors mimic the real offshore conditions so all accelerometers are positioned above water while the strain gauges are placed subsea.

We sample the data at a frequency of 1651 Hz using NI9134 and NI9135 DAQ modules. To remove noise around DC and measurement noise, we bandpass filter the data with cut-off frequencies at 6 and 80 Hz. We use operational modal analysis to extract the modal parameters from the system [35]. For the identification process, we decimate the data to a new sampling frequency of 206 Hz [48], and we calculate the correlation function and spectral density matrices using a segment size of 1024 [35]. To remove uncorrelated measurement noise, we omit the first ten discrete time lags. We apply the Eigen-system Realization Algorithm (ERA) [49] to identify modal parameters from the correlation function matrix using two block rows in the Hankel block matrices and five singular values in the singular value decomposition, see Table 7.1 and Fig. 7.7.

Then we created a finite element model of the scale model in Nastran/Patran and updated the modulus of elasticity of the model to match the modal parameters of the modes with primary focus on matching mode shapes. The update was a compromise between all five modes where the frequency of the first two bending modes are a bit too high in the finite element model compared to the experimental modes while the second two finite element bending modes are too low. The experimental mode shapes are similar to the mode shapes from the finite element model as seen in the MAC values in Fig. 7.8.

We integrate the acceleration response from the accelerometers twice to get the displacement, $\mathbf{y}(t)$, by the use of the Fourier transformation [35].

$$\mathbf{y}(t) = \mathcal{F}^{-1} \left(\frac{1}{-\omega^2} \mathcal{F}(\ddot{\mathbf{y}}(t)) \right) \quad (7.26)$$

where $\mathcal{F}(\cdot)$ and $\mathcal{F}^{-1}(\cdot)$ denote the standard and inverse Fourier transformation, respectively.

Then, we estimate the strain response in all points where strain gauges were positioned, see Fig. 7.6, and we apply Rainflow Counting [50].

Without frequency bands

We use all five mode shapes on the filtered response for strain estimation. Figs. 7.9-7.20 display the results of the strain estimation using the different sets of mode shapes.

Generally, the expanded mode shapes, using the leave- p -out implementation of the local correspondence principle, lead to the smallest normalised error of fatigue damage, but they also lead to three instances where they underestimate the fatigue damage compared to the other expansion techniques.

Both expanded experimental and finite element mode shapes provide a good basis for strain estimation for strain gauge A and B, which are located on the main column of the structure. Generally for strain gauge A and B, all mode shapes lead to a minor underestimation of the fatigue damage, see Fig. 7.14, since they all underestimate the number of cycles for low strain ranges, see Fig. 7.19. The noise floor of the strain gauges is located at -120 dB, see Figs. 7.17 and 7.18, and this creates a potential source of error since the strain gauges are used as a reference. Whenever the estimated strain drops below the noise

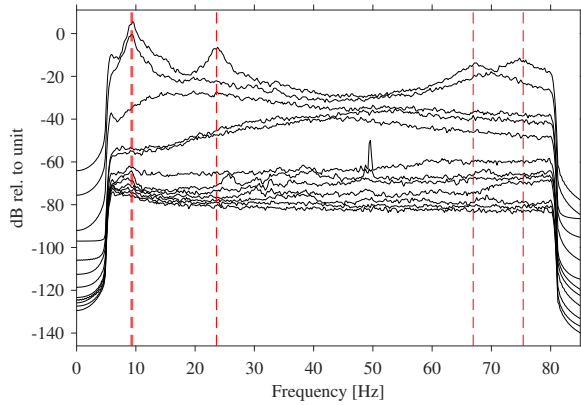


Figure 7.7: Singular values of spectral density matrix from scale model and the identified modes from an operational modal analysis using the Eigensystem Realization Algorithm (ERA) [49]

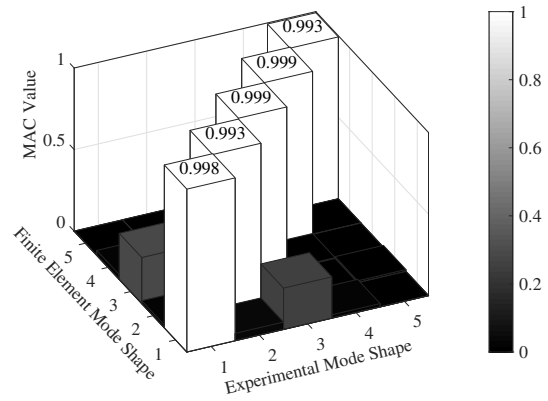


Figure 7.8: Modal Assurance Criterion (MAC) between experimental and finite element mode shapes

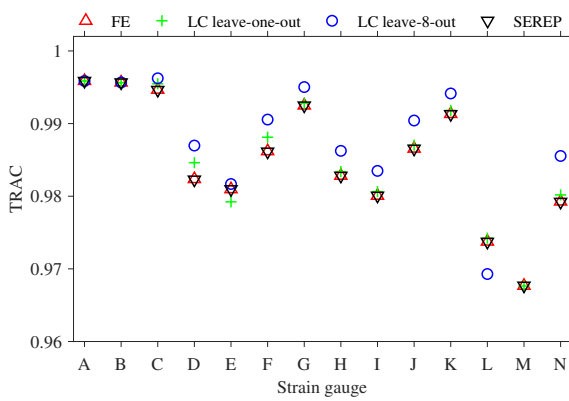


Figure 7.9: Scale model of an offshore platform without frequency bands: Time Response Assurance Criterion (TRAC), Eq. (7.20)

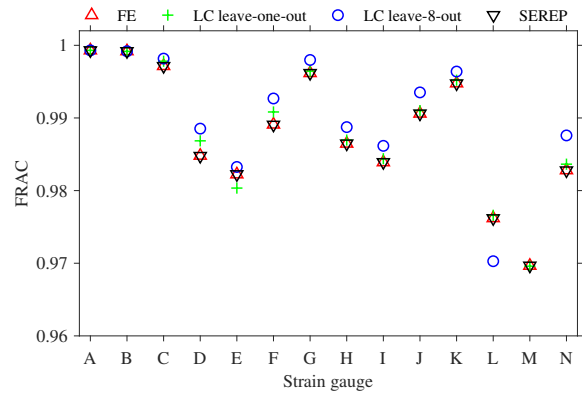


Figure 7.10: Scale model of an offshore platform without frequency bands: Frequency Response Assurance Criterion (FRAC), Eq. (7.20)

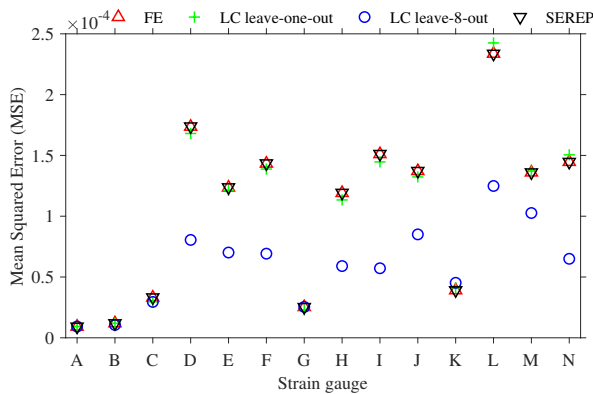


Figure 7.11: Scale model of an offshore platform without frequency bands: Mean Squared Error (MSE), Eq. (7.21)

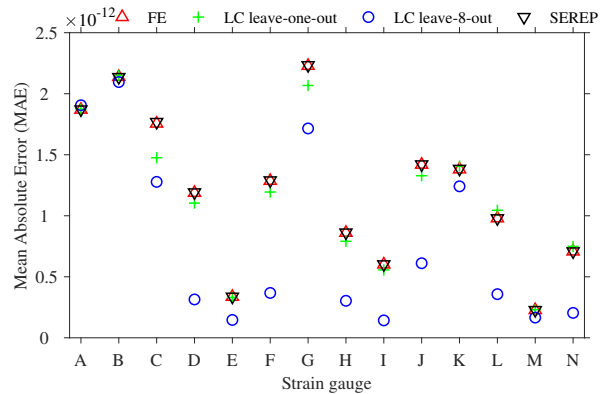


Figure 7.12: Scale model of an offshore platform without frequency bands: Mean Absolute Error (MAE), Eq. (7.22)

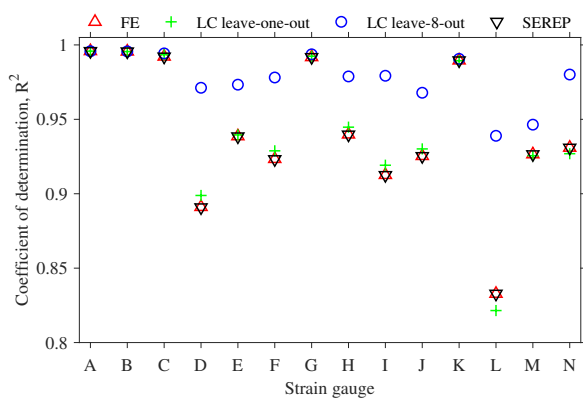


Figure 7.13: Scale model of an offshore platform without frequency bands: coefficient of determination (R^2), Eq. (7.23)

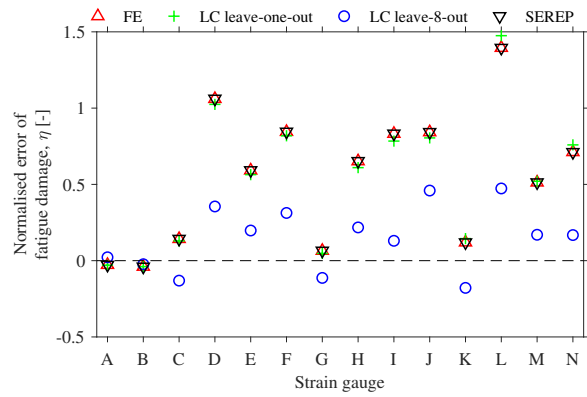


Figure 7.14: Scale model of an offshore platform without frequency bands: normalised error of fatigue damage (η), Eq. (7.25)

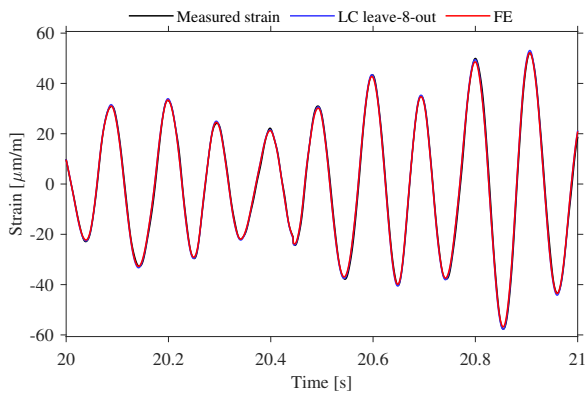


Figure 7.15: Scale Model of an offshore platform without frequency bands: Time History, Strain Gauge A

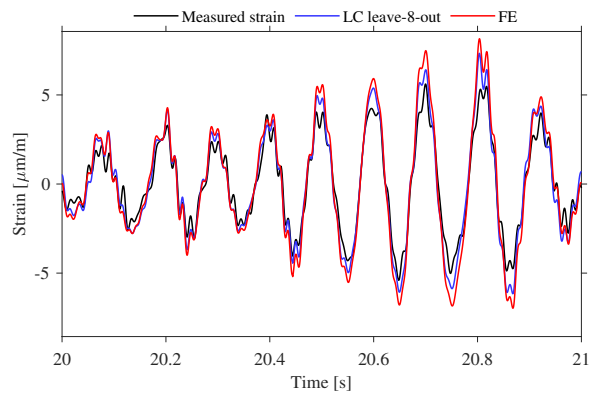


Figure 7.16: Scale Model of an offshore platform without frequency bands: Time History, Strain Gauge L

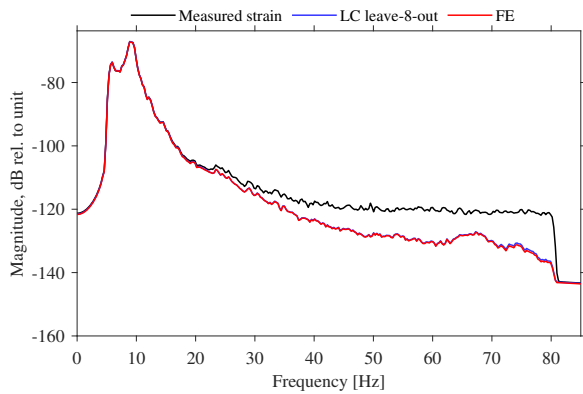


Figure 7.17: Scale Model of an offshore platform without frequency bands: Frequency Spectrum, Strain Gauge A

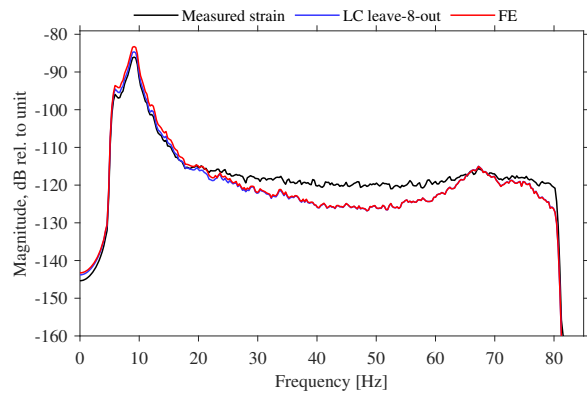


Figure 7.18: Scale Model of an offshore platform without frequency bands: Frequency Spectrum, Strain Gauge L

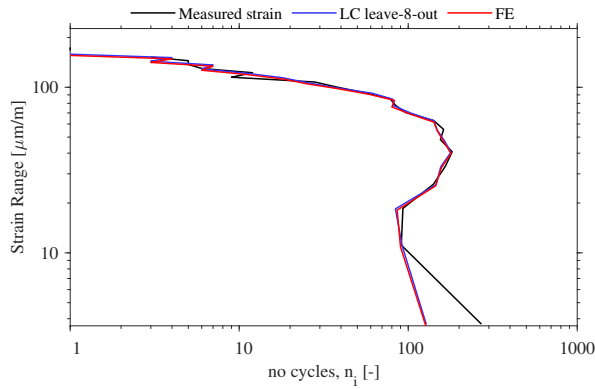


Figure 7.19: Scale Model of an offshore platform without frequency bands: Strain Range Histogram, Strain Gauge A

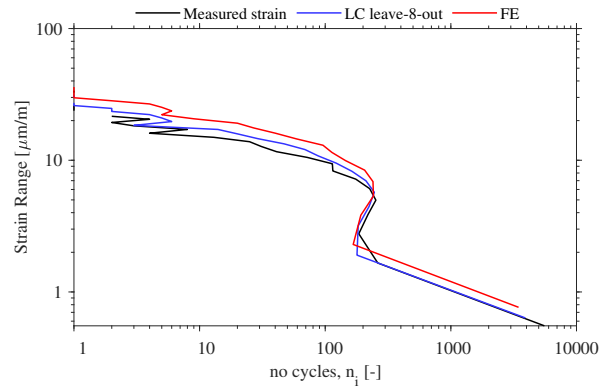


Figure 7.20: Scale Model of an offshore platform without frequency bands: Strain Range Histogram, Strain Gauge L

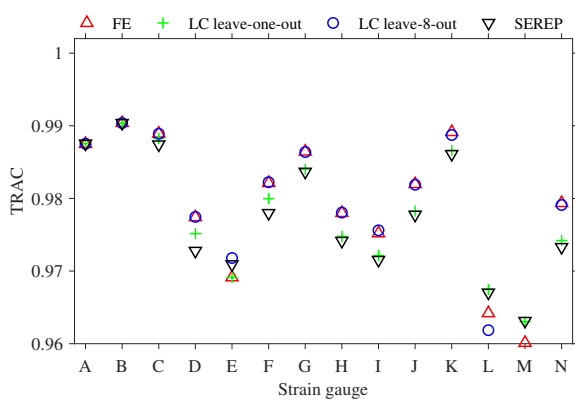


Figure 7.21: Scale model of an offshore platform with frequency bands: Time Response Assurance Criterion (TRAC), Eq. (7.20)

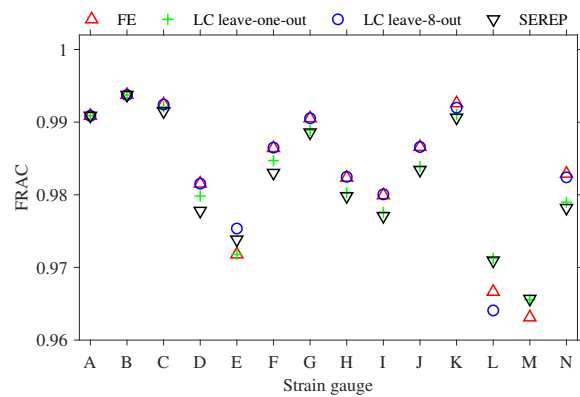


Figure 7.22: Scale model of an offshore platform with frequency bands: Frequency Response Assurance Criterion (FRAC), Eq. (7.20)

floor, we are unaware of the actual quality of the estimation process. We will, however, see a drop in all quality measurements and we will underestimate (in regard to the reference sensor) the fatigue damage.

The TRAC and FRAC values for sensors L and M are better for the finite element mode shapes than for the local correspondence principle with leave-8-out, see Figs. 7.9 and 7.10. These values are, however, misleading as Figs. 7.16 and 7.20 show. Moreover, the other quality measurements contradict the TRAC and FRAC values for sensors L and M indicating that the local correspondence principle with leave-8-out leads to the best estimation. The amplitude, using finite element modes, is too big, which leads to a shifted Strain Range Histogram and therefore incorrect fatigue damage.

The MSE, Fig. 7.11, and MAE, Fig. 7.12, are difficult to comparable across strain gauges since the level of strain response changes considerable for each sensor. Therefore, we can mainly use these metrics to analyse the errors between the different sets of mode shapes for each strain gauge - separately. The coefficient of determination, Fig. 7.13, and the new normalised error of fatigue damage, Fig. 7.14, are relative metrics that are comparable across strain gauges and even other structures.

With frequency bands

We apply two frequency bands with a transition at 30 Hz: the first band, 6 – 30 Hz, contains the first three modes while the second band, 30 – 80 Hz, contains the fourth and fifth mode. Figs. 7.21-7.32 show the results of the strain estimation with the frequency bands.

By applying frequency bands, the finite element mode shapes lead to, approximately, the same results as the expanded experimental mode shapes using the leave- p -out implementation of the local correspondence principle. For some strain gauges, it exceeds the expansion techniques in terms of the coefficient of determination and normalised error of fatigue damage, see Figs. 7.25 and 7.26. Generally for the expanded experimental mode shapes, the use of frequency bands has a minor influence on the strain estimation. Therefore, SEREP and the traditional local correspondence principle produce virtual sensors

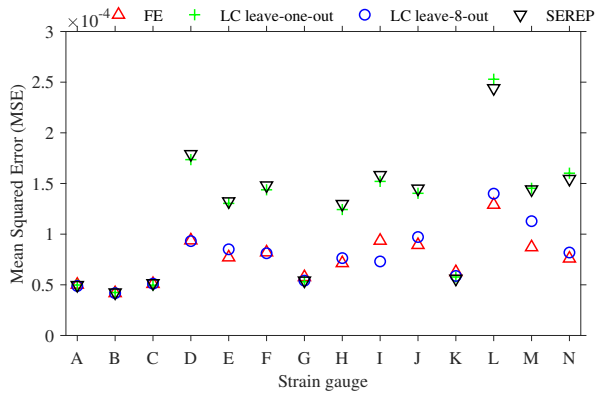


Figure 7.23: Scale model of an offshore platform with frequency bands: Mean Squared Error (MSE), Eq. (7.21)

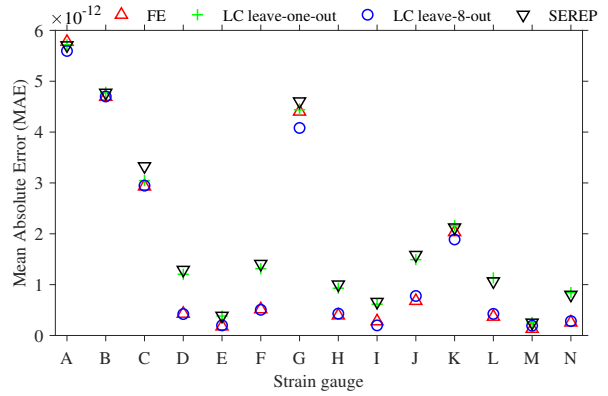


Figure 7.24: Scale model of an offshore platform with frequency bands: Mean Absolute Error (MAE), Eq. (7.22)

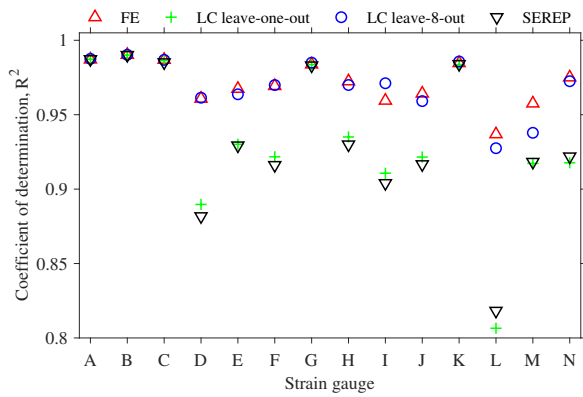


Figure 7.25: Scale model of an offshore platform with frequency bands: coefficient of determination (R^2), Eq. (7.23)

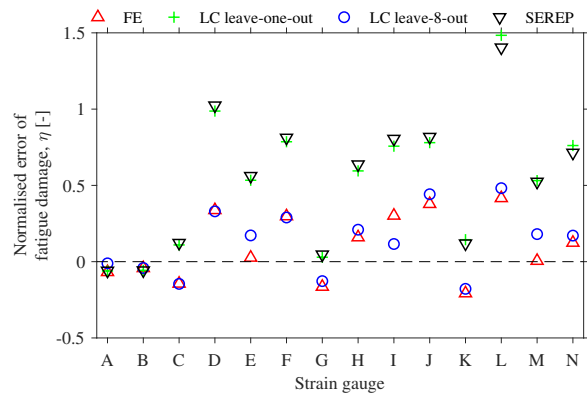


Figure 7.26: Scale model of an offshore platform with frequency bands: normalised error of fatigue damage (η), Eq. (7.25)

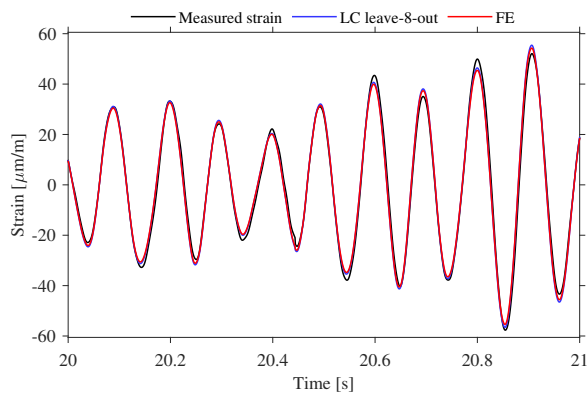


Figure 7.27: Scale Model of an offshore platform with frequency bands: Time History, Strain Gauge A

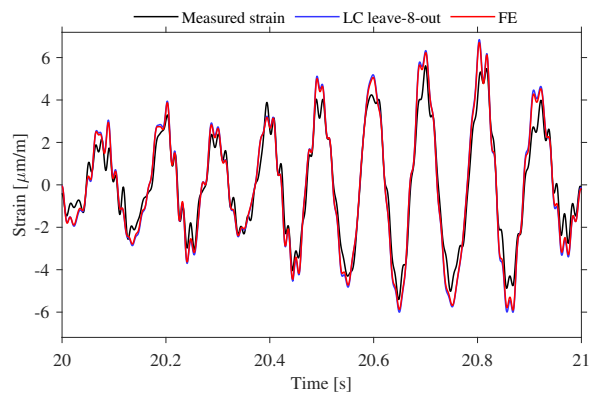


Figure 7.28: Scale Model of an offshore platform with frequency bands: Time History, Strain Gauge L

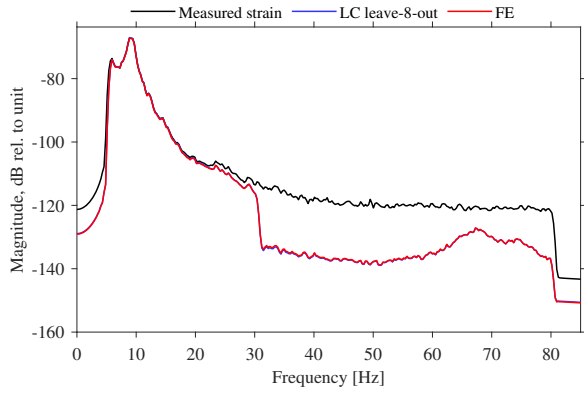


Figure 7.29: Scale Model of an offshore platform with frequency bands: Frequency Spectrum, Strain Gauge A

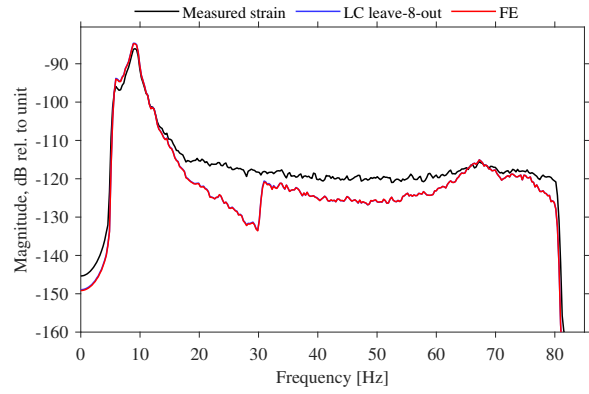


Figure 7.30: Scale Model of an offshore platform with frequency bands: Frequency Spectrum, Strain Gauge L

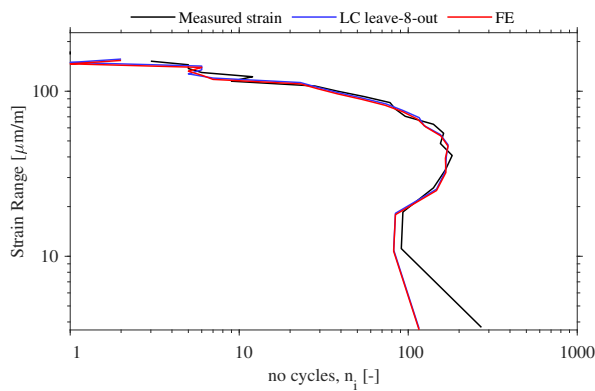


Figure 7.31: Scale Model of an offshore platform with frequency bands: Strain Range Histogram, Strain Gauge A

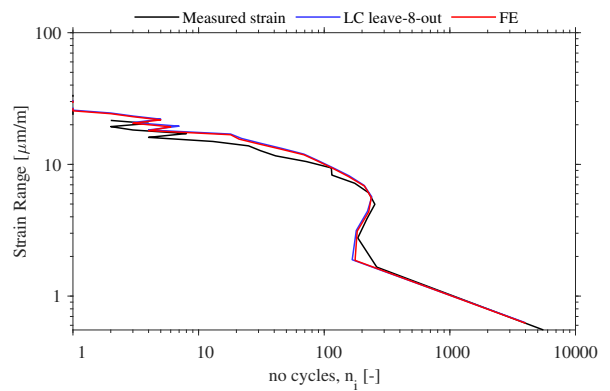


Figure 7.32: Scale Model of an offshore platform with frequency bands: Strain Range Histogram, Strain Gauge L

with more errors than the finite element mode shapes or the leave- p -out implementation of the local correspondence principle. In this case, these two expansion techniques have fitting errors that lead to worse strain estimation than the use of the finite element mode shapes. The expansion of experimental mode shapes, however, depends on the number of finite element mode shapes that is used as a basis for expansion [5]. This parameter study was outside the scope of this paper.

In the frequency domain, we observe a shift in energy at the transition, 30 Hz, between the two frequency bands, see Figs. 7.29 and 7.30. Thus, the strain estimation has issues with modal truncation [36] due to frequency bands where the chosen mode shapes do not span the entire response. Here the subspace projection removes some of the physical response. This causes the normalised error of fatigue damage to amplify slightly for all techniques. Thus, the use of frequency bands increases the chance of modal truncation since the truncated number of modes - associated with a frequency band - might have an insufficient span of the response in the given band. It, however, increases the accuracy of the strain estimation using the finite element model.

7.9 Conclusion

This paper finds that expanding experimental mode shapes can increase the accuracy of a stress estimation using the modal expansion since the expanded mode shapes better span the response of the actual system. Hence, expansion of experimental mode shapes by a finite element model has the potential to reduce the modelling errors of the finite element model. The expansion is, however, a fitting process, which might introduce fitting errors. The experimental mode shapes must be closer to the actual system than the finite element mode shape. Thus, mode shape expansion should be used carefully.

This paper introduced a new implementation of the local correspondence principle by the use of leave- p -out cross-validation. In the presented case study, the new leave- p -out implementation of the local correspondence principle outperforms SEREP and the original local correspondence principle.

This paper finds that the quality measurements TRAC and FRAC values might mislead the quality of strain/stress estimation since they are independent of amplitude differences. Since stress ranges/amplitudes are the most crucial part of fatigue damage, these quality measurements should be used with care. Furthermore, this paper finds that the MSE and MAE values are difficult to compare across different sensors or different case studies since the amplitudes of these values depend on the level of response at each sensor. Therefore, this paper introduced a new quality measurement, normalised error of fatigue damage, for stress estimation based on the normalised fatigue damage. The new quality measurement takes amplitudes into account and it are comparable with across different sensors and with other studies.

Acknowledgements

The authors acknowledge the funding received from the Centre for Oil and Gas - DTU/Danish Hydrocarbon Research and Technology Centre (DHRTC).

The authors thank Anders Skaftø from Aarhus University for his helpful discussions and suggestions on mode shape expansion.

References

- [1] C. R. Farrar and K. Worden. *Structural Health Monitoring: A Machine Learning Perspective*. John Wiley and Sons, Ltd, Chichester, West Sussex, UK, 2013.
- [2] O. Loland and C. J. Dodds. Experiences in developing and operating integrity monitoring systems in the north sea. *Proceedings of Offshore Technology Conference*, 2:313–320, 1976.
- [3] L. Liu, S. M. Kuo, and M. Zhou. Virtual sensing techniques and their applications. In *2009 International Conference on Networking, Sensing and Control*, pages 31–36, March 2009.
- [4] M. Tarpø, B. Nabuco, A. Skaftø, J. Kristoffersen, J. Vestermark, S. Amador, and R. Brincker. Operational modal analysis based prediction of actual stress in an offshore structural model. *Procedia Engineering, X International Conference on Structural Dynamics EURO-DYN 2017*, 199:2262–2267, 2017.
- [5] A. Skaftø, J. Kristoffersen, J. Vestermark, U. T. Tygesen, and R. Brincker. Experimental study of strain prediction on wave induced structures using modal decomposition and quasi static ritz vectors. *Engineering Structures*, 136:261–276, 4/1 2017.

- [6] P. Avitabile and P. Pingle. Prediction of full field dynamic strain from limited sets of measured data. *Shock and Vibration*, 19(5):765–785, 2012.
- [7] A. Iliopoulos, W. Weijtjens, D. Van Hemelrijck, and C. Devriendt. Fatigue assessment of offshore wind turbines on monopile foundations using multi-band modal expansion. *Wind Energy*, 20(8):1463–1479, 2017.
- [8] M. Tarpø, T. Friis, Bruna Nabuco, S Amador, E. Katsanos, and R. Brincker. Operational modal analysis based stress estimation in friction systems. In Gaetan Kerschen, editor, *Nonlinear Dynamics, Volume 1*, pages 143–153, Cham, 2019. Springer International Publishing.
- [9] Bruna Nabuco, Marius Tarpø, Amina Aïssani, and Rune Brincker. Reliability analysis of offshore structures using oma based fatigue stresses. *ASME 2017 36th International Conference on Ocean, Offshore and Arctic Engineering*, 3A: Structures, Safety and Reliability:8, 2017.
- [10] Maximilian Henkel, Wout Weijtjens, and Christof Devriendt. Validation of virtual sensing on subsoil strain data of an offshore wind turbine. *8th International Operational Modal Analysis Conference - IOMAC' 19*, page 10, 2019.
- [11] H.P. Hjelm, R. Brincker, J. Gaugaard-Jensen, and K. Munch. Determination of stress histories in structures by natural input modal analysis. *Proceedings of IMAC XXIII International Modal Analysis Conference*, 12:838–844, 2006.
- [12] Alexandros Iliopoulos, Wout Weijtjens, Danny Van Hemelrijck, and Christof Devriendt. Full-field strain prediction applied to an offshore wind turbine. In Sez Atamturktur, Tyler Schoenherr, Babak Moaveni, and Costas Papadimitriou, editors, *Model Validation and Uncertainty Quantification, Volume 3*, pages 349–357, Cham, 2016. Springer International Publishing.
- [13] J. Kullaa. Bayesian virtual sensing in structural dynamics. *Mechanical Systems and Signal Processing*, 115:497 – 513, 2019.
- [14] Bruna Nabuco, Tobias Friis, Marius Tarpø, Sandro Amador, and Evangelos I. Katsanos and Rune Brincker. Nonlinear strain estimation based on linear parameters. *ASME 2018 37th International Conference on Ocean, Offshore and Arctic Engineering*, 3: Structures, Safety, and Reliability:7, 2018.
- [15] P. Ren and Z. Zhou. Strain estimation of truss structures based on augmented kalman filtering and modal expansion. *Advances in Mechanical Engineering*, 9(11):1–10, 2017. Structural health monitoring of the truss structure is often confronted with spatial incomplete measured data due to the reasons of the cost of the sensors,...
- [16] C. Papadimitriou, C.P. Fritzen, P. Kraemer, and E. Ntotsios. Fatigue predictions in entire body of metallic structures from a limited number of vibration sensors using kalman filtering. *Structural Control and Health Monitoring*, 18(5):554–573, 2011.
- [17] K. Maes, A. Iliopoulos, W. Weijtjens, C. Devriendt, and G. Lombaert. Dynamic strain estimation for fatigue assessment of an offshore monopile wind turbine using filtering and modal expansion algorithms. *Mechanical Systems and Signal Processing*, 76-77:592–611, 2016.
- [18] S. E. Azam, E. Chatzi, and C. Papadimitriou. A dual kalman filter approach for state estimation via output-only acceleration measurements. *Mechanical Systems and Signal Processing*, 60-61:866–886, 2015.
- [19] L. Lagerblad, H. Wentzel, and A. Kulachenko. Fatigue damage prediction based on the strain field estimates using a smoothed kalman filter and sparse measurements. *Proceedings of ISMA2018 and USD2018*, pages 2805–2817, 2018.
- [20] P. Ren and Z. Zhou. Strain response estimation for fatigue monitoring of an offshore truss structure. *Pacific Science Review*, 16(1):29–35, 2014.
- [21] D.C. Kammer. Test-analysis model development using an exact modal reduction. *International Journal of Analytical and Experimental Modal Analysis*, 2:174–179, 1987.
- [22] Manuel López Aenlle, Lutz Hermanns, Pelayo Fernández, and Alberto Fraile. Stress estimation in a scale model of a symmetric two story building. page 9, 2013.
- [23] R.J. Guyan. Reduction of stiffness and mass matrices. *AIAA Journal*, 3(2):380–380, 1965.
- [24] M. Levine-West, M. Milman, and A. Kissil. Mode shape expansion techniques for prediction - experimental evaluation. *AIAA Journal*, 34(4):821–829, 1996.
- [25] R.L. Kidder. Reduction of structural frequency equations. *AIAA Journal*, 11(6):892–892, 1973.
- [26] C.A. Miller. Dynamic reduction of structural models. *ASCE Journal of the Structural Division*, 106:2097–2108, 1980.

- [27] J.C. O'Callahan. A procedure for an improved reduced system (irs) model. *Proceedings of the 7th International Modal Analysis Conference*, pages 17–21, 1989.
- [28] J.C. O'Callahan, P.A. Avitabile, and R. Riemer. System equivalent reduction expansion process (serep). *Proceedings of the 7th International Modal Analysis Conference*, 1989.
- [29] D.C. Kammer. A hybrid approach to test-analysis-model development for large space structures. *ASME Journal of Vibration and Acoustic*, 113:325–332, 1991.
- [30] H.-P. Chen. Mode shape expansion using perturbed force approach. *Journal of Sound and Vibration*, 329(8):1177 – 1190, 2010.
- [31] S.W. Smith and C.A. Beattie. Simulations expansion and orthogonalization of measured modes for structure identification. *AIAA Dynamic Specialist Conf., AIAA-90-1218-CP*, 3:261–270, 1990.
- [32] F. Liu. Direct mode-shape expansion of a spatially incomplete measured mode by a hybrid-vector modification. *Journal of Sound and Vibration*, 330(18):4633 – 4645, 2011.
- [33] R. Brincker, A. Skaftø, M. López-Aenlle, A. Sestieri, W. D'Ambrogio, and A. Canteli. A local correspondence principle for mode shapes in structural dynamics. *Mechanical Systems and Signal Processing*, 45(1):91–104, 2013.
- [34] R. W. Clough and J. Penzien. *Dynamics of structures*. CSI Computers & Structures, Inc., Berkeley, Calif., 2nd revised edition, 2003.
- [35] R. Brincker and C. Ventura. *Introduction to operational modal analysis*. John Wiley and Sons, Inc., Chichester, West Sussex, UK, 2015.
- [36] M. Tarpø, M. Vigsø, and R. Brincker. Modal truncation in experimental modal analysis. In M. Mains and B.J. Dilworth, editors, *Topics in Modal Analysis & Testing, Volume 9*, pages 143–152, Cham, 2019. Springer International Publishing.
- [37] L. Debao, Z. Hongcheng, and W. Bo. The principle and techniques of experimental strain modal analysis. *Proceedings of 7th IMAC*, pages 1285–1289, 1989.
- [38] S.-W. Seo, K.-J. Kim, and B.-K. Bae. Estimation of operational strains from vibration measurements: An application to lead wires of chips on printed circuit board. *Journal of Sound and Vibration*, 210(5):567 – 579, 1998.
- [39] A. Skaftø. *Applications of Expansion Techniques in Operational Modal Analysis*. PhD thesis, Aarhus University, DK, 2016.
- [40] Marie Levine-West, Mark Milman, and Andy Kissil. Mode shape expansion techniques for prediction: Experimental evaluation. *AIAA Journal*, 34(4):821–829, 1996.
- [41] A. Sestieri. Structural dynamic modification. *Sadhana*, 25(3):247–259, 2000.
- [42] Martin Ø.Ø. Jull, Sandro D.R. Amador, Anders Skaftø, Jannick B. Hansen, Manuel L. Aenlle, and Rune Brincker. One-step fe model updating using local correspondence and mode shape orthogonality. *Shock and Vibrations*, 2019:12, 2019.
- [43] K.P. Murphy. *Machine learning : a probabilistic perspective*. MIT Press, Cambridge, Mass., 2012.
- [44] W. Heylen and S. Lammens. Frac: a consistent way of comparing frequency response functions. *Proceedings of the Conference on Identification in Engineering Systems*, pages 48–57, 1996.
- [45] P.C. Hansen, V. Pereyra, and G. Scherer. *Least squares data fitting with applications*. Johns Hopkins University Press, Baltimore, MD, USA, 2013.
- [46] A. Almar-Naess. *Fatigue Handbook: Offshore Steel Structures*. Tapir Academic Press, Trondheim, Norway, 3rd edition, 1985.
- [47] M.M. Pedersen. Introduction to metal fatigue. Technical report, 2018.
- [48] R. G. Lyons. *Understanding digital signal processing*. Prentice Hall, Upper Saddle River, N.J., USA, 3rd. edition, 2011.
- [49] J. N. Juang and R. S. Pappa. An eigensystem realization algorithm for modal parameter identification and model reduction. *Journal of Guidance*, 8(5):620–627, 1985.
- [50] C. Amzallag, J.P. Gerey, J.L. Robert, and J. Bahuaud. Standardization of the rainflow counting method for fatigue analysis. *International Journal of Fatigue*, 16(4):287 – 293, 1994.

Chapter 8

Paper 5 - Full-field strain estimation of subsystems within time-varying and nonlinear systems using modal expansion

“
Chaos was the law of nature; Order was
the dream of man”

Henry Adams

Status

- Second round of review at Mechanical Systems and Signal Processing as of writing

8.1 Introduction

The modal expansion technique assumes a linear and stationary system with proportional viscous damping to create virtual sensors. The reality is, however, not as ideal as these assumptions where some amount of nonlinearities, nonstationarities, and nonproportional viscous damping exist. For offshore structures, we have marine growth, ingress of water, fluid storage levels, and soil properties that change over time, see chapter 3, and this introduces nonstationarity to the structures. In some cases, bridges connect offshore platforms and this introduces a friction-coupling and nonlinearity to the platforms. Furthermore, structure and soil interaction, structure and water interaction, and extreme waves add further nonlinearities to offshore structures.

For some nonlinear and nonstationary systems, we can model them as multiple subsystems with external nonlinear and nonstationary effect. This is the case for offshore platforms connected with bridges where each platform is a linear subsystem with external friction that couples the subsystem to the entire nonlinear system. In this paper, we apply stress/strain estimation to subsystems within nonstationary (time-varying) and nonlinear systems with general viscous damping.

8.2 Contribution

The author came up with the idea of applying Structural Modification Theory and Linear Algebra to explain the use of modal expansion for nonstationary and nonlinear structures with general viscous damping. Furthermore, the author wrote the paper, performed the experimental tests with Tobias Friis, and applied stress/strain estimation.

8.3 Main findings

We found that the response of a nonlinear and time-invariant system with general viscous damping in \mathbb{R}^N must be a combination of the undamped, linear mode shapes of the underlying system since these mode shapes form a basis for \mathbb{R}^N . We introduced the pseudo modal coordinates, which is the combination of the undamped, linear mode shapes, for the nonlinear and nonstationary system with general damping.

This enables us to apply modal expansion to subsystems within a nonlinear and nonstationary system with general viscous damping. Compared to a linear and stationary system, the complexity increases regarding the sufficient set of mode shapes for an accurate stress/strain estimation of a nonlinear and time-invariant system with general viscous damping. Unfortunately, modal truncation errors become an issue for modal expansion due to the nonlinearity and nonstationary effects and we would require a higher number of mode shapes. Generally, the set of mode shapes should span the global response of the system. In this paper, we prove that, for "linear" subsystems within a nonlinear and nonstationary system, the choice of applied mode shapes is similar to that of a linear system. Thus, for these cases, we can apply stress/strain estimation using the undamped mode shapes of the subsystem with high accuracy and precision.

8.4 Reflections

We conclude that we can apply stress/strain estimation to a "linear" subsystem within nonlinear and nonstationary systems with general viscous damping by the use of a set of linear mode shapes. The set of mode shapes should sufficiently span the response of the structure, as explained in chapter 6.

Full-field strain estimation of subsystems within time-varying and non-linear systems using modal expansion

Marius Tarpø^a, Tobias Friis^b, Christos Georgakis^a, Rune Brincker^b

^aAarhus University, Department of Engineering, Inge Lehmanns Gade 10, Aarhus, Denmark

^bTechnical University of Denmark, Department of Civil Engineering, Brovej B.118, Kgs. Lyngby, Denmark

Abstract

Virtual sensing allows for the estimation of stress and/or strain response in unmeasured locations of a system. Often, these virtual sensing techniques assume a linear and time-invariant system with proportional damping. In this article, one virtual sensing technique - the modal expansion - is proven applicable for stress/strain estimation of subsystems within time-varying and nonlinear systems with general viscous damping where the time-varying and nonlinear effects act externally on the subsystems. This technique uses the mode shapes of the subsystem to expand the response by a subspace projection. It is proven that the mode shapes of the underlying undamped and linear system form a basis for the response of the time-varying and nonlinear systems with general viscous damping. Therefore, a truncation of the mode shapes results in modal truncation errors that depend on the span of the applied mode shapes. Thus using an appropriate set of undamped and linear mode shapes of the subsystem, the modal expansion allows for estimation of the stress/strain response for subsystems within time-varying and nonlinear systems with general viscous damping. This concept is proven both numerically and experimentally.

Keywords: Virtual sensing, structural modification theory, hybrid modal analysis, structural health monitoring

8.6 Introduction

Stress/strain estimation is a subsection within the research field of virtual sensing where physical sensors are extended to unmeasured and inaccessible positions or quantities [1]. Fig. 8.1 outlines the flowchart of virtual sensing. Commonly for all virtual sensing techniques, they require knowledge of the physical sensors and the system in the form of a system model. A process model combines the physical measurements and the system model to generate virtual sensors, and it can even convert the measured quantities into other types of quantities/sensors. In stress/strain estimation, the virtual sensing enables conversion and/or extension of sensors into the full-field stress/strain estimation, and thereby, it enables full-field fatigue analysis.

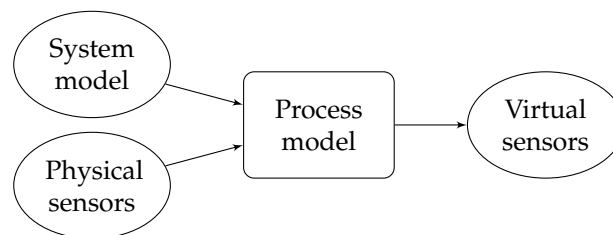


Figure 8.1: Flowchart of virtual sensing

For stress/strain estimation, the most popular process models are: the modal expansion [2–9] and the Kalman filter [10–16]. The modal expansion is a least square regression or a linear transformation technique that uses the mode shapes of a system to transform the response into virtual sensors. It projects the response unto the subspace spanned by the mode shapes and transforms the response to the strain response. The designer of the modal expansion chooses an appropriate set of mode shapes for the technique to work [2, 3, 8]. The Kalman filter and other adaptive filter techniques are optimal predictors and they use the system matrices in the discrete state space form to estimate the stress/strain response by assuming white Gaussian noise on both the system matrices (process noise) and the physical measurements (measurement noise). The designer of the adaptive filter tunes the error-covariance matrices

to ensure satisfactory results [11, 12, 17]. The two different techniques are found to be interchangeable since they lead to similar estimations of the strain response [10, 12].

In the literature of virtual sensing, stress/strain estimation is applied with success to a wide range of civil and mechanical structures. During the 1950s, stress/strain estimation had its tentative beginnings where analytical relationships between response and strain for beams or plates were investigated [18–20]. These analytical expressions dominated stress/strain estimation until the 1990's where transformation matrices were applied to the field. In 1995, Okubo and Yamaguchi [21] introduced a displacement-to-strain transformation matrix calculated from strain and displacement measurements for dynamic strain prediction. Seo et al. [22] used the displacement-to-strain transformation matrix with mode shapes under free boundary conditions as basis vectors to express the mode shapes under operational boundary conditions using the same expression, which was later termed "structural modification theory" [23]. In 2005, Hjelm et al. [5] and Graugaard-Jensen et al. [6] applied the modal expansion for full-field strain estimation to a laboratory structure and a lattice tower under operational conditions. As the first, Papadimitriou et al. [11] applied the Kalman filter (an adaptive filter) to strain estimation in a numerical simulation in 2011. In 2015, Palanisamy et al. [15] studied strain estimation with the Kalman filter for non-zero mean excitation. Gevinski et al. [9] applied modal expansion in the frequency domain under the term hybrid modal analysis. In 2016, Maes et al. [12] compared strain estimation using the Kalman filter, the joint input-state estimation algorithm, and the modal expansion on an offshore monopile wind turbine in the Belgian North Sea and applied data fusion to combine accelerometers and strain gauges. J. Kullaa [24] applied dynamic substructuring to modal expansion in numerical simulations by replacing the mode shapes of the full system with component modes of the subsystem. To account for the quasi-static response, Iliopoulos et al. [3] combined accelerometers and strain gauges to modal expansion for strain estimation on an offshore monopile wind turbine. Skaftø et al. [2] applied Ritz vectors (pseudo modes) to the multi-banded modal expansion technique to accommodate for the quasi-static response of wave-induced structures. In recent years, machine learning algorithms have been applied to strain estimation where Lu et al. [25] used pattern recognition on the Shenzhen Bay Stadium and Deng et al. [26] applied learning to modal expansion. In 2020, Tarpø et al. [8] studied the effect of applying expanded experimental mode shapes to modal expansion and stress estimation, finding, that the expansion is similar to an update of the system model and it can increase accuracy. Recently, stress/strain estimation is applied to nonlinear structures where Risaliti et al. [27] applied the augmented extended Kalman filter to estimate the load and strain field on nonlinear mechanical systems by the means of the implicit equation of motion. Furthermore, Tarpø et al. [4] utilised modal expansion for strain estimation of a numerical offshore platform with friction and Nabuco et al. [7] applied a displacement-to-strain transformation matrix of two friction-coupled scaled offshore platforms.

For now, the theory limits the modal expansion technique to time-invariant and linear systems. In this paper, we address stress/strain estimation using the modal expansion technique for subsystems within time-varying and nonlinear systems with general viscous damping by extending the theory with structural modification theory. It is known that a change of a system results in a set of mode shapes that are a linear combination of the original undamped normal mode shapes [23]. This paper extends this concept to changes that result in coupled, time-variant, and nonlinear systems with general viscous damping. Therefore, the response of this new system could be described by the same vector space as the original system since the undamped mode shapes form a basis for \mathbb{R}^N . Thus, we can use the uncoupled and undamped normal modes of a subsystem in the modal expansion to estimate the strain/stress response of the coupled subsystem as long as any nonlinear and time-varying effect act externally on the subsystem. We are, however, unable to extend the full-field virtual sensors beyond the subsystems, from which we measure the response, using uncoupled mode shapes. Furthermore, we need a sufficient set of mode shapes from the subsystem to span the response and this introduces the problem of modal truncation errors [28].

We organise this paper as follows: Section 8.7.1 sets up the equation of motion and Section 8.7.2 introduces modal expansion and strain estimation for linear system. Section 8.7.3 introduces structural modification theory and proves that the response of coupled, nonlinear, and time-varying systems with general viscous damping is a linear combination of the uncoupled and undamped mode shapes. Section 8.7.4 introduces the concepts of pseudo modal coordinates, which is the linear combination of the normal modes. In Section 8.7.5, we combine modal expansion and the pseudo modal coordinates for strain estimation in case of coupled, nonlinear, and time-varying systems with general viscous damping. We find that modal expansion is limited to strain estimation of the measured subsystems where the nonlinear and time-varying effects act externally on the subsystems. Finally, in Section 8.8, we validate the theory on several numerical simulations and an experimental case study with two friction-coupled platforms in

the laboratory.

8.7 Theory

8.7.1 Equation of motion

The response of a linear and stationary system with viscous damping is the solution of an ordinary differential equation - called the equation of motion [29, 30].

$$\mathbf{M}\ddot{\mathbf{y}}(t) + \mathbf{C}\dot{\mathbf{y}}(t) + \mathbf{K}\mathbf{y}(t) = \mathbf{x}(t) \quad (8.1)$$

where $\mathbf{y}(t) \in \mathbb{R}^N$, $\dot{\mathbf{y}}(t) \in \mathbb{R}^N$, and $\ddot{\mathbf{y}}(t) \in \mathbb{R}^N$ are the displacement, velocity, and acceleration of the system, $\mathbf{M} \in \mathbb{R}^{N \times N}$, $\mathbf{C} \in \mathbb{R}^{N \times N}$, and $\mathbf{K} \in \mathbb{R}^{N \times N}$ are the mass, damping, and stiffness matrix, $\mathbf{x}(t) \in \mathbb{R}^N$ is the external excitation vector, and N is the total number of degrees-of-freedom (DOF) in the system. When we have proportional viscous damping, we can use the undamped equation of motion to find the mode shapes of the system through the eigenvalue problem. The eigenvalue problem arises when we separate the general solution of the equation of motion in time and space [29, 31].

$$\mathbf{M}^{-1}\mathbf{K}\boldsymbol{\phi}_i = \omega_i^2\boldsymbol{\phi}_i \quad (8.2)$$

where ω_i is angular frequency of the i^{th} mode and $\boldsymbol{\phi}_i \in \mathbb{R}^N$ is the undamped mode shape vector for the i^{th} mode. The undamped mode shape is called a normal mode.

If the mass and stiffness matrices are symmetric and positive semi-definite matrices with full rank [31], there exists N real eigenvalues and N linearly independent eigenvectors - even though the eigenvalues may be indistinct [32]. The modal matrix, $\boldsymbol{\Phi} = [\boldsymbol{\phi}_1, \boldsymbol{\phi}_2, \dots, \boldsymbol{\phi}_N] \in \mathbb{R}^{N \times N}$, span \mathbb{R}^N and the mode shapes, the column vectors in the modal matrix, are linearly independent to each other [31]. Thus, the modal matrix is an (eigen-)basis of the eigenvectors for \mathbb{R}^N [32] and it is orthogonal with respect to the mass and stiffness matrix [29–31]. In short, any response, $\mathbf{y}(t)$, in \mathbb{R}^N is a linear combination of these mode shapes and this phenomenon is called the modal superposition.

$$\mathbf{y}(t) = \boldsymbol{\Phi}\mathbf{q}(t) \quad (8.3)$$

where $\mathbf{q}(t) \in \mathbb{R}^N$ is called the coordinate vector or the modal coordinates and it holds the coefficients of the linear combination of the mode shapes. The modal expansion is a linear coordinate transformation from the physical space into the modal space.

Throughout the paper, we use the system response, $\mathbf{y}(t)$, mode shapes, $\boldsymbol{\Phi}$, and modal coordinates, $\mathbf{q}(t)$, as variables for different systems.

8.7.2 Strain estimation using modal expansion

In this section, we will introduce modal expansion for strain estimation. We assume a linear relationship between the strain response and the displacement of the system.

$$\boldsymbol{\varepsilon}(t) = \mathbf{T}_\varepsilon\mathbf{y}(t) \quad (8.4)$$

where $\boldsymbol{\varepsilon}(t) \in \mathbb{R}^b$ is the strain response of the system in b locations and $\mathbf{T}_\varepsilon \in \mathbb{R}^{b \times N}$ the displacement-to-strain transformation matrix.

We insert the modal superposition from Eq. (8.3) and define the strain mode shape as the static strain caused by a deflection corresponding to each mode shape [22].

$$\begin{aligned} \boldsymbol{\varepsilon}(t) &= \mathbf{T}_\varepsilon\boldsymbol{\Phi}\mathbf{q}(t) \\ &= \boldsymbol{\Phi}_\varepsilon\mathbf{q}(t) \end{aligned} \quad (8.5)$$

where $\boldsymbol{\Phi}_\varepsilon$ is the strain mode shape matrix.

In reality, we have a truncated set of normal mode shapes, $\tilde{\boldsymbol{\Phi}} = [\boldsymbol{\phi}_1, \dots, \boldsymbol{\phi}_K] \in \mathbb{R}^{N \times K}$, which is an approximation of the underlying linear subspace of the system. Moreover, we measure the system response, $\mathbf{y}_a(t) \in \mathbb{R}^{a \times 1}$, in a points on the system.

$$\mathbf{y}(t) = \begin{bmatrix} \mathbf{y}_a(t) \\ \mathbf{y}_d(t) \end{bmatrix}, \quad \tilde{\boldsymbol{\Phi}} = \begin{bmatrix} \tilde{\boldsymbol{\Phi}}_a \\ \tilde{\boldsymbol{\Phi}}_d \end{bmatrix} \quad (8.6)$$

where $(\cdot)_a$ denotes the active DOFs and $(\cdot)_d$ denotes the inactive DOFs.

We estimate the modal coordinates by transforming the measured response, $\mathbf{y}_a(t)$, using the normal mode shapes, $\tilde{\Phi}_a$, see Eq. (8.3).

$$\hat{\mathbf{q}}(t) = \tilde{\Phi}_a^\dagger \mathbf{y}_a(t) \quad (8.7)$$

where $(\cdot)^\dagger$ denotes the Moore–Penrose pseudo inverse.

We insert the estimated pseudo modal coordinates into Eq. (8.5).

$$\hat{\boldsymbol{\varepsilon}}(t) = \tilde{\Phi}_\varepsilon \hat{\mathbf{q}}(t) \quad (8.8)$$

where $\hat{\boldsymbol{\varepsilon}}(t)$ is the estimated strain response of the entire system and $\tilde{\Phi}_\varepsilon$ is the truncated strain modal matrix.

The main assumption of modal expansion is that a set of mode shapes span the subspace of a measured response. Modal expansion is essentially a least square regression technique that projects the measured response onto the column space of the applied mode shapes, $\tilde{\Phi}_a$, reduces the response to this linear subspace, and expands the response. Thus, the modal expansion technique allows for estimation of the stress/strain response for linear system if we apply an appropriate set of mode shapes, which span the majority of the system response. The set of mode shapes should be selected by an agreement between the natural frequency and the excitation frequency but also by the matrix product of the transposed mode shape and the spatial distribution of the excitation to avoid modal truncation errors [28]. Furthermore, the accuracy of modal expansion also depends on the number and position of sensors. This issue relates to the stability of the inversion of the reduced and truncated modal matrix, $\tilde{\Phi}_a$, and the condition number of this modal matrix indicates the level of stability.

8.7.3 Structural modification theory

In this section, we will study the linear subspace spanned by the original linear mode shapes as the system is modified or changed. This is used to study the validity of modal expansion with linear mode shapes as the actual system diverts from the original system, which the mode shapes stem from. First, it is assumed the system has a change in all system matrices while the damping is still proportional.

$$(\mathbf{M} + \Delta\mathbf{M})\ddot{\mathbf{y}}(t) + (\mathbf{C} + \Delta\mathbf{C})\dot{\mathbf{y}}(t) + (\mathbf{K} + \Delta\mathbf{K})\mathbf{y}(t) = \mathbf{x}(t) \quad (8.9)$$

where $\Delta\mathbf{M} \in \mathbb{R}^{N \times N}$, $\Delta\mathbf{C} \in \mathbb{R}^{N \times N}$, and $\Delta\mathbf{K} \in \mathbb{R}^{N \times N}$ hold the perturbation for the mass, damping, and stiffness matrix.

Structural modification theory proves that this new system has a new set of mode shape vectors that are a linear combination of the original system [23].

$$\tilde{\Phi} = \Phi \mathbf{P} \quad (8.10)$$

where $\mathbf{P} \in \mathbb{R}^{N \times N}$ is a matrix that contains the linear combination of mode shapes. Since both modal matrices, Φ and $\tilde{\Phi}$, are bases for \mathbb{R}^N , they are linearly dependent of each other. Thus, a set of mode shapes from a modified system is a linear combination of the original mode shapes. In linear algebra, the matrix \mathbf{P} is called the change of basis matrix, the (coordinate) transformation matrix, or the change of coordinates matrix from Φ to $\tilde{\Phi}$ [32, 33]. Moreover, the matrix \mathbf{P} maps the modal coordinates of the new mode shapes, $\tilde{\Phi}$, to the coordinates of the original mode shapes, Φ .

Eq. (8.10) is only valid for the full set of mode shapes but it still holds for a limited number of mode shapes if the changes between the systems are small [34]. Sondipon [35] investigates the derivatives of eigenvalues and eigenvectors in a nonproportional viscously damped dynamic system to analyse the rate of changes and sensitivity. Finding, the sensitivity of a mode shape depends, considerably, on the surrounding modes in terms of natural frequency [35]. Brincker et al. [34] extended the sensitivity equations to finite but small changes in the mass and stiffness matrices, similarly proving that a change for a given mode shape is primarily described as a linear combination of the closest modes (in term of frequency). Thus, any changes to a mode shape are approximated by a finite set of the closest, surrounding mode shapes. A small change requires few modes, however, as the size of changes increases so does the number of modes. These conclusions hold for all kind of small perturbations.

Thus, we could use a suitable subset of mode shapes from the original system for strain estimation of a perturbed system using modal expansion and still have low modal truncation errors. In the following

subsections, we will extend this concept of a linear subspace spanned by the original mode shapes for coupled, time-variant, and/or nonlinear systems with general viscous damping.

Coupled systems

In this section, we will study coupling of systems - similar to dynamic sub-structuring - for strain estimation when the exact coupling is unknown. In the literature, J. Kullaa [24] applied dynamic substructuring to modal expansion when the coupling of one subsystem is known to the main system. We begin with two uncoupled linear systems, A and B , and we rewrite the two corresponding equations of motion into one equation.

$$\begin{bmatrix} \mathbf{M}_A & \mathbf{0} \\ \mathbf{0} & \mathbf{M}_B \end{bmatrix} \begin{bmatrix} \ddot{\mathbf{y}}_A(t) \\ \ddot{\mathbf{y}}_B(t) \end{bmatrix} + \begin{bmatrix} \mathbf{C}_A & \mathbf{0} \\ \mathbf{0} & \mathbf{C}_B \end{bmatrix} \begin{bmatrix} \dot{\mathbf{y}}_A(t) \\ \dot{\mathbf{y}}_B(t) \end{bmatrix} + \begin{bmatrix} \mathbf{K}_A & \mathbf{0} \\ \mathbf{0} & \mathbf{K}_B \end{bmatrix} \begin{bmatrix} \mathbf{y}_A(t) \\ \mathbf{y}_B(t) \end{bmatrix} = \begin{bmatrix} \mathbf{x}_A(t) \\ \mathbf{x}_B(t) \end{bmatrix} \quad (8.11)$$

where the subscripts $(\cdot)_A$ and $(\cdot)_B$ denote the DOFs related to the subsystems.

We find the uncoupled mode shapes through the eigenvalue problem of the undamped equation of motion.

$$\Phi = \begin{bmatrix} \Phi_A & \mathbf{0} \\ \mathbf{0} & \Phi_B \end{bmatrix} \quad (8.12)$$

We add a change to the system matrices so the systems are coupled together.

$$\left(\begin{bmatrix} \mathbf{M}_A & \mathbf{0} \\ \mathbf{0} & \mathbf{M}_B \end{bmatrix} + \Delta \mathbf{M} \right) \begin{bmatrix} \ddot{\mathbf{y}}_A(t) \\ \ddot{\mathbf{y}}_B(t) \end{bmatrix} + \left(\begin{bmatrix} \mathbf{C}_A & \mathbf{0} \\ \mathbf{0} & \mathbf{C}_B \end{bmatrix} + \Delta \mathbf{C} \right) \begin{bmatrix} \dot{\mathbf{y}}_A(t) \\ \dot{\mathbf{y}}_B(t) \end{bmatrix} + \left(\begin{bmatrix} \mathbf{K}_A & \mathbf{0} \\ \mathbf{0} & \mathbf{K}_B \end{bmatrix} + \Delta \mathbf{K} \right) \begin{bmatrix} \mathbf{y}_A(t) \\ \mathbf{y}_B(t) \end{bmatrix} = \begin{bmatrix} \mathbf{x}_A(t) \\ \mathbf{x}_B(t) \end{bmatrix} \quad (8.13)$$

Using structural modification theory, the new set of coupled mode shapes are a linear combination of the uncoupled mode shapes.

$$\begin{aligned} \tilde{\Phi} &= \Phi \mathbf{P} \\ &= \begin{bmatrix} \Phi_A & \mathbf{0} \\ \mathbf{0} & \Phi_B \end{bmatrix} \mathbf{P} \end{aligned} \quad (8.14)$$

Thus, the uncoupled mode shapes span the response of the coupled system and, moreover, they span the response of each subsystem in the coupled system. Therefore, we can use the uncoupled mode shapes of a subsystem for strain estimation when the mode shape components of the coupled subsystem are unknown. We cannot, however, extend the strain estimation beyond a subsystem to another subsystem if we do not have measurements of the other subsystem or know the coupling between the subsystems. Uncoupled mode shapes limit modal expansion to the subsystems from which we have measurements.

Nonlinear and time-varying system with general viscous damping

Let us consider a nonlinear and time-varying system with general viscous damping within \mathbb{R}^N .

$$\mathbf{M}\ddot{\mathbf{y}}(t) + \mathbf{C}\dot{\mathbf{y}}(t) + \mathbf{K}\mathbf{y}(t) + \mathbf{f}_{nl}(\mathbf{E}(t)) = \mathbf{x}(t) \quad (8.15)$$

where $\mathbf{f}_{nl}(\mathbf{E}(t)) \in \mathbb{R}^N$ is a general nonlinear and time-varying effect vector that depends on the energy (or conditions) in the system, $\mathbf{E}(t) \in \mathbb{R}^N$, which again depends on time. In this article, the term energy is used to cover both the energy in the system and any conditions, which causes nonlinear and/or time-varying changes to the system.

In the case of a linear system, $\mathbf{f}_{nl}(\mathbf{E}(t)) = \mathbf{0}$, we have an eigenvalue problem in the state space formulation. For underdamped modes, the $2N$ eigenvalues and mode shapes appear in complex conjugated pairs due to the non-proportional viscous damping [30, 31, 36].

$$\begin{bmatrix} -\mathbf{M}^{-1}\mathbf{C} & -\mathbf{M}^{-1}\mathbf{K} \\ \mathbf{I} & \mathbf{0} \end{bmatrix} = \Theta [\lambda_n] \Theta^{-1} \quad (8.16)$$

where $\Theta \in \mathbb{C}^{2N \times 2N}$ contains the eigenvectors in conjugated pairs as column vectors and $[\lambda_n] \in \mathbb{C}^{2N \times 2N}$ is a diagonal matrix with the modal poles in conjugated pairs. Here the eigenvectors, Θ , hold the mode shape and modal poles as follows

$$\Theta = \begin{bmatrix} [\lambda_n] \tilde{\Phi} & [\lambda_n^*] \tilde{\Phi}^* \\ \tilde{\Phi} & \tilde{\Phi}^* \end{bmatrix} \quad (8.17)$$

where $\tilde{\Phi} \in \mathbb{C}^{N \times N}$ is the complex modal matrix, $(\cdot)^*$ denotes the complex conjugate, and $[\tilde{\Phi} \ \tilde{\Phi}^*] \in \mathbb{C}^{N \times 2N}$ form a \mathbb{R} -basis of dimension $2N$. The upper part relates to modal velocity while the lower part relates to modal displacement.

For nonlinear systems, the traditional understanding of the modes breaks down [37]. Due to the energy dependency of the nonlinear system, a direct separation into time and space solutions is impossible for the nonlinear equation of motion, Eq. (8.15) [37]. In this paper, we assume that the equation of motion for a nonlinear system has an energy dependent solution in both time and space. Therefore a set of complex and nonlinear mode shapes exists as a spatial solution and this set depends on the same parameters as the nonlinear force vector, \mathbf{f}_{nl} . In terms of algebra, a basis for \mathbb{R}^N exists as a function of the energy in the system, thus, the basis changes according to the nonstationarity and nonlinearity. The reader should note that the notion of a solution in space for a time-varying and nonlinear system is, however, constructed since it will change continuously and accordingly to the energy in the system.

The nonlinear mode shapes occur in complex conjugated pairs due to the nonproportional viscous damping.

$$\Theta(\mathbf{E}(t)) = \begin{bmatrix} [\lambda_n(\mathbf{E}(t))] \tilde{\Phi}(\mathbf{E}(t)) & [\lambda_n(\mathbf{E}(t))^*] \tilde{\Phi}^*(\mathbf{E}(t)) \\ \tilde{\Phi}(\mathbf{E}(t)) & \tilde{\Phi}^*(\mathbf{E}(t)) \end{bmatrix} \quad (8.18)$$

where $\tilde{\Phi}(\mathbf{E}(t)) \in \mathbb{C}^{N \times N}$ and $\tilde{\Phi}^*(\mathbf{E}(t)) \in \mathbb{C}^{N \times N}$ are the complex nonlinear modal matrix and they are complex conjugates of each other. Since these mode shapes form a spatial solution for any level of energy, $\mathbf{E}(t)$, then a linear combination - as function of the energy - equals the system response. Thus, a nonlinear coordinate transformation exists that maps the physical response of the nonlinear system into a complex and nonlinear modal space.

$$\begin{aligned} \mathbf{y}(t) &= [\tilde{\Phi}(\mathbf{E}(t)) \ \tilde{\Phi}^*(\mathbf{E}(t))] \begin{bmatrix} \mathbf{q}_f(\mathbf{E}(t)) \\ \mathbf{q}_f^*(\mathbf{E}(t)) \end{bmatrix} \\ &= \Psi(\mathbf{E}(t)) \mathbf{q}_c(\mathbf{E}(t)) \end{aligned} \quad (8.19)$$

where $\Psi(\mathbf{E}(t)) \in \mathbb{C}^{N \times 2N}$ is the modal matrix containing conjugated pairs of mode shapes and $\mathbf{q}_c(\mathbf{E}(t)) \in \mathbb{C}^{2N}$ is the modal coordinates. We can write any basis of \mathbb{R}^N as a linear combination of another basis since they are linear dependent [33]. Therefore $\Psi(\mathbf{E}(t))$ and Φ are linearly dependent since they are both vector bases for \mathbb{R}^N for any level of energy, $\mathbf{E}(t)$.

$$\Psi(\mathbf{E}(t)) = \Phi \mathbf{P}(\mathbf{E}(t)) \quad (8.20)$$

where $\mathbf{P}(\mathbf{E}(t)) \in \mathbb{C}^{N \times 2N}$ is the change of basis matrix, which holds the combination of normal modes. An alternative proof for the relationship in Eq. (8.20) is given in Appendix 8.A.

Hence, the complex nonlinear mode shapes are an energy dependent linear combination of the normal mode shape of the undamped system. Therefore, a nonlinear system with general viscous damping has an underlying linear subspace spanning the normal mode shapes of the undamped linear system.

8.7.4 Pseudo modal coordinates

In this subsection, we will introduce the pseudo modal coordinates, $\mathbf{q}_p(t)$. Let us say that we have a time-varying and nonlinear system with general viscous damping and it has time and energy dependent complex and nonlinear mode shapes, $\Psi(\mathbf{E}(t))$, which form a basis for the system response in \mathbb{R}^N .

$$\mathbf{y}(t) = \Psi(\mathbf{E}(t)) \mathbf{q}_c(\mathbf{E}(t)) \quad (8.21)$$

Using structural modification theory, we express these mode shape through an exact linear relationship of the underlying normal modes, Φ . Moreover, $\mathbf{P}(\mathbf{E}(t))$ maps the modal coordinates of complex nonlinear mode shapes to those of the normal mode shape, which we define as pseudo modal coordinates, $\mathbf{q}_p(\mathbf{E}(t))$.

$$\mathbf{q}_p(\mathbf{E}(t)) = \mathbf{P}(\mathbf{E}(t)) \mathbf{q}_c(\mathbf{E}(t)) \quad (8.22)$$

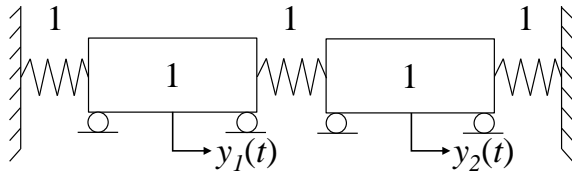


Figure 8.2: Linear two degree-of-freedom system

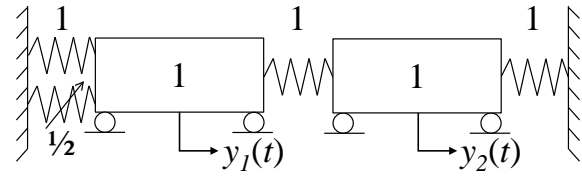


Figure 8.3: Nonlinear two degree-of-freedom system

The pseudo modal coordinates are the linear combination of the underlying normal modes that corresponds to the system response. These coordinates hold all of the nonstationarity, complexity from the general viscous damping, and/or the nonlinearity.

We rewrite the modal decomposition from Eq. (8.21) using Eq. (8.22) so it resembles the traditional modal decomposition.

$$\mathbf{y}(t) = \Phi \mathbf{q}_p(\mathbf{E}(t)) \quad (8.23)$$

Thus, a complex system has a linear subspace where the undamped mode shapes from the original system span the system response.

Example of pseudo modal coordinates

In this example, we will show that a nonlinear system has a linear subspace spanned by the underlying normal modes. To illustrate the concept of pseudo modal coordinates, we introduce a two DOF system (it is the same system as in [32]), see Fig. 8.2, with the following equation of motion.

$$\begin{bmatrix} 1 & 0 \\ 0 & 1 \end{bmatrix} \begin{bmatrix} \dot{y}_1(t) \\ \dot{y}_2(t) \end{bmatrix} + \begin{bmatrix} 2 & -1 \\ -1 & 2 \end{bmatrix} \begin{bmatrix} y_1(t) \\ y_2(t) \end{bmatrix} = \begin{bmatrix} 0 \\ 0 \end{bmatrix} \quad (8.24)$$

The linear mode shapes are

$$\Phi = \begin{bmatrix} 1 & 1 \\ 1 & -1 \end{bmatrix} \quad (8.25)$$

Using the Reduced Row Echelon Form (Gauss-Jordan elimination) [32], we can prove that this modal matrix spans \mathbb{R}^2 and it is linearly independent. Thus, it is a basis for \mathbb{R}^2 .

We simulate the free response of this linear two DOF system with an initial displacement corresponding to the second mode, $[1, -1]^\top$, and no initial velocity, see Fig. 8.4 (a) and (b). The two DOFs move out-of-phase and the relation between the two is linear, hence, the motion corresponds to a straight line in configuration space. Only the modal coordinate for the second mode oscillates with the natural frequency of the second mode, see Fig. 8.4 (c).

To introduce nonlinearity into the system, we add a cubic spring between the boundary and the first mass, see Fig. 8.3.

$$\begin{bmatrix} 1 & 0 \\ 0 & 1 \end{bmatrix} \begin{bmatrix} \dot{y}_1(t) \\ \dot{y}_2(t) \end{bmatrix} + \begin{bmatrix} 2 & -1 \\ -1 & 2 \end{bmatrix} \begin{bmatrix} y_1(t) \\ y_2(t) \end{bmatrix} + \begin{bmatrix} \frac{1}{2}y_1^3(t) \\ 0 \end{bmatrix} = \begin{bmatrix} 0 \\ 0 \end{bmatrix} \quad (8.26)$$

Again, we simulate the free response of the nonlinear two DOF system from an initial displacement of $[8.476, 54.232]^\top$ and no initial velocity, so we have an internal resonant nonlinear normal mode [32], see Fig. 8.5 (a) and (b). The simulations are carried out in the state space format [38] where the system of equations are formulated with the classical linear terms and with the addition of a term containing all the nonlinear forces. It is notable that the solution of Eq. (8.26), in a state space formulation, is provided in discrete time format by assuming a linear variation of the external forces and nonlinear forces between the successive time steps, i.e., so-called first order hold (more details are provided by Lòpez-Almansa et al. [38] and Lu et al. [39]). The simulations are then performed by time-stepping through the response and the nonlinear forces are iterated within each time step. The two DOFs in the system vibrate out of unison, therefore, the motion in configuration space is a curved line. See [37] for more information on nonlinear normal modes and internal resonance for nonlinear systems.

Since the underlying linear mode shapes are a basis for \mathbb{R}^N , the nonlinear response is a linear combination - the pseudo modal coordinates - of these linear mode shape vectors, see Fig. 8.5 (c). The pseudo

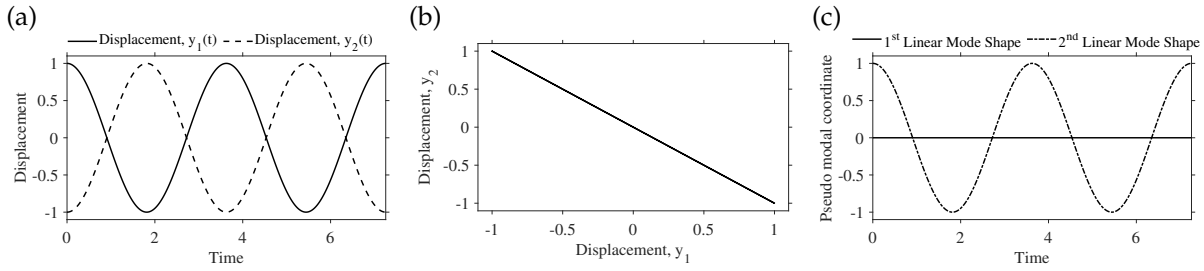


Figure 8.4: The linear two degree-of-freedom system from Fig. 8.2: (a) the response of the system, (b) the same response in configuration space, and (c) modal coordinates of the response with the underlying linear mode shapes

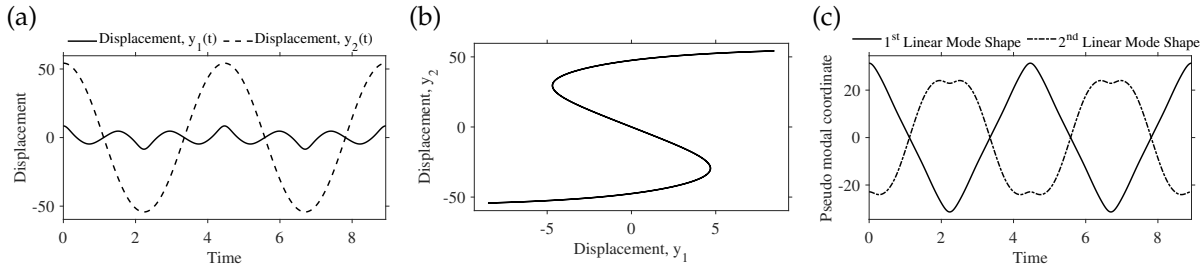


Figure 8.5: The nonlinear two degree-of-freedom system from Fig. 8.3: (a) the response of the system, (b) the same response in configuration space, and (c) pseudo modal coordinates of the response with the underlying linear mode shapes

modal coordinates are periodic but they are comprised by multiple sinusoids unlike the linear case. Thus, each pseudo modal coordinate has multiple oscillating frequencies - even for internal resonance.

8.7.5 Strain estimation using pseudo modal coordinates

In this section, we will combine pseudo modal coordinates and modal expansion for strain estimation. We have a time-varying and nonlinear system with general viscous damping. We estimate the pseudo modal coordinates by projecting the measured response, $\mathbf{y}_a(t)$, onto the subspace spanned by the normal mode shapes, $\tilde{\Phi}_a$, see Eq. (8.23).

$$\hat{\mathbf{q}}_p(\mathbf{E}(t)) = \tilde{\Phi}_a^+ \mathbf{y}_a(t) \tag{8.27}$$

To estimate the strain response, we insert the estimated pseudo modal coordinates into Eq. (8.5).

$$\hat{\boldsymbol{\varepsilon}}(t) = \tilde{\Phi}_\varepsilon \hat{\mathbf{q}}_p(\mathbf{E}(t)) \tag{8.28}$$

where $\hat{\boldsymbol{\varepsilon}}(t)$ is the estimated strain response of the entire system and $\tilde{\Phi}_\varepsilon$ is the truncated strain modal matrix.

Thus, this indicates that the modal expansion technique allows for estimation of the stress/strain response for time-varying and nonlinear systems with general viscous damping. The reader should note that this is only valid if we apply an appropriate set of undamped and linear mode shapes, which span the majority of the system response. The issue of modal truncation (selecting mode shapes) is, however, complicated since the sensitivity equations are inapplicable to a nonlinear system. The perturbations from linear system, which yield the nonlinearity, are not necessarily small changes in the system. As the perturbation from the original linear system increases, the number of modes to accurately span the response increases. Whenever the column space of the truncated modal matrix inaccurately spans the system response then we have a modal truncation error [28]. The fact that sensitivity of mode shapes depends on the surrounding modes might be inapplicable to nonlinear systems. Therefore, the contributions of higher modes might be more influential and distinct than that of a linear system and this leads to a substantial issue of modal truncation.

In the following, we will study the selection of linear undamped mode shapes of a special case of nonlinear and time-varying systems where the issue of modal truncation is similar to a linear system. We will consider a subsystem inside a nonlinear and time-varying system with non-proportional viscous

damping where the time-varying and nonlinear effects act externally on the subsystem. In the following, we rewrite Eq. (8.15) into two subsystem: A and B .

$$\begin{bmatrix} \mathbf{M}_{AA} & \mathbf{M}_{AB} \\ \mathbf{M}_{BA} & \mathbf{M}_{BB} \end{bmatrix} \begin{bmatrix} \ddot{\mathbf{y}}_A(t) \\ \ddot{\mathbf{y}}_B(t) \end{bmatrix} + \begin{bmatrix} \mathbf{C}_{AA} & \mathbf{C}_{AB} \\ \mathbf{C}_{BA} & \mathbf{C}_{BB} \end{bmatrix} \begin{bmatrix} \dot{\mathbf{y}}_A(t) \\ \dot{\mathbf{y}}_B(t) \end{bmatrix} + \begin{bmatrix} \mathbf{K}_{AA} & \mathbf{K}_{AB} \\ \mathbf{K}_{BA} & \mathbf{K}_{BB} \end{bmatrix} \begin{bmatrix} \mathbf{y}_A(t) \\ \mathbf{y}_B(t) \end{bmatrix} + \begin{bmatrix} \mathbf{f}_{nl,A}(\mathbf{E}(t)) \\ \mathbf{f}_{nl,B}(\mathbf{E}(t)) \end{bmatrix} = \begin{bmatrix} \mathbf{x}_A(t) \\ \mathbf{x}_B(t) \end{bmatrix} \quad (8.29)$$

We calculate and rearrange the upper equations related to the A^{th} subsystem.

$$\mathbf{M}_{AA}\ddot{\mathbf{y}}_A(t) + \mathbf{C}_{AA}\dot{\mathbf{y}}_A(t) + \mathbf{K}_{AA}\mathbf{y}_A(t) = \mathbf{x}_A(t) - \mathbf{f}_{nl,A}(\mathbf{E}(t)) - \mathbf{M}_{AB}\ddot{\mathbf{y}}_B(t) - \mathbf{C}_{AB}\dot{\mathbf{y}}_B(t) - \mathbf{K}_{AB}\mathbf{y}_B(t) \quad (8.30)$$

In the following, we consider the case where the nonlinear and time-varying force, $\mathbf{f}_{nl,A}$, acts externally on the A^{th} subsystem. On the left-hand side of the equation, we have an uncoupled linear subsystem. On the right-hand side, we have all external terms, which contain the external force and the coupling to the entire system. We combine all the external terms in one external term, $\hat{\mathbf{x}}_{all,A}(t)$.

$$\mathbf{M}_{AA}\ddot{\mathbf{y}}_A(t) + \mathbf{C}_{AA}\dot{\mathbf{y}}_A(t) + \mathbf{K}_{AA}\mathbf{y}_A(t) = \hat{\mathbf{x}}_{all,A}(t) \quad (8.31)$$

Thus, we can interpret the subsystem as a linear system with an external force, which depends on the external excitation, the coupling to the entire system (both linear, nonlinear, and time-varying coupling), and external nonlinear and time-varying effects. Notably, the subsystem is parametrically excited since the external force depends on the response of the subsystem [40]. This linear subsystem has a set of linear mode shapes, Φ_A , that span its response. Therefore, we can use the undamped linear mode shapes of the subsystem for strain estimation. We need a sufficient number of undamped mode shapes from the subsystem to approximate the pseudo modal coordinates. The same rules for selecting mode shapes in modal expansion for a linear system apply for a subsystem of a nonlinear and time-variant system as long as the nonlinear effects act externally on the subsystem. We should consider both frequency and spatial distribution of the external force, $\hat{\mathbf{x}}_{all,A}(t)$, when we select the number of modes to include in the modal expansion technique.

A crucial limitation of strain estimation using pseudo mode shapes is nonlinearly coupled subsystems. Similar to the linear case, we cannot expand measurements from one subsystem to another if the coupling between the subsystems is unknown. In practice, actual nonlinear coupling is, however, often associated with large quantities of uncertainty. Thus, this uncertainty large limits the strain estimation to the measured subsystem.

8.8 Case studies

We will prove that a set of normal mode shapes is sufficient for strain estimation of a substructure with external nonlinear and time-varying effects using the modal expansion. In a numerical study, we will verify the concept of pseudo modal coordinates for strain estimation using the full response of a time-varying and nonlinear structure with general viscous damping and the full set of linear mode shape, thus, we remove the issues of modal truncation errors and sensor position. Finally, in an experimental study, we apply strain estimation to a nonlinear test-specimen comprised of two subsystems coupled by friction using the mode shapes from a linear finite element model.

8.8.1 Quality measures

Multiple approaches exist for evaluating the strain estimation and they have different strengths and weaknesses. In this paper, we have chosen to apply the Time Response Assurance Criterion (TRAC) and Normalised Error of Fatigue Damage (NEFD), which are described in the following.

Time Response Assurance Criterion (TRAC)

The TRAC [41] is a popular quality measures in the field of stress/strain estimation. TRAC values indicate a general correlation between two signals where a value of 1 corresponds to perfect correlation while a value of 0 indicates independence between the signals. It is, however, independent of amplitude differences.

Table 8.1: Modal parameters of the underlying linear system from the numerical simulation study

| Mode | 1 | 2 | 3 | 4 | 5 | 6 | 7 | 8 | >8 |
|-------------------|-------|-------|-------|-------|-------|-------|-----|-------|------------------------|
| Frequency (Hz) | 18.84 | 24.17 | 118.1 | 151.5 | 330.7 | 424.1 | 648 | 831.1 | >1071 |
| Damping Ratio (%) | 10 | 10 | 2.5 | 2.5 | 2.5 | 2.5 | 2.5 | 2.5 | $\frac{100}{\sqrt{2}}$ |

$$TRAC_i = \frac{\left(\boldsymbol{\varepsilon}_{t,i}^\top \widehat{\boldsymbol{\varepsilon}}_{t,i}\right)^2}{\left(\boldsymbol{\varepsilon}_{t,i}^\top \boldsymbol{\varepsilon}_{t,i}\right) \left(\widehat{\boldsymbol{\varepsilon}}_{t,i}^\top \widehat{\boldsymbol{\varepsilon}}_{t,i}\right)} \quad (8.32)$$

where $\boldsymbol{\varepsilon}_{t,i}$ is the entire discrete time history of the measured strain response for the i^{th} strain gauge arranged in a column vector, and similarly, $\widehat{\boldsymbol{\varepsilon}}_{t,i}$ is the estimated strain response at the same location.

Normalised Error of Fatigue Damage (NEFD)

It is important to evaluate the stress estimation in fatigue damage when the estimation is intended for a fatigue analysis. For this propose, we apply the NEFD [8], which is based on the SN-curve (excluding the effect of a bilinear SN curve) and the Palgreen-Miners Rule.

$$\eta_i = \frac{\hat{D}_i - D_i}{D_i} = \frac{\sum_{j=1}^{\hat{n}_{cycles}} \frac{\Delta \hat{\sigma}_j^m}{C}}{\sum_{j=1}^{n_{cycles}} \frac{\Delta \sigma_j^m}{C}} - 1 = \frac{\sum_{j=1}^{\hat{n}_{cycles}} \Delta \hat{\varepsilon}_j^m}{\sum_{j=1}^{n_{cycles}} \Delta \varepsilon_j^m} - 1 \quad (8.33)$$

where D_i and \hat{D}_i are the cumulated fatigue damage for the measured and estimated signal, respectively, in the i^{th} fatigue location, n_{cycles} and \hat{n}_{cycles} are the total number of counted cycles for the measured and estimated signal, respectively, $\Delta \sigma_j$ and $\Delta \hat{\sigma}_j$ denote the stress range from cycle counting, C is the fatigue capacity (the intercept of $\log(N)$ axis in the SN curve), m is the "slope" of the SN curve, and $\Delta \varepsilon_j$ and $\Delta \hat{\varepsilon}_j$ are the strain range from cycle counting. In this paper, we apply the rainflow counting algorithm [42]. Thus, we can use the summation of the strain ranges to the power of m for a measured and estimated signal to calculate the normalised fatigue damage. Here $\eta_i = 0$ indicates a perfect estimation of the strain response in terms of fatigue damage while a negative value indicates an underestimation of fatigue damage, and a positive value indicates an overestimation of fatigue damage. For the remainder of this paper, we will use $m = 3$, which corresponds to welded steel structures [43].

8.8.2 Numerical simulation study on cantilever beam

In this case, we use a numerical simulation of two cantilever beams, see Fig 8.6, to prove the concept of pseudo modal coordinates for strain estimation in the case of time-varying and nonlinear systems with general viscous damping. Here we use all DOFs from the left beam, which is a subsystem that is nonlinearly coupled to the other beam. Table 8.1 lists the modal parameters of the linear and uncoupled beams with proportional damping. All higher modes, above the eighth mode, have high damping ratios to mainly include their quasi-static contribution. The two beams are connected in three different manners where the coupled system is nonlinear and has non-proportional damping. In case a, the two beams are coupled with a friction element in top of both beams and a single-degree-of-freedom system is added in top of the first beam, working as a tuned mass damper, while time-varying masses are added to both beams in three locations marked with large dots, see Fig. 8.7 (a). The time-varying masses increase from zero to two kg and back to zero during the simulation and the total mass of the left beam is 5.11 kg. In case b, the two beams are connected by a spring in top and the first beam has a contact spring with high stiffness in the top, see Fig. 8.7 (b). In case c, the two beams are connected by a cubic spring and an additional cubic spring is added to top of the first beam, see Fig. 8.7 (c). We apply strain estimation to all cases where we calculate the pseudo modal coordinates from the full response using the linear uncoupled mode shapes of the left cantilever beam. From the pseudo modal coordinates, we estimate the full-field strain field using the linear strain mode shapes.

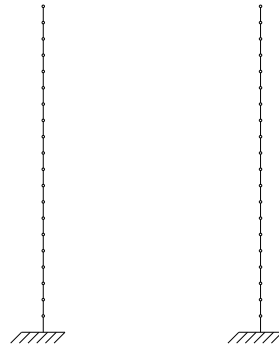


Figure 8.6: Numerical test-specimen

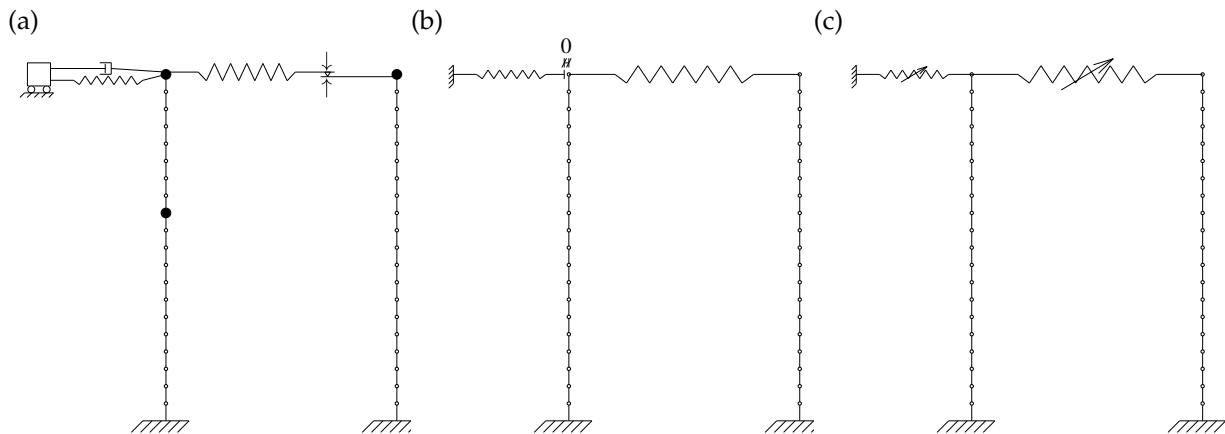


Figure 8.7: (a) Friction-coupled with time-varying mass (marked with large dots) and tuned mass damper, (b) coupled systems with nonlinear contact spring, and (c) coupled with a cubic spring

For the uncoupled system, the linear damping matrix, describing the linear inherent structural damping, is composed by the desired damping ratios of the considered modes and the principles of proportional damping [29]. As the beams are coupled, the viscous damping becomes nonproportional. The simulations are performed with the same state space technique as described in Section 8.7.4. For all simulations, uncorrelated Gaussian white noise excites the numerical model in all DOFs.

Results and discussion

In these numerical case studies, we have studied strain estimation for systems with nonlinear friction-coupling, nonlinear contact springs, cubic springs, a tuned-mass-damper, and time-varying masses. Figs. 8.8, 8.10, and 8.12 show the strain estimation at five evenly distributed nodes for case a, b, and c respectively, while Figs. 8.9, 8.11, and 8.13 contain the spectral density of strain estimation using the first four singular values for case a, b, and c respectively. The mean square errors of the strain estimation, using the pseudo modal coordinates, are of a magnitude of 10^{-35} and all TRAC values are one for the entire full-field strain response for all cases. Thus, proving, the underlying linear mode shapes of a single beam form a basis for a nonlinear and time-varying system with general viscous damping.

8.8.3 Experimental study on friction-coupled scale model of two offshore platforms

In this experimental case study, we will study strain estimation for nonlinear systems with a limited number of sensors and mode shapes. As test-specimen, we use two models of platforms in the laboratory, see Fig. 8.14, that we couple by a bridge introducing friction. Thus, the platforms are linear subsystems within a nonlinearly coupled system. We want to estimate the strain response of the small platform using mode shapes of this uncoupled platform. Of the two platforms, the small platform changes the most when the two platforms are coupled. First, we estimate the strain response in a linear and uncoupled

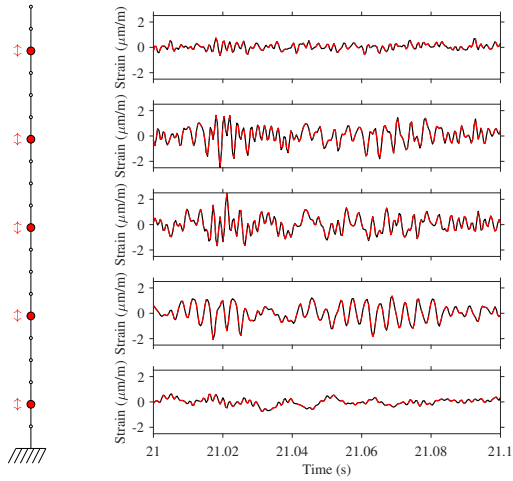


Figure 8.8: Case a: the estimated strain response (red dotted line) and the correct strain response (black line) in five locations marked on the cantilever beam on the left

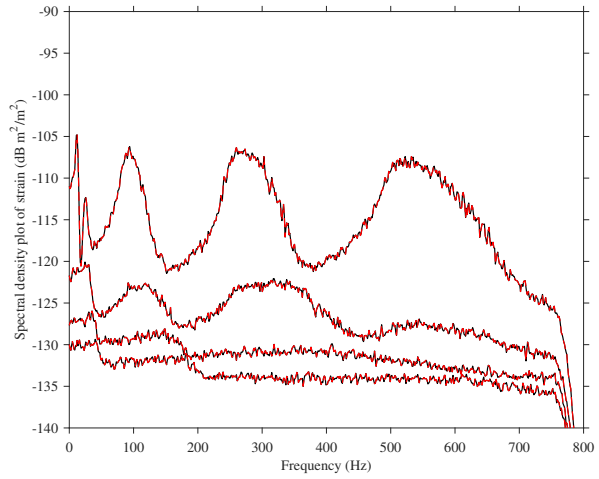


Figure 8.9: Case a: the first four singular values of the spectral density matrix of both the estimated full-field strain response (red dotted line) and the correct full-field strain response (black line) calculated using Welch averaging method with segments of 2048 data points and 50 % overlap

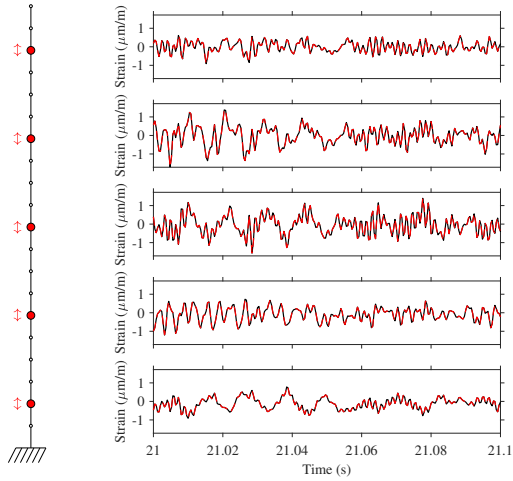


Figure 8.10: Case b: the estimated strain response (red dotted line) and the correct strain response (black line) in five locations marked on the cantilever beam on the left

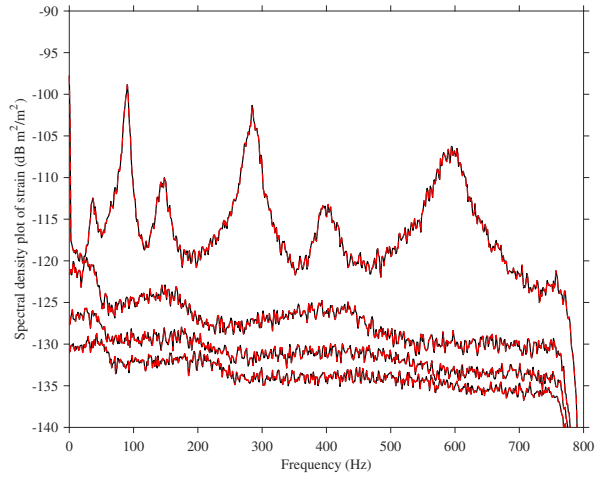


Figure 8.11: Case b: the first four singular values of the spectral density matrix of both the estimated full-field strain response (red dotted line) and the correct full-field strain response (black line) calculated using Welch averaging method with segments of 2048 data points and 50 % overlap

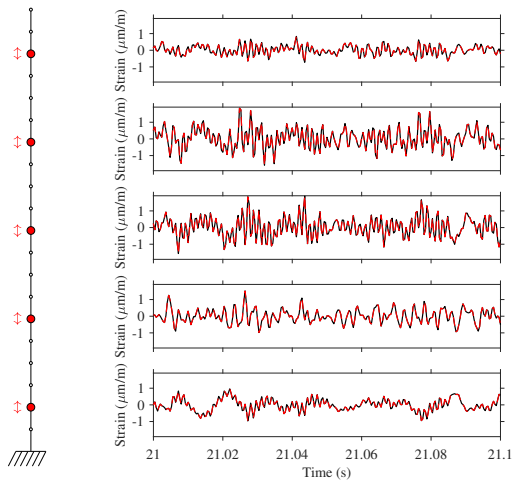


Figure 8.12: Case c: the estimated strain response (red dotted line) and the correct strain response (black line) in five locations marked on the cantilever beam on the left

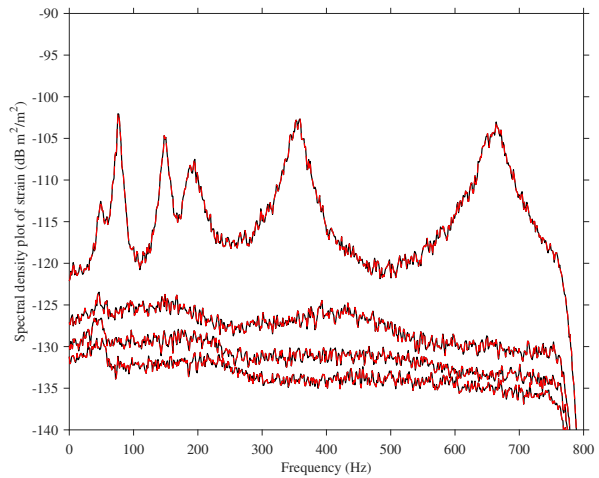


Figure 8.13: Case c: the first four singular values of the spectral density matrix of both the estimated full-field strain response (red dotted line) and the correct full-field strain response (black line) calculated using Welch averaging method with segments of 2048 data points and 50 % overlap

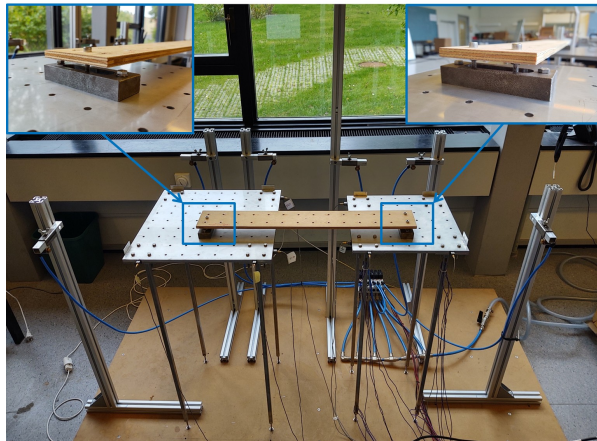


Figure 8.14: The two scaled platforms with the bridge, which applies friction-coupling between the platforms in the nonlinear case study

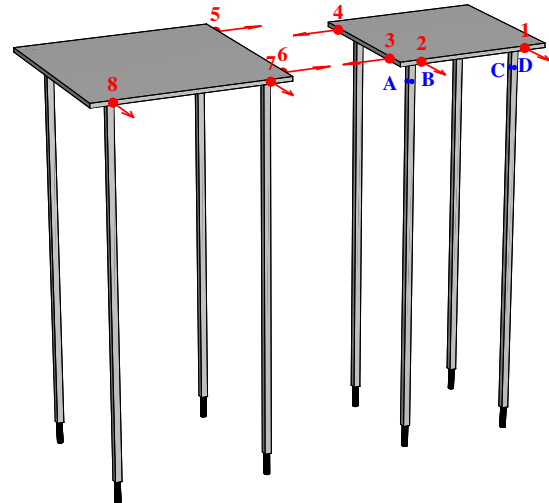


Figure 8.15: Position of sensors on the test specimen, the red arrows represent the eight Brüel & Kjær 4508-B uniaxial accelerometers and the blue dots represent the eight HBM 1-LY11-6/120 strain gauges measuring along the longitudinal direction of the members

case then we couple the two platforms with a bridge, which induces a friction connection, thus, the platforms become nonlinear.

8.8.4 System

We apply eight Brüel & Kjær 4508-B uniaxial accelerometers and eight HBM 1-LY11-6/120 strain gauges, see Fig. 8.15. The measured strain response of opposite sides of each member is subtracted and divided by two to reduce noise and normal forces in the cross section. This results in four strain gauges that we use as reference sensors for the strain estimation, see Fig. 8.15.

Compressed air excited the two platforms to generate loading with white noise characteristics. The data was sampled with a frequency of 1651 Hz and it was afterwards decimated to a new sampling frequency of 412.75 Hz.

To update a finite element model, we identify the modal parameters using operational modal analysis where we perform two separate analyses to identify the modal parameter of each platform. To identify the modal parameters of the linear setup, we estimate the correlation function matrix from all accelerometers attached to the given platform using a test with duration of 20 minutes from the linear setup and apply the Eigensystem Realization Algorithm (ERA) [44] using two block rows in the Hankel matrix and reducing to six singular values. The estimated correlation function matrix included 513 discrete time lags. This time length ensures low statistical errors in the estimation of the correlation function matrix. The biased error on the envelope of the modal auto-correlation function is less than 4% for the first mode of the small platform [45]. The operational modal analysis results in six identified modes, see Fig. 8.16 (a), where three of these relates to the small platform, see Fig. 8.16 (b) and Table 8.2.

We created a finite element model in Ansys 18.2 of the small platform. The model has a total of 996 nodes and 657 elements. We updated the supports, Youngs Modulus, and the density of finite element model to reduce the difference in frequency between the experimental modes and finite element modes and to ensure a spatial resemblance using the Modal Assurance Criterion (MAC). Table 8.2 shows the modal parameter from the updated finite element model and the operational modal analysis.

To apply strain estimation using the modal expansion, we need the displacement of the small platform. Using the Fourier transformation properties, we integrate the acceleration, $\ddot{\mathbf{y}}(t)$, from the accelerometers twice to the displacement, $\mathbf{y}(t)$ [30].

$$\mathbf{y}(t) = \mathcal{F}^{-1} \left(\frac{1}{-\omega^2} \mathcal{F}(\ddot{\mathbf{y}}(t)) \right) \quad (8.34)$$

where $\mathcal{F}(\cdot)$ and $\mathcal{F}^{-1}(\cdot)$ denote the standard and inverse Fourier transformation, respectively.

¹The first two modes are closely-spaced so they are rotated within their subspace to get the best MAC values with the mode shapes from the finite element model, see [30]

Table 8.2: Modal parameters of the small platform

| Mode | | 1 | 2 | 3 |
|--|----------------|----------|----------|----------|
| Updated finite element model | Frequency (Hz) | 3.561 | 3.628 | 6.670 |
| Operational modal analysis | Frequency (Hz) | 3.560 | 3.596 | 6.665 |
| | Difference (%) | -3.8e-03 | -8.9e-01 | -7.5e-02 |
| Modal Assurance Criterion (MAC) | (-) | 0.818 | 0.918 | 0.998 |
| MAC, rotating modes in subspace ¹ | (-) | 1.00 | 1.00 | 0.998 |

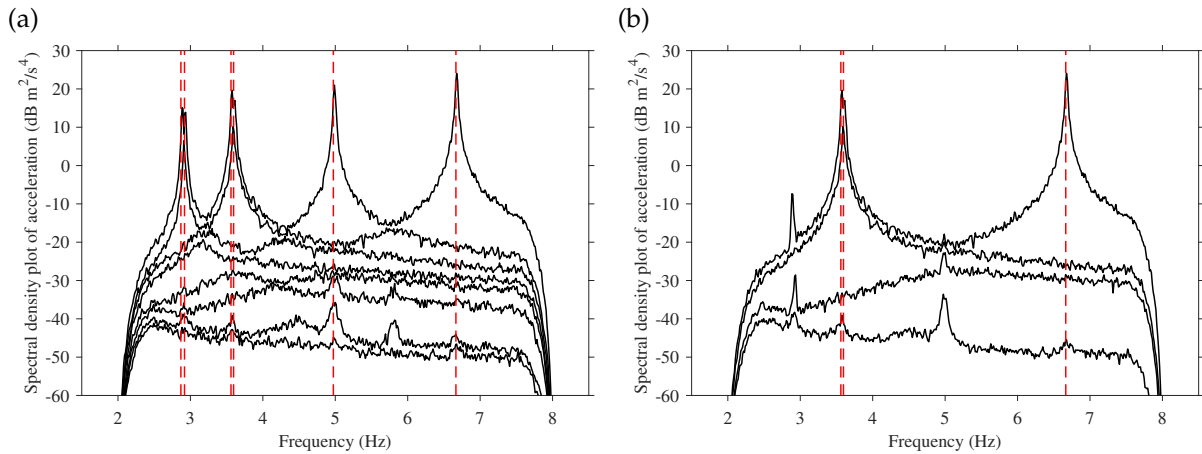


Figure 8.16: Linear setup: singular values of spectral density matrix calculated using Welch averaging method with segments of 2^{15} data points and 50 % overlap and the identified modes from an operational modal analysis using the Eigensystem Realization Algorithm (ERA) [44]: (a) both platforms and (b) small platform

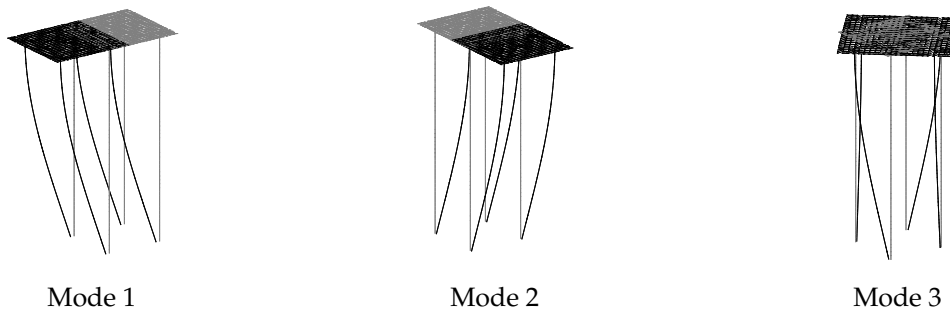


Figure 8.17: The first three mode shapes from the finite element model of the small platform

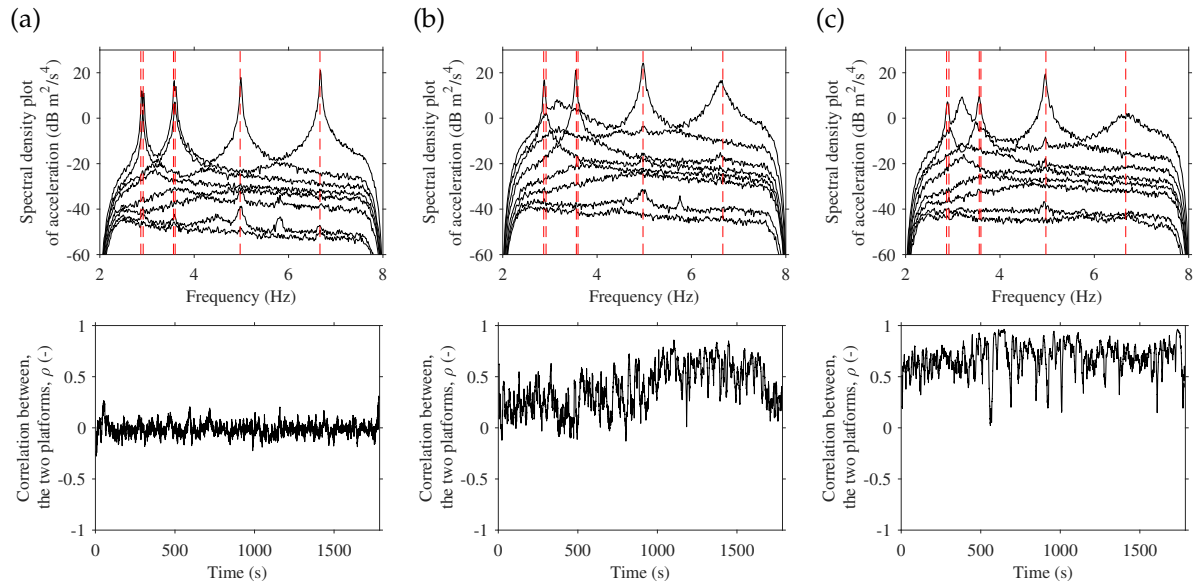


Figure 8.18: Each column represents one of the three considered cases, (a) mainly slip state, (b) interchanging states, and (c) mainly stick state. In the top, the singular values of the spectral matrix (black line) are plotted with the identified modes of the linear setup (red dotted line) to illustrate the change from the linear setup. In the bottom, the correlation of the mean movement of the two platforms in the direction of the bridge is calculated as the correlation coefficient with 2062 data points

In the nonlinear case, we add the bridge between the two platforms, see Fig. 8.14, which introduces friction-coupling. In the slip state of the friction-coupling, the two platforms move, primarily, separately as two unconnected structures while they share movement in the stick state. For the slip state, the movement of the two platforms is uncorrelated while the two platforms have highly correlated movement for the stick state. Furthermore, in the slip state, we have a total of six modes in the given frequency range while we only have five modes in the stick state where the bending modes of each platform - in direction of the other structure - merge into one. Since we add friction, the platforms have a decreased level of movement in the stick state. Under a given level of random excitation, the two platforms switch between the two states. Fig. 8.18 illustrates this phenomenon. For the nonlinear setup, we use a level of excitation where we have interchanging states for the strain estimation, see Fig. 8.18 (b). Here the peak, at approximately three Hz, indicates interchanging states and the third torsional mode of the large platform transfers some energy to the small platform at a frequency of approximately five Hz, see Fig. 8.18. Thus, the two platforms are friction-coupled and nonlinear.

Results

We perform strain estimation with a time duration of 20 minutes for both the linear and nonlinear setup using the same three mode shapes from the updated finite element model. Figs. 8.19 and 8.20 show a zoom of the estimated and measured strain response for the linear and nonlinear setup while Fig. 8.21 shows the spectral density of the estimated and measured strain response for the linear and nonlinear setup.

For the quality measurement, we separated each data sets into 20 subsets with a length of a single minute. This is done to access the distribution of the metrics. Fig. 8.22 shows the TRAC values while Fig. 8.23 shows the NEFD values for both the linear and nonlinear setup. Generally, the quality measures are similar for both the linear and nonlinear setup. The quality measures from the linear setup have higher scatter than the measures from the nonlinear setup. For strain gauges A and C, the linear setup provides the quality measures with the best results while the nonlinear setup ensure the best result for strain gauges B and D. There might be a small amount of modal truncation errors present in the estimation of strain in A and B due to higher modes (local modes in the leg of the platform) contributing to the response for the nonlinear setup.

In Fig. 8.23, all NEFD values show an underestimation of fatigue damage. This could be caused by the measurement noise (noise floor) on the strain gauges, so the reference signals contain noise, which results in a higher fatigue damage for the reference signal than what it should have. It could also be related to modal truncation errors or modelling errors of the finite element model. In [8], it is observed that

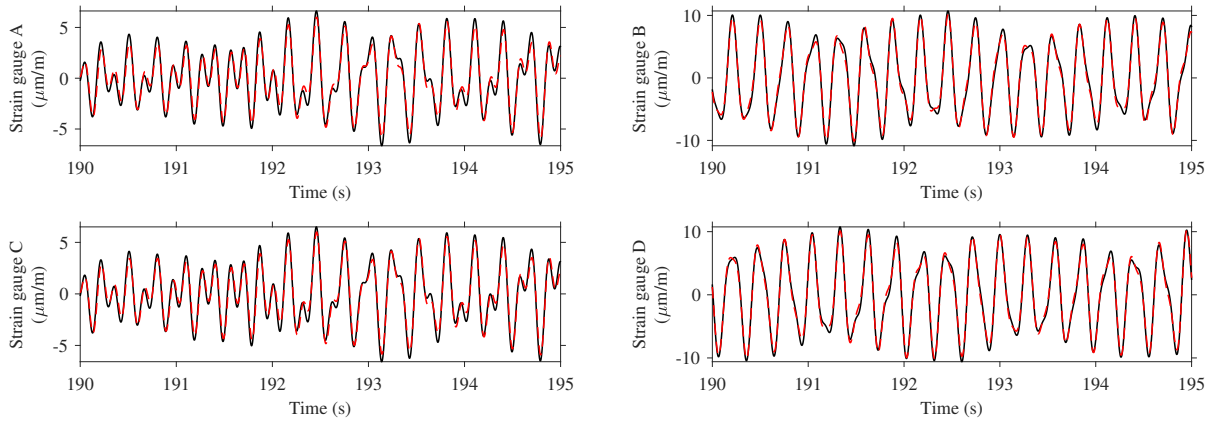


Figure 8.19: Linear case: zoom of measured (black line) and estimated (red dotted line) strain response

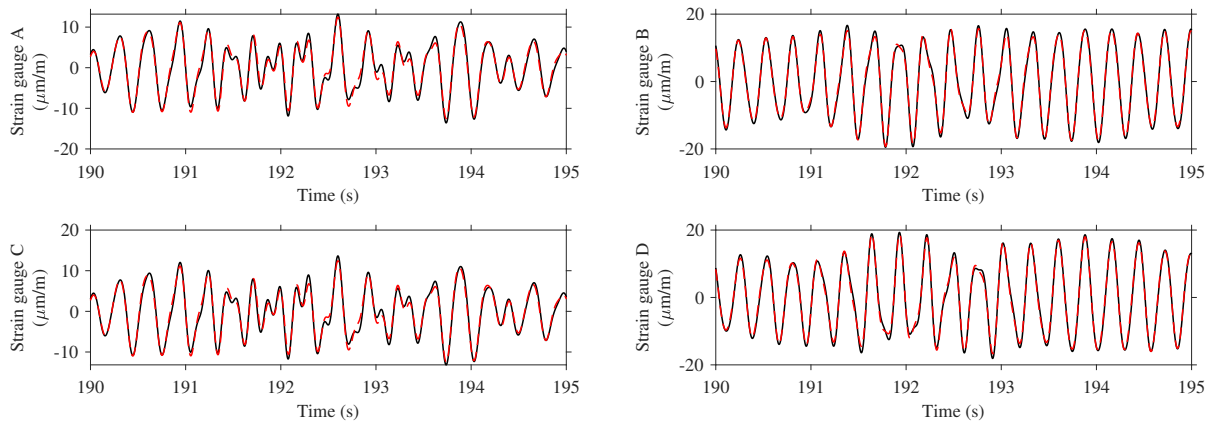


Figure 8.20: Nonlinear case: zoom of measured (black line) and estimated (red dotted line) strain response

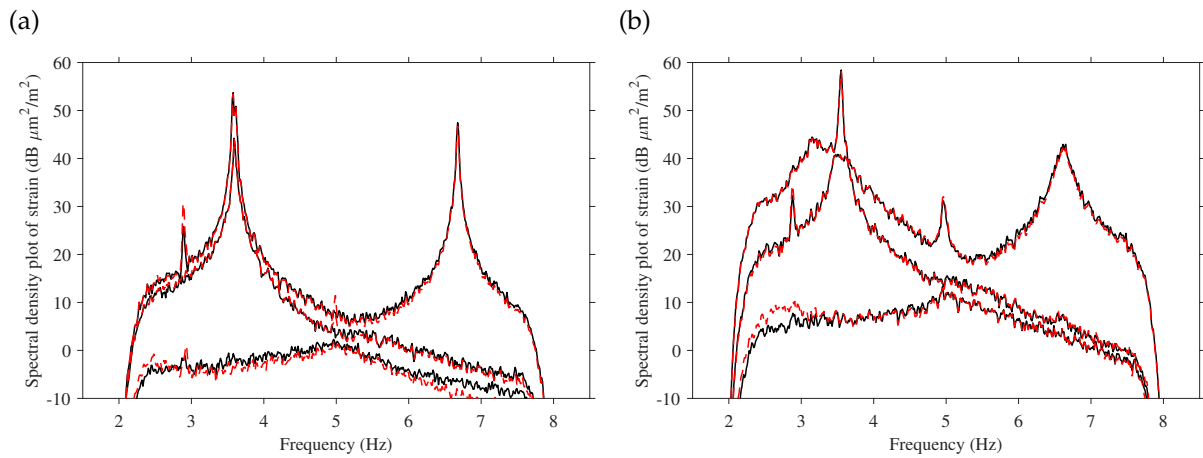


Figure 8.21: Singular values of spectral density matrix from the measured (black line) and estimated (red dotted line) strain response calculated using Welch averaging method with segments of 2^{15} data points and 50% overlap: (a) linear setup and (b) nonlinear setup

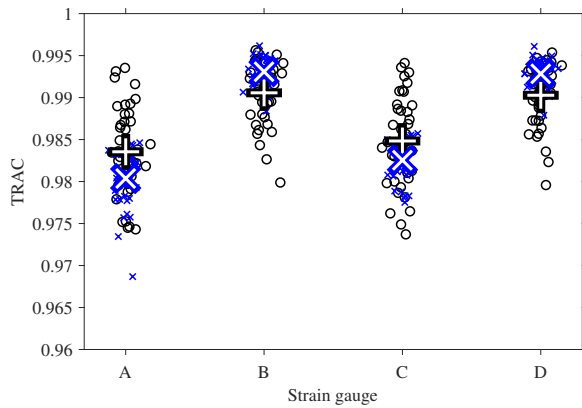


Figure 8.22: The Time Response Assurance Criterion (TRAC) values for the linear (black circles) and nonlinear case (blue crosses) together with the sample mean value for the linear (black plus sign) and nonlinear case (blue cross)

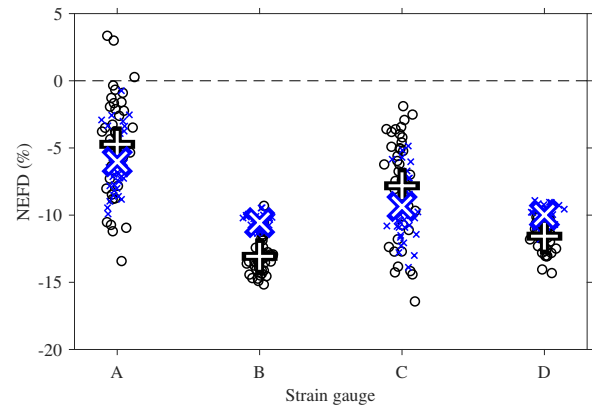


Figure 8.23: Normalised Error of Fatigue Damage (NEFD) for the linear (black circles) and nonlinear case (blue crosses) together with the sample mean value for the linear (black plus sign) and nonlinear case (blue cross)

modelling errors on the mode shapes result in either overestimation or underestimation of the fatigue damage in strain estimation due to errors in the amplitude of the strain estimation.

8.9 Conclusion

In this paper, we have proven that the undamped, linear mode shapes span the response of nonlinear and time-varying systems with general viscous damping. This is applied to stress/strain estimation of subsystems within these systems using the modal expansion method. Here the nonlinear and time-varying effects act externally on each subsystem so we can interpret the subsystems as linear with external force, which depends on the response of the subsystems. Therefore, the undamped, linear mode shapes of the subsystem are used to estimate the stress/strain response of the linear subsystems within the nonlinear and time-varying systems with general viscous damping. The theory is verified by three numerical studies of nonlinear and/or time-varying structures with general viscous damping.

By truncating the number of undamped, linear mode shapes, we approximate the subspace of the response with a modal truncation error. The level of this error depends on the span of the undamped, linear mode shapes and the extent of the change from the undamped system to the new system. For the modal expansion technique, we can use this principle to estimate stress/strain for linear subsystems within nonlinear and time-varying systems with general viscous damping by an appropriate set of undamped, linear mode shapes. This is verified by an experimental case study with two scale models of offshore platforms in a laboratory coupled by friction. Here the scaled platforms are linear subsystems coupled nonlinearly together to a nonlinear system. Here the same accuracy was observed for the nonlinear setup as for the linear setup though the test-specimen acted nonlinearly.

Acknowledgements

The authors acknowledge the funding received from the Centre for Oil and Gas - DTU/Danish Hydrocarbon Research and Technology Centre (DHRTC).

Appendix 8.A Relationship between the complex nonlinear mode shapes and undamped linear mode shapes

Now, we will set up a relationship between the complex nonlinear and undamped mode shapes. First, we go back to the undamped version of the equation of motion without excitation within \mathbb{R}^N .

$$\mathbf{M}\ddot{\mathbf{y}}(t) + \mathbf{K}\mathbf{y}(t) = \mathbf{0} \quad (8.35)$$

We know that the undamped and linear system has the normal mode shapes, Φ that decorrelate the equations into the modal space but we will now find these mode shapes in a different way. Since we

can use any basis to describe a vector in \mathbb{R}^N then we use the nonlinear vector basis spanned by the complex and nonlinear mode shapes, Eq. (8.19), as basis for the linear system response and insert into the equation of motion, Eq. (8.35).

$$\mathbf{M} \frac{\partial^2}{\partial t^2} (\mathbf{\Psi}(\mathbf{E}(t)) \mathbf{q}_c(t)) + \mathbf{K} \mathbf{\Psi}(\mathbf{E}(t)) \mathbf{q}_c(t) = \mathbf{0} \quad (8.36)$$

This equation of motion is coupled but we can set up a new eigenvalue problem for any given level of energy. We assume a solution of the form: $\mathbf{q}_c(t) = \mathbf{T}(\mathbf{E}(t)) \tilde{\mathbf{q}}(\mathbf{E}(t))$.

$$\mathbf{M} \frac{\partial^2}{\partial t^2} (\mathbf{\Psi}(\mathbf{E}(t)) \mathbf{T}(\mathbf{E}(t)) \tilde{\mathbf{q}}(\mathbf{E}(t))) + \mathbf{K} \mathbf{\Psi}(\mathbf{E}(t)) \mathbf{T}(\mathbf{E}(t)) \tilde{\mathbf{q}}(\mathbf{E}(t)) = \mathbf{0} \quad (8.37)$$

We rearrange into a nonlinear eigenproblem.

$$\mathbf{M}^{-1} \mathbf{K} \mathbf{\Psi}(\mathbf{E}(t)) \mathbf{T}(\mathbf{E}(t)) \tilde{\mathbf{q}}(\mathbf{E}(t)) = - \frac{\partial^2}{\partial t^2} (\mathbf{\Psi}(\mathbf{E}(t)) \mathbf{T}(\mathbf{E}(t)) \tilde{\mathbf{q}}(\mathbf{E}(t))) \quad (8.38)$$

There is, however, a solution that simplifies this nonlinear eigenproblem to a linear problem.

$$\tilde{\mathbf{q}}(\mathbf{E}(t)) = \exp[i\omega_i t] \quad , \quad \mathbf{\Phi} = \mathbf{\Psi}(\mathbf{E}(t)) \mathbf{T}(\mathbf{E}(t)) \quad (8.39)$$

Then we obtain the proper eigenvalue-eigenvector equation.

$$\mathbf{M}^{-1} \mathbf{K} \mathbf{\Phi} = [\omega_i^2] \mathbf{\Phi} \quad (8.40)$$

We rewrite the solution of the eigenvectors, Eq. (8.39).

$$\mathbf{\Psi}(\mathbf{E}(t)) = \mathbf{\Phi} \mathbf{P}(\mathbf{E}(t)) \quad (8.41)$$

where $\mathbf{P}(\mathbf{E}(t)) \in \mathbb{C}^{N \times 2N}$ is the change of basis matrix, which holds the combination of normal modes.

References

- [1] L. Liu, S. M. Kuo, and M. Zhou. Virtual sensing techniques and their applications. In *2009 International Conference on Networking, Sensing and Control*, pages 31–36, March 2009.
- [2] A. Skafte, J. Kristoffersen, J. Vestermarck, U. T. Tygesen, and R. Brincker. Experimental study of strain prediction on wave induced structures using modal decomposition and quasi static ritz vectors. *Engineering Structures*, 136:261–276, 4/1 2017.
- [3] Alexandros Iliopoulos, Wout Weijtjens, Danny Van Hemelrijck, and Christof Devriendt. Fatigue assessment of offshore wind turbines on monopile foundations using multi-band modal expansion. *Wind Energy*, 20(8):1463–1479, 2017.
- [4] M. Tarpø, T. Friis, B. Nabuco, S. Amador, E. Katsanos, and R. Brincker. Operational modal analysis based stress estimation in friction systems. In Gaetan Kerschen, editor, *Nonlinear Dynamics, Volume 1*, pages 143–153, Cham, 2019. Springer International Publishing.
- [5] H.P. Hjelm, R. Brincker, J. Gaugaard-Jensen, and K. Munch. Determination of stress histories in structures by natural input modal analysis. *Proceedings of IMAC XXIII International Modal Analysis Conference*, 12:838–844, 2006.
- [6] J. Graugaard-Jensen, Rune Brincker, H. P. Hjelm, and K. Munch. Modal based fatigue monitoring of steel structures. *Structural Dynamics EURO-DYN 2005: Proceedings of 6th International Conference on Structural Dynamics*, pages 305–310, 2005.
- [7] B. Nabuco, T. Friis, M. Tarpø, S. Amador, E.I. Katsanos, and R. Brincker. Nonlinear strain estimation based on linear parameters. *ASME 2018 37th International Conference on Ocean, Offshore and Arctic Engineering*, 3: Structures, Safety, and Reliability:7, 2018.
- [8] M. Tarpø, B. Nabuco, C. Georgakis, and R. Brincker. Expansion of experimental mode shape from operational modal analysis and virtual sensing for fatigue analysis using the modal expansion method. *International Journal of Fatigue*, 130:105280, 2020.
- [9] Jakerson Gevinski and Robson Pederiva. Dynamic strain prediction using modal parameters. *Journal of the Brazilian Society of Mechanical Sciences and Engineering*, 38, 06 2015.

- [10] P. Ren and Z. Zhou. Strain estimation of truss structures based on augmented kalman filtering and modal expansion. *Advances in Mechanical Engineering*, 9(11):1–10, 2017. Structural health monitoring of the truss structure is often confronted with spatial incomplete measured data due to the reasons of the cost of the sensors,...
- [11] C. Papadimitriou, C.P. Fritzen, P. Kraemer, and E. Ntotsios. Fatigue predictions in entire body of metallic structures from a limited number of vibration sensors using kalman filtering. *Structural Control and Health Monitoring*, 18(5):554–573, 2011.
- [12] K. Maes, A. Iliopoulos, W. Weijtjens, C. Devriendt, and G. Lombaert. Dynamic strain estimation for fatigue assessment of an offshore monopile wind turbine using filtering and modal expansion algorithms. *Mechanical Systems and Signal Processing*, 76-77:592–611, 2016.
- [13] S. E. Azam, E. Chatzi, and C. Papadimitriou. A dual kalman filter approach for state estimation via output-only acceleration measurements. *Mechanical Systems and Signal Processing*, 60-61:866–886, 2015.
- [14] P. Ren and Z. Zhou. Strain response estimation for fatigue monitoring of an offshore truss structure. *Pacific Science Review*, 16(1):29–35, 2014.
- [15] Rajendra Prasath Palanisamy, Soojin Cho, Hyunjun Kim, and Sung-Han Sim. Reconstruction of unmeasured strain responses in bottom-fixed offshore structures by multimetric sensor data fusion. *Smart Structures and Systems*, 15:489–503, 2015.
- [16] K. Maes, G. De Roeck, G. Lombaert, A. Iliopoulos, D. Van Hemelrijck, C. Devriendt, and P. Guillaume. Continuous strain prediction for fatigue assessment of an offshore wind turbine using kalman filtering techniques. In *2015 IEEE Workshop on Environmental, Energy, and Structural Monitoring Systems (EESMS) Proceedings*, pages 44–49, July 2015.
- [17] Phil Kim and Lynn Huh. *Kalman filter for beginners : with MATLAB examples*. CreateSpace, United States, 2011.
- [18] Denis Gordon Karczub. *The prediction of dynamic stress and strain in randomly vibrating structures using vibrational velocity measurements*. PhD thesis, The University of Western Australia, 1996.
- [19] F. V. Hunt. Stress and strain limits on the attainable velocity in mechanical vibration. *The Journal of the Acoustical Society of America*, 32(9):1123–1128, 1960.
- [20] Stephen H. Crandall. Relation between strain and velocity in resonant vibration. *The Journal of the Acoustical Society of America*, 34(12):1960–1961, 1962.
- [21] N. Okubo and K. Yamaguchi. Prediction of strain distribution under operating condition by the use of modal analysis. *Proceedings of the International Modal Analysis Conference XIII*, 210(5):91–96, 1995.
- [22] S.-W. Seo, K.-J. Kim, and B.-K. Bae. Estimation of operational strains from vibration measurements: An application to lead wires of chips on printed circuit board. *Journal of Sound and Vibration*, 210(5):567 – 579, 1998.
- [23] A. Sestieri. Structural dynamic modification. *Sadhana*, 25(3):247–259, 2000.
- [24] Jyrki Kullaa. Virtual sensing of structural vibrations using dynamic substructuring. *Mechanical Systems and Signal Processing*, 79:203 – 224, 2016. Special Issue from ICEDyn 2015.
- [25] Wei Lu, Jun Teng, Qiushi Zhou, and Qiexin Peng. Stress prediction for distributed structural health monitoring using existing measurements and pattern recognition. *Sensors*, 18(2), 2018.
- [26] Huaxia Deng, Haicong Zhang, Jun Wang, Jin Zhang, Mengchao Ma, and Xiang Zhong. Modal learning displacement–strain transformation. *Review of Scientific Instruments*, 90(7):075113, 2019.
- [27] Enrico Risaliti, Tommaso Tamarozzi, Martijn Vermaut, Bram Cornelis, and Wim Desmet. Multibody model based estimation of multiple loads and strain field on a vehicle suspension system. *Mechanical Systems and Signal Processing*, 123:1 – 25, 2019.
- [28] Marius Tarpø, Michael Vigsø, and Rune Brincker. Modal truncation in experimental modal analysis. In Michael Mains and Brandon J. Dilworth, editors, *Topics in Modal Analysis & Testing, Volume 9*, pages 143–152, Cham, 2019. Springer International Publishing.
- [29] R. W. Clough and J. Penzien. *Dynamics of structures*. CSI Computers & Structures, Inc., Berkeley, Calif., 2nd revised edition, 2003.
- [30] Rune Brincker and Carlos Ventura. *Introduction to operational modal analysis*. John Wiley and Sons, Inc., Chichester, West Sussex, UK, 2015.
- [31] A.K. Chopra. *Dynamics of Structures: Theory and Applications to Earthquake Engineering*. Prentice Hall International Series in Civil Engineering And. Pearson/Prentice Hall, 2007.

- [32] Erwin Kreyszig, Herbert Kreyszig, and Edward J. Norminton. *Advanced engineering mathematics*. John Wiley And Sons Ltd, Hoboken, NJ, 10th edition, 2011.
- [33] Jörg Liesen and Volker Mehrmann. *Vector Spaces*, pages 115–133. Springer International Publishing, Cham, 2015.
- [34] R. Brincker, A. Skaftø, M. López-Aenlle, A. Sestieri, W. D’Ambrogio, and A. Canteli. A local correspondence principle for mode shapes in structural dynamics. *Mechanical Systems and Signal Processing*, 45(1):91–104, 2013.
- [35] Adhikari Sondipon. Rates of change of eigenvalues and eigenvectors in damped dynamic system. *AIAA Journal*, 37(11):1452–1458, 1999.
- [36] Anestis S. Veletsos and Carlos E. Ventura. Modal analysis of non-classically damped linear systems. *Earthquake Engineering & Structural Dynamics*, 14(2):217–243, 1986.
- [37] G. Kerschen, M. Peeters, J.C. Golinval, and A.F. Vakakis. Nonlinear normal modes, part i: A useful framework for the structural dynamicist. *Mechanical Systems and Signal Processing*, 23(1):170 – 194, 2009. Special Issue: Non-linear Structural Dynamics.
- [38] F. López-Almansa, A. H. Barbat, and J. Rodellar. Ssp algorithm for linear and non-linear dynamic response simulation. *International Journal for Numerical Methods in Engineering*, 26(12):2687–2706, 1988.
- [39] L.-Y. Lu, L.-L. Chung, L.-Y. Wu, and G.-L. Lin. Dynamic analysis of structures with friction devices using discrete-time state-space formulation. *Computers & Structures*, 84(15–16):1049 – 1071, 2006.
- [40] Jon Juel Thomsen. *Vibrations and Stability: Advanced Theory, Analysis, and Tools*. Springer Verlag, 2003.
- [41] P. Avitabile and P. Pingle. Prediction of full field dynamic strain from limited sets of measured data. *Shock and Vibration*, 19(5):765–785, 2012.
- [42] C. Amzallag, J.P. Gerey, J.L. Robert, and J. Bahuaud. Standardization of the rainflow counting method for fatigue analysis. *International Journal of Fatigue*, 16(4):287 – 293, 1994.
- [43] M.M. Pedersen. Introduction to metal fatigue. Technical report, Department of Engineering, Aarhus University, 2018.
- [44] J. N. Juang and R. S. Pappa. An eigensystem realization algorithm for modal parameter identification and model reduction. *Journal of Guidance*, 8(5):620–627, 1985.
- [45] Marius Tarpø, Tobias Friis, Christos Georgakis, and Rune Brincker. The statistical errors in the estimated correlation function matrix for operational modal analysis. *Journal of Sound and Vibration*, page 115013, 2019.

Chapter 9

Paper 6 - Tilt errors of linear accelerometers attached to dynamic systems with tilt motion caused by the system response

‘(*Nothing in life is to be feared, it is only to be understood. Now is the time to understand more, so that we may fear less* ’)

Marie Curie

Status

- Submitted to Journal of Sound and Vibrations, summer 2020

9.1 Introduction

As stated in section 3, there are three main obstacles in estimating the stress/strain response in the quasi-static region of offshore platforms:

- The quasi-static response of a dynamic system (modal truncation)
- The drift of accelerations
- The tilt of accelerometers

In the paper, we will study accelerometers, which rotate due to tilt motion and measure components of the gravitational acceleration. This tilt effect is well-documented for static or quasi-static conditions and it is utilised in tilt-sensing applications. In this paper, we will study the tilt effect on accelerometers attached to a linear and time-invariant system under dynamic conditions where the tilt motion stems from the dynamic response of the system itself.

9.2 Contribution

Rune Brincker made an original note on the tilt error and this author made an additional note on tilt error on dynamic systems to set up an impulse and frequency response function matrix for the measured acceleration with tilt error. The author combined and completely rewrote the two notes, wrote additional sections, changed and extended the theory, performed a literature review on the subject, and conducted the experimental case study.

9.3 Main findings

We found that, due to the gravitational acceleration, the rotational displacement pollutes the measured translational acceleration of the system in the DOFs where an accelerometer is attached to the system.

We derived expressions for the impulse and frequency response function matrix for the measured acceleration of a tilting accelerometer that expresses the tilt error. Additionally, we introduced two methods for estimating the tilt angle that are applicable for tilt reduction. Finally, we verified the theory and illustrated the reduction of the tilt error on a test specimen in the laboratory.

9.4 Reflections

This paper furthers our understanding of the tilt error on accelerometers and it brings the research field closer to overcoming the obstacles in stress/strain estimation in the quasi-static region of offshore platforms. We can apply either of the introduced techniques to reduce the tilt error on the measured acceleration of offshore structures.

Tilt errors of linear accelerometers attached to dynamic systems with tilt motion caused by the system response

Marius Tarpø^a, Bruna Nabuco^b, Rubén Boroschek^c, Rune Brincker^b

^aAarhus University, Department of Engineering, Inge Lehmanns Gade 10, Aarhus, Denmark

^bTechnical University of Denmark, Department of Civil Engineering, Brovej B.118, Kgs. Lyngby, Denmark

^cUniversity of Chile, Department of Civil Engineering, Av. Blanco Encalada 2002, Santiago, Chile

Abstract

Translational inertia sensors - like the accelerometer - can measure the translational acceleration but they are incapable of distinguishing between translational and tilt motions. As an accelerometer tilts, it will measure a component of the gravitational acceleration along with the translational acceleration of the sensors. This results in a tilt error on the measured acceleration that masks the actual translational acceleration. In this paper, tilt error is studied for accelerometers attached to linear, stationary, and dynamic systems where the tilt motion originates from the system response. Mathematical formulations of the tilt errors are introduced where an impulse and frequency response function matrix for the measured acceleration from accelerometers is derived. It is proven that the tilt error is a pollution by the rotational displacement on the translational acceleration of the accelerometers. Thus, the displacement of a dynamic system merges with its acceleration in the presence of tilt errors and the level of tilt error depends on the system and the excitation. In this paper, two methods are introduced to reduce the tilt error. Both theory and tilt reduction are verified on a test-specimen in the laboratory.

Keywords: Accelerometers, tilt sensing, tilt motion, tilt-to-horizontal coupling

9.6 Introduction

An accelerometer is an inertia sensor that measures proper acceleration (the acceleration experienced by the sensor itself) [1]. A wide range of accelerometers exists with different strengths and weaknesses where they exist as uni-, bi-, tri-, or multi-axial versions. Characteristics of accelerometers include sensitivity, frequency range (bandwidth), measuring range, and linearity of the sensors [1]. Some accelerometers are capable of true Direct Current (DC) measurements while others have built-in filters. In general, the sensor is attached to a movable object, which may undergo rotational motion, so the sensor measures acceleration in a fixed direction(s) relative to the sensor itself and these forces are transformed to accelerations. Therefore, they do not measure the acceleration in a fixed coordinate system but in a relative coordinate system to the rotation of the sensor.

An accelerometer measures all acceleration including the gravitational acceleration, which is a constant force directed toward the centre of the earth [1]. Therefore, as an accelerometer undergoes rotational motion - tilt -, the accelerometer measures a component of the gravitational acceleration along with the actual acceleration of the sensor. Even an accelerometer - incapable of true DC measurements - measures a component of the gravitational acceleration when the sensor rotates dynamically. This is a well-known phenomenon and it is used to estimate, detect, and/or sense the tilt angle of an object using accelerometers in static or quasi-static conditions where the sensors are affected by gravitational acceleration and unaffected by a translational acceleration of the sensor [1–8]. Under dynamic conditions, the rotation of an accelerometer causes a tilt error in the measured acceleration [9, 10]. Brincker and Ventura [10] made a basic introduction to the effect of tilt on accelerometers for structural health monitoring. Boroschek and Legrand [9] experimentally studied the effect of static and dynamic tilt motion on accelerometer when the measured acceleration is double-time integrated to displacement. They found that tilt angles cause distortion - at low frequency and the frequency of rotation - in the measured acceleration of accelerometer. In the literature, tilt errors for inertia sensors are studied with a focus on earthquake and strong motion where the rotational components of the ground motion transfer to the inertia sensor [11–15]. Here Fabrice et al. [16] reviewed configurations for separation of horizontal and tilt motion with focus on seismological studies and seismic isolation applications. To the best of the authors' knowledge, the erroneous effect of tilt motion on accelerometers is scarcely studied under dynamic conditions when the tilt effect is not caused by ground motion.

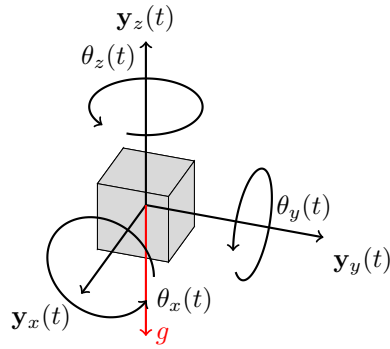


Figure 9.1: An accelerometer is a single node with six-degrees-of-freedom and it can measure translational acceleration in one, two, or three principal directions (also known as uni-, bi-, and triaxial)

In this paper, we will investigate the effect of tilting accelerometers where we exclude the sensitivity range of accelerations and other measurement errors. This paper provides an introduction to the tilt of accelerometers: how this influences accelerometer measurements of acceleration on linear, time-invariant, and dynamic systems, and how this influence is reduced. In contrast to previously published papers, this paper focuses on the dynamic conditions for accelerometers and the effect of tilt motion - not caused by ground motion. In this paper, we will derive an impulse and frequency response function matrix for the measured acceleration of accelerometers mounted to a dynamic system by assuming small tilt angles. Furthermore, we will prove that tilt errors are caused by the rotational displacements of an accelerometer that pollute the measured translational acceleration. Therefore, tilt is a dynamic error where the level of tilt error relates to the relationship of the rotational displacement and the translational acceleration of an accelerometer. Dependent on the level of error, tilt motions cause an amplitude error in the measured acceleration that will result in an error in the identification process of mode shapes. We verify both the theory of tilt error and tilt reduction on a test-specimen in the laboratory.

9.7 Theory

In this section, we will introduce the tilt error of rotating linear accelerometers. Whenever an accelerometer rotates - or tilts - the sensor measures a component of the gravitational acceleration that depends on the tilt angle [1–4, 6–10]. Thus, tilt motion influences the measured acceleration due to the influence of the gravitational acceleration. For accelerometers attached to dynamic systems, the tilt creates an error in the measurement of the actual acceleration. In the following sections, we will formulate the statement in a mathematical form.

The reader should note that different definitions exist for angles eg. roll, yaw, and pitch angles (Euler angles). In this paper, we will define angle as the rotation around each primary axis: rotation around the x -axis is θ_x , rotation around the y -axis is θ_y , and rotation around the z -axis is θ_z .

9.7.1 Tilt error

Let us say that we have a network of accelerometers that measures the linear or translational accelerations in a finite set of Degree-Of-Freedom (DOF) on a rigid body. The acceleration of the rigid body is given by

$$\dot{\mathbf{y}}(t) = [\dot{\mathbf{y}}_a(t) \quad \dot{\boldsymbol{\theta}}(t)]^T \tag{9.1}$$

where $\mathbf{y}(t)$ is the full displacement vector, t is time, $\mathbf{y}_a(t)$ is the DOFs corresponding to the location of accelerometers, and $\boldsymbol{\theta}(t)$ is the rotational DOFs of the sensors.

Next, let us say that the error signal from the tilt is $\boldsymbol{\varepsilon}(t)$, so the signal $\mathbf{s}(t)$ measured by the accelerometers is

$$\mathbf{s}(t) = \dot{\mathbf{y}}_a(t) + \boldsymbol{\varepsilon}(t) \tag{9.2}$$

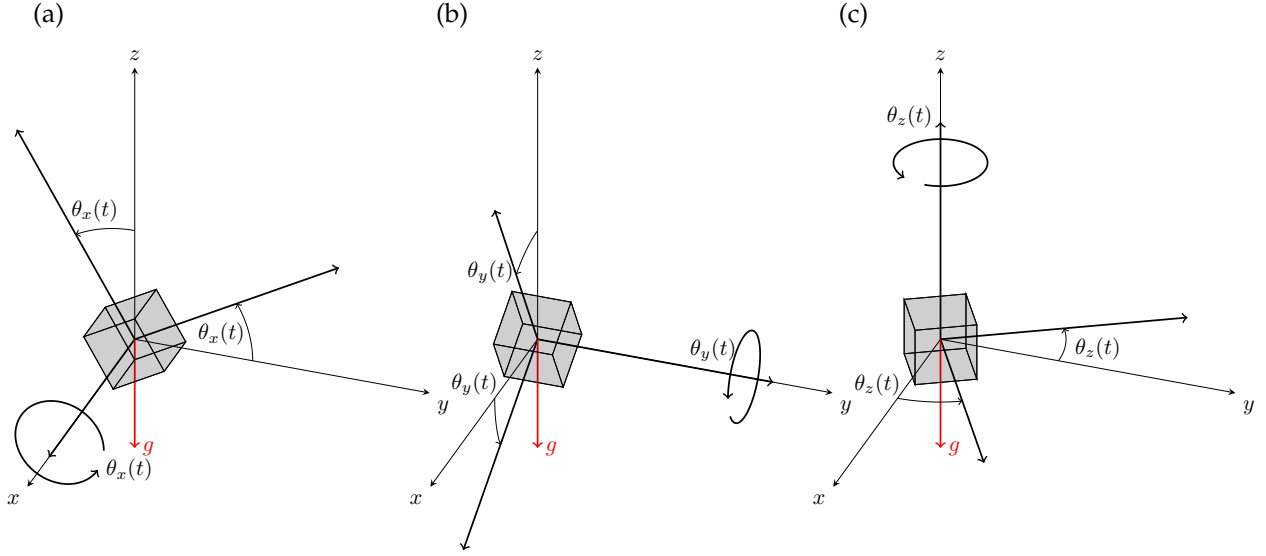


Figure 9.2: As the accelerometer tilts, it measures a component of gravitational acceleration: (a) rotation, θ_x , around the x -axis, (b) rotation, θ_y , around the y -axis, and (c) rotation, θ_z , around the z -axis

For simplicity, we will derive the following for a triaxial accelerometer, $\mathbf{s}(t) \in \mathbb{R}^3$, but the derivation is expandable to any network of accelerometers. Thus, we have a triaxial accelerometer mounted in a single point, measuring the translational acceleration in the main directions, see Fig. 9.1. In the case of no rotation of the triaxial accelerometer, we can express the static tilt error.

$$\boldsymbol{\varepsilon}(t) = \mathbf{g}, \text{ for } \boldsymbol{\theta}(t) = \mathbf{0} \quad (9.3)$$

where $\mathbf{g} = [0 \ 0 \ -g]^T$ is the gravity vector accounting for the constant signal in the vertical direction.

Next, we will introduce rotation around the x -, y -, and z -axes - denoted as θ_x , θ_y , and θ_z , see Fig. 9.2, and we organise these rotations in a vector.

$$\boldsymbol{\theta}(t) = [\theta_x(t) \ \theta_y(t) \ \theta_z(t)]^T \quad (9.4)$$

We express the error as the accelerometer tilts by multiplying with the rotation matrix.

$$\boldsymbol{\varepsilon}(t) = \mathbf{R}(\boldsymbol{\theta}(t)) \mathbf{g} \quad (9.5)$$

where $\mathbf{R}(\boldsymbol{\theta}(t))$ is composed by the basic rotation matrices.

$$\mathbf{R}(\boldsymbol{\theta}(t)) = \begin{bmatrix} 1 & 0 & 0 \\ 0 & \cos(\theta_x(t)) & \sin(\theta_x(t)) \\ 0 & -\sin(\theta_x(t)) & \cos(\theta_x(t)) \end{bmatrix} \begin{bmatrix} \cos(\theta_y(t)) & 0 & -\sin(\theta_y(t)) \\ 0 & 1 & 0 \\ \sin(\theta_y(t)) & 0 & \cos(\theta_y(t)) \end{bmatrix} \begin{bmatrix} \cos(\theta_z(t)) & \sin(\theta_z(t)) & 0 \\ -\sin(\theta_z(t)) & \cos(\theta_z(t)) & 0 \\ 0 & 0 & 1 \end{bmatrix} \quad (9.6)$$

Thus, the tilt error is given by

$$\boldsymbol{\varepsilon}(t) = g [\sin(\theta_y(t)) \ -\cos(\theta_y(t)) \sin(\theta_x(t)) \ -\cos(\theta_x(t)) \cos(\theta_y(t))]^T \quad (9.7)$$

We rewrite this vector using calculation rules for products of sines and cosines [17] so we end with the following expression in vector-matrix form for the measured acceleration.

$$\boldsymbol{\varepsilon}(t) = \mathbf{G}_1 \cos(\mathbf{G}_2 \boldsymbol{\theta}(t)) + \mathbf{P}_1 \sin(\mathbf{P}_2 \boldsymbol{\theta}(t)) \quad (9.8)$$

where

$$\mathbf{G}_1 = g \begin{bmatrix} 0 & 0 & 0 \\ 0 & 0 & 0 \\ 0 & -\frac{1}{2} & -\frac{1}{2} \end{bmatrix}, \quad \mathbf{G}_2 = \begin{bmatrix} 0 & 0 & 0 \\ 1 & 1 & 0 \\ 1 & -1 & 0 \end{bmatrix}, \quad \mathbf{P}_1 = g \begin{bmatrix} 1 & 0 & 0 \\ 0 & -\frac{1}{2} & -\frac{1}{2} \\ 0 & 0 & 0 \end{bmatrix}, \quad \mathbf{P}_2 = \begin{bmatrix} 0 & 1 & 0 \\ 1 & 1 & 0 \\ 1 & -1 & 0 \end{bmatrix} \quad (9.9)$$

The term with cosine relates to the sensor that measures vertical acceleration while the term with sine relates to the accelerometers measuring in horizontal directions.

Next, we will simplify these expressions by assuming small angles - $\cos(\theta) \approx 1$, $\sin(\theta) \approx \theta$ - so we rewrite the tilt error, Eq. (9.7)

$$\boldsymbol{\varepsilon}(t) = g [\theta_y(t) \quad -\theta_x(t) \quad -1]^T \quad (9.10)$$

Assuming small angles, we rewrite the tilt error, Eq. (9.8), into a vector-matrix form

$$\boldsymbol{\varepsilon}(t) = \mathbf{g} + \mathbf{P}\boldsymbol{\theta}(t) \quad (9.11)$$

where

$$\mathbf{P} = \begin{bmatrix} 0 & 1 & 0 \\ -1 & 0 & 0 \\ 0 & 0 & 0 \end{bmatrix} g \quad (9.12)$$

Thus, we can express the measured accelerations as

$$\mathbf{s}(t) = \ddot{\mathbf{y}}_a(t) + \mathbf{g} + \mathbf{P}\boldsymbol{\theta}(t) \quad (9.13)$$

Thus, the displacement of the accelerometers in the form of the rotational DOFs pollutes the measured acceleration.

9.7.2 Tilt error for dynamic systems

Next, we apply structural/mechanical dynamics to the issue of tilt to study tilt under dynamic conditions. We assume that the accelerometers are perfectly attached to a linear, time-invariant, and dynamic system so the equation of motion gives the system response [18].

$$\mathbf{M}\ddot{\mathbf{y}}(t) + \mathbf{C}\dot{\mathbf{y}}(t) + \mathbf{K}\mathbf{y}(t) = \mathbf{x}(t) \quad (9.14)$$

where \mathbf{M} , \mathbf{C} , and \mathbf{K} are the mass, damping, and stiffness matrices, $\mathbf{y}(t)$, $\dot{\mathbf{y}}(t)$, and $\ddot{\mathbf{y}}(t)$ are displacement, velocity, and acceleration of the system, and $\mathbf{x}(t)$ is the excitation vector.

The accelerometers are mounted to a structure where we have full acceleration of the system and the mode shapes

$$\ddot{\mathbf{y}}(t) = [\ddot{\mathbf{y}}_a(t) \quad \ddot{\boldsymbol{\theta}}(t) \quad \ddot{\mathbf{y}}_d(t)]^T, \quad \boldsymbol{\Phi} = [\boldsymbol{\Phi}_a \quad \boldsymbol{\Phi}_\theta \quad \boldsymbol{\Phi}_d]^T \quad (9.15)$$

where $\boldsymbol{\Phi}$ is the full modal matrix, $[\]_a$ denotes the (translational) DOFs corresponding to the location of accelerometers, $[\]_\theta$ denotes the rotational DOFs of the sensors, and $[\]_d$ denotes the remaining DOFs.

Assuming small angles, we transform the measured acceleration to the frequency domain by applying the Fourier transformation to Eq. (9.13).

$$\begin{aligned} \mathbf{S}(\omega) &= \mathcal{F}(\ddot{\mathbf{y}}_a(t)) + \mathcal{F}(\mathbf{g}) + \mathcal{F}(\mathbf{P}\boldsymbol{\theta}(t)) \\ &= \mathbf{Y}_a(\omega) + \delta(\omega)\mathbf{g} + \mathbf{P}\boldsymbol{\theta}(\omega) \end{aligned} \quad (9.16)$$

where $\mathcal{F}(\cdot)$ denotes the Fourier transformation, $\mathbf{Y}(\omega)$ is the Fourier transformation of the displacement, and $\delta(\omega)$ is the Dirac delta function.

We apply the modal superposition [18] to express the measured acceleration in modal acceleration.

$$\mathbf{S}(\omega) = \boldsymbol{\Phi}_a \ddot{\mathbf{Q}}(\omega) + \delta(\omega)\mathbf{g} + \mathbf{P}\boldsymbol{\Phi}_\theta \frac{\ddot{\mathbf{Q}}(\omega)}{\omega^2} \quad (9.17)$$

where $\mathbf{Q}(\omega)$ is the modal coordinates in the frequency domain.

We rewrite Eq. (9.17)

$$\mathbf{S}(\omega) = \delta(\omega)\mathbf{g} + \left(\boldsymbol{\Phi}_a + \frac{\mathbf{P}\boldsymbol{\Phi}_\theta}{\omega^2} \right) \ddot{\mathbf{Q}}(\omega) \quad (9.18)$$

We insert the frequency response function matrix for the modal accelerations [18].

$$\mathbf{S}(\omega) = \delta(\omega)\mathbf{g} + \left(\boldsymbol{\Phi}_a + \frac{\mathbf{P}\boldsymbol{\Phi}_\theta}{\omega^2} \right) \omega^2 [H_n(\omega)] \boldsymbol{\Phi}^T \boldsymbol{\chi}(\omega) \quad (9.19)$$

where $[H_n(\omega)]$ is a diagonal matrix with the frequency response functions of the modal coordinates and $\mathbf{X}(\omega)$ is the excitation vector in the frequency domain.

We define a frequency response function matrix of the measured acceleration from accelerometers on a system with tilt as

$$\mathbf{H}_s(\omega) = \left(\boldsymbol{\Phi}_a + \frac{\mathbf{P}\boldsymbol{\Phi}_\theta}{\omega^2} \right) \omega^2 [H_n(\omega)] \boldsymbol{\Phi}^T \quad (9.20)$$

Inside the frequency response function matrix of the measured acceleration, we have an error term, $\frac{\mathbf{P}\boldsymbol{\Phi}_\theta}{\omega^2}$, due to tilt motion. Thus, the tilt error depends on the system and excitation where the error increases as the excitation frequency decreases. Besides, the relationship between the rotational displacement and the translational acceleration defines the level of tilt. Generally, the tilt error dominates at low frequencies on the frequency response function of the accelerometers due to the term $\frac{1}{\omega^2}$ on the error. Furthermore, the term $\delta(\omega)\mathbf{g}$ is a DC measurement that we can remove by detrending the measured accelerations. Some accelerometers are, however, incapable of true DC measurements so they exclude this term, $\delta(\omega)\mathbf{g}$, but Eq. (9.20) still holds in the frequency range of these sensors.

We extend the theory to the impulse response function matrix of the measured acceleration of an accelerometer with tilt error.

$$\begin{aligned} \mathbf{h}_s(t) &= \left(\boldsymbol{\Phi}_a + \mathbf{P}\boldsymbol{\phi}_\theta \left[\omega_d^{-2} \right] \right) [\dot{h}_i(t)] \boldsymbol{\Phi}^T \\ &= \sum_{i=1}^N \left(\boldsymbol{\phi}_{i,a} + \frac{\mathbf{P}\boldsymbol{\phi}_{i,\theta}}{\omega_d^2} \right) \dot{h}_i(t) \boldsymbol{\phi}_i^T \end{aligned} \quad (9.21)$$

where ω_d is the damped frequency of each mode and $h_i(t)$ is the impulse response function of the i^{th} mode.

As consequence of Eq. (9.21), the tilt error increases on the impulse response functions as the natural frequencies of the system decrease. Thus, we get an amplitude difference for an estimation of the impulse response function due to the tilt error, and, in modal analysis, this leads to an erroneous estimation of the mode shape. In general, any estimation of the modal parameters from a free decay measured by tilting accelerometers results in erroneous estimation of the mode shape.

9.8 Remove tilt errors

The tilt error is removable from the acceleration when we know the tilt angles [9]. If we have a triaxial accelerometer mounted in a point, measuring the components in the main directions, and we know the rotations vector, we find the error signal, Eq. (9.11), and then remove the influence of the tilt using Eq. (9.13) to isolate the true acceleration signal.

$$\begin{aligned} \ddot{\mathbf{y}}_a(t) &= \mathbf{s}(t) - \boldsymbol{\varepsilon}(t) \\ &= \mathbf{s}(t) - \mathbf{g} - \mathbf{P}\boldsymbol{\theta}(t) \end{aligned} \quad (9.22)$$

Often, we mainly have an estimate of the tilt angles, thus, we can only reduce the tilt error. Furthermore, we can apply band-pass filters to the tilt angles, $\boldsymbol{\theta}(t)$, depending on our confidence in the estimated tilt angles.

9.8.1 Uniaxial accelerometer

In the case, we have an uniaxial accelerometer that measures acceleration in the direction of a unit vector, $\mathbf{u} = [u_x \ u_y \ u_z]^T$, we construct a measured acceleration vector, $\mathbf{s}(t)$, from the scalar signal, $s(t)$, measured by the sensor.

$$\mathbf{s}(t) = \mathbf{u}s(t) \quad (9.23)$$

Then we use Eq. (9.22) to remove the tilt, and, finally, project the signal on the direction vector to obtain the true 1D acceleration signal

$$\begin{aligned} \ddot{y}_a(t) &= \mathbf{u}^T (\mathbf{u}s(t) - \boldsymbol{\varepsilon}(t)) \\ &= \mathbf{u}^T (\mathbf{u}s(t) - \mathbf{g} - \mathbf{P}\boldsymbol{\theta}(t)) \end{aligned} \quad (9.24)$$

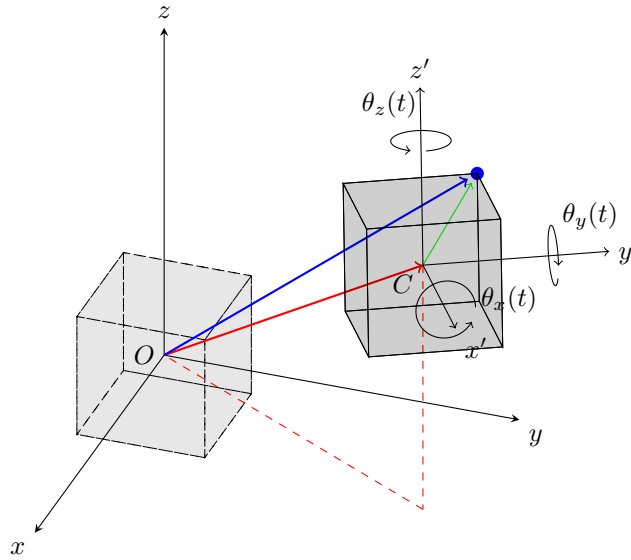


Figure 9.3: The principle of a rigid body motion

Since the direction vector is unity so that $\mathbf{u}^T \mathbf{u} = 1$, we rewrite the equation

$$\ddot{y}_a(t) = s(t) - \mathbf{u}^T \mathbf{g} - \mathbf{u}^T \mathbf{P} \boldsymbol{\theta}(t) \quad (9.25)$$

We arrive at the general result for the true acceleration

$$\ddot{y}_a(t) = s(t) - u_x g \theta_y(t) + u_y g \theta_x(t) + u_z g \quad (9.26)$$

9.9 Estimating tilt angles

Preferably, we measure the tilt angles directly with an inclinometer (tilt sensor) [1]. This is, however, impossible in some cases. In this section, we assume that we only have accelerometers in the sensor network. We can estimate the tilt angles from accelerometers mounted on a structure with random vibrations. In this paper, we will study two methods for estimating tilt angles based on accelerometers. Firstly, we estimate the tilt angles by simple geometry and the accelerometers that measure acceleration caused purely by rotational motion. Secondly, we estimate the tilt by virtual sensing where we expand the displacement to the rotational degrees of freedom.

In both cases, we need to integrate the measured acceleration signals twice to obtain the displacements that are proportional to the angles. Here we should be aware of numerical drift caused by the integration process. In the presents of drift in the displacement signal, this drift error is transferred into the "cleaned" acceleration signal so the signal does not contain the tilt effect but a drift error at low frequencies.

9.9.1 Pure rotational motion in one direction

First, let us assume that a subset of sensors are mounted on a rigid body. We can describe any rigid body motion by a translational motion of the centre of gravity and an angular rotation motion around the centre of gravity [19], see Fig. 9.3. Let us assume that the rigid body does not undergo any translational motion in one direction. In civil engineering applications, this is often the vertical direction. In this case, any measured motion - in that direction - is caused by rotation. By assuming small angles, we express the displacement - caused by pure rotation - of the rigid body, see Fig. 9.4.

$$\mathbf{y}_0(t) = \mathbf{R} \boldsymbol{\theta}_0(t) \quad (9.27)$$

where $\mathbf{y}_0(t)$ is the motion caused purely by rotation and \mathbf{R} is a rotation matrix that contains the geometrical distances from the centre of gravity to each sensor.

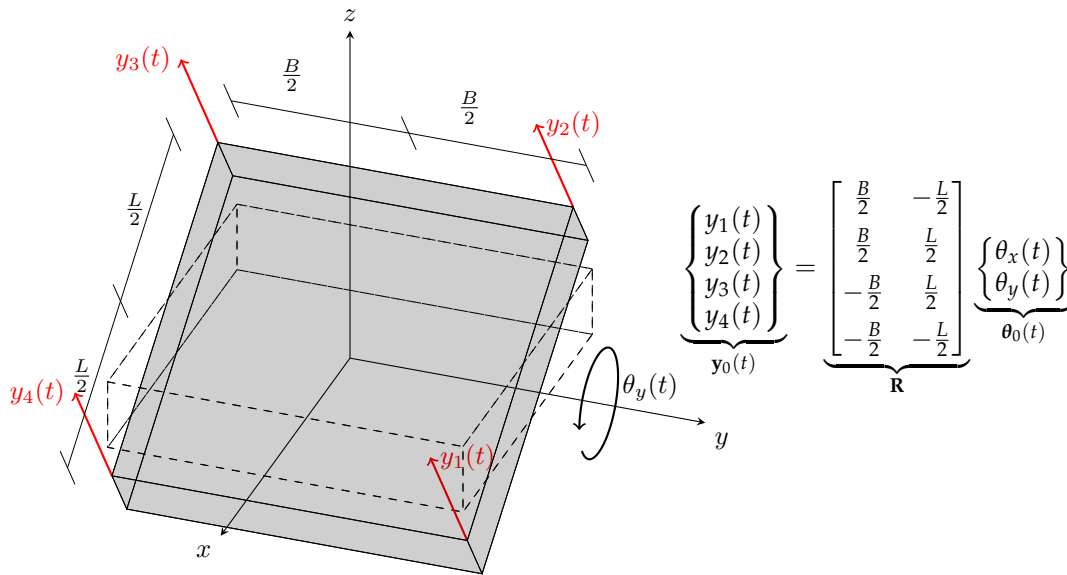


Figure 9.4: The principle of detecting tilt angles by accelerometers with purely rotational motion

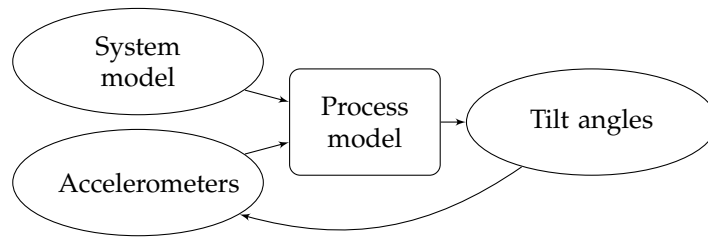


Figure 9.5: Flowchart of virtual sensing for estimating tilt angles from accelerometers

When the number of elements in $y_0(t)$ is larger than or equal to 2, then we can estimate the tilt angles.

$$\hat{\theta}_0(t) = \mathbf{R}^\dagger y_0(t) \tag{9.28}$$

where $(\cdot)^\dagger$ denotes the Moore–Penrose (pseudo) inverse. The more overdetermined the problem is the better for the estimate.

9.9.2 Virtual sensing

Additionally, we could apply virtual sensing [20], which we illustrate as a flowchart in Fig. 9.5. For the given application of estimating the tilt angles, we transform the signal from the physical accelerometers to virtual tilt measurements for each sensor by applying a system model and a process model. This type of virtual sensing is also called response estimation or expansion. We should, however, be aware that the estimated tilt angles are slightly erroneous because they are based on signals containing tilt error. Therefore, the estimated angles themselves are influenced by the tilt error on the accelerometers. In principle, we have to remove the influence of the tilt motion on the tilt angles themselves. This is done by an iterative process.

In the literature of response estimation, the most applied system model is a highly correlated finite element model but it could take any form. Likewise, the most common process models include the modal expansion [21–23] and adaptive filters like the Kalman filter [24].

9.10 Case Study - laboratory test

We will study the effect of tilt motion on a test-specimen in the laboratory by comparing the measured acceleration from accelerometers to the measured acceleration from another sensor unaffected by the



Figure 9.6: Test-specimen in the laboratory

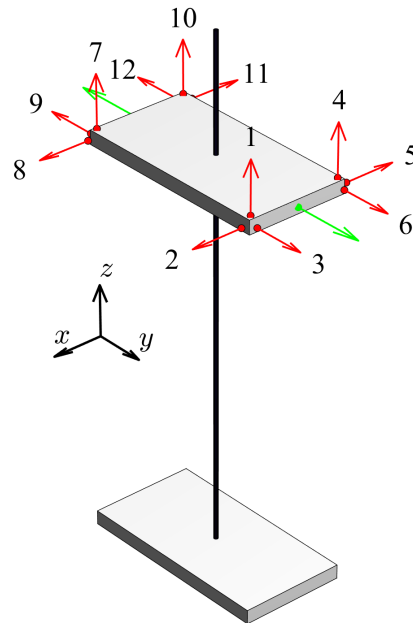


Figure 9.7: Position and direction of the 12 accelerometers (red arrows) and two lasers (green arrows) on the test-specimen

gravity acceleration. Furthermore, we will estimate tilt angles and apply tilt reduction.

9.10.1 Setup

The test-specimen is comprised of an aluminium circular beam with a diameter of 6 mm and a thickness of 1 mm with wooden blocks ($392 \times 202 \times 27$ mm) attached at each end of the beam where one block is clamped to the ground. The position of the second wooden block is adjustable to obtain different lengths between the blocks. We use two different setups where we adjust the length between the wooden blocks so the test-specimen has a height of 762 and 798 mm in the setups. Fig. 9.6 illustrates the test-specimen.

We use 12 accelerometers of the type Brüel & Kjær 4508-B, 100mV/g and two lasers of type Micro-Epsilon optoNCDT 1300 to measure the wooden block at the top, see Fig. 9.7. The reader should note that the applied accelerometers are incapable of true DC measurements (0.3-8000 Hz AC accelerometers). We excite the structure with a Brüel & Kjær impact hammer of the type 8206, 22.5mV/N, so we have a free decay of the system.

Using standard experimental modal analysis in a Multiple-Input/Multiple-Output (MIMO) formulation, we apply multiple impact loads to the test-specimen at different locations. We organise all the free decays (0.2 s after each impact) in a matrix, and we estimate the modal parameters from this matrix using a stabilization diagram based on the Ibrahim time-domain method [10, 25], see Fig 9.8. Fig. 9.9 illustrates the five mode shapes from the identification process and Table 9.1 holds the identified modal parameters.

9.10.2 Model

We create a simple model of the test-specimen simplified to 2D - corresponding to the yz -plane from Fig. 9.7 - with one translational and one rotational DOF, see the system in Fig. 9.10 (a). The first and fourth mode from the identification process from the experimental analysis correspond to the given plane. The model is updated to resemble the experimental analysis in terms of natural frequencies, see the modal parameter in Table 9.1. Fig. 9.10 (b-c) illustrates the two mode shapes of the system. We use Eq. (9.20)

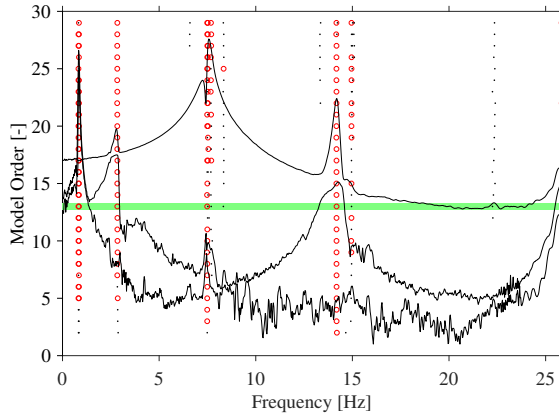


Figure 9.8: Stabilization diagram using the Ibrahim time-domain method [25] where red circles (o) indicate stable modes, black dots (·) indicate spurious modes, and the green bar indicates the selected model order for height 762 mm

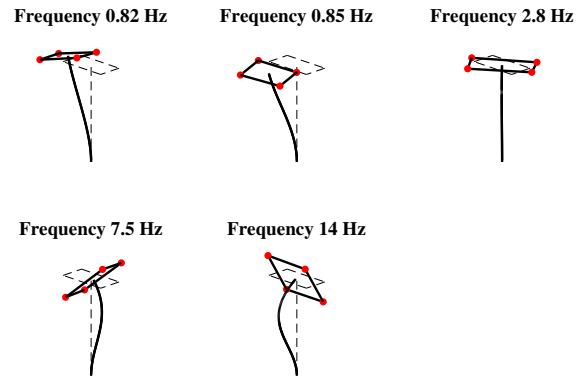


Figure 9.9: Experimental mode shapes corresponding to Fig. 9.8 for height 762 mm

and the mode shapes from Table 9.1 to plot the frequency response function matrix of the measured acceleration in Fig. 9.11 for both setups.

Table 9.1: Modal parameters of the 2 DOF system in Fig. 9.10 (a) and estimated frequency

| Mode | | 1 | 2 |
|----------------|---------------------------------|------------------------|------------------------|
| Height: 762 mm | Experimental frequency [Hz] | 0.82 | 7.5 |
| | Frequency [Hz] | 0.83 | 7.5 |
| | Mode shape [-] | $[0.27 \quad -0.53]^T$ | $[0.015 \quad 0.79]^T$ |
| | Modal Assurance Criterion (MAC) | 0.97 | 0.99 |
| Height: 798 mm | Experimental frequency [Hz] | 0.75 | 7.3 |
| | Frequency [Hz] | 0.76 | 7.4 |
| | Mode shape [-] | $[0.29 \quad -0.53]^T$ | $[0.014 \quad 0.79]^T$ |
| | Modal Assurance Criterion (MAC) | 0.98 | 0.99 |

9.10.3 Data analysis

We apply an impact load next to and in the direction of one of the lasers and measure both displacement from the lasers and the acceleration from the accelerometers. This results in a free decay of the test specimen in the yz -plane. Assuming for the given frequency range of interest, the wooden block is rigid and we calculate the acceleration of the block as a mean value. For the accelerometers, the mean acceleration of the wooden block in the y -direction is the mean value of accelerometers 3, 6, 9, and 12. For the lasers, the acceleration is the mean value of the data from both lasers differentiated twice to obtain acceleration. Data from both lasers and accelerometers are bandpass filtered with cut-off frequencies of 0.5 and 1.1 Hz. Fig. 9.12 shows the acceleration from the accelerometers and lasers where we observe an amplitude difference between the two types of sensors. Furthermore, the amplitude difference is slightly different for the two setups where the ratios of standard deviations between accelerometers and lasers are 1.72 and 1.78 for the height of 762 and 798 mm respectively.

First, we want to apply the theory from section 9.7.2 to find an explanation for the amplitude difference. We can use the impulse response function matrix of the measured acceleration from Eq. (9.21) to find the error caused by tilt.

$$\begin{aligned}
 \mathbf{h}_{i,s}(t) &= \begin{pmatrix} \boldsymbol{\phi}_{i,a} - \frac{g\boldsymbol{\phi}_{i,\theta}}{\omega_d^2} \end{pmatrix} \ddot{h}_i(t) \boldsymbol{\phi}_i^T \\
 &= \begin{pmatrix} 1 - \frac{g\boldsymbol{\phi}_{i,\theta}}{\omega_d^2 \boldsymbol{\phi}_{i,a}} \end{pmatrix} \boldsymbol{\phi}_{i,a} \dot{h}_1(t) \boldsymbol{\phi}_i^T
 \end{aligned} \tag{9.29}$$

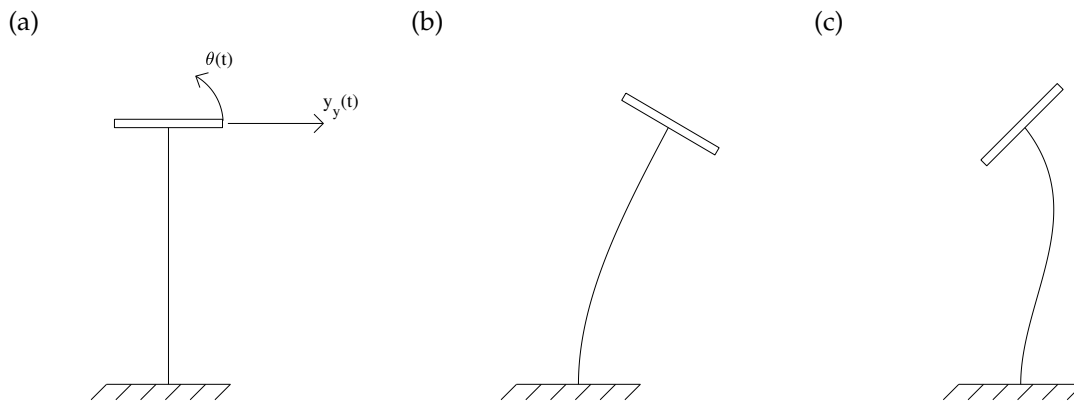


Figure 9.10: The numerical model for movement in the yz -plane (a) the two degree-of-freedom system model, (b) first mode shape, and (c) second mode shape (corresponding to the fourth experimental mode)

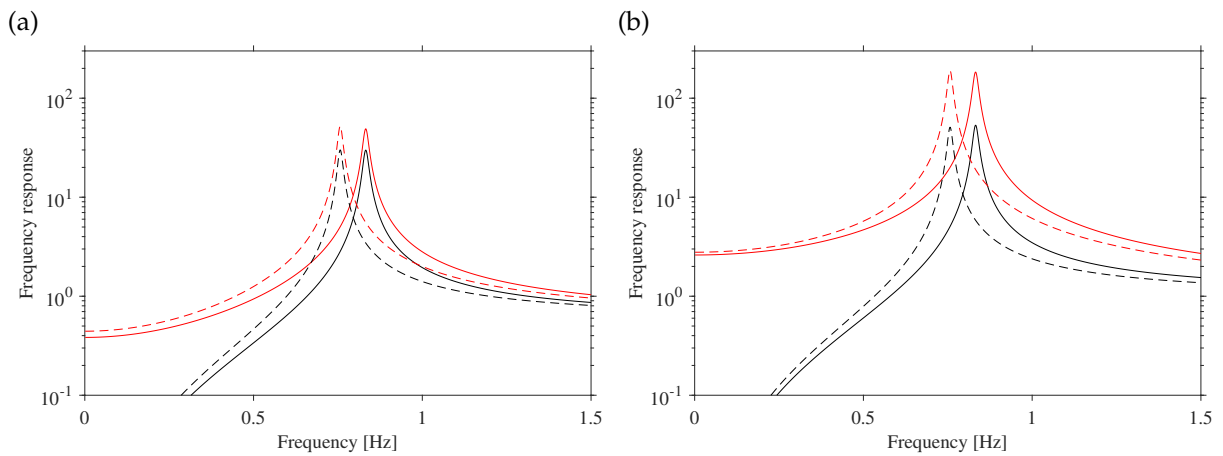


Figure 9.11: The frequency response function of actual acceleration (black) and the measured acceleration by an accelerometer with tilt error (red) where the solid lines correspond to a height of 762 mm and the dashed lines correspond to a height of 798 mm, (a) for translational force and (b) for the rotational force (force moment)

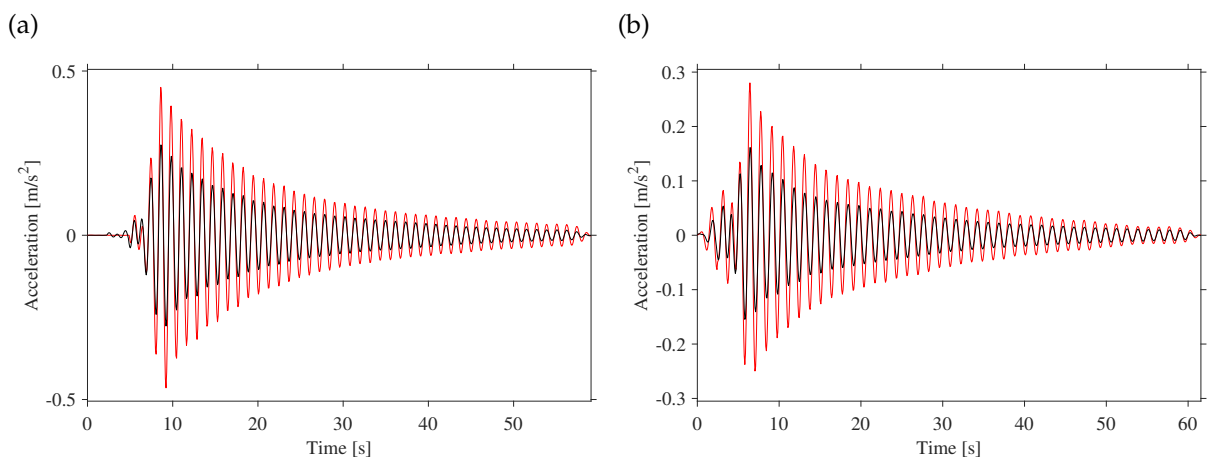


Figure 9.12: The measured acceleration of the accelerometers (red) as the mean value of sensor 3, 6, 9, and 12 and the acceleration of the lasers (black) as the mean value of both laser for (a) height 762 mm and (b) 798 mm

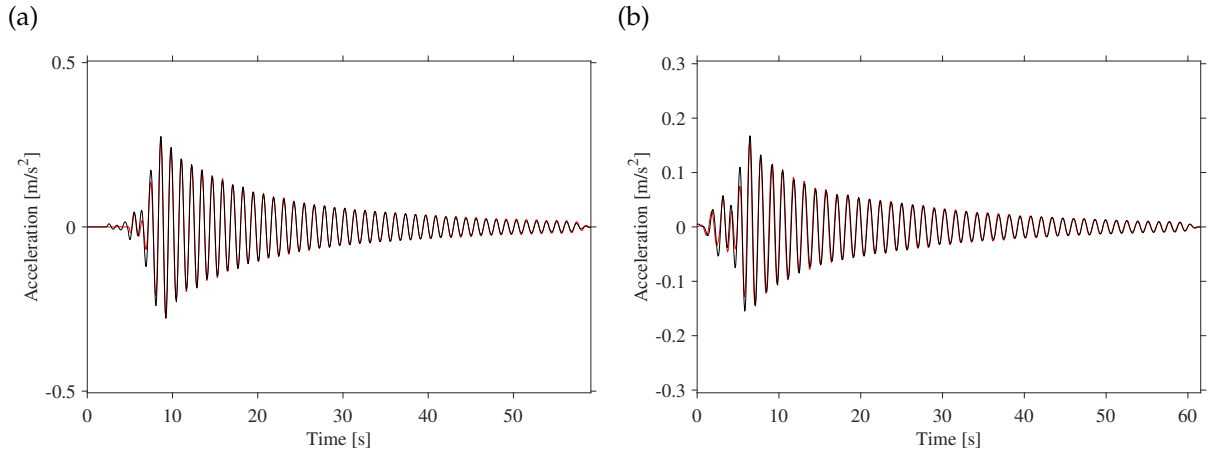


Figure 9.13: The corrected acceleration of the accelerometers using Eq. (9.29) and Table 9.2 (red) as the mean value of sensor 3, 6, 9, and 12 and the acceleration of the lasers (black) as the mean value of both laser for (a) height 762 mm and (b) 798 mm

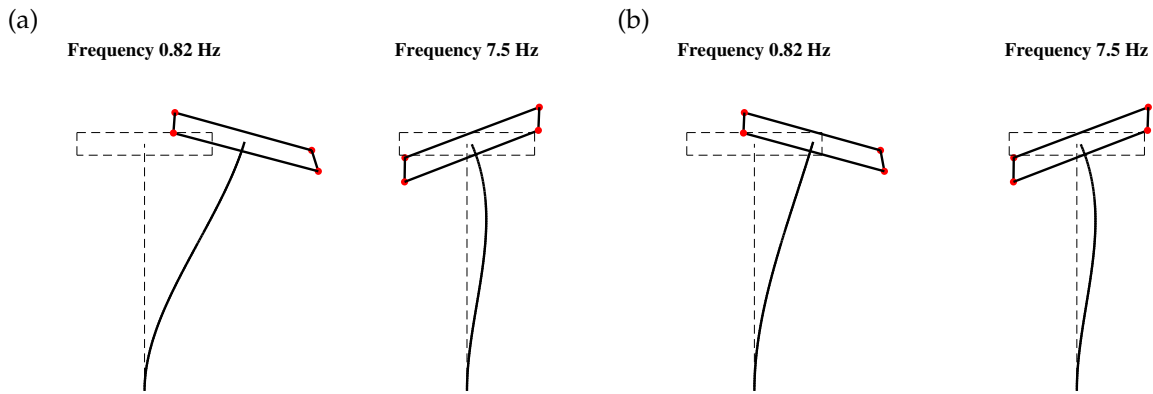


Figure 9.14: The corrected mode shapes estimated from the accelerometers, Eq. (9.29) and Table 9.2: (a) original estimated mode shapes, (b) corrected mode shapes adjusted for tilt error

Thus, we have an expression for an amplitude difference caused by the tilt error for each mode. We apply the modal parameter from Table 9.1 to calculate the amplitude difference for both setups, see Table 9.2.

We assume that the free decay in Fig. 9.12 is mainly comprised of the first mode. The amplitude difference - based on the analytic expression for tilt - corresponds well with the ratio of standard deviation between accelerometers and lasers. We apply these amplitude differences to adjust the measured acceleration from the accelerometer, see Fig. 9.13. This corrected the amplitude of the acceleration from the accelerometers so they have similar amplitude as the lasers. Similarly, we adjust the estimated mode shapes for the tilt effect in Fig. 9.14 where we obtain a better resemblance to the mode shapes from the model, see Fig. 9.10. Here the MAC-value increases to above 0.99 for the first mode shape as compared to the values in Table 9.1.

Table 9.2: The amplitude difference on a free decay due to tilt error on accelerometer

| | Mode | 1 | 2 |
|----------------|---|------|------|
| Height: 762 mm | $1 - \frac{g\phi_{i,\theta}}{\omega_d^2\phi_{i,a}}$ | 1.70 | 1.22 |
| Height: 798 mm | $1 - \frac{g\phi_{i,\theta}}{\omega_d^2\phi_{i,a}}$ | 1.79 | 1.26 |

Finally, we estimate the tilt angles using the four vertical sensors (unaffected by translational motion) and we conclude that the assumption of small angles is valid for the given case, see Fig. 9.15. This tilt

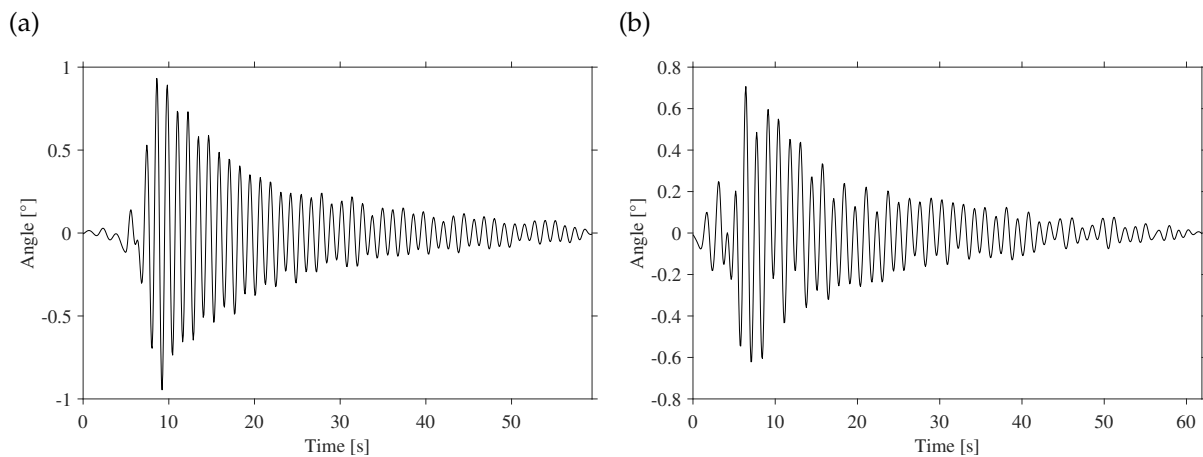


Figure 9.15: Tilt estimation, θ_x , for (a) height 762 mm and (b) 798 mm

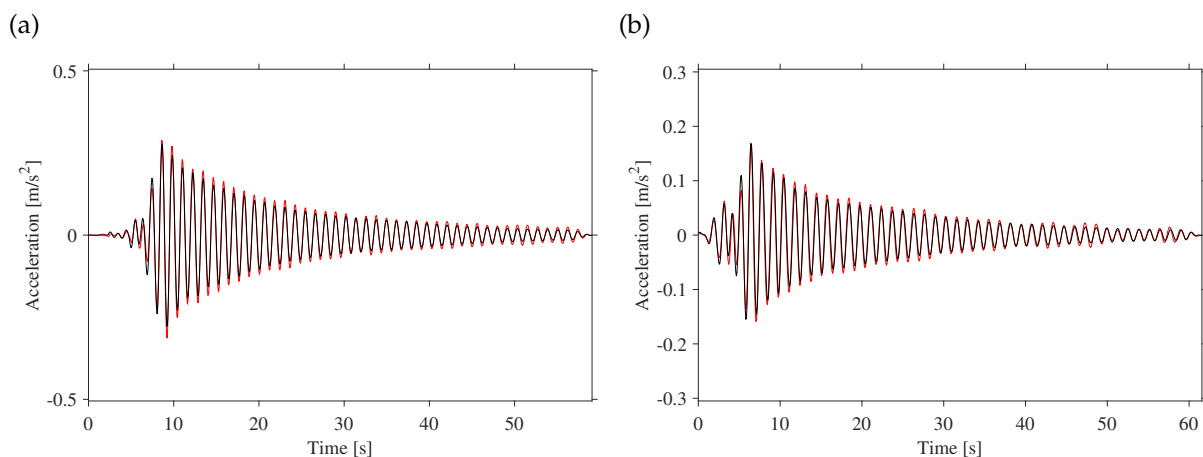


Figure 9.16: Tilt reduction on the measured acceleration of the accelerometers (red) as the mean value of sensor 3, 6, 9, and 12 and the acceleration of the lasers (black) for (a) height 762 mm and (b) 798 mm

sensing application introduces a small amount of noise in the estimated tilt angles so they do not form a free decay of a single mode. We reduce the tilt error by applying Eq. (9.22), see Fig. 9.16. By reducing the tilt error, we obtain a similar amplitude between accelerometers and lasers.

9.10.4 Discussion

For the case study, we observed an amplitude difference in acceleration from the accelerometers and the lasers on the same test-specimen. Here the accelerometers overestimate the acceleration with at-least 70% compared to the lasers (this factor is case dependent). This difference could be caused or influenced by measurement noise or the double differentiation of the displacement data from the lasers. The amplitude difference is, however, explainable by the theory from section 9.7.2 and we can reduce the difference by estimating the tilt angles and reducing the tilt effect. By applying the theory, we adjust the mode shapes estimated from the free decay and we obtain estimated mode shapes that better resemble the mode shapes from the model. Thus, both theory of the tilt error for dynamic systems and tilt reduction of acceleration measured by accelerometers are validated in this study.

9.11 Conclusion

In this paper, we have studied the effect of tilting accelerometer where the accelerometer rotates/tilts from its original position and erroneously measures a component of the gravitational acceleration along with the actual acceleration of the sensor. The novelty of this paper is that it focuses on accelerometers attached to a linear and time-invariant system under dynamic conditions where the system response itself causes tilt motion of the sensors. We have proven that the tilt error is a pollution of the measured translation acceleration caused by the rotational displacement of the sensor. We set up mathematical formulations of the tilt error on the accelerometer and derive an expression for the frequency response function matrix and impulse response function matrix of accelerometers attached to a dynamic system. These expressions indicate that tilt error would be transferred to an experimental identification of mode shapes using accelerometers. Furthermore, we introduced two methods of reducing the tilt error by estimating the tilt angles solely by the accelerometers. The theory is validated by an experimental study in the laboratory.

Acknowledgements

The authors acknowledge the funding received from the Centre for Oil and Gas - DTU/Danish Hydrocarbon Research and Technology Centre (DHRTC).

The authors thank Torkil Nedergaard for the construction of the test-specimen and Jannick Balleby Hansen for assisting with the experimental setup in the laboratory.

References

- [1] Jacob Fraden. *Handbook of Modern Sensors: Physics, Designs, and Applications*. Springer International Publishing, London, UK, 2016.
- [2] Yinsheng Weng, Shudong Wang, Hongcai Zhang, Hairong Gu, and Xueyong Wei. A high resolution tilt measurement system based on multi-accelerometers. *Measurement*, 109:215 – 222, 2017.
- [3] R. Rajesh and I. Baranilingesan. Tilt angle detector using 3-axis accelerometer. *International Journal of Scientific Research in Science and Technology*, 4:784–791, 02 2018.
- [4] Kimberly Tuck. Tilt sensing using linear accelerometers. *Freescale semiconductor, application note*, (AN3461), 2007. Rev. 2.
- [5] Mark Pedley. Tilt sensing using a three-axis accelerometer. *Freescale semiconductor, application note*, (AN3461), 2013. Rev. 6.
- [6] Jiye Qian, Bin Fang, Weibin Yang, Xiao Luan, and Hai Nan. Accurate tilt sensing with linear model. *Sensors Journal, IEEE*, 11:2301 – 2309, 11 2011.
- [7] Luczak, Sergiusz. Novel algorithm for tilt measurements using mems accelerometers. *MATEC Web Conf.*, 157:08005, 2018.

- [8] Christopher J Fisher. Using an accelerometer for inclination sensing. *AN-1057, Application note, Analog Devices*, pages 1–8, 2010.
- [9] Rubén Boroschek and Denis Legrand. Tilt motion effects on the double-time integration of linear accelerometers: An experimental approach. *Bulletin of the Seismological Society of America*, 96:2072–2089, 01 2007.
- [10] Rune Brincker and Carlos Ventura. *Introduction to operational modal analysis*. John Wiley and Sons, Inc., Chichester, West Sussex, UK, 2015.
- [11] Vladimir M. Graizer. Effect of tilt on strong motion data processing. *Soil Dynamics and Earthquake Engineering*, 25(3):197 – 204, 2005.
- [12] Erhard Wielandt and T. Forbriger. Near-field seismic displacement and tilt associated with the explosive activity of stromboli. *Ann. Geofis.*, 42:407–416, 06 1999.
- [13] C. Collette, Stef Janssens, P. Fernandez-Carmona, Kurt Artoos, Michael Guinchard, C. Hauviller, and A. Preumont. Review: Inertial sensors for low-frequency seismic vibration measurement. *Bulletin of the Seismological Society of America*, 102:1289–1300, 08 2012.
- [14] Fabrice Matichard, Richard Mittleman, and Matthew Evans. On the Use of Mechanical Filters to Attenuate the Transmission of Tilt Motion to Inertial Sensors. *Bulletin of the Seismological Society of America*, 106(3):987–1001, 04 2016.
- [15] Shihao Yuan, Andreino Simonelli, Chin-Jen Lin, Felix Bernauer, Stefanie Donner, Thomas Braun, Joachim Wassermann, and Heiner Igel. Six Degree-of-Freedom Broadband Ground-Motion Observations with Portable Sensors: Validation, Local Earthquakes, and Signal Processing. *Bulletin of the Seismological Society of America*, 05 2020.
- [16] Fabrice Matichard and Matthew Evans. Review: Tilt-Free Low-Noise Seismometry. *Bulletin of the Seismological Society of America*, 105(2A):497–510, 04 2015.
- [17] Milton Abramowitz and Irene A. Stegun. *Handbook of Mathematical Functions, With Formulas, Graphs, and Mathematical Tables.*. Dover Publications, Inc., NY, USA, ninth dover printing, tenth gpo printing edition, 1972.
- [18] R. W. Clough and J. Penzien. *Dynamics of structures*. CSI Computers & Structures, Inc., Berkeley, Calif., 2nd revised edition, 2003.
- [19] Masato Abe. Chapter 6 - vehicle body roll and vehicle dynamics. In Masato Abe, editor, *Vehicle Handling Dynamics (Second Edition)*, pages 153 – 186. Butterworth-Heinemann, second edition edition, 2015.
- [20] L. Liu, S. M. Kuo, and M. Zhou. Virtual sensing techniques and their applications. In *2009 International Conference on Networking, Sensing and Control*, pages 31–36, March 2009.
- [21] Anders Skaftø. *Applications of Expansion Techniques in Operational Modal Analysis*. PhD thesis, Aarhus University, DK, 2016.
- [22] Alexandros Iliopoulos. *Virtual sensing techniques for response estimation and fatigue assessment of offshore wind turbines*. PhD thesis, Vrije Universiteit Brussel, 2017.
- [23] Marius Tarpø, Bruna Nabuco, Christos Georgakis, and Rune Brincker. Expansion of experimental mode shape from operational modal analysis and virtual sensing for fatigue analysis using the modal expansion method. *International Journal of Fatigue*, 130:105280, 2020.
- [24] R.E. Kalman. A new approach to linear filtering and prediction problems. *Journal of Basic Engineering*, 82:35–45, 1960.
- [25] S. R. Ibrahim and E. C. Mikulcik. A method for the direct identification of vibration parameters from the free response. *The Shock and Vibration Inform. Ctr. Shock and Vibration Bull.*, pages 183–198, 1977.

Chapter 10

Paper 7 - Preliminary study: Quasi-static strain estimation above the sea for an offshore tripod structure in the North Sea

((In actual fact, we should recognise the general principle that a lack of information cannot be remedied by any mathematical trickery))

Cornelius Lanczos

Status

- Unpublished paper

10.1 Introduction

This chapter covers quasi-static strain estimation of an offshore platform - the Valdemar platform (tripod structure) in the North Sea - but the study is unfinished due to time constraints and unexpected issues and complexity in the application. At this stage, the paper is predominately conceptual.

For offshore structures, the quasi-static response, caused by waves, strongly contributes to the overall fatigue life and a successful application of stress/strain estimation must correctly predict the stress history caused by this wave loading. As stated in section 3, we have multiple obstacles for the quasi-static stress/strain estimation for offshore structures. Unfortunately, these obstacles overlap in the frequency domain. The tilt error of accelerometers often takes place at low frequencies [1] where the drift of the displacement also occurs due to the numerical integration from acceleration. Moreover, the wave spectrum has its peak frequency - and most energy - below the first natural frequency of the structure and this causes a quasi-static response. This quasi-static response is often not well represented by a few modes in the modal superposition, thus, modal truncation errors are an issue for stress/strain estimation using modal expansion. We have these sources of errors located at the same frequency region and this complicates matters. In this paper, we focus on an application of stress/strain estimation on an operating offshore structure where we will study the effect of pseudo mode shapes for structures with a quasi-static response.

The reader should note that a configuration of sensor setup was impossible for this Ph.D. project. Therefore, the application is restricted to accelerometers as the primary physical sensors and strain gauges as the reference located above the sea.

10.2 Contribution

The author came up with the idea to test the different techniques for pseudo mode shapes. The new pseudo mode based on the residual error is proposed by the author.

10.3 Main findings

The study is inconclusive and the estimated strain response does not match well with the measured strain response for the quasi-static strain response. The complexity of the application under the actual operating conditions is far higher than anticipated. Thus, additional research is required for a successful application of quasi-static strain estimation on the Valdemar platform.

10.4 Reflections

The complexity of quasi-static strain estimation was underestimated for the application on the Valdemar platform since there are many sources of potential errors in the application. We deal with tilt errors on the accelerometer, the drift of acceleration in the numerical integration process, sensitivity of accelerometers, measurement errors on both accelerometers and strain gauges, the sensitivity of the reduced system model for pseudo mode shapes, the accuracy of the pseudo mode shapes, calibration of the system model, etc.. It is difficult to separate these errors in the given application so we are unaware of the extent of each source of error. Instead of handling everything at once, we need to take a step back and handle the issues separately and validate any solutions in separate studies. This is a more sound scientific approach; however, we did not anticipate all these errors beforehand.

Unfortunately, there are many unproven ideas in this paper. The subspace of residual method did not work since there was no null-space of the dynamic mode shapes from which to find principal components. The assumption - that we could divide the wave loading into approximated sets of temporal variations and spatial distributions to calculate pseudo mode shapes - is still just a hypothesis.

Preliminary study: Quasi-static strain estimation above the sea for an offshore tripod structure in the North Sea

Marius Tarpø^a, Bruna Nabuco^b, Ulf Tyge Tygesen^c, Christos Georgakis^a, Rune Brincker^b

^aAarhus University, Department of Engineering, Inge Lehmanns Gade 10, Aarhus, Denmark

^bTechnical University of Denmark, Department of Civil Engineering, Brovej B.118, Kgs. Lyngby, Denmark

^cRamboll Oil & Gas, Bavneshøjvej 5, Esbjerg, Denmark

Abstract

In this paper, we introduce a preliminary study of strain estimation on an offshore tripod structure in the North Sea where we focus on the issues of quasi-static strain estimation. The structure is the Valdemar platform that is equipped with a sensor network consisting of accelerometers, Global Positioning Systems (GPS), strain gauges, and wave radar. In this study, the accelerometers are applied as the main sensors for strain estimation. There are no strain gauges installed on the structure subsea so stress/strain estimation is impossible to validate subsea. Therefore, this study is restricted to strain estimation above sea. For quasi-static strain estimation caused by wave-loading, the first few mode shapes inaccurately span the response since higher modes contribute to the response with a residual effect. In this study, we apply pseudo modes to compensate for residual effect. The study is inconclusive due to unforeseen issues in the application and external difficulties that caused problems in the project's time-frame. This paper presents the lessons learned and the issues discovered relating to the application of quasi-static strain estimation. Therefore, the paper is predominately conceptual.

Keywords: Stress estimation, virtual sensing, fatigue analysis, structural health monitoring, modal expansion

10.6 Introduction

Virtual sensing is a technique that expands measurements to unmeasured locations and/or transforms the measurements into new quantities [2]. Here, stress/strain estimation is a subcategory within virtual sensing that estimates the full-field stress/strain response of a system. In turn, the estimated stress history paves the way for fatigue assessments of the system so that an estimated fatigue life is available. Thus, virtual sensing holds a potential for lifetime extensions for systems prone to fatigue damage. Therefore, considerable research has been conducted for stress/strain estimation for offshore structures [3–21]. The wave loading has both a quasi-static and dynamic effect on an offshore structure and there are several successful applications for dynamic stress/strain estimation [5, 6, 13, 15, 17, 19] while applications for quasi-static stress/strain estimation are sparse. For wave-induced structures, the quasi-static response, caused by the wave loading, has a major contribution to the overall fatigue damage and, therefore, it is vital to extend stress/strain estimation to the quasi-static effect. For quasi-static stress/strain estimation at a low-frequency domain, we encounter multiple issues. We are outside the strictly dynamic response so the structural response might not only be comprised by a few modes. Thus, modal truncation could become an issue for stress/strain estimation using modal expansion due to the residual effects of higher modes. Furthermore, we deal with sensitivity, measurement noise, and tilt error for accelerometers that are amplified in the double numerical integration to displacement and this causes an erroneous drift in the displacement signal. In the literature, Skafte et al. [3] used Ritz vectors to account for the quasi-static response due to waves for offshore structures in the laboratory on a scale model and Iliopoulos et al. [5, 21] used a similar technique by a static calculation of the deflection shape by a representative load. Furthermore, Iliopoulos et al. [21] estimated the quasi-static strain response by strain gauges of an offshore monopile wind turbine. Palanisamy et al. [12] studied strain estimation in a numerical setting using the Kalman filter for non-zero mean excitation and they found that accelerometers/acceleration are ineffective for estimation of the quasi-static response near 0 Hz.

In this paper, we will study quasi-static stress/strain estimation for offshore structures with an emphasis on modal truncation error. Modal truncation is a simplified representation of a system by a truncated set of modes. In the literature, the modal truncation was studied since the calculation of all eigenvalues and eigenvectors proved impractical for large systems. Consequently, a truncation of modal

superposition was adapted to decrease the computational time. This modal truncation might, however, lead to errors in the quasi-static response due to the residual effect of higher modes [22–25]. Thus, this led to the creation of static correction terms, which are added to the dynamic response to reduce the residual effect, and pseudo modes, which are load-dependent vector as a substitution of or addition to the mode shapes [23, 24, 26–31]. In particular, the modal truncation effect (residual effect) is studied in the field of calculating the response of offshore structures [23, 26, 28, 32]. In recent years, Maes et al. [33] used the term dummy modes for the static correction added to experimental load estimation although the formulation of dummy modes is similar to the modal truncation augmentation method (pseudo modes). Furthermore, Tarpø et al. [34] studied modal truncation errors in an experimental setting for modal analysis and found that the modal truncation error not only depends on the frequency content of the load but also on the spatial distribution of the load. In particular, the modal truncation error of each mode depends on the convolution of the impulse response function and the temporal variation of the excitation while it also depends on the inner vector product between the mode shape and the spatial distribution of the excitation.

In this paper, we will study an application of quasi-static strain estimation on an operating offshore platform in the North Sea. The study is inconclusive but it is a starting point for solving the difficult problem of quasi-static stress/strain estimation. Therefore, the presented work is predominately conceptual and it can serve as an underlying basis for future research in the topic. We organise the paper as follows: in Section 10.7, we introduce the theory of structural dynamics, modal superposition, modal truncation, quasi-static residual effect, and deflection shapes due to wave loading. Section 10.8 introduces virtual sensing with the modal expansion technique and section 10.9 explains static correction and pseudo modes to reduce the residual effect with a focus on application in virtual sensing. In section 10.10, we apply virtual sensing on an offshore platform - the Valdemar platform in the North Sea - with focus on strain estimation.

10.7 Structural dynamics

The response of a linear and stationary system with viscous damping is the solution of the equation of motion [35, 36].

$$\mathbf{M}\ddot{\mathbf{y}}(t) + \mathbf{C}\dot{\mathbf{y}}(t) + \mathbf{K}\mathbf{y}(t) = \mathbf{x}(t) \quad (10.1)$$

where $\mathbf{M} \in \mathbb{R}^{N \times N}$, $\mathbf{C} \in \mathbb{R}^{N \times N}$, and $\mathbf{K} \in \mathbb{R}^{N \times N}$ are the mass, damping, and stiffness matrix, $\mathbf{y}(t) \in \mathbb{R}^N$, $\dot{\mathbf{y}}(t) \in \mathbb{R}^N$, and $\ddot{\mathbf{y}}(t) \in \mathbb{R}^N$ are the displacement, velocity, and acceleration of the system, $\mathbf{x}(t) \in \mathbb{R}^N$ is the external excitation vector, and N is the total number of degrees-of-freedom (DOFs) in the system. In the case of proportional damping, we use the undamped equation of motion to find the mode shapes of the system through the eigenvalue problem [35, 36].

$$\mathbf{K}\boldsymbol{\phi}_i = \omega_i^2 \mathbf{M}\boldsymbol{\phi}_i, \quad i \in \mathbb{N} \quad (10.2)$$

where $\boldsymbol{\phi}_i \in \mathbb{R}^N$ is the mass normalised undamped mode shape vector for the i^{th} mode and ω_i is the angular frequency of the i^{th} mode.

Any response of a linear structure is positioned in the vector-space of its mode shapes, which is called modal superposition.

$$\begin{aligned} \mathbf{y}(t) &= \sum_{i=1}^N \boldsymbol{\phi}_i q_i(t) \\ &= \boldsymbol{\Phi} \mathbf{q}(t) \end{aligned} \quad (10.3)$$

where $q_i(t)$ is the modal coordinate for mode i , $\boldsymbol{\Phi} \in \mathbb{R}^{N \times N}$ is the modal matrix, which holds the mode shapes as column vectors, and $\mathbf{q}(t) \in \mathbb{R}^N$ is the modal coordinate of the modes. The modal superposition transforms the physical space into the modal space.

The mode shapes are orthogonal to the mass and stiffness matrix [35, 36].

$$\boldsymbol{\Phi}^T \mathbf{M} \boldsymbol{\Phi} = \mathbf{I}, \quad \boldsymbol{\Phi}^T \mathbf{K} \boldsymbol{\Phi} = [\omega_i^2] \quad (10.4)$$

We can use these orthogonal equations to express the inverse mass and stiffness matrices as a sum of the outer products of the mode shapes.

$$\mathbf{M}^{-1} = \sum_{i=1}^N \boldsymbol{\phi}_i \boldsymbol{\phi}_i^\top, \quad \mathbf{K}^{-1} = \sum_{i=1}^N \frac{\boldsymbol{\phi}_i \boldsymbol{\phi}_i^\top}{\omega_i^2} \quad (10.5)$$

10.7.1 Steady-state response

In this section, we document the traditional theory of calculating the steady-state response. In the following, we will consider a fixed spatial distribution of the load.

$$\mathbf{x}(t) = \mathbf{F}\mathbf{s}(t) \quad (10.6)$$

where $\mathbf{F} \in \mathbb{R}^{N \times n}$ is the spatial distribution of the load, $\mathbf{s}(t) \in \mathbb{R}^n$ is the temporal variation of the load, and n is the number of components in the load.

We assume a steady-state response so the system response becomes a spatial distribution (deflection shape) of the temporal variation of load, $\mathbf{y}(t) = \boldsymbol{\Delta}\mathbf{s}(t)$. We insert this response and the force, Eq. (10.6) into the equation of motion, Eq. (10.1).

$$\begin{aligned} -\omega^2 \mathbf{M}\boldsymbol{\Delta}\mathbf{s}(t) + i\omega \mathbf{C}\boldsymbol{\Delta}\mathbf{s}(t) + \mathbf{K}\boldsymbol{\Delta}\mathbf{s}(t) &= \mathbf{F}\mathbf{s}(t) \\ (-\omega^2 \mathbf{M} + i\omega \mathbf{C} + \mathbf{K})\boldsymbol{\Delta} &= \mathbf{F} \end{aligned} \quad (10.7)$$

where $\boldsymbol{\Delta} \in \mathbb{R}^{N \times n}$ is the deflection shape.

We isolate the deflection shape of the steady-state response.

$$\boldsymbol{\Delta} = (-\omega^2 \mathbf{M} + i\omega \mathbf{C} + \mathbf{K})^{-1} \mathbf{F} \quad (10.8)$$

As the excitation frequency decreases, the contribution from both the mass matrix (inertia forces) and damping matrix (damping forces) decreases. As the excitation frequency tends toward zero, we approach the static deflection shape.

$$\lim_{\omega \rightarrow 0} \boldsymbol{\Delta} = \mathbf{K}^{-1} \mathbf{F} \quad (10.9)$$

10.7.2 Modal superposition and truncation

The Duhamels integral (a convolution integral) is the solution to the equation of motion [35, 36]. Here, we write it for the modal domain.

$$q_i(t) = h_i(t) * \boldsymbol{\phi}_i^\top \mathbf{x}(t), \quad i \in \mathbb{N} \quad (10.10)$$

where $h_i(t)$ is the impulse response function for the i^{th} mode and $*$ denotes the convolution operation.

We use the modal superposition, Eq. (10.3), to obtain the full response from the modal coordinates. In practice, we often apply modal truncation, which is a system simplification. We truncate the modal superposition, Eq. (10.3), to include K modes then we have an unknown error in our representation of the structural response - called the modal truncation error or the residual effect.

$$\begin{aligned} \mathbf{y}(t) &= \sum_{i=1}^K \boldsymbol{\phi}_i q_i(t) + \sum_{i=K+1}^N \boldsymbol{\phi}_i q_i(t) \\ &= \tilde{\mathbf{y}}(t) + \mathbf{e}(t) \end{aligned} \quad (10.11)$$

where $\tilde{\mathbf{y}}(t) \in \mathbb{R}^N$ is simplified dynamic response and $\mathbf{e}(t) \in \mathbb{R}^N$ is the modal truncation error (residual effect).

As long as this modal truncation error is insignificant then the truncation of the modal superposition is acceptable. In the following, we will demonstrate how to access the modal truncation by studying the contribution of each mode in the form of its modal coordinate. Let us assume that the load is separable into a fixed spatial distribution and temporal variation, Eq. (10.6), thus, we can calculate the modal coordinates as a convolution, Eq. (10.10).

$$\begin{aligned} q_i(t) &= h_i(t) * \boldsymbol{\phi}_i^\top \mathbf{F}\mathbf{s}(t), \quad i \in \mathbb{N} \\ &= \boldsymbol{\phi}_i^\top \mathbf{F} h_i(t) * \mathbf{s}(t), \quad i \in \mathbb{N} \end{aligned} \quad (10.12)$$

Consequently, the contribution of each mode depends on the convolution of the impulse response function and the temporal variation of the load. It also depends on the inner vector product between the given mode shape and the spatial distribution of the load. Therefore, the residual effect depends on both frequency range and spatial distribution of the load [34].

Quasi-static residual effect

In this case, we truncate the modal superposition to include K modes that substantially contribute to the dynamic response. We assume that these K modes contribute with a dynamic response while higher modes contribute with a residual effect. Thus, we assume that the majority of the system response has a subspace that this truncated set of mode shapes spans. Moreover, we assume low damping on these residual modes. Therefore, we have a quasi-static residual effect, $e(t)$, with no dynamic amplification of the residual modes so the modal coordinates for these residual modes become a static version of Eq. (10.10).

$$q_i^*(t) = \frac{\boldsymbol{\phi}_i^\top}{\omega_i^2} \mathbf{x}(t), \quad i \in \mathbb{N} > K \quad (10.13)$$

Then we insert this into the modal truncation error.

$$\mathbf{e}^*(t) = \sum_{i=K+1}^N \frac{\boldsymbol{\phi}_i \boldsymbol{\phi}_i^\top}{\omega_i^2} \mathbf{x}(t) \quad (10.14)$$

We insert the inverse of the stiffness matrix, Eq. (10.5), which is a sum of outer products of the mode shapes, into the operational deflection shape.

$$\mathbf{e}^*(t) = \left(\mathbf{K}^{-1} - \sum_{i=1}^K \frac{\boldsymbol{\phi}_i \boldsymbol{\phi}_i^\top}{\omega_i^2} \right) \mathbf{x}(t) \quad (10.15)$$

This equation is the static correction term known as the mode acceleration method [24, 35]. This term is used in the calculation of the system response to correct for the contribution of residual modes.

In the case that we have a load with a fixed spatial distribution, Eq. (10.6) then we can further rewrite the static correction term.

$$\begin{aligned} \mathbf{e}^*(t) &= \left(\mathbf{K}^{-1} - \sum_{i=1}^K \frac{\boldsymbol{\phi}_i \boldsymbol{\phi}_i^\top}{\omega_i^2} \right) \mathbf{F} \mathbf{s}(t) \\ &= \boldsymbol{\Delta} \mathbf{s}(t) \end{aligned} \quad (10.16)$$

where $\boldsymbol{\Delta} \in \mathbb{R}^{N \times n}$ is matrix holding the operational deflection shapes of the residual effect as column vectors.

$$\boldsymbol{\Delta} = \left(\mathbf{K}^{-1} - \sum_{i=1}^K \frac{\boldsymbol{\phi}_i \boldsymbol{\phi}_i^\top}{\omega_i^2} \right) \mathbf{F} \quad (10.17)$$

These deflection shapes are also called pseudo modes and this formulation is called the modal truncation augmentation method [24, 30]. To illustrate why these deflection shapes are often called pseudo modes, assumed modes, or dummy modes, let us insert the static correction term from Eq. (10.16) into the response from Eq. (10.11).

$$\begin{aligned} \mathbf{y}(t) &= \sum_{i=1}^K \boldsymbol{\phi}_i q_i(t) + \mathbf{e}^*(t) \\ &= \tilde{\boldsymbol{\Phi}} \mathbf{q}(t) + \boldsymbol{\Delta} \mathbf{s}(t) \end{aligned} \quad (10.18)$$

We rewrite the equation to a combined matrix form that resembles the modal superposition, Eq. (10.3)

$$\begin{aligned} \mathbf{y}(t) &= \begin{bmatrix} \tilde{\boldsymbol{\Phi}} & \boldsymbol{\Delta} \end{bmatrix} \begin{bmatrix} \mathbf{q}(t) \\ \mathbf{s}(t) \end{bmatrix} \\ &= \hat{\boldsymbol{\Phi}} \mathbf{q}_p(t) \end{aligned} \quad (10.19)$$

where $\hat{\Phi} \in \mathbb{R}^{N \times K+n}$ is the pseudo modal matrix that contains both mode shapes and deflection shapes and $\mathbf{q}_p(t) \in \mathbb{R}^{K+n}$ holds the coefficients of the linear combination of the pseudo modal matrix. In this way, the deflection shapes become pseudo modes that are included along with the mode shapes in a pseudo modal matrix.

10.7.3 Wave loading and deflection shapes

In this section, we will apply the previous sections to wave-induced structures to analyse the response. For simplicity, we assume in this section that the structure in question is a cylinder/pile. Firstly, we want to set up the wave loading on an offshore structure. Using linear wave theory, the velocity in the x -direction of a single wave is

$$u(t, z) = \frac{H\omega}{2} \frac{\cosh(k(h+z))}{\sinh(kh)} \cos(\omega t - kx) \quad (10.20)$$

where H is the wave height, k is wave number, h is the water depth, ω is the cyclic frequency of the wave, and z is the principal axis perpendicular to the seabed.

The acceleration in the x -direction is

$$\dot{u}(t, z) = -\frac{H\omega^2}{2} \frac{\cosh(k(h+z))}{\sinh(kh)} \sin(\omega t - kx) \quad (10.21)$$

We apply Morison's equation to obtain the wave loading in the x -direction on a cylinder/pile [37].

$$x(t, z) = C_I \frac{\rho d^4 \pi}{4} \dot{u}(t, z) + C_D \frac{\rho d}{2} u(t, z) |u(t, z)| \quad (10.22)$$

where C_I is the coefficient of inertia (mass), C_D is the coefficient of drag, ρ is the water mass density, and d is the pile diameter.

We insert the velocity, Eq. (10.20), and acceleration, Eq. (10.21), of the wave into Morison's equation, Eq. (10.22), and we exchange the coordinate z with a vector, $\mathbf{z} \in \mathbb{R}^N$.

$$\begin{aligned} \mathbf{x}(t) = & -C_I \frac{\rho d^4 \pi}{4} \frac{H\omega^2}{2} \frac{\cosh(k(h+\mathbf{z}))}{\sinh(kh)} \sin(\omega t - kx) + \dots \\ & C_D \frac{\rho d}{2} \left(\frac{H\omega}{2} \frac{\cosh(k(h+\mathbf{z}))}{\sinh(kh)} \right)^2 \cos(\omega t - kx) | \cos(\omega t - kx) | \end{aligned} \quad (10.23)$$

We divide the loading into components of spatial distributions and temporal variations for both the inertial and drag dominated wave loading.

$$\mathbf{x}(t) = \mathbf{f}_I s_I(t) + \mathbf{f}_D s_D(t) \quad (10.24)$$

where $\mathbf{f}_I \in \mathbb{R}^N$ is a vector holding the spatial distribution of the inertia-dominated wave load, $s_I(t)$ is the temporal variation of the inertia-dominated wave load, $\mathbf{f}_D \in \mathbb{R}^N$ is a vector holding the spatial distribution of the drag-dominated wave load, and $s_D(t)$ is the temporal variation of the drag-dominated wave load. Here, the spatial distributions depend on the wave.

$$\mathbf{f}_I = \omega^2 H \frac{\cosh(k(h+\mathbf{z}))}{\sinh(kh)}, \quad \mathbf{f}_D = \left(\omega H \frac{\cosh(k(h+\mathbf{z}))}{\sinh(kh)} \right)^2 \quad (10.25)$$

We are, however, dealing with multiple waves with different characteristics defined by the wave spectrum and we combine the load using superposition.

$$\mathbf{x}(t) = \sum_i \mathbf{f}_{I,i} s_{I,i}(t) + \mathbf{f}_{D,i} s_{D,i}(t) \quad (10.26)$$

Let us now assume that we will approximate the load by dividing the wave spectrum into N_{wave} segments; each with corresponding wave height, wave number, and cyclic frequency.

$$\begin{aligned} \mathbf{x}(t) & \approx \sum_{i=1}^{N_{wave}} \mathbf{f}_{I,i} s_{I,i}(t) + \mathbf{f}_{D,i} s_{D,i}(t) \\ & \approx \mathbf{F}_I \mathbf{s}_I(t) + \mathbf{F}_D \mathbf{s}_D(t) \end{aligned} \quad (10.27)$$

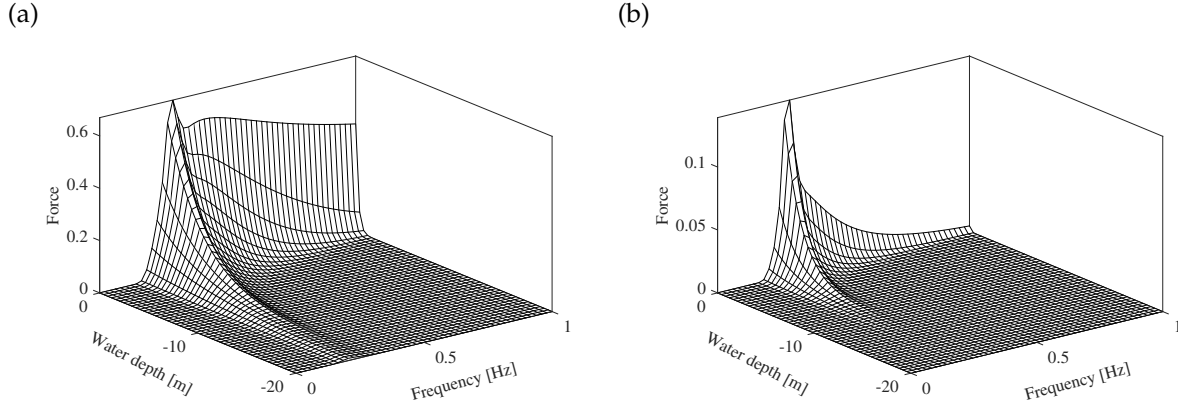


Figure 10.1: The spatial distribution of wave loading from JONSWAP with a peak frequency of 0.137 Hz, a significant wave height of 2.02 m, and a peak enhancement coefficient of 2.38: (a) inertia-dominated wave loading, and (b) drag-dominated wave load

where $\mathbf{F}_I \in \mathbb{R}^{N \times N_{wave}}$ holds the spatial distributions of the inertia-dominated wave loading as column vectors, $\mathbf{s}_I(t) \in \mathbb{R}^{N_{wave}}$ holds the temporal variation of the inertia-dominated wave load, $\mathbf{F}_D \in \mathbb{R}^{N \times N_{wave}}$ holds the spatial distributions of the drag-dominated wave loading as column vectors, and $\mathbf{s}_D(t) \in \mathbb{R}^{N_{wave}}$ holds the temporal variation of the drag-dominated wave load. Fig. 10.1 shows an example of the spatial distributions of the inertia- and drag-dominated wave loading as function of wave depth and wave frequency. Here, the dependency on wave frequency is evident for the spatial distribution of the wave loading.

We will rewrite eq. (10.27) to an combined matrix-vector formulation.

$$\begin{aligned} \mathbf{x}(t) &\approx [\mathbf{F}_I \quad \mathbf{F}_D] \begin{Bmatrix} \mathbf{s}_I(t) \\ \mathbf{s}_D(t) \end{Bmatrix} \\ &\approx \mathbf{F}_w \mathbf{s}(t) \end{aligned} \quad (10.28)$$

where $\mathbf{F}_w \in \mathbb{R}^{N \times 2N_{wave}}$ holds $2N_{wave}$ spatial distributions of the load and $\mathbf{s}(t) \in \mathbb{R}^{2N_{wave}}$ holds the same number of temporal variations of the load.

If we were to calculate the deflection shapes (or deflection shape of the residual effect) based on \mathbf{F}_w then we would obtain $2N_{wave}$ different shapes, $\Delta \in \mathbb{R}^{N \times 2N_{wave}}$. Thus, for the quasi-static response, a wave-induced structure vibrates with multiple deflection shapes. Furthermore, each deflection shape is a linear combination of all the mode shapes that depends on the natural frequency of the mode and the inner matrix product between the mode shape and the spatial distribution of the wave-loading. Here, the inner matrix product can include higher modes.

$$\begin{aligned} \Delta &= \mathbf{K}^{-1} \mathbf{F}_w \\ &= \sum_{i=1}^N \boldsymbol{\phi}_i \frac{\boldsymbol{\phi}_i^T \mathbf{F}_w}{\omega_i^2} \end{aligned} \quad (10.29)$$

For offshore structures, the strain response and curvature above the waves are near zero in the quasi-static response since deformation mainly occurs subsea. Fig. 10.2 illustrates an example of a simplified offshore structure (simplified to a cantilever beam with mass at the end). To obtain the correct curvature, we need more than the first few mode shapes using modal superposition.

Furthermore, the matrix, Δ , containing the deflection shapes, is likely to be rank deficient so we could reduce the matrix to hold fewer deflection shapes. Let us say that the matrix has rank k , where $k < 2N_{wave}$, then we can use the singular value decomposition where the first k left singular vectors form an orthogonal basis for the column space for the matrix that contains the deflection shapes.

The reader should note that the wave loading in this section does not stretch in accordance with the wave elevation since the equations are based on linear wave theory, therefore; the wave loading is defined from the seabed to mean water level.

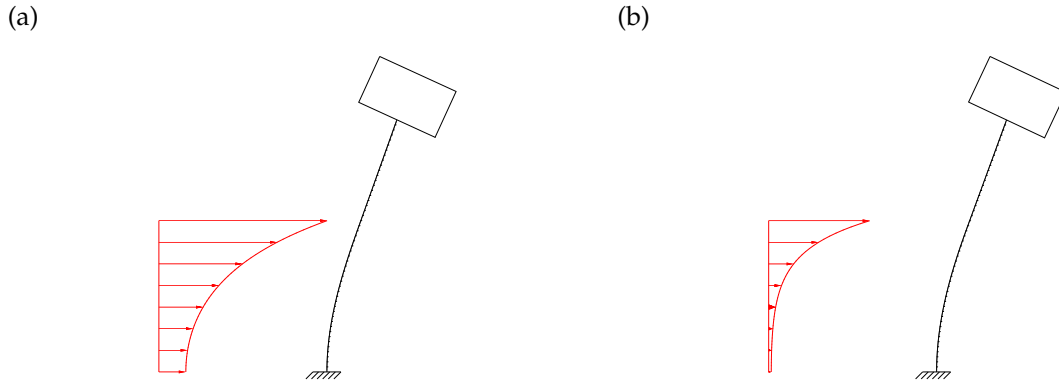


Figure 10.2: Example of deflection shape based on the spatial distribution of wave loading from JONSWAP with a peak frequency of 0.137 Hz, a significant wave height of 2.02 m, and a peak enhancement coefficient of 2.38 for: (a) inertia-dominated wave loading, and (b) drag-dominated wave load

10.8 Virtual sensing

Virtual sensing transforms measured quantities to the full-state of the system from where we extract specific data of the system at any location of the system [2]. This datum is called a virtual sensor. We can divide virtual sensing into four components: system model, physical sensors, process model, and virtual sensor. The system model is a mathematical model of the system [38] that contains all the necessary information of the system and sensors for the particular application; this information is also called states of the system. The physical sensors are a network of sensors which measure different quantities of the system. The process model transforms the information of the system model and physical sensors into virtual sensors by estimating the full-state of the system. Fig. 10.3 illustrates the flowchart of virtual sensing.

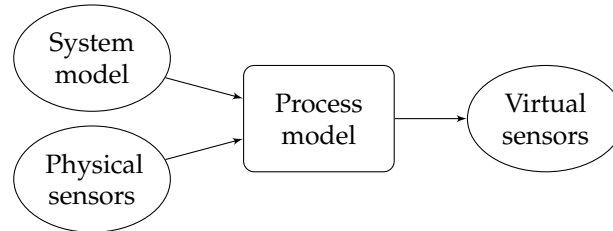


Figure 10.3: Flowchart of virtual sensing

10.8.1 Modal expansion - least-square regression

The modal expansion is a process model for virtual sensing that uses the modal superposition, Eq. (10.3), to estimate the modal coordinates from the spatial limited physical sensors through a least-square regression. We have a truncated modal matrix with K mode shapes, $\tilde{\Phi} = [\phi_1 \ \phi_2 \ \dots \ \phi_K]$, which is our system model. We take the modal superposition with a modal truncation error, Eq. (10.11), and introduce measured and unmeasured DOFs.

$$\begin{aligned}
 \begin{bmatrix} \mathbf{y}_a(t) \\ \mathbf{y}_d(t) \end{bmatrix} &= \begin{bmatrix} \tilde{\Phi}_a \\ \tilde{\Phi}_d \end{bmatrix} \mathbf{q}(t) + \begin{bmatrix} \mathbf{e}_a(t) \\ \mathbf{e}_d(t) \end{bmatrix} \\
 &= \begin{bmatrix} \tilde{\mathbf{y}}_a(t) \\ \tilde{\mathbf{y}}_d(t) \end{bmatrix} + \begin{bmatrix} \mathbf{e}_a(t) \\ \mathbf{e}_d(t) \end{bmatrix}
 \end{aligned} \tag{10.30}$$

where $(\cdot)_a$ denotes the measured DOFs and $(\cdot)_d$ denotes the unmeasured DOFs. For modal expansion, we call the modal matrix - reduced to the measured DOFs, $\tilde{\Phi}_a = [\phi_{a,1} \ \phi_{a,2} \ \dots \ \phi_{a,K}]$ - for the reduced system matrix.

Unfortunately, we will also have measurement noise, $\mathbf{n}(t)$, in the measured response, $\mathbf{y}_m(t)$.

$$\mathbf{y}_m(t) = [\tilde{\Phi}_a] \mathbf{q}(t) + \mathbf{e}_a(t) + \mathbf{n}(t) \quad (10.31)$$

Using modal expansion, we can estimate the pseudo modal coordinates

$$\hat{\mathbf{q}}(t) = \tilde{\Phi}_a^\dagger (\mathbf{y}_a(t) + \mathbf{e}_a(t) + \mathbf{n}(t)) \quad (10.32)$$

Since the modal truncation error has a subspace orthogonal to column space of the truncated modal matrix, $C(\tilde{\Phi}_a)$, then $\tilde{\Phi}_a^\dagger \mathbf{e}_a(t) = \mathbf{0}$. The reader should, however, note that this is not the case in presence of modelling errors.

$$\hat{\mathbf{q}}(t) = \tilde{\Phi}_a^\dagger \mathbf{y}_a(t) + \tilde{\Phi}_a^\dagger \mathbf{n}(t) \quad (10.33)$$

To estimate the full-field strain response, we use the strain mode shapes, which is defined as the strain response caused by a deflection corresponding to a mode shape [39].

$$\hat{\boldsymbol{\varepsilon}}(t) = \tilde{\Phi}_\varepsilon \hat{\mathbf{q}}(t) \quad (10.34)$$

where $\hat{\boldsymbol{\varepsilon}}(t)$ is the estimated full-field strain response and $\tilde{\Phi}_\varepsilon$ is the strain mode shape matrix.

An important aspect of the modal expansion is the stability of this inverse process for the accuracy of the virtual sensor. We will introduce the concept of sensitivity (also called observability) of the reduced system model to describe the extent to which a virtual sensor changes due to a small change in the system model or measured data of the physical sensors. The system model is reduced to the measured DOFs and it should - in its reduced form - distinguish between the different states of the system based on the physical sensors. The reduced system model should be so sensitive that we can satisfactorily estimate the state of the system. It should, however, not be so sensitive that it becomes unstable where a small level of noise results in an erroneous estimation of state. Generally, there is a trade-off between sensitivity and instability (uncertainty). The sensitivity of the reduced system model depends on the number and position of the physical sensor, excitation, and the system. We will highlight some important aspects of modal truncation for modal expansion. Whenever one of the reduced mode shapes tends toward a zero vector, $\boldsymbol{\phi}_{a,j} \approx \mathbf{0}$, the reduced modal matrix tends toward rank deficiency and we cannot estimate the corresponding modal coordinate. Furthermore, the reduced modal matrix is also rank deficient if two mode shapes - in their reduced forms corresponding to the measured DOFs - are linear dependent, $\boldsymbol{\phi}_{a,j} \propto \boldsymbol{\phi}_{a,k}$. Here, both states are equally likely and the reduced system model is unstable.

10.8.2 Modal expansion - weighted least-square regression

Alternatively, we could apply the weighted least-square regression in the modal expansion [40]. Here, we introduce the covariance matrix of the measurement noise on the physical sensors. This enables us to distinguish between the importance of each physical sensor used for virtual sensing. We can estimate the pseudo modal coordinates as

$$\hat{\mathbf{q}}_p(t) = \left(\tilde{\Phi}_a^\top \mathbf{W} \tilde{\Phi}_a \right)^{-1} \tilde{\Phi}_a^\top \mathbf{W} \mathbf{y}_m(t) \quad (10.35)$$

where \mathbf{W} is the weight matrix and it is defined as the inverse of the covariance matrix of the measurement noise.

$$\mathbf{W} = \left(\mathbb{E} [\mathbf{n}(t) \mathbf{n}(t)^\top] \right)^{-1} \quad (10.36)$$

We can use the weighted least-square when we have different types of sensors. This version of modal expansion enables sensor fusion of sensors with different levels of measurement noise.

10.9 Static correction and pseudo mode shapes

In this section, we will discuss methods for static corrections that reduce the modal truncation error or residual effect.

Pseudo modes are additional mode shapes or operational deflection shapes that we insert into a truncated modal matrix to better span the response of interest. Thus, we use a combination of eigenvectors and pseudo modes dependent on the particular loading in a pseudo modal matrix.

$$\hat{\Phi} = [\tilde{\Phi} \quad \Delta] \quad (10.37)$$

where $\hat{\Phi} \in \mathbb{R}^{N \times K+n}$ is the pseudo modal matrix, $\tilde{\Phi} \in \mathbb{R}^{N \times K}$ is the truncated modal matrix with K mode shapes, and $\Delta \in \mathbb{R}^{N \times n}$ holds the deflection shapes or pseudo mode shapes.

Ideally, the pseudo modal matrix should have linearly independent column vectors and the pseudo modes should be linearly independent of applied mode shapes. In that case, the pseudo modal matrix is linearly dependent and it increases the condition number so the truncated pseudo modal matrix becomes unstable. Thus, the pseudo modal matrix is near rank deficient and ill-conditioned. We can overcome this problem by orthogonalising the pseudo modal matrix to the mass and stiffness matrix by solving the following eigenvalue problem.

$$\hat{\phi}_i^\top \mathbf{K} \hat{\phi}_i \mathbf{z}_i = \hat{\omega}_i^2 \hat{\phi}_i^\top \mathbf{M} \hat{\phi}_i \mathbf{z}_i \quad (10.38)$$

Then we obtain the final pseudo mode shapes.

$$\varphi_i = \hat{\phi}_i \mathbf{z}_i \quad (10.39)$$

We should normalise φ_i so it resembles the other mode shapes in terms of vector length. In least-square regression, this is called column scaling and it reduces the condition number and increases the stability of the reduced system model [41]. In this paper, we mass normalise each mode in Eq. (10.37).

$$\varphi_i = \frac{\hat{\phi}_i}{\sqrt{\hat{\phi}_i^\top \mathbf{M} \hat{\phi}_i}} \quad (10.40)$$

10.9.1 Mode acceleration

This method is a static correction to the truncated response and it is based on the stiffness matrix and the load vector. This method assumes that the truncated modes influence the response with a static contribution whereas the dynamic response stems from the included modes. There are many different versions of the Modal Acceleration Method and most of them are essentially the same, as shown by Soriano et al. [42].

In the case of K included modes in the modal superposition, the static correction is calculated as Eq. (10.15).

$$\bar{\mathbf{e}}(t) = \left(\mathbf{K}^{-1} - \sum_{i=1}^K \frac{\hat{\phi}_i \hat{\phi}_i^\top}{\omega_i^2} \right) \mathbf{x}(t) \quad (10.41)$$

In structural health monitoring, the exact load history is unknown so this method has limited application in this field.

10.9.2 Ritz vectors

Traditionally, a set of orthogonal Ritz vectors is used instead of the eigenvector to calculate the system response to reduce the computational time significantly. There are many approaches to calculating the Ritz vectors where Wilson made one of the first versions [43].

We will use the Ritz vectors as pseudo modes in the modal expansion to reduce the modal truncation error. In the literature of stress/strain estimation, Skaftø et al. [3] applied Ritz vectors as "assumed modes", "pseudo modes", or "dummy modes" to reduce modal truncation for the quasi-static response of wave-induced structures. Assuming the load has a spatial distribution that is time-invariant, see Eq. (10.6), we calculate the first Ritz vector as the static deflection shape caused by the spatial distribution of the load, Eq. (10.9).

$$\begin{aligned} \Delta &= \mathbf{K}^{-1} \mathbf{F} \\ &= \Phi [\omega_i^{-2}] \Phi^\top \mathbf{F} \end{aligned} \quad (10.42)$$

A Ritz vector is a linear combination of all mode shapes. Therefore, the pseudo modal matrix - containing both mode shapes and the Ritz vectors - has an issue: the column vectors in the pseudo modal matrix are linearly dependent.

10.9.3 Modal truncation augmentation method

This method is an extension of the mode acceleration and it is not just a static correction. We need to know the spatial distribution of the load (loading pattern). In this method, we calculate some pseudo eigenvectors based on the spatial distribution of the load and stiffness matrix. It is calculated as the static deflection shape with an exclusion of K dynamic modes.

$$\Delta = \left(\mathbf{K}^{-1} - \sum_{i=1}^K \frac{\boldsymbol{\phi}_i \boldsymbol{\phi}_i^\top}{\omega_i^2} \right) \mathbf{F} \quad (10.43)$$

This equation equals Eq. (10.17); thus, the modal truncation augmentation method corresponds to a quasi-static residual effect. Unlike the Ritz vectors, these modal truncation augmentation vectors are not a linear combination of the applied K dynamic modes.

10.9.4 Subspace of residuals method

This method is novel and was created by the authors for this paper. The method applies principal component analysis and it estimates the subspace of the residual effect to substitute for the most dominant residual mode shape that the modal truncation omitted. The technique requires that the reduced and truncated mode shapes, $\tilde{\boldsymbol{\Phi}}_a$, inaccurately span the measured and spatial limited response, $\mathbf{y}_a(t)$.

When we truncate the modal superposition then we have some response that we cannot express with the chosen set of mode shapes. We can find this residual effect by projecting the response onto the null space of $\boldsymbol{\Phi}_a^\top$.

$$\hat{\mathbf{e}}_a(t) = (\mathbf{I} - \boldsymbol{\Phi}_a \boldsymbol{\Phi}_a^\dagger) \mathbf{y}_a(t) \quad (10.44)$$

Let us say the modal truncation error, $\mathbf{e}_a(t)$, has a subspace, V , which is spanned by some column vectors, \mathbf{v}_i . The reader should note that this subspace is also the null space of $\boldsymbol{\Phi}_a^\top$.

$$V = \text{span} \{ \mathbf{v}_1 \ \mathbf{v}_2 \ \dots \ \mathbf{v}_H \} \quad (10.45)$$

Hence, we have a transformation matrix and its column vectors are the basis for the subspace V .

$$\mathbf{V} = [\mathbf{v}_1 \ \mathbf{v}_2 \ \dots \ \mathbf{v}_H] \quad (10.46)$$

Thus, we express the residual effect as a linear combination of these vectors.

$$\begin{aligned} \hat{\mathbf{e}}_a(t) &= \sum_{i=1}^H \mathbf{v}_i \tilde{q}_i(t) \\ &= \mathbf{V} \tilde{\mathbf{q}}_i(t) \end{aligned} \quad (10.47)$$

We calculate the covariance matrix of the residual effect.

$$\begin{aligned} \mathbf{C} &= \mathbb{E} [\hat{\mathbf{e}}_a(t) \hat{\mathbf{e}}_a(t)^\top] \\ &= \mathbf{V} \mathbb{E} [\tilde{\mathbf{q}}_i(t) \tilde{\mathbf{q}}_i(t)^\top] \mathbf{V}^\top \end{aligned} \quad (10.48)$$

We will perform a singular value decomposition on the covariance matrix

$$\mathbf{C} = \mathbf{U}_a \mathbf{S} \mathbf{U}_a^\top \quad (10.49)$$

Thus, the singular vectors are approximately equivalent to the transformation matrix, $\mathbf{V} \approx \mathbf{U}_a$. The corresponding singular values, \mathbf{S} , tell us how much each column vector contributes to the response. This is a principal component analysis and we can approximate the missing subspace of the response by the most dominant singular vectors.

The singular vector, \mathbf{U}_a , could be expanded where we could use the Ritz vector or the finite element mode shapes as the basis for the expansion of the singular vectors. The most important numbers of singular vectors, J , are used as pseudo mode shapes.



Figure 10.4: Experimental study: The Valdemar platform in the North Sea [44]

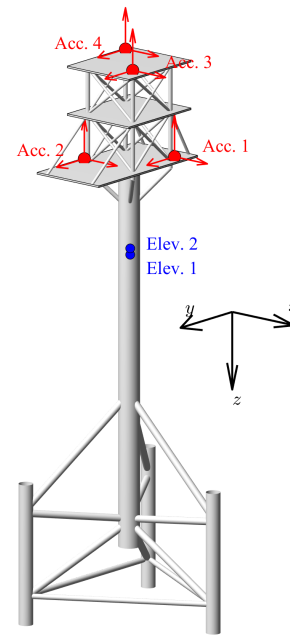


Figure 10.5: Experimental study: Position and direction of triaxial accelerometers (red arrows) and strain gauges measuring the direction of the member (blue dots)

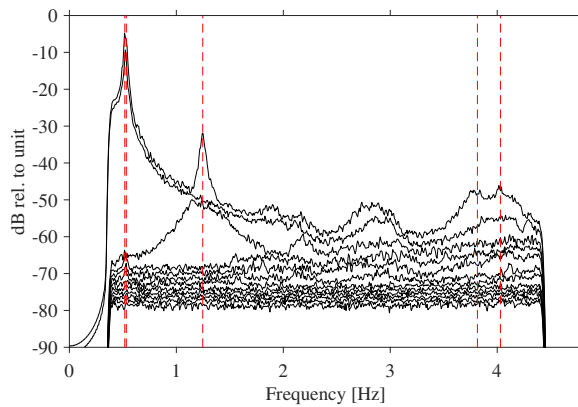


Figure 10.6: Experimental study: Singular values of spectral density function matrix of accelerometers (black) and estimated modes (red dashed line)

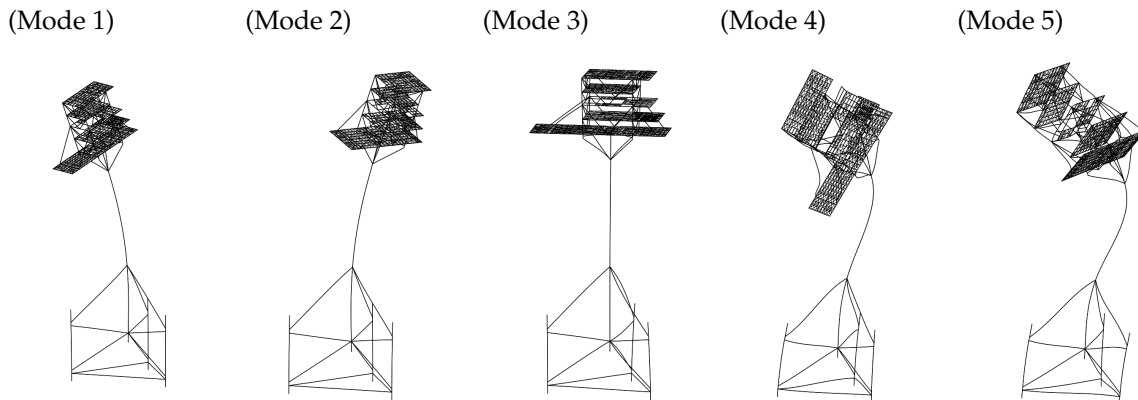


Figure 10.7: Mode shapes from finite element model of the Valdemar structure

Table 10.1: Experimental study: Modal parameters of the Valdemar platform

| Mode | | 1 | 2 | 3 | 4 | 5 |
|---------------------------------|----------------|--------|-------|--------|-------|-------|
| Finite element model | Frequency [Hz] | 0.519 | 0.522 | 1.288 | 3.736 | 3.887 |
| Operational modal analysis | Frequency [Hz] | 0.518 | 0.532 | 1.247 | 3.815 | 4.030 |
| Difference | [%] | -0.251 | 1.902 | -3.292 | 2.076 | 3.538 |
| Modal Assurance Criterion (MAC) | [-] | 0.999 | 0.998 | 0.989 | 0.960 | 0.900 |

10.10 Case study - offshore platform

The studied structure is the unmanned Valdemar offshore platform, which is a tripod structure positioned in the North Sea at a water depth of 42.7 m, see Fig. 10.4. The structure is equipped with four triaxial accelerometers that measure the structural acceleration in a total of 12 signals, see Fig. 10.5. Four strain gauges are placed in pairs at 11.5 (elevation 1) and 12.2 m (elevation 2) above the mean water level. Here, the accelerometers are used as the physical sensors for strain estimation at the same locations as the strain gauges, which are used as a reference for the estimation. Each dataset has a duration of an hour and a sample rate of 128 Hz. Furthermore, the structure is equipped with three wave radars and two Global Positioning Systems (GPS). For this study, we divide the response into three regions given by the frequency bands: static (0 – 0.1 Hz), quasi-static (0.1 – 0.45 Hz), and dynamic region (> 0.45 Hz).

The reader should note that the reference strain gauges do not measure the quasi-static effect of the wave loading since they are positioned above the sea. The spatial distributions of the wave loading ensure that there is no static stress above the waves, see Fig. 10.10. Thus, the measured strain response is inertia dominated in the quasi-static domain since they only measure the dynamic effect of the wave loading. In the planned installation of the sensors, the strain gauges were intended to be positioned near the surface of the sea. In practice, this, however, proved impossible since the waves washed away the scaffold during the installation. Thus, the strain gauges were installed at a safer location higher on the main column. Therefore, the measured strain response has a low amplitude due to the location of the sensors and it results in a low signal-to-noise ratio. The location of the strain gauges is not ideal for verifying strain estimation of the quasi-static effect of the wave loading.

To update and validate a system model, we apply operational modal analysis [1] to estimate the modal parameter of the structure in operation. We decimated the acceleration from the accelerometers to a new sampling rate of 16 Hz and applied a bandpass filter with cut-off frequencies of 0.4 and 4.4 Hz. We estimate the unbiased correlation function matrix [45] and reduce the statistical errors in this matrix by the algorithm by Tarpø et al. [46]. The Ibrahim time-domain technique [47] estimates the modal parameters from the estimated correlation function matrix and Table 10.1 shows the estimated parameters and Fig. 10.6 shows the identified modes atop the spectral density matrix. The reader should note that the fourth and fifth modes are weakly excited and difficult to estimate and we could only estimate these two modes in selected datasets. Thus, we should be cautious regarding the accuracy of these two modes.

Based on as-built technical drawings, we have created a finite element model in Ansys with 1156 beam elements and 452 shell elements. We simplified the structure since we are primarily interested in the global response from the first five modes, see the mode shapes in Fig. 10.7. We update the finite element model based on its first five modes to resemble the estimated modes using operational modal analysis, see Table 10.1. For more information on the finite element model, we refer the reader to [6]. In general, we obtained a high correlation between the model and the results from operational modal analysis but the Modal Assurance Criterion (MAC) for the fifth mode is off. Due to the uncertainty on the estimated modal parameters of the fourth and fifth mode, we assume the finite element model resembles the actual system for global behaviour.

For the given application, there is a lot of noise in the estimation of modal parameters - especially for the fourth and fifth modes. We assess this estimation error to exceed the modelling errors of the finite element model so an expansion of experimental mode shapes is disadvantageous to the finite element mode shapes for modal expansion [4]. Therefore, we apply the finite element mode shapes in this case study.

All data are bandpass filtered with cut-off frequencies of 0.1 and 1 Hz. The strain gauges are dominated by noise above 1 Hz where they are unfit for use as reference sensors; therefore, we limit the analysis to strains below 1 Hz. The low cut-off frequency is chosen to eliminate the static region and

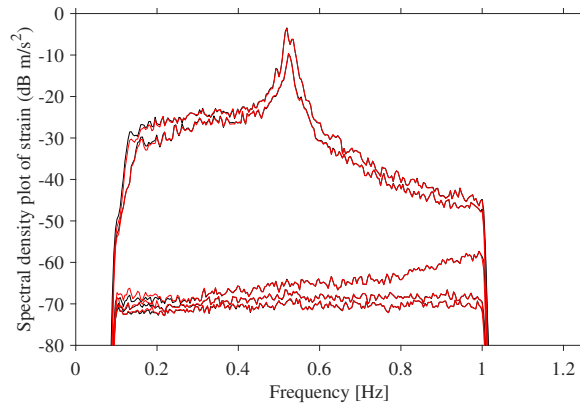


Figure 10.8: Tilt reduction of measured accelerometers: singular values of spectral density matrix from the measured (black line) and tilt reduced acceleration (red line)

reduce the numerical drift of the displacement caused by integrating the acceleration twice using the Fourier transformation.

$$\mathbf{y}(t) = \mathcal{F}^{-1} \left(\frac{1}{-\omega^2} \mathcal{F}(\ddot{\mathbf{y}}(t)) \right) \quad (10.50)$$

where $\mathcal{F}(\cdot)$ and $\mathcal{F}^{-1}(\cdot)$ denote the standard and inverse Fourier transformation, respectively.

We use the vertical sensors to reduce the tilt effects on the accelerometers [48], see Fig. 10.8. The reduction is minor but the reduction is amplified in the integration to displacement.

10.10.1 Simplification of spatial distribution of the wave loading

As derived in Section 10.7.3, we would have $2N_{wave}$ pseudo modes in each principal direction, where N_{wave} is the number of segments for the wave spectrum. There are issues with the spatial distributions of the wave loading for modal expansion since we need an overdetermined problem as it requires more physical sensors than pseudo mode shapes. Thus, we need to reduce the number of pseudo modes.

In this study, we will simplify the loading conditions for the pseudo mode shape to the main column. Furthermore, we have chosen a spatial distribution that corresponds to the peak frequency of a JON-SWAP fitted to the data of wave radars, see Fig. 10.9. Preliminary simulations indicate that the choice of wave frequency for the spatial distribution primarily affects the Valdemar structure subsea where no sensors are located. For this study, we focus on stress/strain estimation above the sea so the choice is of minor importance. We note that this spatial distribution is an estimation that corresponds to an averaged spatial distribution at mean water level. Using superposition, we split the wave loading into contributions from inertia-dominated and drag-dominated wave loading in the two principal directions, x and y . Thus, we split the wave loading into four spatial distributions. The deflection shape is illustrated in Fig. 10.10 in the principal axis y . When the wave loading is only applied to the main column, the deflection shapes of inertia or drag spatial distribution are near identical. Therefore, we will focus on the inertia-dominated spatial distribution of the load for the pseudo modes. The reader should note that we cannot express the deflection shapes of the wave loading as a linear combination of the first five modes since the five mode shapes cannot make a shape with the correct curvature. Therefore, we need the contribution of higher modes to accurately describe the quasi-static response caused by waves.

The reduced form - corresponding to the location of sensors - of the first two mode shapes and Ritz vectors in both principal directions are similar where the angle between the two subspaces of these are 5.5° . Furthermore, the condition number of the pseudo modal matrix is quite high, 21, indicating that we are dealing with an unstable reduced system model. To conclude, the Ritz vector and the first two mode shapes are quite similar and this challenges the separation of the response. Using the modal truncation augmentation method, the angle of the subspace between the first two mode shapes and the two deflection shapes is 66.5° while the condition number of the reduced pseudo modal matrix is 1.92. In theory, the modal truncation augmentation method provides a better basis for modal expansion than the Ritz vector method.

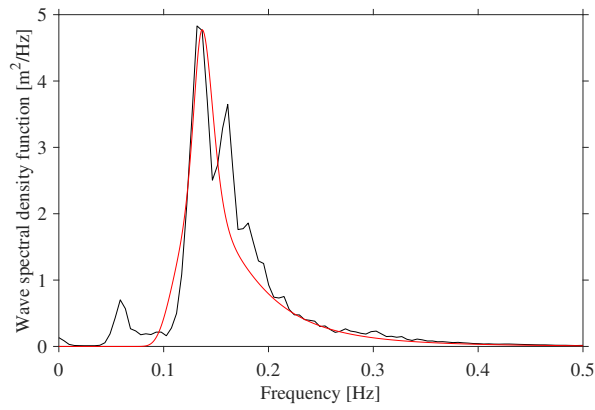


Figure 10.9: Wave spectral density function from wave radar (black) and JONSWAP with a peak frequency of 0.137 Hz, a significant wave height of 2.02 m, and a peak enhancement coefficient of 2.38 (red)

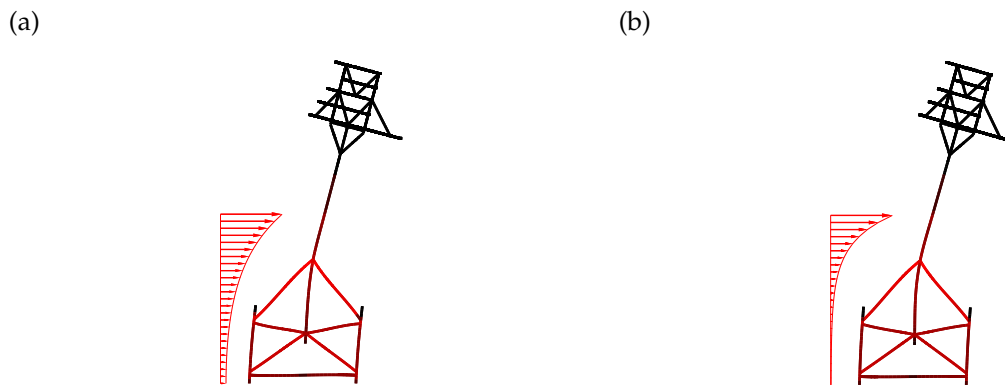


Figure 10.10: Deflection shapes in y -axis for: a) inertial-related, and b) drag-related spatial distribution of the wave loading

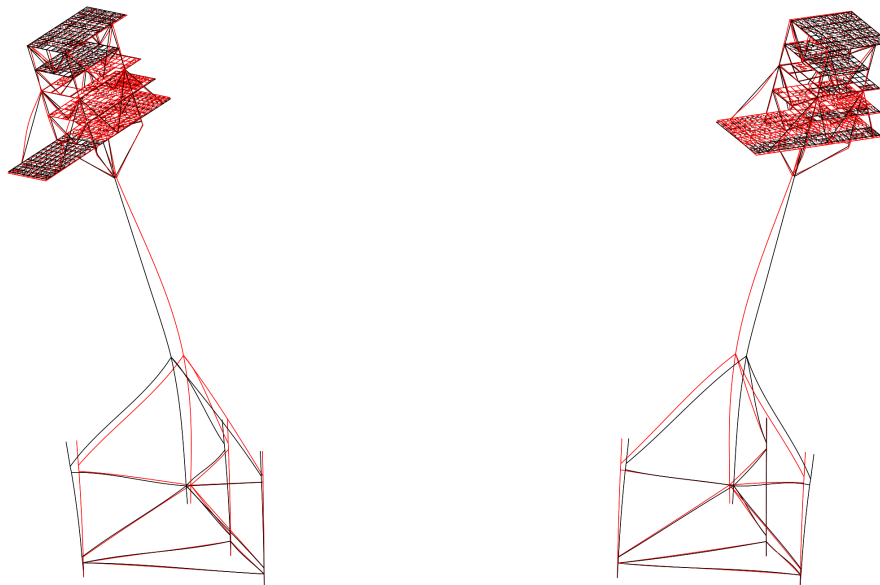


Figure 10.11: Deflection shape from inertia-dominated wave loading in two directions (black) and best approximation using five mode shapes (red)

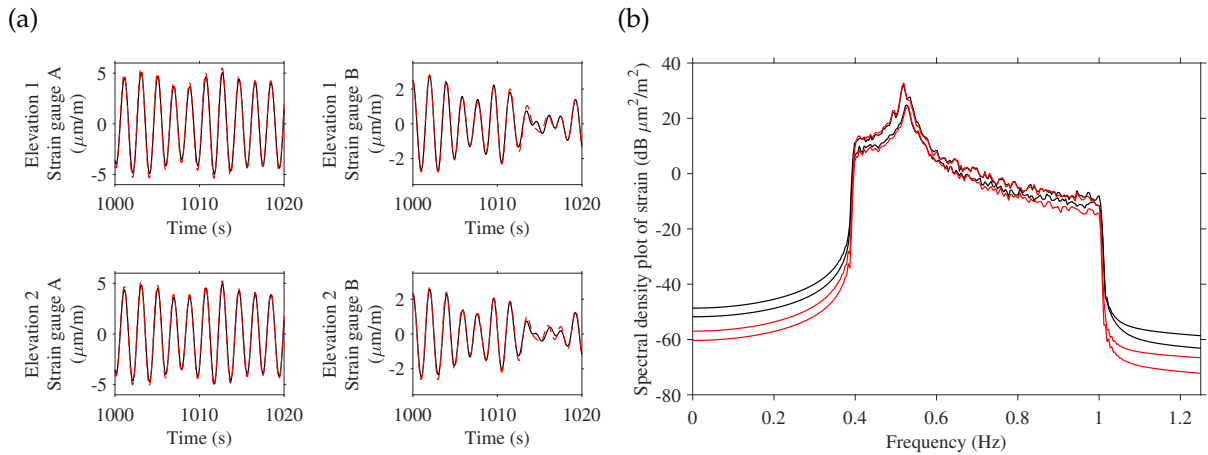


Figure 10.12: Strain estimation using five dynamic modes in dynamic region: (a) zoom of measured (black line) and estimated (red dotted line) strain response in the time domain, and (b) singular values of spectral density matrix from the measured (black line) and estimated (red line) strain response calculated using Welch averaging method with 50% overlap.

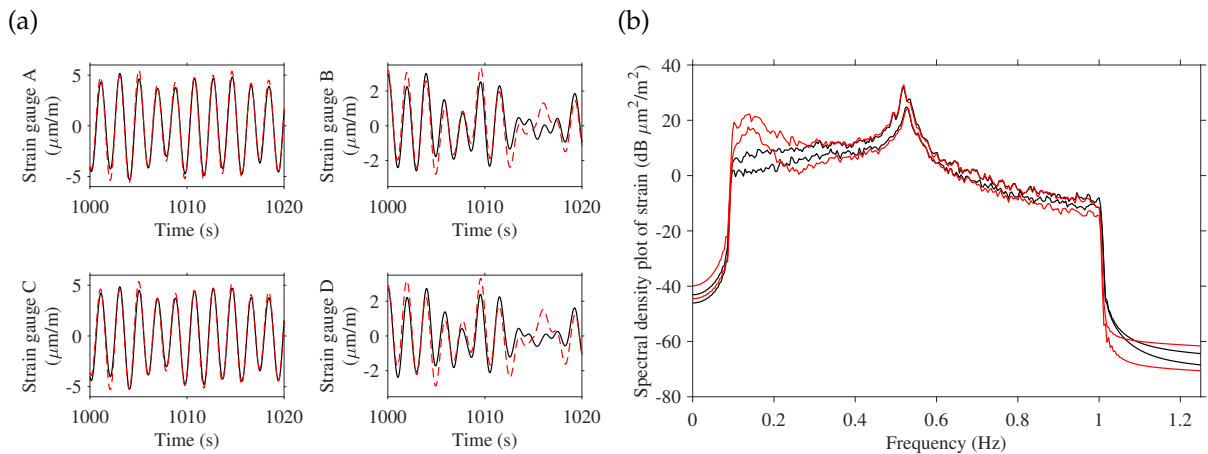


Figure 10.13: Strain estimation using five dynamic modes in quasi-static and dynamic region: (a) zoom of measured (black line) and estimated (red dotted line) strain response in the time domain, and (b) singular values of spectral density matrix from the measured (black line) and estimated (red line) strain response calculated using Welch averaging method with 50% overlap.

10.10.2 Dynamic modes in dynamic and quasi-static region

Firstly, we will use the dynamic modes without pseudo modes to study the issue of modal truncation for quasi-static strain estimation. We have studied strain estimation with both the first three and five modes in the modal matrix where the latter provides the best setup. We note that the authors studied the setup with three modes in [6] and the inclusion of the two additional modes was explored after this publication.

We will restrict ourselves to the dynamic range 0.4 – 1.0 Hz in the first application, see Fig. 10.12 for the results, where the estimation is highly correlated with the measured strain response. Next, we move into the quasi-static region 0.1 – 1.0 and Fig. 10.13 illustrates the results. Here, we overestimate the strain response below 0.4 Hz.

10.10.3 Compare Ritz vectors, modal truncation augmentation method, and subspace of residuals method

We will calculate the pseudo modes based on the inertia-dominated wave loading, which is a simplification of the actual loading conditions. We calculate the pseudo modes related to the Ritz vector and modal truncation augmentation method. We apply multi-band modal expansion containing two frequency bands with a transition at 0.4 Hz. The first band at 0.1 – 0.4 Hz contains the pseudo modes in both principal directions and the first two mode shapes while the second band at 0.4-1.0 Hz holds the first five modes. Fig. 10.14 shows the results for Ritz vectors as pseudo modes and Fig. 10.15 displays

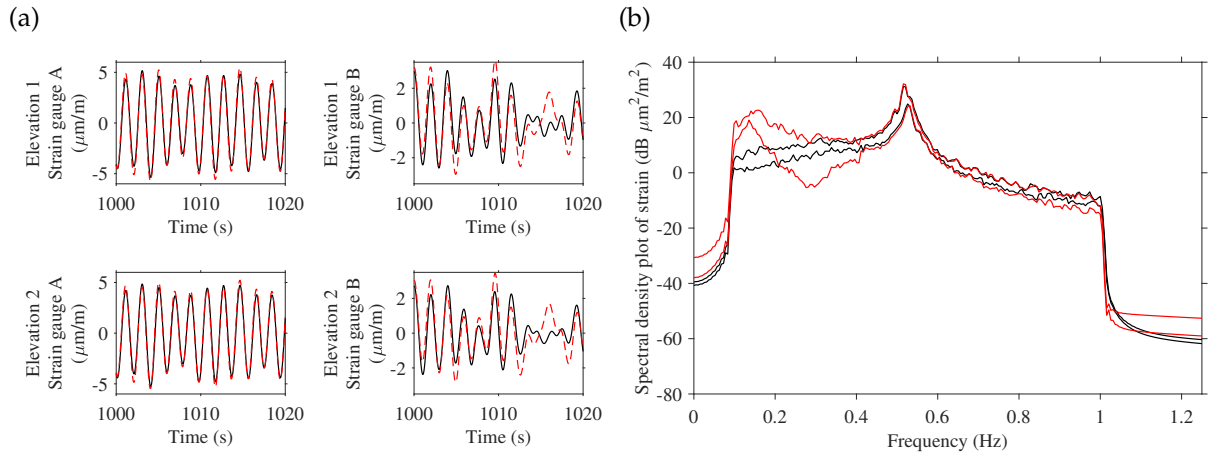


Figure 10.14: Strain estimation with pseudo modes using the Ritz vector method: (a) zoom of measured (black line) and estimated (red dotted line) strain response in the time domain, and (b) singular values of spectral density matrix from the measured (black line) and estimated (red line) strain response calculated using Welch averaging method with 50% overlap.

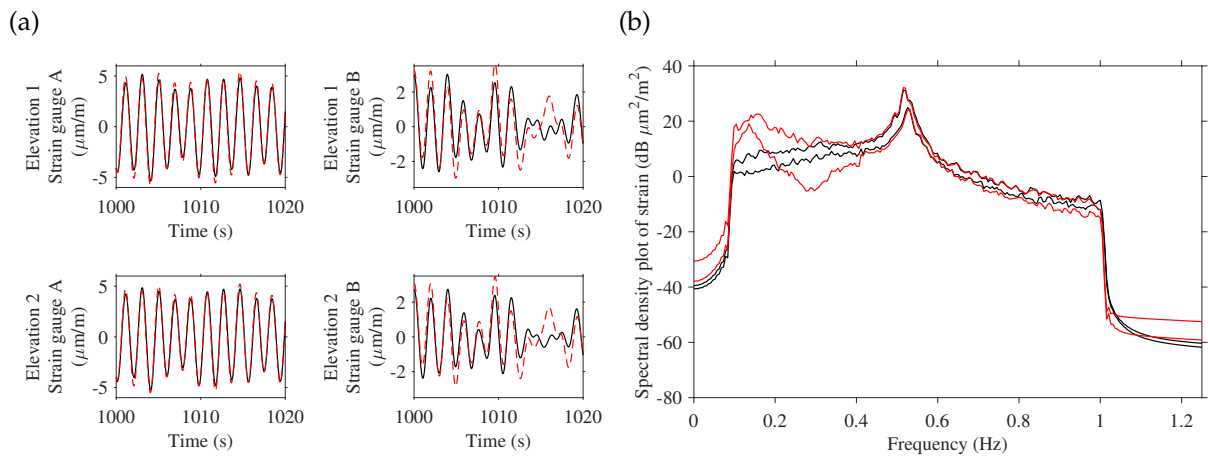


Figure 10.15: Strain estimation with pseudo modes using the modal truncation augmentation method: (a) zoom of measured (black line) and estimated (red dotted line) strain response in the time domain, and (b) singular values of spectral density matrix from the measured (black line) and estimated (red line) strain response calculated using Welch averaging method with 50% overlap.

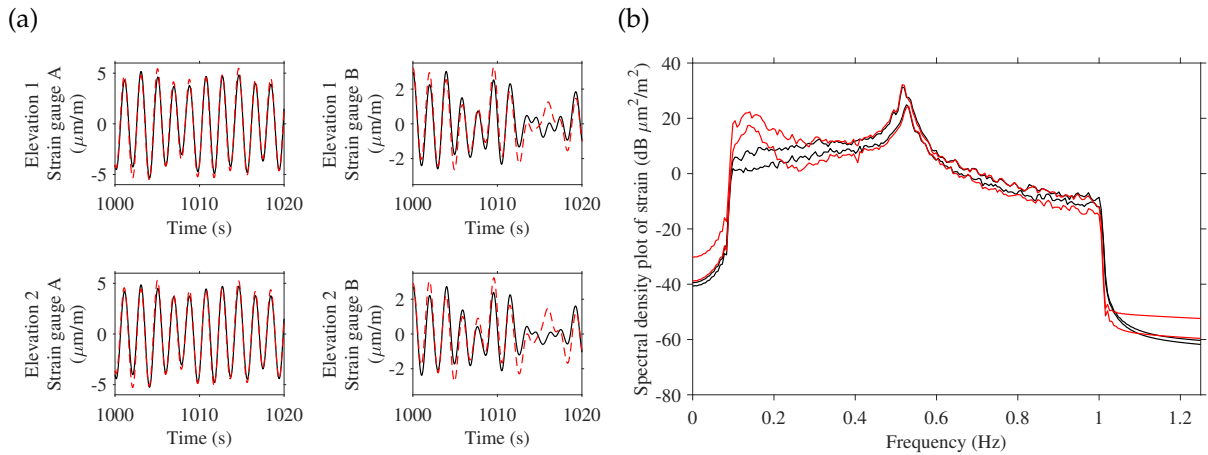


Figure 10.16: Strain estimation with pseudo modes using the subspace of residuals method: (a) zoom of measured (black line) and estimated (red dotted line) strain response in the time domain, and (b) singular values of spectral density matrix from the measured (black line) and estimated (red line) strain response calculated using Welch averaging method with 50% overlap.

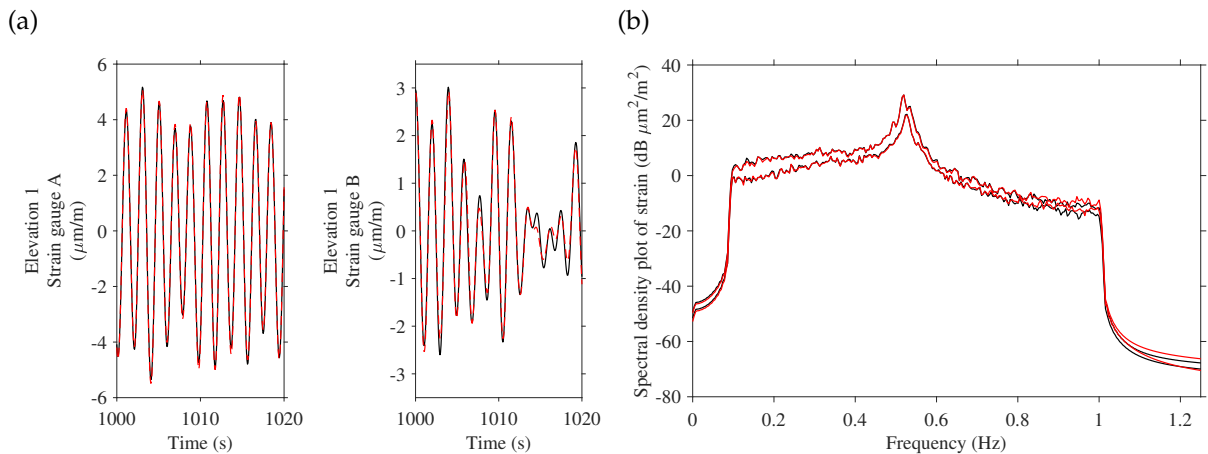


Figure 10.17: Strain estimation with sensor fusion using strain gauges from elevation 2 as physical sensor: (a) zoom of measured (black line) and estimated (red dotted line) strain response in the time domain, and (b) singular values of spectral density matrix from the measured (black line) and estimated (red line) strain response calculated using Welch averaging method with 50% overlap.

the results for the modal truncation augmentation method as pseudo modes. There is, however, no distinguishable difference between the Ritz vector method and the modal truncation augmentation method as pseudo mode shapes in this application of strain estimation. The condition number is higher for the Ritz vector but it is - for the given noise level - insignificant for strain estimation.

For the subspace of residuals method, we use the leave-p-out-cross-validation implementation of the local correspondence principle technique [4] to expand the first two singular vectors from the covariance matrix using the first five mode shapes as a basis. The subspace of residuals method does not work since the dynamic modes incorrectly span the entire response. There is simply no residual effect, which we can apply principal component analysis to. Thus, for the time being, the subspace of residuals method is unproven and we should test the method in further studies.

Neither technique for pseudo mode shape results in well-correlated strain estimation in this case study. Since virtual sensing is a process with three main components - the physical sensors, system model, and process model - then we cannot dismiss the idea of pseudo modes in virtual sensing. The issues, which prevent us from a well-correlated strain estimation, could stem from any or a combination of the three components. It could be the accelerometers: sensitivity at low frequency, numerical integration and the resulting drift, position and number of accelerometers. It could come from modelling errors in the finite element model or pseudo modes. It could also result from the modal expansion technique.

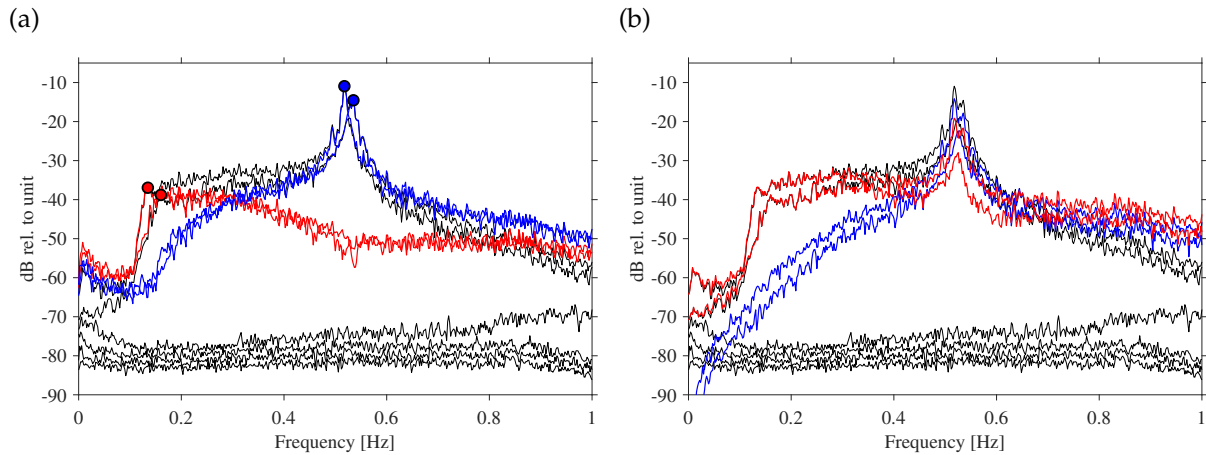


Figure 10.18: Singular values of spectral density function matrix of accelerometers calculated using Welch averaging method with 50% overlap (black line), quasi-static acceleration (red line), and dynamic acceleration (blue line): (a) frequency domain decomposition [49] analysis of the static and dynamic domain, and (b) acceleration estimation using the four strain gauges and the first two modes

10.10.4 Sensor fusion

We will apply sensor fusion by including two of strain gauges with the 12 accelerometers in the modal expansion so we only have two strain gauges as reference. For modal expansion, we transition from the regular least-square regression to a weighted least-square regression. We can adjust the weight matrix so it is primarily based on the strain gauges and we obtain strain estimation that is very close to the measured strain response, see Fig. 10.17. It is, however, an unimpressive achievement since the strain gauges - used as physical sensors in modal expansion - are located 0.7 m above the reference strain gauges and the structure is more than 75 m height. We therefore need more reference sensors to confirm the sensor fusion technique.

10.10.5 Frequency domain decomposition and acceleration estimation by strain gauges

In this study, we will use two different approaches to decorrelate the acceleration measured by the accelerometers into quasi-static and dynamic components. We perform a frequency domain decomposition [49] to analyse the acceleration and study the separation into dynamic and quasi-static acceleration. We estimate the spectral density matrix from the measured acceleration using the Welch averaging method and apply singular value decomposition on the matrix. We select two singular vectors at 0.135 and 0.160 Hz as the quasi-static deflection shape and two singular vectors at 0.517 and 0.535 Hz corresponding to the first and second modes. The angle between the two subspaces spanned by the quasi-static deflection shape and the first and second mode shape is 6.6° and the condition number of all singular vectors is 21.35. Using the two sets of singular vectors, we decorrelate the acceleration into the quasi-static and dynamic acceleration, see Fig. 10.18 (a).

Next, we will swap the physical and the references sensors for the virtual sensing application so we use the four strain gauges as physical sensors to estimate the acceleration in the same locations where the accelerometers are mounted. Since the strain response, at the strain gauges, relates to inertia, we will use the first two mode shapes for the modal expansion. The reader should note that we cannot recreate the measured acceleration through the strain gauges since these do not measure the quasi-static response, unlike the accelerometers. We use this estimated acceleration to access the dynamic portion of the measured acceleration. Then the quasi-static response equals the residual acceleration between the measured and the estimated acceleration from the strain gauges. Fig. 10.18 (b) illustrates the result in the frequency domain.

Now we have two different decorrelations of the acceleration into quasi-static and dynamic response, see Fig. 10.18. The two approaches for decorrelation resemble each other but the results are not identical. The dynamic response from the acceleration estimation has less energy at low frequency, see Fig. 10.18 (b), whereas the frequency domain decomposition has difficulties with separating the acceleration into quasi-static and dynamic components, see Fig. 10.18 (a).

Furthermore, we performed a principal component analysis on the residual acceleration from the acceleration estimation to find the main deflection shape of the missing response. Unfortunately, the principal component vectors are close to the first and second modes. Thus, the quasi-static portion of the measured acceleration is largely spanned by the first two mode shapes.

10.11 Discussion and conclusion

In this preliminary paper, we introduced different pseudo mode shapes for modal expansion to reduce the modal truncation error in quasi-static stress/strain estimation. We applied the techniques to the Valdemar platform located in the North Sea but we were unsuccessful in achieving good correlation between estimated and measured strain response in the quasi-static region. Generally, we estimate the strain response with high precision in the dynamic region but we overestimate the strain response in the quasi-static region. The strain estimation using five dynamic mode shapes is similar to strain estimation using pseudo modes from the Ritz vector method or the modal truncation augmentation method. Moreover, we approach virtual sensing from both the accelerometers and the strain gauges as physical sensors and we could not achieve proper agreement between the two types of sensors. It is difficult to pinpoint the exact reason for the lack of success due to the many components, which make a virtual sensor. The reason might relate to the system model, the physical sensors, the process model, the reference sensors, or any combination thereof. In the system model, we could have issues with the calibration of the finite element model or the pseudo modes as a representation of the quasi-static effect caused by the wave loading. For the physical sensor, we could have issues with the accelerometers in terms of sensitivity, measurement noise, or the position and number of sensors. For the reference sensors, the location of the strain gauges was not ideal for quasi-static strain estimation and it resulted in a low signal-to-noise ratio. Furthermore, the strain gauges could have issues with measurement noise, potential misalignment, and temperature sensitivity. Based on the network of accelerometers, the quasi-static and dynamic response are near indistinguishable from each other. In other words, we have a near unstable reduced system model where the quasi-static response is primarily a small rotation difference from the dynamic response. This instability introduces errors in the stress/strain estimation since the states are difficult to separate.

It would seem that we cannot apply accelerometers as the only physical sensors for virtual sensing in the static region. Here the integration error - caused by integrating the acceleration twice to obtain displacement - dominates since the integration process amplifies measurement noise in the acceleration signal. The measurement noise relates to the sensitivity of the accelerometer. In the plots with frequency domain decomposition of the spectral density matrix, the noise floor follows $\frac{1}{\omega^2}$ and it approaches the actual system response. We should use other sensors in this frequency region in order to obtain reliable results.

We were able to successfully apply sensor fusion using the weighted least-square with both accelerometers and strain gauges. We could use two of the strain gauges in the modal expansion in a sensor fusion using weighted least-square regression. Here, we increased our confidence in the strain gauges until we obtained results that largely corresponded to the strain gauges. Then we can easily estimate the other two strain gauges.

In conclusion, we need further research before an application of quasi-static strain estimation is feasible on the Valdemar platform.

Acknowledgements

The authors acknowledge the funding received from the Centre for Oil and Gas - DTU/Danish Hydrocarbon Research and Technology Centre (DHRTC).

The authors thank Michael Vigsø from Aarhus University for his helpful discussions and suggestions on the topic of modal truncation and pseudo mode shapes.

References

- [1] R. Brincker and C. Ventura. *Introduction to operational modal analysis*. John Wiley and Sons, Inc., Chichester, West Sussex, UK, 2015.

- [2] L. Liu, S. M. Kuo, and M. Zhou. Virtual sensing techniques and their applications. In *2009 International Conference on Networking, Sensing and Control*, pages 31–36, March 2009.
- [3] A. Skafte, J. Kristoffersen, J. Vestermark, U. T. Tygesen, and R. Brincker. Experimental study of strain prediction on wave induced structures using modal decomposition and quasi static ritz vectors. *Engineering Structures*, 136:261–276, 4/1 2017.
- [4] M. Tarpø, B. Nabuco, C. Georgakis, and R. Brincker. Expansion of experimental mode shape from operational modal analysis and virtual sensing for fatigue analysis using the modal expansion method. *International Journal of Fatigue*, 130:105280, 2020.
- [5] A. Iliopoulos, W. Weijtjens, D. Van Hemelrijck, and C. Devriendt. Full-field strain prediction applied to an offshore wind turbine. *Conference Proceedings of the Society for Experimental Mechanics Series*, 3:349–357, 2016.
- [6] Bruna Nabuco, Marius Tarpø, Ulf T. Tygesen, and Rune Brincker. Fatigue stress estimation of an offshore jacket structure based on operational modal analysis. *Shock and Vibration*, 2020:12, 2020.
- [7] B. Nabuco, M. Tarpø, A. Aïssani, and R. Brincker. Reliability analysis of offshore structures using oma based fatigue stresses. *ASME 2017 36th International Conference on Ocean, Offshore and Arctic Engineering*, 3A: Structures, Safety and Reliability:8, 2017.
- [8] B. Nabuco, T. Friis, M. Tarpø, S. Amador, E.I. Katsanos, and R. Brincker. Nonlinear strain estimation based on linear parameters. *ASME 2018 37th International Conference on Ocean, Offshore and Arctic Engineering*, 3: Structures, Safety, and Reliability:7, 2018.
- [9] M. Henkel, J. Häfele, W. Weijtjens, C. Devriendt, C.G. Gebhardt, and R. Rolfes. Strain estimation for offshore wind turbines with jacket substructures using dual-band modal expansion. *Marine Structures*, 71:102731, 2020.
- [10] Alexandros Iliopoulos. *Virtual sensing techniques for response estimation and fatigue assessment of offshore wind turbines*. PhD thesis, Vrije Universiteit Brussel, 2017.
- [11] K. Maes, G. De Roeck, G. Lombaert, A. Iliopoulos, D. Van Hemelrijck, C. Devriendt, and P. Guillaume. Continuous strain prediction for fatigue assessment of an offshore wind turbine using kalman filtering techniques. In *2015 IEEE Workshop on Environmental, Energy, and Structural Monitoring Systems (EESMS) Proceedings*, pages 44–49, July 2015.
- [12] Rajendra Prasath Palanisamy, Soojin Cho, Hyunjun Kim, and Sung-Han Sim. Reconstruction of unmeasured strain responses in bottom-fixed offshore structures by multimetric sensor data fusion. *Smart Structures and Systems*, 15:489–503, 2015.
- [13] Alexandros N. Iliopoulos, Christof Devriendt, Sokratis N. Iliopoulos, and Danny Van Hemelrijck. Continuous fatigue assessment of offshore wind turbines using a stress prediction technique. *Proc. SPIE 9064, Health Monitoring of Structural and Biological Systems 2014*, 9064:11, 2014.
- [14] Rajendra Prasath Palanisamy, Wonsul Kim, Sung-Han Sim, and Jin-Hak Yi. Reconstruction of unmeasured strain responses in bottom-fixed offshore structures by multimetric sensor data fusion. *Procedia Engineering*, 188:96 – 101, 2017.
- [15] Alexandros Iliopoulos, Christof Devriendt, Patrick Guillaume, and Danny Van Hemelrijck. Continuous Fatigue Assessment of an Offshore Wind Turbine Using a Limited Number of Vibration Sensors. In Le Cam, Vincent, Mevel, Laurent, Schoefs, and Franck, editors, *EWSHM - 7th European Workshop on Structural Health Monitoring*, Nantes, France, July 2014. IFFSTTAR, Inria, Université de Nantes.
- [16] N. Noppe, K. Tatsis, E. Chatzi, C. Devriendt, and W. Weijtjens. Fatigue stress estimation of offshore wind turbine using a kalman filter in combination with accelerometers. page 9, 2018.
- [17] Alexandros Iliopoulos, Wout Weijtjens, Danny Van Hemelrijck, and Christof Devriendt. Full-field strain prediction applied to an offshore wind turbine. In Sez Atamturktur, Tyler Schoenherr, Babak Moaveni, and Costas Papadimitriou, editors, *Model Validation and Uncertainty Quantification, Volume 3*, pages 349–357, Cham, 2016. Springer International Publishing.
- [18] M. Tarpø, T. Friis, B. Nabuco, S. Amador, E. Katsanos, and R. Brincker. Operational modal analysis based stress estimation in friction systems. In Gaetan Kerschen, editor, *Nonlinear Dynamics, Volume 1*, pages 143–153, Cham, 2019. Springer International Publishing.
- [19] K. Maes, A. Iliopoulos, W. Weijtjens, C. Devriendt, and G. Lombaert. Dynamic strain estimation for fatigue assessment of an offshore monopile wind turbine using filtering and modal expansion algorithms. *Mechanical Systems and Signal Processing*, 76-77:592–611, 2016.

- [20] M. Tarpø, B. Nabuco, A. Skafte, J. Kristoffersen, J. Vestermark, S. Amador, and R. Brincker. Operational modal analysis based prediction of actual stress in an offshore structural model. *Procedia Engineering, X International Conference on Structural Dynamics EUROdyn 2017*, 199:2262–2267, 2017.
- [21] Alexandros Iliopoulos, Wout Weijtjens, Danny Van Hemelrijck, and Christof Devriendt. Fatigue assessment of offshore wind turbines on monopile foundations using multi-band modal expansion. *Wind Energy*, 20(8):1463–1479, 2017.
- [22] D.C. Lui, H.L. Chung, and W.M. Chang. The errors caused by modal truncation in structure dynamic analysis. *IMAC XVIII – 18th International Modal Analysis Conference*, pages 1455–1460, 2000.
- [23] O. E. Hansteen and K. Bell. On the accuracy of mode superposition analysis in structural dynamics. *Earthquake Engineering and Structural Dynamics*, 7:405–411, 1979.
- [24] B. Bart Besselink, U. Tabak, A. Agnieszka Lutowska, van de Wouw N Nathan, H. Henk Nijmeijer, DJ Rixen, ME Michiel Hochstenbach, and WHA Wil Schilders. A comparison of model reduction techniques from structural dynamics, numerical mathematics and systems and control. *Journal of Sound and Vibration*, 332(19):4403–4422, 2013.
- [25] N. Roy and A. Girard. Impact of residual modes in structural dynamics. *Proceedings of the European Conference on Spacecraft Structure, Materials and Testing*, 2005.
- [26] P. Léger, J. M. Ricles, and L. J. Robayo. Reducing modal truncation error in wave response analysis of offshore structures. *Communications in applied numerical methods*, 6(1):7–16, 1990.
- [27] P. Léger and E. L. Wilson. Generation of load dependent ritz transformation vectors in structural dynamics. *Engineering Computations*, 4(4):309–318, 1987.
- [28] J. H. Vugts, I. M. Hinesm, R. Nataraja, and W. Schumm. Modal superposition vs. direct solution techniques in the dynamic analysis of offshore structures. *BOSS'79, Proceedings of the Second International Conference on Behaviour of Off-Shore Structures*, pages 23–29, 1979.
- [29] R. R. Arnold, R. L. Citerley, M. Chargin, and D. Galant. Application of ritz vectors for dynamic analysis of large structures. *Computers & Structures*, 21(3):461–467, 1985.
- [30] J. M. Dickens, J. M. Nakagawa, and M. J. Wittbrodt. A critique of mode acceleration and modal truncation augmentation methods for modal response analysis. *Computers & Structures*, 62(6):985–998, 1997.
- [31] M. Dhileep and P. R. Bose. A comparative study of "missing mass" correction methods for response spectrum method of seismic analysis. *Computers and Structures*, 86(21):2087–2094, 2008.
- [32] N. R. Maddox. On the number of modes necessary for accurate response and resulting forces in dynamic analysis. *Journal of Applied Mechanics ASME*, 42(2):516–517, 1975.
- [33] K. Maes and G. Lombaert. The influence of out-of-band modes in system inversion. *Mechanical Systems and Signal Processing*, 115:173 – 187, 2019.
- [34] Marius Tarpø, Michael Vigsø, and Rune Brincker. Modal truncation in experimental modal analysis. In Michael Mains and Brandon J. Dilworth, editors, *Topics in Modal Analysis & Testing, Volume 9*, pages 143–152, Cham, 2019. Springer International Publishing.
- [35] R. W. Clough and J. Penzien. *Dynamics of structures*. CSI Computers & Structures, Inc., Berkeley, Calif., 2nd revised edition, 2003.
- [36] A.K. Chopra. *Dynamics of Structures: Theory and Applications to Earthquake Engineering*. Prentice Hall International Series in Civil Engineering And. Pearson/Prentice Hall, 2007.
- [37] J.R. Morison, J.W. Johnson, and S.A. Schaaf. The force exerted by surface waves on piles. *The American Institute of Mining, Metallurgical, and Petroleum Engineers*, 2:149 – 154, 1950.
- [38] Erwin Kreyszig, Herbert Kreyszig, and Edward J. Norminton. *Advanced engineering mathematics*. John Wiley And Sons Ltd, Hoboken, NJ, 10th edition, 2011.
- [39] S.-W. Seo, K.-J. Kim, and B.-K. Bae. Estimation of operational strains from vibration measurements: An application to lead wires of chips on printed circuit board. *Journal of Sound and Vibration*, 210(5):567 – 579, 1998.
- [40] J. Kullaa. Bayesian virtual sensing in structural dynamics. *Mechanical Systems and Signal Processing*, 115:497 – 513, 2019.
- [41] P. C. Hansen, V. Pereyra, and G. Scherer. *Least squares data fitting with applications*. Johns Hopkins University Press, Baltimore, MD, 2013.
- [42] H. L. Soriano and F. Venâncio Filho. On the modal acceleration method in structural dynamics. mode truncation and static correction. *Computers and Structures*, 29(5):777–782, 1988.

- [43] Edward L. Wilson, Ming-Wu Yuan, and John M. Dickens. Dynamic analysis by direct superposition of ritz vectors. *Earthquake Engineering & Structural Dynamics*, 10(6):813–821, 1982.
- [44] Anders Skafte, Ulf Tyge Tygesen, and Rune Brincker. Expansion of mode shapes and responses on the offshore platform valdemar. In Fikret Necati Catbas, editor, *Dynamics of Civil Structures, Volume 4*, pages 35–41, Cham, 2014. Springer International Publishing.
- [45] Julius S. Bendat and Allan G. Piersol. *Random Data: Analysis and Measurement Procedures*. Wiley-Blackwell, Hoboken, N.J., USA, 4th edition, 2010.
- [46] Marius Tarpø, Tobias Friis, Peter Olsen, Martin Juul, Christos Georgakis, and Rune Brincker. Automated reduction of statistical errors in the estimated correlation function matrix for operational modal analysis. *Mechanical Systems and Signal Processing*, 132:790 – 805, 2019.
- [47] S. R. Ibrahim and E. C. Mikulcik. A method for the direct identification of vibration parameters from the free response. *The Shock and Vibration Inform. Ctr. Shock and Vibration Bull.*, pages 183–198, 1977.
- [48] Marius Tarpø, Bruna Nabuco, Rubén Boroschek, and Rune Brincker. Tilt errors of linear accelerometers attached to dynamic systems with tilt motion caused by the system response. *Submitted to Mechanical Systems and Signal Processing*, page 16, 2020.
- [49] R. Brincker, L. M. Zhang, and P. Andersen. Modal identification of output-only systems using frequency domain decomposition. *Smart Materials and Structures*, 10(3):441–445, 2001.

Chapter 11

Conclusion

Reasoning draws a conclusion, but does not make the conclusion certain, unless the mind discovers it by the path of experience

Roger Bacon

In this Ph.D. project, we studied selected aspects and issues of stress/strain estimation for offshore structures.

In chapter 3, we conducted a narrative literature review of stress/strain estimation. We conclude that it is an active and growing research field. Generally, we observed a lack of consensus and common terminology in the field. We introduced a terminology based on other scientific fields. The study revealed several points and issues on the subject that have not been fully addressed in the literature. In terms of accuracy, stress/strain estimation has not advanced since 2005 where the modal expansion technique was introduced. In the meantime, we have seen new techniques introduced but these are not superior (performance-wise) to the modal expansion technique. Furthermore, the evaluation of stress/strain estimation is complex due to the entire process of virtual sensing. Often, the evaluation is based on the final virtual sensors in laboratory applications or numerical simulations. In the literature, there are few applications under operational conditions that evaluate the precision, achievability and practicality. The study, also, unveiled a challenge for stress/strain estimation: amplitude difference between true and estimated stress/strain response. Here, the estimated fatigue damage amplifies with a factor of the amplitude difference to the power of m , see Eq. (3.4). Thus, even small differences in the estimation lead to erroneous estimation of the fatigue damage. There are many factors which might cause an amplitude difference, including tilt motions, misalignment, and incorrect calibration of accelerometers or incorrect update of the system model. This challenges the confidence in the technique intended for fatigue analysis.

In Paper 1 and Paper 2, we studied the statistical errors in the estimation of the correlation function matrix for operational modal analysis. We intended to reduce the errors of the estimated modal parameters in operational modal analysis so that we reduce the calibration error of the system model for stress/strain estimation. In Paper 1, see chapter 4, we studied the statistical errors in an analytical perspective to understand the behaviour of the error and the phenomenon of the noise tail. We found that the envelope of the modal auto-correlation function is Rice distributed so the envelope is biased in the noise tail. Furthermore, the zero crossings are unbiased but the variance increases linearly in the noise tail. In Paper 2, chapter 5, we introduced a novel algorithm for reducing statistical errors and the algorithm reduced the biased error on the estimated modal parameters while it increased stability in the identification process. This research increases our confidence in the estimated modal parameters which could inspire more confidence in calibration and updating of a system model based on the estimated modal parameter.

In Paper 3, see chapter 6, we studied modal truncation, which is the reduction of modes to describe a system. In the terminology for virtual sensing introduced in chapter 3, it is a simplification of the system model to the essential and relevant information for the given application. In this appended paper, we prove that the contribution of each mode depends on the convolution of the temporal variation of the load and the impulse response function and the inner vector product between the spatial distribution of the load and the mode shape. We can use this as a guideline for selecting an appropriate set of mode shapes for stress/strain estimation.

In Paper 4, see chapter 7, we found that an expansion of experimental mode shapes could reduce modelling errors of the system model using in the modal expansion. Therefore, this expansion is equivalent to a calibration of the system model. We saw an amplitude difference between the measured and estimated strain response using mode shapes from the finite element model. Here, the expanded experimental mode shapes reduced this amplitude difference. The expansion process could, however, introduce fitting errors in the expansion process as seen for the original local correspondence principle and System Equivalent Reduction Expansion Process (SEREP). Thus, we introduced a new implementation of the local correspondence principle using leave- p -out-cross-validation, which provided a better expansion. In the case study in chapter 7, the errors in the expansion process easily exceeded the modelling errors if the fitting was performed incorrectly. Therefore, we would discourage applying expansion of mode shapes without a reference signal to check the fitting errors.

We have found in Paper 5, see chapter 8, that the normal undamped mode shapes can still be used to estimate the strain response for subsystems within a nonlinear and time-variant system with general viscous damping where the nonlinear and time-variant effects act externally on the subsystem. We prove that the full set of normal undamped mode shapes forms a basis for \mathbb{R}^N and the nonlinear and nonstationary mode shapes are a linear combination of the underlying normal undamped mode shapes that depend on the nonlinearity and nonstationarity. The accuracy of virtual sensing becomes a problem of the modal truncation since the applied set of normal undamped mode shapes should span the response of the nonlinear and nonstationary system with general damping. In the case of a subsystem with external nonlinear and time-variant effects, the nonlinear and time-variant effects act as an external load on the subsystem and we can interpret the subsystem as linear with parametric excitation. In this case, the choice of mode shapes is similar to a linear system and should be based on the temporal variation and spatial distribution of this nonlinear and time-variant load.

In Paper 6, see chapter 9, we studied the effect of the gravitational acceleration on accelerometers undergoing rotational/tilting movements. Since the accelerometers can measure the gravitational acceleration, the tilt motion of accelerometers introduces an error in the measured acceleration. When the accelerometer is mounted on a structure, the tilt angle depends on the structure and the excitation. Thus, the rotational displacement of the structure pollutes the measurement of the translational acceleration. We introduced impulse and frequency response function matrices to account for the tilt error in the measured acceleration from accelerometers. For an offshore structure with modes of low frequencies and excitation with lower frequency content, the tilt errors are present in the quasi-static response. For stress/strain estimation, we must reduce this tilt error to obtain better virtual sensors.

In Paper 7, see chapter 10, we applied stress/strain estimation to the Valdemar platform located in the North Sea with an emphasis on the application of pseudo mode shapes to account for the quasi-static response. The research is, however, incomplete since unforeseen issues and time constraints forced us to discontinue the project. In this study, we found new issues for quasi-static stress/strain estimation that we did not anticipate in the planning of the Ph.D. project. Generally, we obtained a good correlation between the estimated and measured dynamic strain response while we overestimated the quasi-static strain response. This overestimation could be attributed to many different sources of errors in the application. We could have issues with sensitivity and measurement noise on the sensors (including the strain gauges used for reference), tilt errors on the accelerometers, modelling error in the system model, the accuracy of the pseudo mode shapes, the sensitivity of the reduced system model, drift of the displacement due to the double numerical integration of the acceleration, etc.. Generally, we need to measure the quasi-static effect if we hope to apply virtual sensing. Moreover, accelerometers - as the main physical sensor for stress/strain estimation - are problematic due to the integration of acceleration to displacement for low frequencies. Therefore, accelerometers are not ideal as the primary sensor on structures with quasi-static behaviour.

In this Ph.D. project, multiple issues were uncovered for stress/strain estimation for offshore structures and a selection of these were studied in the project. We studied the statistical errors in correlation-driven operational modal analysis to provide a better basis for the calibration of the system model utilised in stress/strain estimation. A study on modal truncation was performed to assist in the choice of mode shapes in the system model for modal expansion. This provides a practitioner with the tools to choose an appropriate set of mode shapes for modal expansion. Following this, we studied the expansion of experimental mode shapes to calibrate the system model intended for stress/strain estimation. This study helps the practitioner to reduce modelling errors in the system model if the experimental mode shapes have a reasonable level of noise. Then we applied modal expansion for stress/strain estimation of "linear" subsystems within a nonlinear and time-variant system. We studied tilt errors on accelerometers to provide the practitioner with theory and techniques to reduce errors in the physical

sensors for virtual sensing. Finally, we applied stress/strain estimation on the Valdemar platform in the North Sea and uncovered issues for future research.

We will end this conclusion with some important remarks for stress/strain estimation and virtual sensing that practitioners should keep in mind. Firstly, we are unable to expand something that we do not measure. Therefore, we cannot estimate localised behaviour based on the measurement of global behaviour. For offshore structures, we are unable to estimate localised subsea stress/strain response based on measurements of the global response above water. Furthermore, uncertain connections between any subsystems limit virtual sensors to the subsystems from which we measure. These connections would have high levels of uncertainty so their behaviour is difficult to predict and they could be complex, nonlinear, and/or time-variant couplings between subsystems. For offshore platforms, the bridges, which connect platforms, are an example of such an uncertain connection since they introduce nonlinear friction-coupling. Therefore, we can only estimate the stress history of the measured platforms. Moreover, we should be aware of the effect of errors in the estimated stress history when we calculate the estimated fatigue damage using the Palgren-Miner rule. Here, the estimated stress amplitude of each stress cycle is taken to the power of m (3 for welded stress structures) so any error in the stress amplitude is amplified. Thus, even small errors in the estimation accumulate and amplify in the calculation of fatigue damage. Here, the support/boundary conditions are very important in stress/strain estimation and the corresponding estimated fatigue damage. A small change in the boundary conditions might result in a potentially large error in the fatigue damage due to modelling errors in the system model. Furthermore, the boundary conditions complicate the validation and calibration of the system model when these conditions are uncertain and/or should be modelled as a spring connection.

Chapter 12

Future works

“
*Life can only be understood backwards;
 but it must be lived forwards*”

Søren Kierkegaard

Every selection has a corresponding and unavoidable deselection while hindsight leaves us wiser. This Ph.D. project is no exception. It is simply impossible to cover all research aspects of stress/strain estimation in a single Ph.D. project. Thus upon completion of this project, further research is needed for stress/strain estimation. This chapter outlines some important issues for the further research that must be solved before an actual application of stress/strain estimation can be realised for lifetime extension of offshore structures.

At the given readiness level of stress/strain estimation, we need to validate the concept under actual conditions - outside numerical simulations or laboratories - at actual systems and structures. For these applications of stress/strain estimation, the complexity tends to increase outside these controlled environments. This complexity under any operational conditions should be studied before an actual application of stress/strain estimation is viable. Such applications will test the achievability and practicality of the applied virtual sensing technique. Furthermore, some reference sensors must be positioned near fatigue-critical locations to validate the concept of estimating fatigue damage before actual applications of stress/strain estimation are realisable. For offshore structures, we need subsea strain measurements of actual structures in operation. The strain gauges on the Valdemar platform have low levels of strain response and they are located far from the fatigue-critical locations. Subsea measurements are required to validate the concept of virtual sensing under the actual conditions.

Moreover, we need to study the potential amplitude error in stress/strain estimation since stress amplitude/range is important for fatigue life using Palmgren-Miner rule. Here, the partial fatigue damage raises each stress amplitudes to the m^{th} power so any error is amplified. Thus, we need accurate estimates of the stress amplitude of each cycle and possible solutions, to decrease amplitude errors, are vital to increase trust in the estimation of the stress/strain history.

Stress/strain estimation requires further research regarding quasi-static response. The problem should be divided into research components to study separately. We need investigations of the spatial distribution of wave loading and the corresponding static deflection shapes. We need to consider sensors other than accelerometers at low frequencies or apply sensor fusion to accurately measure the quasi-static response of offshore structures. Sensor fusion could potentially provide a better sensor network for virtual sensing. Here, the weighted least-square regression techniques is a simple extension of the modal expansion to include sensor fusion. For future work, the “weighted modal expansion” should be studied. In the quasi-static response, there is a potential for residual effects from the higher modes. Here, the sensitivity of the reduced system model is an important research field. We should consider an investigation into the potential rank deficiency in modal expansion for the reduced pseudo modal matrix. We could consider blind source separation and similar solutions to separate quasi-static response from the dynamic response. Finally, we could apply wave mapping - e.g. using radar, buoys, and/or lidar - to estimate the wave loading so we can calculate an additional estimate of the quasi-static response.

Appendix A

Other publications

“What is history? An echo of the past in the future; a reflex from the future on the past”

Victor Hugo

In this appendix, we put the work of the unappended publications, which were published or written during the Ph.D. project, into the context of the history for and contribution to the project.

A.1 Main author

Experimental determination of structural damping of a full-scale building with and without tuned liquid dampers

- *Experimental determination of structural damping of a full-scale building with and without tuned liquid dampers*

M. Tarpø, C. Georgakis, A. Brandt, & R. Brincker

Submitted to Structural Control and Health Monitoring summer 2020

The paper is an experimental assessment of the modal properties of a high-rise building - with and without tuned liquid dampers. This assessment is based on both ambient tests (operational modal analysis) and full-scale excitation tests. This is the only journal paper with Marius Tarpø as the main author that is not appended in the Ph.D. thesis, as a result of it being deemed too far removed from the main Ph.D. project.

Back in 2013, an original paper was submitted to the Journal of Performance of Constructed Facilities that warranted major revisions, which were never undertaken by the original authors. In 2019, Marius Tarpø was tasked to unearth the old data, reanalyse, and completely rewrite the original paper. This resulted in a completely new paper with a slightly shifted focus.

The effect of operational modal analysis in strain estimation using the modal expansion

- *The effect of operational modal analysis in strain estimation using the modal expansion*

M. Tarpø, B. Nabuco, C. Georgakis, & R. Brincker

Conference proceedings of IOMAC 2019

This paper was a conference version of Paper 4 and it was written during the completion of this. For this paper, the author came up with the idea, performed the data analysis, and wrote the paper.

Statistical error reduction for correlation-driven operational modal analysis

- *Statistical error reduction for correlation-driven operational modal analysis*

M. Tarpø, P. Olsen, M. Juul, S. Amador, T. Friis, & R. Brincker

Conference proceedings of ISMA 2018

This paper was a conference version of Paper 2 and it was written during the completion of this paper. For this paper, the author came up with the idea, performed the data analysis, and wrote the paper.

Operational modal analysis based stress estimation in friction systems

- *Operational modal analysis based stress estimation in friction systems*
M. Tarpø, T. Friis, B. Nabuco, S. Amador, E. Katsanos, & R. Brincker
Conference proceedings of IMAC 2018

This was our first attempt to apply stress/strain estimation to nonlinear structures. It was a numerical case study for an offshore platform with friction applied to the topside. The stress estimation was largely unaffected by the applied friction. The paper was excluded from the thesis since Paper 5 better reflects the theory and application of stress estimation for nonlinear systems. For this paper, the author wrote the paper and performed the analysis within the paper. The second co-author - Tobias Friis - simulated the numerical response of the platform with and without friction.

On minimizing the influence of the noise tail of correlation functions in operational modal analysis

- *On minimizing the influence of the noise tail of correlation functions in operational modal analysis*
M. Tarpø, P. Olsen, S. Amador, M. Juul, & R. Brincker
Procedia Engineering 199, 1038-1043

In this paper, we proposed an algorithm for detecting the noise tail. This paper is not included as an appended paper in the thesis since Paper 1 and Paper 2 cover the same topic more extensively. For this paper, the author wrote the paper, created the algorithm, and performed the analysis within the paper. Cosupervisor Rune Brincker had the idea to estimate the position/location of the noise tail by fitting two lines to the logarithmic envelope of the correlation functions.

Operational modal analysis based prediction of actual stress in an offshore structural model

- *Operational modal analysis based prediction of actual stress in an offshore structural model*
M. Tarpø, B. Nabuco, A. Skafte, J. Kristoffersen, J. Vestermark, S. Amador, & R. Brincker
Procedia Engineering 199, 2262-2267

The paper focuses on strain estimation of a scale model of an offshore platform and was the first paper written by the author. The research was mainly conducted to familiarise the author with the topic so the paper provides little new knowledge to the research community. For this paper, the author wrote the paper, conducted the experiments, and performed the analysis within the paper.

A.2 Co-author

Best linear approximation of nonlinear and nonstationary systems using Operational Modal Analysis

- *Best linear approximation of nonlinear and nonstationary systems using Operational Modal Analysis*
T. Friis, **M. Tarpø**, E. Katsanos, & R. Brincker
Mechanical Systems and Signal Processing

The paper was written in order to better understand what happens to the correlation function matrix for nonlinear systems. We found that the correlation function matrix is the best linear approximation that minimises the mean square error between the measured response and synthesised response based on the best linear system. For stress/strain estimation, this furthers our understanding of the estimated mode shapes of nonlinear and nonstationary systems using operational modal analysis since these mode shapes are applied in modal expansion. For this paper, the author of this thesis contributed with inputs for both analytic derivations and the case studies and performed the main proofreading and editorial service of the paper.

Fatigue Stress Estimation of an Offshore Jacket Structure Based on Operational Modal Analysis

- *Fatigue Stress Estimation of an Offshore Jacket Structure Based on Operational Modal Analysis*
B. Nabuco, **M. Tarpø**, U. T. Tygesen, & R. Brincker
Shock and Vibration, 2020

In this paper, we estimated the strain history of the Valdemar platform in the North Sea - excluding the quasi-static response. Thus, it was a proof of concept for dynamic strain estimation for offshore structures under the actual conditions. For this paper, the author contributed with inputs for the finite element updating and the stress estimation while the author reviewed and edited the paper.

Equivalent linear systems of nonlinear systems

- *Equivalent linear systems of nonlinear systems*
T. Friis, **M. Tarpø**, E. Katsanos, & R. Brincker
Journal of Sound and Vibrations, 2020, Volume 469

This paper focuses on three different approaches to estimate equivalent linear systems. The paper is not directly tied to stress/strain estimation since it relates to nonlinear systems, which we might encounter in offshore structures. It is, however, a tool that we could apply in the design and/or analysis of offshore structures. For this paper, the author contributed with inputs to both the idea and the case studies and the author edited the paper.

Operational modal analysis based linear system identification of systems with elasto-perfectly-plastic nonlinear behaviour

- *Operational modal analysis based linear system identification of systems with elasto-perfectly-plastic nonlinear behaviour*
T. Friis, **M. Tarpø**, E. Katsanos, & R. Brincker
Conference proceedings of IOMAC 2019

In this paper, we studied the estimation of stiffness and viscous damping with operational modal analysis on a nonlinear system in a simulated study. This paper was a preliminary study that we extended in another paper regarding equivalent linear systems from the correlation-driven operational modal analysis. For this paper, the author of this thesis contributed to the conception of the research work, reviewed, and edited the paper.

Automated operational modal analysis using sliding filters and time domain identification techniques

- *Automated operational modal analysis using sliding filters and time domain identification techniques*
P. Olsen, **M. Tarpø**, M. Juul, & R. Brincker
Submitted to the Journal Mechanical Systems and Signal Processing summer 2019

This is a paper on automated operational modal analysis where we applied sliding filters to create an alternative stability diagram, which we cleaned and clustered to estimate the modal parameters automatically. Initially, an automated identification process was intended for this Ph.D. project but we reduced the focus on this aspect as the Ph.D. project progressed. This paper is a precursor of the initial Ph.D. plan. For this paper, the author contributed to the creation of the algorithm, the author wrote the main text for the experimental case study, and the author did the modal tracking in this study to test the tracking over multiple datasets.

Operational modal analysis and fluid-structure interaction

- *Operational modal analysis and fluid-structure interaction*
M. Vigsø, T. Kabel, **M. Tarpø**, R. Brincker, & C. Georgakis
Conference proceedings of ISMA 2018

In this paper, the main author, Michael Vigsø, wanted to see the effect of surrounding water on a test specimen in a wave flume. The effective mass of the water changed the modal parameters of the test specimen. Interestingly, the frequencies of some modes moved so they became closely spaced with new modes as the water level increased. Hence, the mode shapes of the new closely spaced modes began to merge. For this paper, the author made contributions to the operational modal analysis in this paper and edited the paper.

Output-only damping estimation of friction systems in ambient vibrations

- *Output-only damping estimation of friction systems in ambient vibrations*
T. Friis, E. Katsanos, **M. Tarpø**, S. Amador, & R. Brincker
Conference proceedings of ISMA 2018

In this paper, we studied damping estimates of friction systems with random vibrations. We extended the study into two journal papers "Equivalent linear systems of nonlinear systems" and "Best linear approximation of nonlinear and nonstationary systems using Operational Modal Analysis". For this paper, the author contributed to the conception of the research work, reviewed, and edited the paper.

Nonlinear strain estimation based on linear parameters

- *Nonlinear strain estimation based on linear parameters*
B. Nabuco, T. Friis, **M. Tarpø**, S. Amador, E. Katsanos, & R. Brincker
ASME 2018 37th International Conference on Ocean, Offshore and Arctic Engineering

This was another attempt of applying stress/strain estimation to nonlinear structures. Here, we created a linear strain-to-displacement-transformation matrix from a linear setup and used this transformation matrix to estimate strain for nonlinear setups of the same test specimen with success. For this paper, the author reviewed and edited the paper.

Scenario based approach for load identification

- *Scenario based approach for load identification*
M. Vigsø, **M. Tarpø**, J.B. Hansen, C.T. Georgakis, & R. Brincker
Conference proceedings of IMAC 2018

This paper applies different scenarios of the spatial distribution of load to estimate the load. Load identification is an alternative virtual sensing technique to stress/strain estimation. For this paper, the author helped with the experiment, supported in the data analysis, and edited the manuscript.

Reliability Analysis of Offshore Structures Using OMA Based Fatigue Stresses

- *Reliability Analysis of Offshore Structures Using OMA Based Fatigue Stresses*

B. Nabuco, **M. Tarpø**, A. Aïssani, & R. Brincker

ASME 2017 36th International Conference on Ocean, Offshore and Arctic Engineering

Our first attempt to assess the reliability of stress/strain estimation. For this paper, the author was mainly responsible for the stress estimation applied in the paper and edited the manuscript.



Ph.D. Dissertation
Author: Marius Tarpø
Supervisor: Christos Georgakis, Aarhus University
Co-supervisor: Rune Brincker, Technical University of Denmark

Department of Engineering
Aarhus University, Denmark